Four-Chamber Endocardial Surface Reconstruction from MR Images and Application to Geometry and Mechanics Analysis on Healthy Subjects and Mitral Regurgitation Patients

by

Xiaoxia Zhang

A Dissertation submitted to the Graduate Faculty of
Auburn University
in partial fulfillment of the
requirements for the Degree of
Doctor of Philosophy

Auburn, Alabama
August 4, 2018

Keywords: Mesh Model Reconstruction, Cardiac MRI, Mitral Regurgitation, Atrial Geometry,
Myocardial Mechanics

Approved by
Thomas S. Denney Jr., Professor of Electrical and Computer Engineering
Ray Dillion, Professor of Veterinary Medicine
Gopikrishna Deshpande, Associate Professor of Electrical and Computer Engineering
Adil Bashir, Associate Professor of Electrical and Computer Engineering

ABSTRACT

Heart failure is a common cause of hospitalization and the leading cause of death in the world [1]. It is usually secondary to a primary cardiovascular disease (CVD) and it is estimated that by 2030, about 23.6 million people will die from a type of CVD. CVD is a problem that crosses both gender and ethnicity, and worsens with age. Therefore, effective diagnosis and early treatment of CVDs are significantly important. Medical imaging techniques, providing useful information in diagnosis, visualization and monitoring, have been dramatically developed and improved. Magnetic resonance imaging (MRI) is one such technique, becoming a leading imaging modality for advanced clinical research, drug studies and patient management due to its high image resolution, minimal invasion and reproducibility compared with other conventional imaging techniques.

Functional and geometric analysis of the left ventricle (LV) of the human heart have been well developed using MRI, however, analysis of the LV has its limitations in the presence of some cardiovascular disease [2-4]. Research in shape development and functional analysis of right ventricle (RV), left atrium (LA) and right atrium (RA) are limited by their complicated geometries. LA functions along with volume-time curves provide powerful and incremental information on LA performance and are considered as predictors of cardiovascular morbidity and mortality [5-8]. However, in current clinical practice, changes in the LA geometry and function have been defined using long-axis views, which use a shape assumption, and the result depends on the orientation of the long axis views. Similar problems occur in the evaluation of RV and RA

geometry and function. RV functional parameters are major markers in a variety of cardiovascular diseases, including pulmonary hypertension, ventricular ischemia or infarction, pulmonary or tricuspid valvular heart diseases [9]. RA volume and size could be early markers of RV dysfunction. Therefore, the analysis of all four chambers and the interaction among them can provide extra information that might suggest subtle abnormalities of cardiac function in patients with normal LV functions.

Mitral valve regurgitation (MR) is one of the causes of heart failure, in which the mitral valve does not operate properly [20]. Correct identification of MR surgical candidates and optimizing the timing of surgery are key in patient management. Currently, the most common surgery guidelines are based on LV function and diameter, which is LV ejection fraction < 60% and/or LV end-systolic dimension >40 mm [22]. However, patients are reported not receiving timely surgery followed the surgery guidelines with worse outcomes and increased morbidity and mortality [96] [99] [100]. As we described, all four chambers have clinical potentials independently and mutually. Therefore, we are motivated to explore more parameters in volume function, geometry and mechanics of LA, RA and RV in addition to LV for optimized surgery timing.

In this dissertation, we first developed a novel 4D (temporal and spatial) surface fitting algorithm to reconstruct subject-specific heart surface of all four chambers from cardiac MRI images. The reconstructed surface had vertex-to-vertex correspondence, which provided more accurate measurements and comprehensive analysis of the heart. This algorithm was validated on two groups through three aspects, including heart volume functions, mechanics and geometries. The two groups consist of a normal subject group with young and old subjects, and a mitral regurgitation patient group with age-matched control subjects. The two groups were imaged with

cine MRI and endocardial contours were semi-automatically identified with a previously developed algorithm implemented in Matlab [77]. Surfaces of all four chambers were reconstructed using the developed algorithm to evaluate the changes in volume functions, chamber geometries and wall motions during the entire imaged cardiac cycle. This procedure was used to investigate the remodeling in functional and geometric parameters of all four chambers versus age and between MR patients and age-matched controls, and the effect of valve repair surgery after 6 months.

ACKNOWLEDGMENTS

First and foremost, I would like to express my sincere thanks to my PhD advisor Dr. Thomas S. Denney Jr., for his professional guidance and consistent encouragement. During my study at Auburn he was always patient in guiding me through my research and shared me with tremendous insightful suggestions and ideas that helped me in becoming a good researcher. His responsible and dedicated working attitude, considerate personality has a great influence on me in many ways. I have learned to be prudent about my own work and to be organized for my projects. It has been a great honor and pleasure to work with him.

I greatly thank my other three committee members, Dr. Adil Bashir, Dr. Gopikrishna Deshpande and Dr. Ray Dillon, for providing professional insights and help for my research work development. I have learned sequence programming with Dr. Adil Bashir. His experience guided me through difficulties, and I appreciated his enlightening ideas and in-depth discussions with him. I am also very thankful for Dr. Ray Dillion. Working with him on the spectroscopy project has been a wonderful research experience. His great insight on my dissertation also helped me to connect my research and the clinical importance. I would also like to thank Dr. Gopi Deshpande for his gracious willing to be my committee member, for his time and great suggestions in statistics on my research.

I also want to express my gratitude to Dr. Louis J. Dell'Italia, Dr. Himanshu Gupta and Dr. Brittany Butts at University of Alabama at Birmingham. Working with Dr. Louis J. Dell'Italia and Dr. Himanshu Gupta is also a remarkable life experience. With their professional knowledge and suggestion on heart failure, our experiments have been successfully conducted, and their profound expertise inspired me deeply on my research from the clinical view. Parts of my research work could not be fulfilled without the help from them. For Dr. Brittany Butts, her selfless sharing of career planning is also a great lesson to me.

I am also very thankful for the other staff members at AU MRI research center: Dr. Ronald J. Beyers, for his professional guidance on MRI experiment and machine operation; Dr. Nouha Salibi for her technical support for the optimal performance of our machines; and Mrs. Julie Rodiek, for her timely coordinating of scan documents and event planning. I also want to particularly thank Nouha Salibi. She has been very encouraging during my time at Auburn.

My thanks also goes to my friends who came to Auburn before me: Wei Zha, Chun G.Schiros, Ming Li, Nikhil Jha and Chenxi Hu, and those who came at the same time or after: Karthik Sreenivasan, Sreenath Pruthvi, Yun Wang and Sinan Zhao. We shared each other with stories and experience, and I have learned a lot from them.

Finally, I want to specially thank my family for unconditional support and love. They always encourage me and respect my decisions. I thank my husband Daoming Lyu dearly. He has been supportive, patient, loving and encouraging. We share joys and sorrows along the way. I am grateful to have him by my side and walk through difficulties in life.

TABLE OF CONTENTS

LIST OF FIGURES

LIST OF TABLES

LIST OF ABBREVIATIONS

LV	Left Ventricle
RV	Right Ventricle
LA	Left Atrium
RA	Right Atrium
ED	End-Diastole
ES	End-Systole
EF	Ejection Fraction
MRI	Magnetic Resonance Imaging
MR	Mitral Regurgitation

Chapter 1 INTRODUCTION

Medical image analysis has been widely used in both research experiments and clinical applications for diagnosing heart disease, brain dysfunction, musculoskeletal injury, etc. Compared to other well established medical imaging techniques like computed tomography (CT), ultrasound and nuclear imaging, MRI provides high spatial resolution and is non-invasive and does not use ionizing radiation, which is required for CT, single-photon emission CT (SPECT), and positron emission tomography (PET). Moreover, MRI scans have superior temporal resolution compared with CT and better spatial resolution and higher signal to noise ratio (SNR) compared to ultrasound.

Mitral valve regurgitation (MR), as one of the causes of heart failure, is a disorder in which the mitral valve does not operate properly [20]. The challenge of optimized surgery timing lies between early surgery and delayed intervention, since the most common surgery guidelines, which are based on only LV parameters, have controversial results [96] [99] [100]. Therefore, in this dissertation, we developed a novel surface fitting algorithm to reconstruct a subject-specific heart surface of all four chambers from cardiac MRI images. In the pursuit of exploring potential biomarkers For the LA, RV and RA in additional to LV parameters for optimized MV surgery, we reconstructed the heart surfaces of MR patients and compared them with that of normal volunteers to capture the remodeling of all four chambers in geometry, volume and wall motion of MR patients.

In this chapter, the anatomy and function of human heart will first be illustrated, followed by a brief introduction on heart failure and mitral regurgitation. Then, different cardiac imaging techniques are introduced. Details of MRI imaging protocols used in the studies proposed in this dissertation are described. A summary of the following chapters is presented at the end of this chapter.

1.1 Cardiac Anatomy

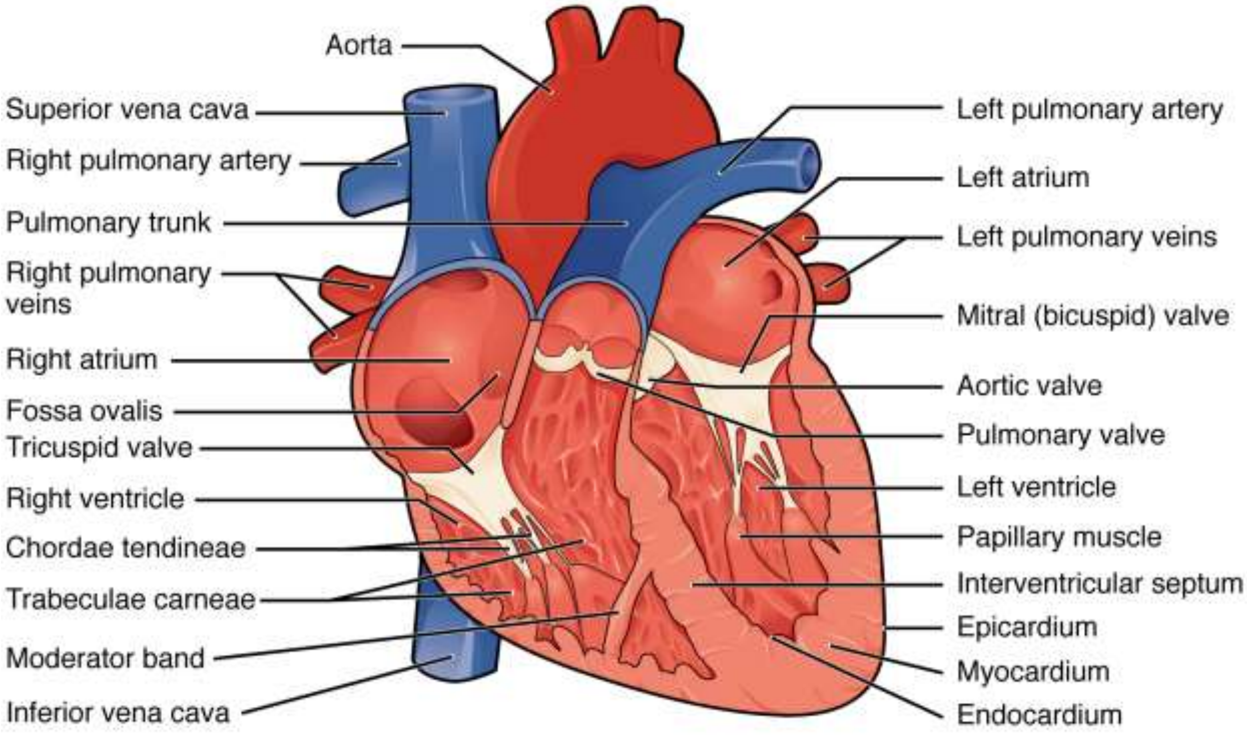

Figure 1.1 Interior view of a human heart [14]

The human heart is located underneath the ribcage, in the center of chest between right and left lungs. It is approximately the size of a fist and weighs between 200 and 425 grams [13]. This size varies with gender, health condition and age.

The heart, a muscular organ, is responsible for the blood cycle throughout the body by receiving blood from the venous blood vessels and pumping up the blood to the rest of body through the arterial blood vessels of the circulatory system [15]. The heart has four chambers, a paired set on each side, to perform this function. Figure 1.1 shows the interior view of the anatomy of a normal human heart. On the left side, the left atrium (LA) and left ventricle (LV) are connected by the mitral valve. The right set is the right atrium (RA) and right ventricle (RV) connected by the tricuspid valve [15]. Those two sets are separated by the septal wall. The walls across the septum are called the free walls. In addition to the two valves connecting the atrium and ventricle, the pulmonary valve connects the right ventricle and the pulmonary artery, and the aortic valve connects the left ventricle and the aorta. The left atrium receives oxygenated blood from the lungs through pulmonary veins, and this oxygenated blood flows into the left ventricle through the mitral valve. The left ventricle pumps the oxygenated blood to the systemic circulation through the aorta. Deoxygenated blood flows from the venous system to the right atrium and goes into the right ventricle through the tricuspid valve. Then the right ventricle ejects the deoxygenated blood to the lungs through the pulmonary artery. The opening and closing of the four valves control the circulation. Figure 1.2 shows the pathway of the cardiovascular system [16]. The mitral valve and the tricuspid valve close to prevent blood from flowing back to the atria while the ventricles pump blood to the arteries.

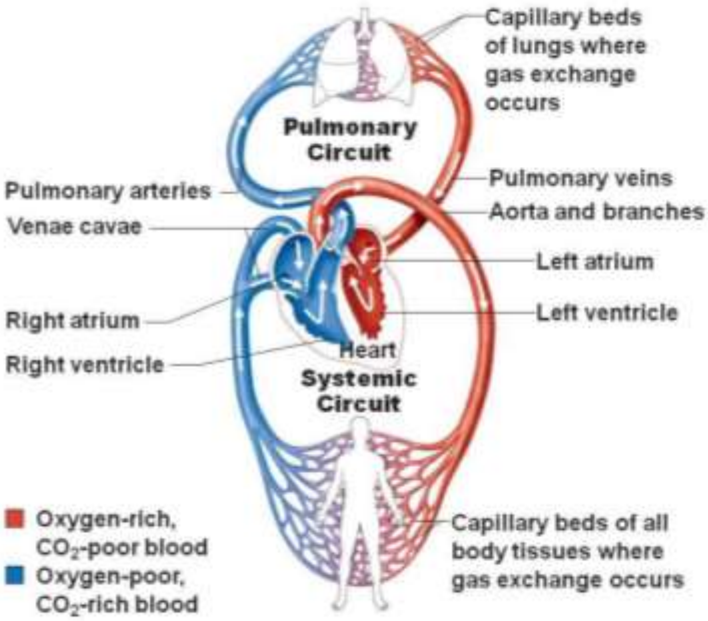

Figure 1.2 The whole cardiovascular system [16]

The pulmonary valve and the aortic valve control the blood flow from the ventricles to the arteries.

1.2 Cardiac Electrical Activity

The myocardium consists of myocytes, whose primary function is to contract. The electrical changes within myocytes control the muscle contraction and relaxation. An electrocardiogram (ECG) is a test that records the electrical activity of the heart, which is shown in Figure 1.3. Action potentials are first generated with polarization of the sinoatrial (SA) node, located at the posterior wall, then spread out across the atria and activate the atrial contraction. The potential can be detected as a P wave in an ECG. Then, these electrical impulses slow down and are collected by the atrioventricular (AV) node, which is located at the inferior-posterior of the inter-atrium wall. The electrical conduction from the AV node to ventricles is significantly slower than that within the atria, which allows for full contraction and depolarization of the atrium before the ventricle contraction triggered by the action potentials through AV node. This can be detected as the QRS complex in an ECG. The T wave represents the repolarization of the ventricles. A complete cardiac cycle can be divided into two phases: systole, from the beginning of R wave till the end of T wave, as the ventricles undergo depolarization to repolarization; and diastole, the rest of the cardiac cycle when the heart is resting and filling.

Both rhythmic and efficient contraction of the heart chambers and appropriate functioning of valves enable a proper functioning heart. During ventricular diastole, the tricuspid valve opens to allow deoxygenated blood to flow from the right atrium to the right ventricle. At the same time, the mitral valve opens to allow the oxygenated blood filling of the left ventricle from the left atrium. During systole, the tricuspid valve closes and the pulmonary valve opens and deoxygenated blood is ejected from the right ventricle to the pulmonary artery which leads to the lungs for oxygen exchange. At the same time, the mitral valve closes and the aortic valve opens to allow ejection of blood from the left ventricle to the aorta. Meanwhile, oxygenated blood flows from the lungs through pulmonary veins to the left atrium, and deoxygenated blood returns from the systemic circulation through the superior and inferior vena cavae to the right atrium. As the papillary muscles contract during systole, they generate pressure on the valve leaflets through the fibrous strands to prevent the valves from opening and leaking blood into the atria.

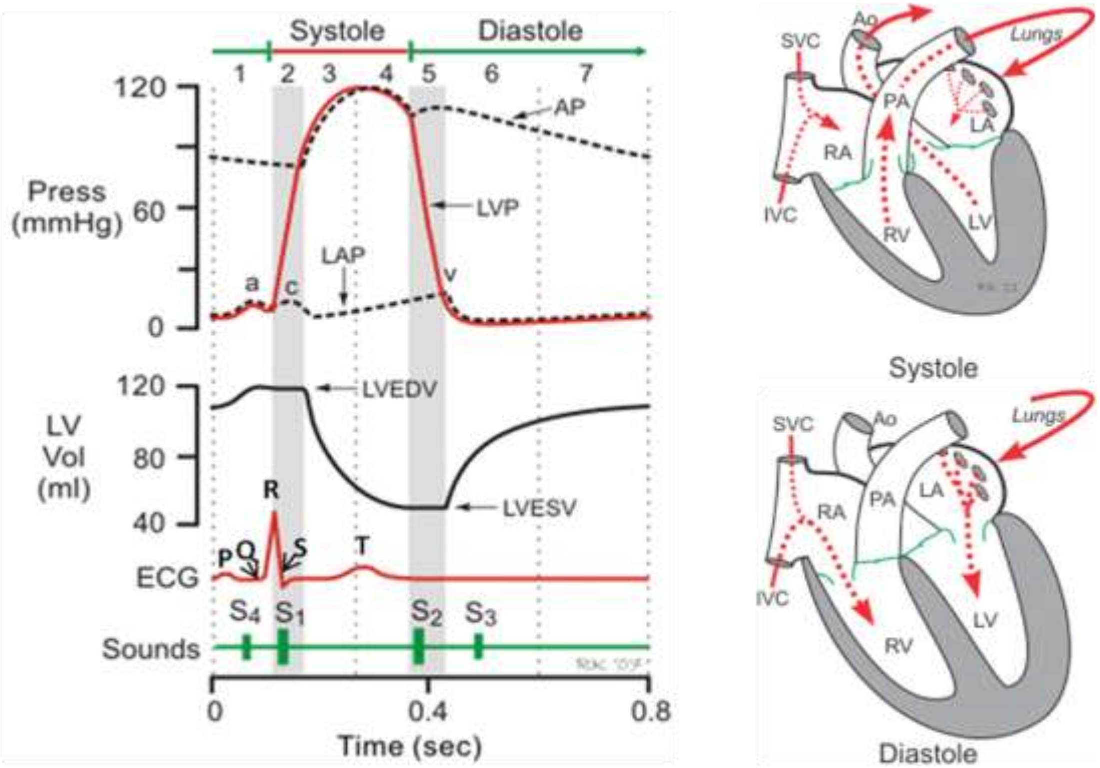

Figure 1.3 Cardiac cycle. The seven phases of the cardiac cycles are, 1, atrial systole; 2, isovolumetric contraction; 3, rapid ejection; 4, reduced ejection; 5, isovolumetric relaxation; 6, rapid filling; 7, reduced filling. [18]

1.3 Cardiac Function

The flowing of blood requires contraction and relaxation of the heart muscle (myocardium), and a complete contraction and relaxation of the heart is a cardiac cycle [17].

Each cardiac cycle is composed of systole and diastole. Figure 1.4 shows a plot of left ventricular volume versus time in a normal volunteer during a cardiac cycle. During systole, the left ventriclular myocardium contracts and blood is ejected into the aorta. During diastole, the ventricle fill with blood. During early diastole, relaxation of the myocardium creates a

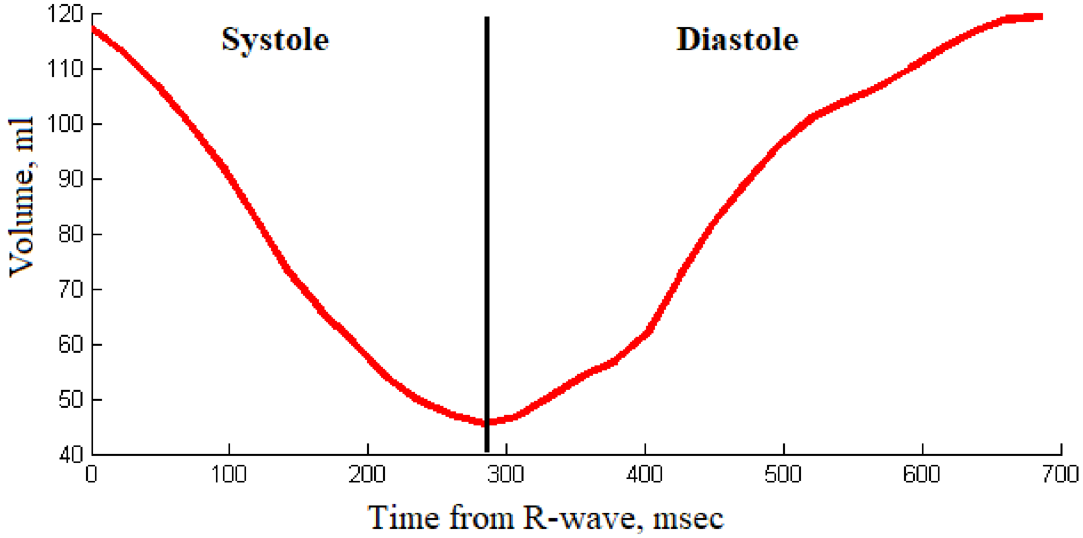

Figure 1.4 Left ventricular volume versus time in a normal volunteer during a cardiac cycle

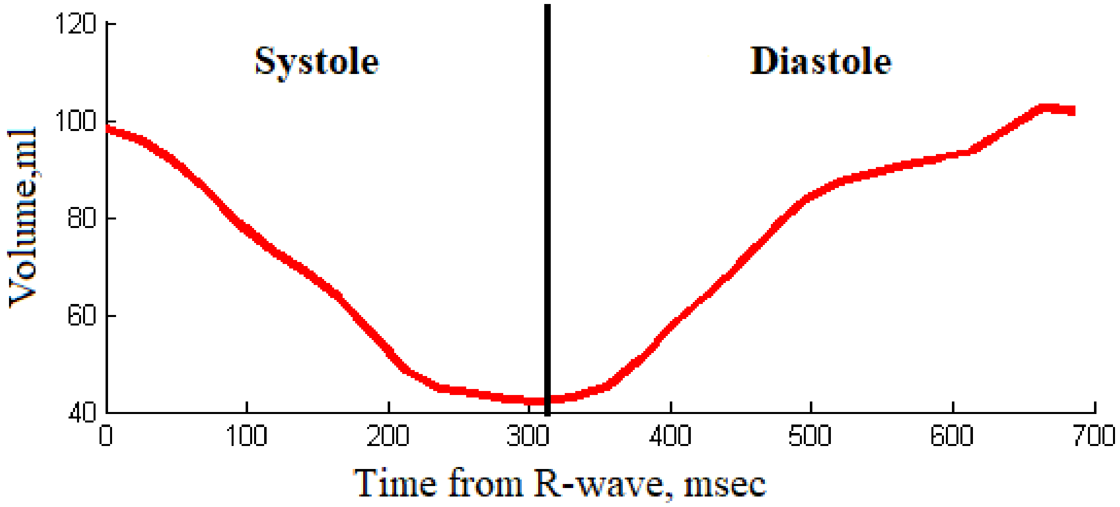

Figure 1.5 Right ventricular volume versus time in a normal volunteer during a cardiac cycle

suction that draws blood passively from the left atrium. Then there is a period called diastasis where the filling rate slows to almost zero. During late diastole, the atrium actively contracts pumps an additional volume of blood into the left ventricle. Figure 1.5 shows a plot of right ventricular volume versus time in a normal volunteer during a cardiac cycle. It is composed of the same phases as the left ventricle, but blood flows in from the right atrium and is ejected into the pulmonary artery.

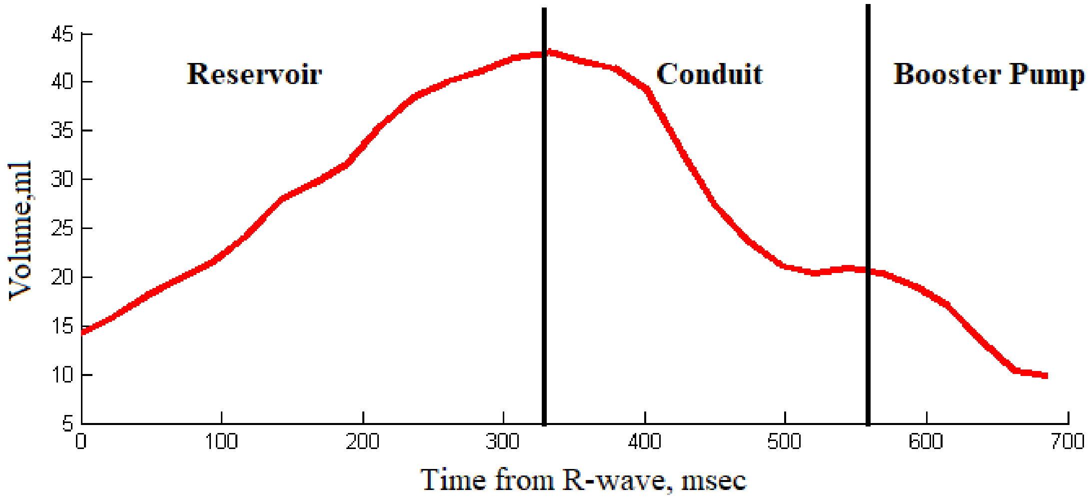

Figure 1.6 Left atrial volume versus time in a normal volunteer during a cardiac cycle

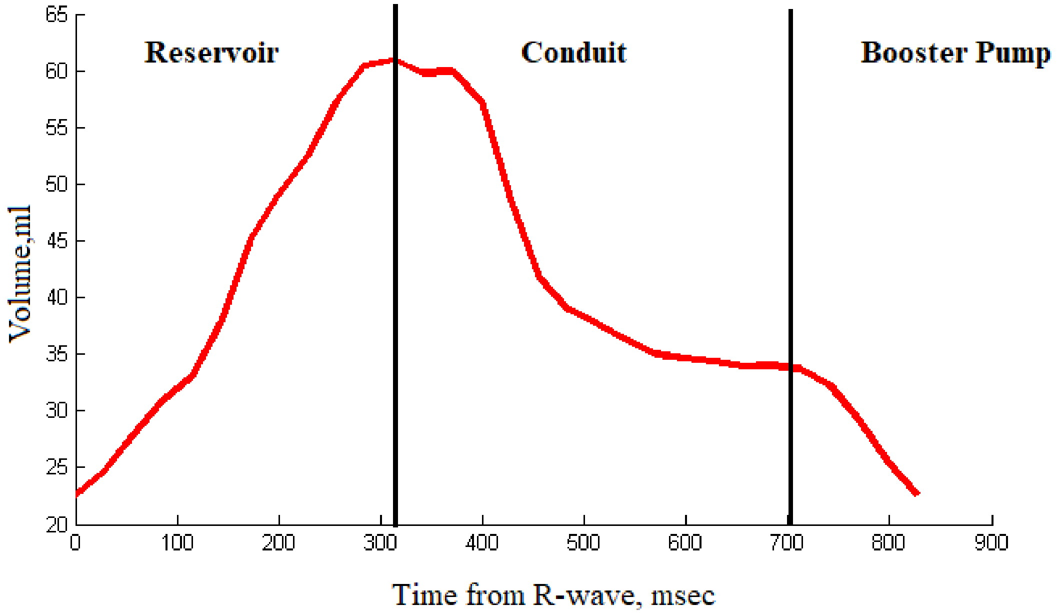

Figure 1.7 Right atrial volume versus time in a normal volunteer during a cardiac cycle

The left atrium (LA), with its vastly dynamic and response to the stretch and secretion of atrial neuropeptides, is far from being a simple transport chamber. Figure 1.6 shows a plot of left atrial volume versus time during a cardiac cycle. LA function has been conventionally divided into three integrated phases: reservoir, conduit and booster-pump [117]. First, as a reservoir: an expansion phase during left ventricular (LV) systole; the LA stores pulmonary venous return during LV contraction and isovolumic relaxation. The total emptying volume and fraction reflect the reservoir function. Secondly, as a conduit, the LA transfers blood passively into the

LV during ventricular diastole. The passive emptying volume, passive emptying fraction and conduit volume reflect LA conduit function. Thirdly, as a booster-pump, the LA actively contracts during the final phase of diastole and contributes between 15% and 30% of LV stroke volume [117]. The LA active emptying volume and active emptying fraction reflect the LA pump function. Figure 1.7 shows a plot of right atrial volume versus time in a normal volunteer during a cardiac cycle. It is composed of the same phases as the left atrial, but deoxygenated blood enters the RA through the vena cava and the coronary sinus, then flows to the right ventricle.

1.4 Heart Failure and Mitral Regurgitation

Heart failure (HF) is a common medical condition, and, if left untreated, can be deadly [19]. It occurs when the heart fails to pump enough blood to the body. Mitral valve regurgitation (MR), also known as mitral insufficiency, is one of the causes of heart failure. It is a disorder in which the mitral valve does not operate properly [20]. Thus, blood is not fully ejected unidirectionally to the aorta, and this leads to the blood leaking backwards through the mitral valve into the left atrium during ventricular contraction. As a result, the heart needs to work harder to provide enough forward cardiac output and resulting with a thinner wall.

Without treatment, MR will develop into severe HF and can lead to death [21]. Correct identification of mitral regurgitation class and optimized timing of surgery are key in management. The conventional guideline for surgery is when the LV ejection fraction (LVEF) < 60% and/or LV end-systolic dimension (LVESD) > 40 mm [22]. But following this guideline, post-operative LV dysfunction is common and is associated with increased morbidity and mortality [20 [84] [109]. Back from 1980s, there is data to demonstrate improved surgical outcomes in patients with early surgery [110]. Several observational studies have consistently demonstrated adverse outcomes from conventional guidelines [111]. The American Heart Association (AHA) and the American College of Cardiology Foundation (ACC) recently updated the conventional guidelines with early intervention [20]. In the updates, it points out that it is reasonable to consider intervention when there is a progressive decrease of LVEF toward 60% or a progressive increase in the LVESD approaching 40 mm. However, there are several reasons that early intervention is not emphasized. First, randomized prospective studies in mixed populations are lacking since the data supporting early surgery are mostly from single-center, non-randomized studies and retrospective registries. Secondly, the benefits of outcomes are mainly for primary degenerative disease and less consistent for other causes. Moreover, it is not straightforward to decide referral for early surgery, grading severe MR is subject to significant variation between clinicians [112]. However, early surgery faces increased risks and decreased rates of successful repair [20]. Therefore, the main issue regards to the timing of surgery relies on the balance between facing the risks of successful repair rates of early surgery and risking irreversible LV dysfunction of late intervention [20].

1.5 Cardiac Imaging Modalities

Medical imaging modalities can roughly be categorized into two types based on their energy sources. One type uses ionizing radiation, such as conventional X-ray and computed tomography (CT), which use X rays, and positron emission tomography (PET) and single-photon emission computed tomography (SPECT), which use gamma rays. Another category does not involve ionizing radiation and includes techniques such as MRI, which uses radiofrequency pulses, and cardiac echocardiography, which uses acoustic energy. Echocardiography, CT, nuclear imaging and MRI are currently the most commonly used imaging modalities in clinical practice.

1.5.1 Echocardiography

Echocardiography, also known as cardiac ultrasound, is the most commonly used tool to evaluate the function and shape of the heart in clinics. A probe with gel on it is placed on the patient’s chest and generates a sound wave that travels into the body. Part of the sound wave is reflected by different layers of the tissue and returns to the probe, which generates vibration. The vibration is translated into electrical pulses into the ultrasonic scanner and processed into images. It is the easiest, safest and most portable method. Because it is non-invasive and has no side effects, it is widely recommended and used in patients during pregnancy. Echocardiography is usually 2D, but 3D echocardiography is possible.

1.5.2 Computed Tomography

Computed Tomography (CT) utilizes tomography to create a 3D volume of transmission images using 2D X-ray images. They are taken around a single rim of rotation where x-rays are delivered to the body of interest in multiple directions. The different radio-densities of different tissue types enable the generation of a large number of 2D x-ray images, revealing the interior of the body. A computer is used to reformat and reconstruct the 2D images and 3D representation of the structures. CT has become an important imaging tool due to its accuracy, high spatial resolution and reasonable price. CT is often used to image the coronary arteries. However, its radiation dose remains a safety concern. Plus, cardiac CT often requires injection of a contrast agent when image soft tissues like the heart. The iodine in the contrast material may cause allergic reaction.

1.5.3 Magnetic Resonance Imaging

MRI is a type of imaging modality that utilizes the quantum properties of nuclear spins in human body. The hydrogen atom is most frequently used in MRI because it is most abundant (about 63%) and most MR sensitive. The acquisition of MRI signals can be categorized as three states: equilibrium state, excitation state and relaxation state. As a proton spins, it generates a small current loop, which generates a small magnetic moment. As an external magnetic field B_0 is applied in Z direction, the protons will align with the field in two different directions, parallel to B_0 in +Z direction and opposite to B_0 in –Z direction, depending on the nuclei energy level and B_0. The net magnetization is called M_0. As the proton has mass, it precesses along the Z direction with a Larmor frequency $\omega=\gamma B_0$, γ is gyromagnetic ratio which is constant for protons, equal to 42.58 MHz/Tesla. For a 1.5 T MRI scanner, B_0=1.5 T and ω = 63.87 MHz, which is within the radio frequency range. This state is called the equilibrium state. Then, the magnetization is excited by another magnetic field B_1 with the same Larmor frequency ω, which is introduced perpendicular to B_0. This energy tips the protons away from the alignment, and they precess towards the XY direction slowly, generating a flip angle from the alignment. The duration of the radiated frequency (RF) pulse determines the flip angle and the amount of net magnetization.

When the transmitter is turned off, the protons will release the energy and return to the equilibrium state. This procedure is called relaxation. There are two types of relaxation, spin-lattice relaxation with a time constant equal to T_1, and spin-spin relaxation with a time constant equal to T_2. For spin-lattice relaxation, the protons release the energy to its lattice, and T_1 is the time it takes for M_z to recover to 63% of M_0. For spin-spin relaxation, protons interact with each other, which interrupts the phase coherence. T_2 is the time it takes for M_{xy} to decay to 37% of M_0. The relaxation time is dependent on the property of different tissues, which helps generate image contrast between tissues. T_1-weighted scans use short T_E and short T_R. T_2-weighted scans use long T_E and long T_R. If a gradient magnetic field is applied along with the main field B_0, a specific region can be selected for imaging, which is called the slice selection.

After collection of the signals, spatial localization is performed, including frequency encoding and phase encoding. After slice selection, a gradient magnetic field is applied to one of the directions perpendicular to the main field, for example, y direction, such that the phase of protons along y direction is proportional along the gradient field. Then, another gradient magnetic field is applied in a direction perpendicular to the main field, and the phase encoding gradient field, x direction. The processional frequencies of the proton spins will differ along this gradient field. This is called frequency encoding. The signals from the phase encoding and frequency encoding form a line in k space. The procedure is repeated for the number of the lines in the matrix to form the entire k space. Fourier Transform of the signals and inverse FT yield a 2D image. This procedure is repeated for different slice selections to obtain images of an entire 3D sample.

1.5.4 Comparison of Imaging Modalities

X-ray is a noninvasive technique, which is quick and painless, but the patient gets a dose of ionizing radiation. Echocardiography is a reliable and cheap medical imaging technique. However, it is very sensitive to small changes in beam angle and imaging window [11]. Plus, echocardiography relies on geometrical assumption, which may introduce assumption error in imaging [12]. Computed Tomography avoids invasive insertion and has good spatial resolution. However, it has drawback in the exposure to ionizing radiation, which increase the possibility of cancer development later in life. Besides that, CT requires contrast agent when imaging soft tissues like the hear, which may be toxic and cause allergy. Intra-luminal abnormalities can be detected by CT [118]. Nuclear imaging has benefits in showing substance concentration and the process of accumulating and expulsing that substance, which is inaccessible in any other way. But it has relatively low resolution and is expensive. Besides those drawbacks, it has potential risks caused by the radioactive component used during procedure, which limits the amount of times a patient can undergo this procedure.

MRI is a noninvasive technique in volumetric and functional assessment without geometric assumption, and the validity and reproducibility in ventricular volumes and function have been well documented [59]. MRI produces high SNR images with relatively high spatial resolution, high temporal resolution and provides excellent soft tissue contrast. MRI does not use ionizing radiation and a contrast agent is not required for most types of cardiac scans [118]. When measuring left ventricular (LV) functional parameters, echocardiography, which uses ultrasound, uses a shape assumption and is sensitive to small changes in beam angle and imaging window [11-12]. Nuclear imaging modalities such as PET and SPECT mainly provide functional information with limited spatial resolution. MRI can provide higher spatial resolution and, in some cases, functional information as well. The drawback of MRI is mainly the long scan and post processing time. MRI is relatively expensive compared to other imaging techniques.

1.6 Standard cardiac cine MRI protocol

A cardiac cine MRI protocol uses ECG-gated and breath-hold steady state free precision (SSFP) technique. In a standard cardiac MRI protocol, it usually includes a 2 chamber (2CH) view orientation, a 4 chamber (4CH) view orientation, a left ventricular outflow tract (LVOT) view orientation and a short axis (SA) view orientation. Figure 1.8 shows the different views of a standard cardiac MRI. The typical imaging parameters are summarized in Table 1-1. In the SA views, there are 10-12 short axis slices that are parallel to each other to cover from LV apex to

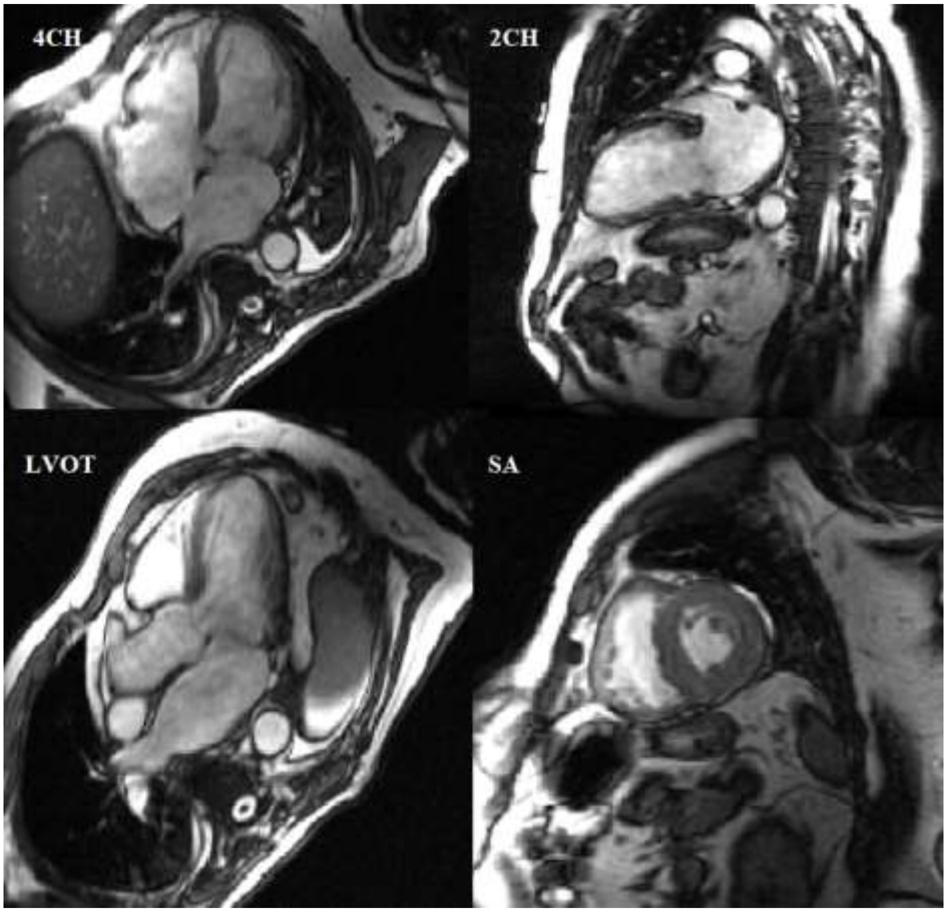

Figure 1.8 Standard cardiac cine MRI orientations.

LV base without any gap between slices. In this dissertation, the standard cardiac cine MRI protocol was used with modification in the slices acquired.

Table 1-1 Typical standard cardiac cine MRI protocol parameters

FOV (cm^2)	40×40
Flip angle (degree)	45
TE (ms)	1.8
TR (ms)	4
Phase per cardiac cycle	20
Slice thickness (mm)	8
Pixel size (mm^2)	1.56×1.56

1.7 Content of the Following Chapters

This dissertation is organized as follows. Chapter 2 reviews literature on algorithms of the heart surface remodeling. The positives and negatives of these techniques are discussed. Chapter 3 describes the 4D surface fitting algorithm of human heart from cine MRI data. It was tested on data from 8 normal subjects and 8 mitral regurgitation patients. Chapter 4 validates the algorithm through the aspect of volume functions by comparing with disk summation methods. Chapter 5 defines the geometry parameters and validates the algorithm in the geometry aspect on a prolate sphere and b-spline LV models. Chapter 6 describes mechanics of heart chamber and validates the algorithm through the comparison with tMRI-based methods in the LV mechanics. Chapter 7 presents a preliminary study to characterize the geometries and mechanics of left and right atria along with ventricles on healthy subjects and the remodeling versus age. Chapter 8 investigates the remodeling of hearts in severe mitral regurgitation patients with preserved left ventricular ejection fraction and track the MV surgery effect on 4 patients. Chapter 9 concludes the work described in earlier chapters and gives directions for potential work in the future.

Chapter 2 PREVIOUS WORK ON HEART SURFACE FITTING

This dissertation mainly investigates new parameters and ways of measuring atrial and ventricular geometries, functions and mechanics based on analysis of LV, LA, RV and RA shapes. Shape analysis of cardiac chambers provides useful information in cardiac global and regional analysis. This has important implications for cardiac diseases, such as mitral regurgitation and pulmonary hypertension. Functional shape analysis can help cardiologists and surgeons in clinical diagnosis, treatment planning, and pre/post-surgery monitoring with better visualization of heart, myocardial motion tracking and volumetric function analysis [37-38]. Therefore, to analyze cardiac shapes, we need to reconstruct endocardial surfaces of all four chambers.

A lot of work has been done in the field of heart surface fitting. For all previous work on heart surface fitting from medical images, they can be roughly categorized as non-model based or model based approaches. In this chapter, we explored different surface fitting techniques from medical images. Most techniques have been well developed and have mature results in terms of providing the most parameter measurements needed in current clinical use [66]. We compared the advantages and disadvantages of those techniques.

2.1 Non-model Based Methods

The non-model based methods do not assume any prior shape or model of the object. The surface fitting procedure is purely driven by image data, which has the best advantage to handle structural variations of the heart chambers. In non-model based methods of fitting surface from medical images, the most popular algorithms are finite elements [36] [38] and marching cubes [40]. We will summarize the main procedures of those algorithms.

In the finite element algorithm, the main idea is to represent a single complicated shape with an approximately equivalent network of simple elements. Those elements are connected by common nodes and each subdivision has its own set of parametric basis functions. The accuracy of the network representation depends on the number of the elements in the network and the order of the basis functions. The larger the number and the order are, the smaller each element is and more accurate the representation is. But more elements and higher order mean more calculation. For each element, the higher order of the basis functions improves the representation accuracy at the expense of computation complexity. Therefore, the balance point is to have just enough elements represented with reasonable basis functions to be adequately accurate within an acceptable computation expense. In [36], the author chose 16 equally spaced elements to represent left atrium and using cubic Hermite basis functions to interpolate on the element. The element parameters are optimized to minimize the error between the surface and the segmented data from MRI images. In [38], the author reconstructed left atrium with 142 bicubic Hermite finite elements and right atrium with 90 elements from CT images. In ventricular modeling, higher-order cubic Hermite finite element interpolation schemes are popular [120]. The main problem with finite element is the expensive computation for a complicated geometry, such as atria and RV, which requires large number of elements and high-order basis function.

In the marching cubes algorithm, a logical cube of eight pixels between two consecutive slices is created first. Four vertices of the cube are from each slice. From the intersection between the segmented image and the cube, an index is assigned. The index serves as a pointer to a pre-calculated table that gives all edge intersections. Figure 2.1 shows the pre-calculated triangulated index table. By moving the logical cube and repeating the procedure, the surface of the object is constructed [40]. The main problem of marching cubes in MRI was that the voxels in cMR were strongly anisotropic. The in-plane resolution of the image is typical 1.5 mm while the out-of-plane resolution (slice thickness) was usually 6 to 10 mm, a few times lower than in-plane resolution. Without additional processing, the generated mesh using marching cubes from MRI images would suffer evident terracing artifacts. To better fit myocardium surfaces, additional processing is needed. In [121], Lotjonen first used marching cubes to generate a surface topology, then searched the Voronoi polygons for triangle nodes on the surface and connected the neiboring Voronoi areas to generate triangles. In [122], the quality of the triangulated mesh was improved by standard mesh modification techniques through curvature adaption. Gibson [123] proposed the surface net concept to deal with terracing artifacts. Although this method was meant for solving the terracing problem in generating meshes from binary segmented data, the problem still persisted.

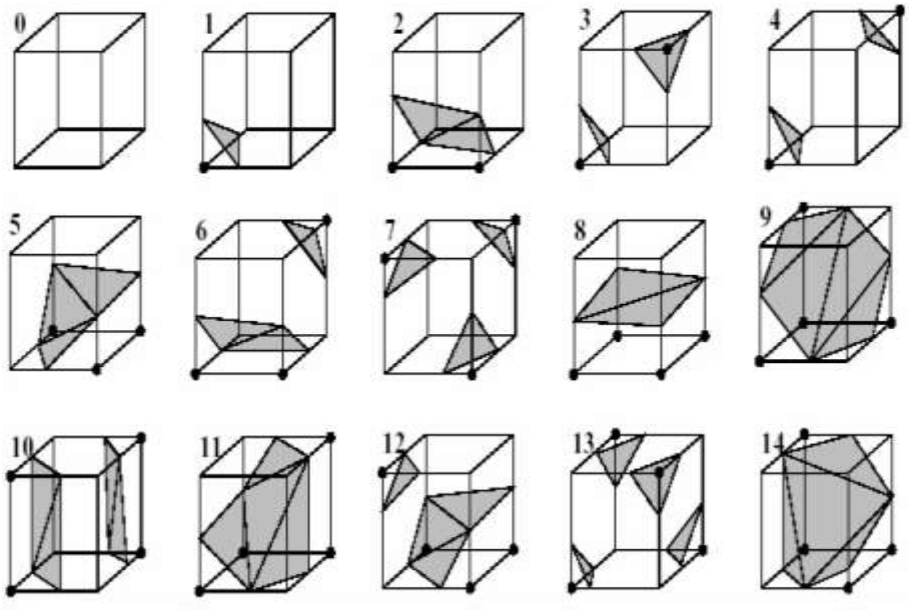

Figure 2.1 Triangulated cubes index table for marching cubes algorithm

Except those two popular non-model based methods, there are other non-model based methods for high resolution data with nearly isotropic voxel size proposed. Such as in [126], the author used open-source toolkits (3D Slicer and Paraview) to create heart surface models from 3D MRI data, which has ~1 mm^3 voxel size. In [44], a surface flattening technique was used in the LA surface reconstructing from CT data with ~1 mm^3 image resolution and 3D MRI data with 1.3 mm^3 resolution.

2.2 Model Based Methods

In model based methods, they exploit a prior model to deform to image data in the surface fitting. There models are usually a statistical model generated from large training datasets [41] or a model constructed from denser image datasets [46] [48], such as CT data has less than 1mm^3 isotropic resolution. In the model-based methods, segmented data is usually registered to the model, then deform the model to the data with penalty to minimize an energy cost function, which is composed of an internal regularization term and an external attraction potential, in an iterative manner. The most famous methods using a statistical model are active shape model (ASM) and active appearance model (AAM) [127] [128]. In ASM, a mean model is constructed using Procrustes analysis [129] from training datasets. Then surface for new dataset is constructed by varying the weight parameter in the mean model. AAM improves ASM in terms of taking the gray level variation into consideration. Besides those two methods, there are also other methods to reconstruct surface from a model. In [124], a high-resolution prior model is used to estimate normal vector for data points from CT scanning, then the surface model is reconstructed using the Screened Poisson Surface Reconstruction algorithm [125], in which the positions and normal vectors of data points are required.

One of the biggest disadvantages of the model based methods is that a holistic model is not accurate enough to represent the whole shape population. The shapes of all four chambers vary among individuals and different pathologies remodel chamber shapes as well. Therefore, the model is not the best way for surface reconstruction to capture shape details and mechanical characters in cardiac surface reconstruction. Moreover, to compute a statistical model requires large datasets and is time consuming, therefore it is difficult to build a statistical model for all possible heart categories. For models from denser images, the model construction is simpler but it is not always accessible to denser images, especially in patients who may be allergic to contrast agent and the scanning is under time pressure.

2.3 Summery

When these mature methods mentioned above, which work successfully in nearly isotropic data with high resolution, are applied on 2D MRI data, several issues arise. For 2D MRI, it typically has 1.5 mm in-plane resolution and usually 6-8 mm in the third dimension. Therefore, those methods suffer evident terracing artifacts and strongly irregular triangles from highly anisotropic data [42] [43], and addition processing to compensate the highly anisotropic resolution is always expensive in computation and time. Such as linear or shape-based interpolation. Linear interpolation method interpolates highly anisotropic data onto an isotropic grid [42] [37] [44]. The basic idea of the shape-based interpolation is to convert the segmented binary image back into a gray image and then interpolate the gray image. In the gray image, the point value is the shortest distance from the cross-sectional boundary, in which the positive values are for points of the object and negative values are for those outside. In the interpolated image, all nonnegative value points constitute the interpolated object [76]. Another issue is that methods with parametric basis functions are always limited to regular shapes, for example elliptical and symmetric LV, due to the limited order and number of basis functions within a reasonable computation time [42] [45].

For the chamber of LV only, except those two aspects to review previous work on heart surface modeling, there are many other ways to categorize surface fitting algorithms. In [42], Dr. Schiros categorized LV surface modeling algorithms into two types: coordinate-based surface modeling and non-coordinate surface modeling. In coordinate-based surface modeling, the fact that left ventricle has a regular shape, which can be approximated as a spherical topology, was used as prerequisite information to construct the 3D surface of the left ventricle by using a spherical model [50-52]. Besides the spherical topology, general cylinder and prolate spheroidal coordinate based models have also been developed [53-56]. Non-coordinated-based surface modeling techniques do not use polar coordinate systems nor assume a regular spherical shape to construct a parametric description of the surface, such as mesh generation methods [57] and contour-connecting methods [58].

2.4 Recent Algorithms

Recently, four new algorithms for fitting surfaces to 2D MRI data have been proposed. A recent paper combined the contrast enhanced MR angiography (MRA) data with late gadolinium enhanced MRI to build an LA surface [49]. The disadvantage of this method requires MRA data and gadolinium injection. The MRA data introduces extra scanning time and gadolinium injection is expensive and not always available in clinical data, such as patients with compromised renal function. Dr. Skrinjar [43] developed a mesh generation algorithm by mapping pre-meshed sphere to segmented data from cardiac MRI short axis images. This method maps along the gradient field of the Laplace’s equation solution between the pre-meshed sphere and segmented boundary of object. This method is time consuming, which takes nearly 2 hours to generate a surface [42]. To address the efficiency issue in Dr. Skrinjar’s algorithm, Dr. Schiors [42] proposed an algorithm by creating surfaces in training data set using Skrinjar’s methods and building a point distribution model from those surface, then adapt it to new data sets. In [38], Dr. Lim developed an algorithm for fitting surface from 2D cardiac MRI data by building contour connectivity and sub-mesh between contours, then propagating the mesh model. More details of those three methods by reconstructing endocardial surfaces from cine MRI data will be described in the following sections.

2.4.1 Dr. Skrinjar's method

Skrinjar et al. [43] proposed an algorithm to map a pre-meshed sphere with nearly equilateral triangles to segmented cardiac MRI short axis images using the gradient field of solution of the Laplace's equation between the sphere and the boundary of the segmented object. Figure 2.2 shows the algorithm in a 2D example.

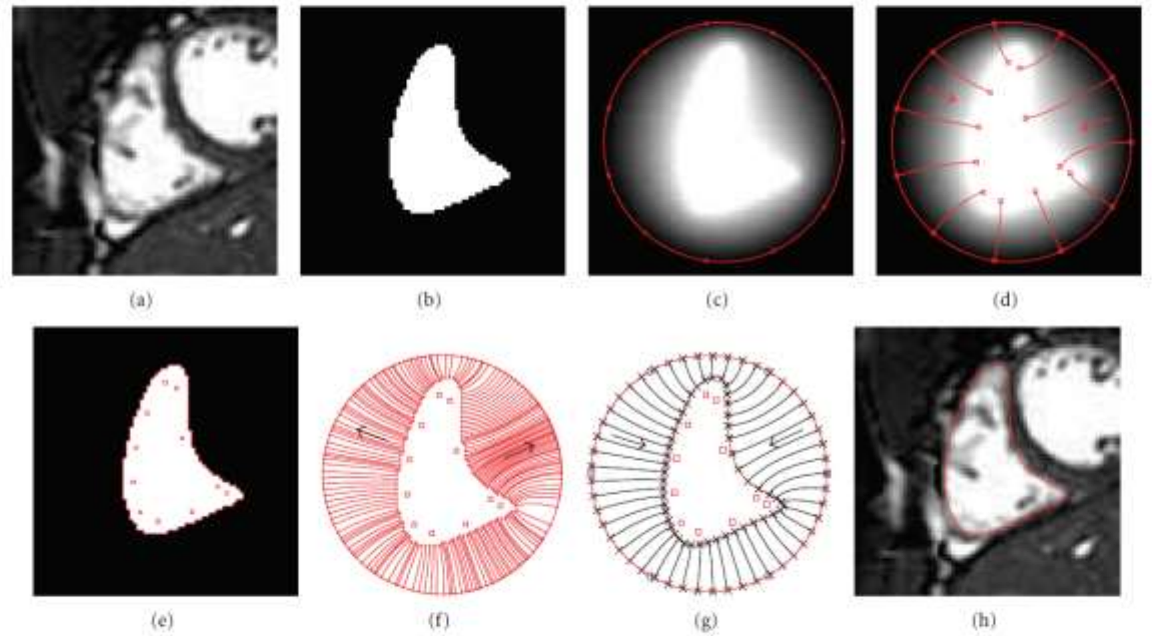

Figure 2.2 Mesh generation summary of Skrinjar's algorithm using a 2D example [43]

In this method, the pre-triangulated sphere was centered at the 3D segmentation, which is from a stack of 2D segmentations in the short axis view (Figure 2.2 (b)), and set the maximum distance from the center to the 3D segmentation boundary as radius. The isotropic segmentation, which was obtained by further resampling the 3D segmentation based on a discrete and regularly-shaped lattice, was then eroded twice. M uniformly sampled points on the pre-meshed sphere were mapped from the sphere to the object along the gradient solution of the Laplace's equation (Equation 2.1) in the domain between the sphere and the eroded segmentation. This procedure is illustrated in Figure 2.2(c, d, and e). Based on the M propagated points (singularity points), the boundary points on the segmentation were propagated from the object back to the sphere in the reverse direction (Figure2.2 (f)). K uniformly-distributed control points on the sphere were defined. Finally, V uniformly distributed point on the sphere was propagated to the object (Figure 2.2 (g)) based on the control points and singularity points, and the propagation stopped by a stopping function which was represented by a pseudo-thin plate spine model.

$$\Delta \mathrm{u} = 0$$

$$\frac{\mathrm{dr(t)}}{\mathrm{d}t} = \nabla u\big(r(t)\big) \tag{2.1}$$

The advantage of this algorithm is that, it has no shape assumption of the heart and it could be applied to objects with any shape that was topologically equivalent to a sphere. Moreover, this method reduced the terracing problems caused by strongly anisotropic segmented data to some extent. However, due to the huge computation in solving Laplace's equations, this algorithm was too time-consuming which would take more than two hours to generate a triangulated mesh of a myocardial surface. Moreover, due to the high gap between in-plane resolution and out-of-plane resolution in cardiac MR images, the terracing problem still exists [42] [52]. Therefore, this algorithm is not applicable for clinical and many research applications.

Furthermore, it was difficult to control the smoothness of the generated surface to balance the need for fitting the contours versus the need for generating a smoothly-varying heart surface.

2.4.2 Dr. Schiros' method

In [42], Dr. Schiros proposed an active mesh generation technique by generating biventricular surfaces using Skrinjar's method for training subjects and deform the point distribution model (PDM) constructed from training surfaces to test subjects. The procedure of the method is shown in Figure 2.3.

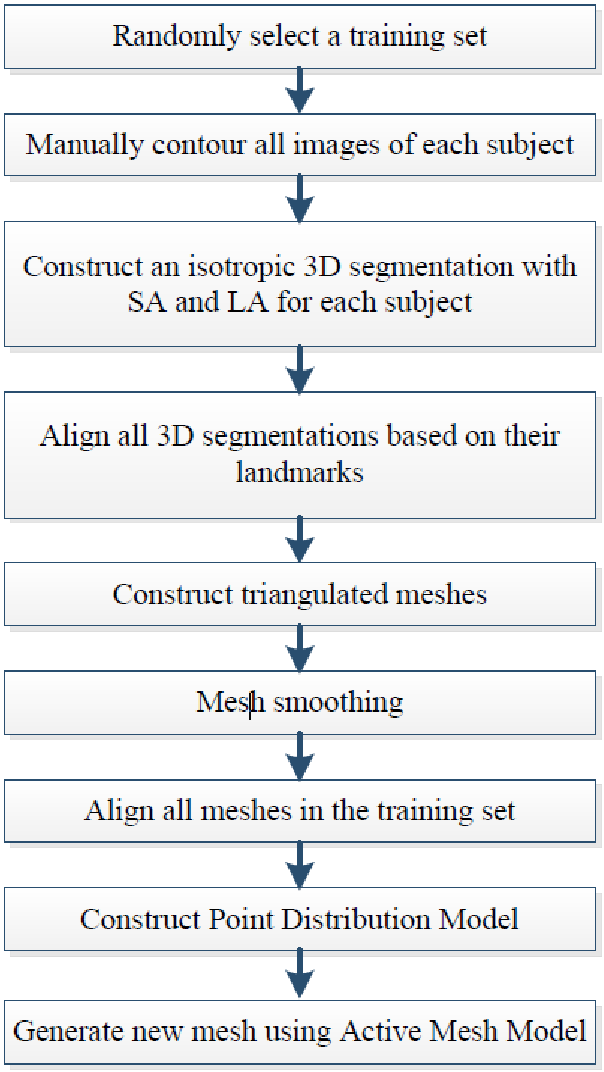

Figure 2.3 Procedure of Dr. Schiros's mesh generation algorithm [42]

To construct a point distribution model (PDM), a set of training subjects is randomly selected. Firstly, in the long axis and short axis views, LV and RV contours on the ED and ES are drawn by experts using an in-house semi-automatic contouring tool with closed B-splines for each subject. Then a 3D isotropic segmentation is generated from the contours of both short axis and long axis by angular interpolation and thresholding. Thirdly, a triangulated mesh is constructed by adapting Skrinjar's Method as introduced in section 2.2.1. Dr. Schiros implemented the surface generation method with additional improvement in the smoothing function. The smoothing function incorporates the surface normal and mapping error, which is shown in Equation 2.5. The propagation of vertices will be along the gradient of u as described in Skrinjar's method, and will stop when the smoothing function E is minimized instead of being determined by the stopping function in Skrinjar's method.

$$E = E_{boundary} + \gamma E_{curv} \qquad 2.2$$

where the $E_{boundary}$ represents the mapping error between the vertices to the boundary, and E_{curv} term controls the smoothness of the surface. γ controls the impact of the smoothness term.

Fourthly, a point distribution model (PDM) is constructed based on the training surface meshes. To ease the impact of the difference in position and orientation, the meshes generated for the subjects in the training set were first aligned. The mean shape of the training set was defined as in Equation 2.6,

$$\bar{m} = \frac{1}{N}\sum_{i=1}^{N} m_i \qquad 2.3$$

And the point distribution model describing the variance of the training set was defined as,

$$m = \bar{m} + \Phi b$$

where Φ was a matrix containing the first *t* eigenvectors calculated by principle component analysis (PCA) over the covariance matrix.

Finally, after the PDM was constructed from the training set, it was deformed to fit to a new subject. The new subject was first segmented and constructed to a 3D isotropic segmentation as in the training set. The deformation was realized by moving each vertex in the PDM along its normal vector to minimize the distance to the segmentation to obtain updated mesh. Then align it with mean shape and update it in the PDM. This procedure was repeated until the mesh converged.

This active shape model was applied on LV and RV successfully. The advantage of this algorithm is that, it takes only 20 seconds to generate a new biventricular surface once the PDM is constructed. However, there are several disadvantages of this mesh generation algorithm. Firstly, large size is needed in the training set and the computation time for generating a mesh in the training set with 1000 vertices is about 2 hours, which result in the large computation time in PDM construction. Moreover, for different pathologies, different PDM is required. Furthermore, in the algorithm, anisotropic segmentation from short axis stack must be interpolated to obtain a 3D isotropic segmentation, which introduce interpolation error.

2.4.3 Dr. Lim's method

Dr. Lim proposed an algorithm to reconstruct heart model from MRI data by creating sub-meshes, which was sandwiched by a pair of adjacent contours in the same timeframe, and then deform sub-meshes to the subsequent timeframe [38].

In this algorithm, the input data were the segmented contours drawn on a set of short-axis MRI images over one cardiac cycle. Using a tree-based approach, contour connectivity was first established to contours from adjacent slices in the same timeframe and to the contour in the subsequent timeframe. The tree-based connectivity is constructed by comparing each contour against contours from adjacent slices and the degree of overlap between each pair when projected onto a same plane was measured as a similarity index. Weak connections were filtered away by setting a minimum similarity index threshold of 30%. With the connectivity tree at the first timeframe for all contours, a 3D surface was then reconstructed by fitting meshes to contour pairs from two adjacent slices. A pair of contours from two adjacent slices was projected onto a common plane that is parallel to both slices and then perform a boundary constrained Delaunay triangulation of the regions where the contours do not overlap. Then project the contours back to their original planes. The surface was further smoothed by improving the average aspect ratio of surface triangles and increasing the vertex count by inserting vertices. The smoothing was achieved by λ|μ algorithm [105], which is a two-step smoothing algorithm with reduced shrinkage effect in the smoothing. Finally, the refined surface at the first timeframe was deformed to the subsequent timeframe without changing the mesh connectivity. The deformation was realized in an independent sub-mesh by sub-mesh manner. The deformation process was controlled by a radial basis function (RBF).

This algorithm was tested on five MRI data sets of the left heart of healthy patients with different slice thickness, which were 5 mm, 8 mm and 10 mm. This algorithm took around 30 minutes to complete a full 4D left heart model consisting 20 timeframes. The advantage of this algorithm is that it has no shape assumption and no training data sets are needed. Plus, the reconstructed surfaces have one-to-one vertex correspondence across the cardiac cycle. However, this algorithm has several drawbacks at the same time. Since the sub-meshes were constructed only from short axis contours, the 3D model has no ventricular or atrial apex information. The mesh was created and deformed in a sub-mesh by sub-mesh manner from adjacent contours, which maintains a high level of conformity to the input contours, but also resulted in the mesh having a “stair-case” look. In another word, the 3D model is not smooth.

Another drawback from the sub-mesh, which is sandwiched by a pair of adjacent contours, is that it requires highly registered short axis contours and small motion artifacts has a large-scale impact on the model.

2.5 Conclusion

In this literature review on the heart surface fitting from medical images, different techniques have been explored. Heart surface fitting techniques for high resolution data (~ $1mm^3$) are well established. However, when applying those techniques to cine MRI data, it suffers from the highly anisotropic resolution, which usually has ~1mm in-plane resolution and 6-10 mm resolution in the slice direction. Moreover, for techniques using shape models, they are usually limited to datasets which is similar to the model shape, and it is time consuming to construct model for different shape categories. Additionally, denser images are not always available to construct a model in practice. Therefore, in this dissertation, we developed a novel heart surface fitting algorithm from highly anisotropic MRI data without any prior shape knowledge. With the fitted surface, volumetric functions, geometries and wall motions of all four chambers of heart can be measured simultaneously and separately.

Chapter 3 FOUR-CHAMBER 4D ENDOCARDIAL SURFACE RECONSTRUCTION FROM CARDIAC MRI DATA

In this chapter, a novel surface fitting algorithm from cardiac MRI data is proposed. With this proposed algorithm, 4D computational heart surface of four chambers can be quickly reconstructed. The surface provides volumetric function analysis, wall motion tracking and geometry estimation. In this chapter, we first introduce the algorithm and validate it on 8 normal subjects and 8 MR patients. From the fitted surfaces, we analyzed volume function and myocardial mechanics. An abstract of this work was presented at ISMRM 2017 [24].

3.1 Introduction and Clinical Motivation

Medical imaging provides useful information in visualization, diagnosis and monitoring. Compared to other medical imaging techniques, MRI is non-invasive and non-radioactive, and MRI images have high spatial resolution. The validity and reproducibility in ventricular volumes and function from MRI images have been well documented [59]. Therefore, this study used 2D cardiac MRI data to reconstruct 4D (3D and time) heart surfaces.

Compared to static 2D images, 4D heart reconstruction allows for further understanding and better visualization of complex geometries of heart chambers, especially prior to surgical intervention. Quantitative shape analysis of cardiac chambers combined with volumetric function analysis has important implications for cardiac disease, such as mitral regurgitation. There is literature indicating that the combination of functional and structural analysis might be a better prognostic indicator of atrial fibrillation [70]. In cases of valvular heart disease, such as mitral regurgitation, full 4D heart models may allow physicians to understand more about the cardiac remodeling process and evaluate the effects of therapeutic intervention on the disease process, which has the potential in optimizing the timing of surgery.

Currently, most research has been done on the LV, since the LV geometry is simpler compared to both atria and RV, and damage to the LV has a larger effect on the body than damage to the other three chambers. However, global LV function has its limitations in some clinical conditions, such as the presence of severe mitral regurgitation [2-4]. The most common guidelines (LVEF<60% and/or LVESD>40mm) for mitral regurgitation surgery timing is reported with post-operative LV dysfunction and associated with increased morbidity and mortality [20 [84] [109]. The function and wall motion analysis of RV and both atria and the inter-chamber relationship have the potential to provide further clinical information [9] [59] [68] [70].

RV function is a marker in a variety of cardiovascular diseases, including pulmonary hypertension, ventricular ischemia or infarction, and pulmonary or tricuspid valvular heart disease [9]. LV and RV have influence on each other via the pulmonary circulation and through the septal wall [12], but the mutual influence and mechanics are incompletely understood [9]. RV has a cross-section varying shape changing from wrapping to an approximate triangle from apex to base. This complexity in geometry is not easily described or modeled and limited the analysis of RV research, including function and true wall motion analysis [11-12] [68-69]. Instead, simpler assessments of RV volume, such as ejection fraction (EF) or fractional area shortening, are more commonly calculated. Most RV measurements rely on linear dimensions and areas from two-chamber and/or four-chamber views. However, a small rotation in the orientation of those long-axis views will introduce wide variations in the measurement [69].

Plus, those simpler assessments do not reflect underlying RV performance and may not be sufficient in guiding diagnosis [11].

Atrial function, including reservoir, conduit, and booster function, are recognized as important predictors of heart failure [4] [61]. LA volumes are widely employed in clinical protocols [59]. Along with LA function, LA volumes provide powerful and incremental information on LA performance and are considered as predictors of cardiovascular morbidity and mortality [5-8]. Pathologic conditions, such as congestive heart failure, atrial fibrillation and valvular heart disease, correlate with LA volume changes [66]. LA remodeling, along with regional motion of LA, provides more supplementary information before diagnostic and surgery [37] [71]. Moreover, LA size increase and dysfunction are related to left ventricular dysfunction.

There is evidence in the literature that RA size could be a determinant and an early marker of right-sided systolic dysfunction [68] [70], and RA volume assessment would be more robust For the RA size than linear dimensions [69]. In [68], the author points out that an abnormal RA volume index is a determinant of right-sided systolic dysfunction. However, less research and fewer clinical outcome data are available on the quantification of RA size and volume compared to the amount of research on the other chambers. In [48], the author summarized the most commonly computed parameters For the RA are obtained from two- and four-chamber views, which have the disadvantage of angle dependency as mentioned before [59]. In our previous work, we proposed a method to combine the 2D disk summation method with tricuspid valve plane For the RA volume [62]. However, the assessment of volume combined with wall motion and geometry characteristics will provide more clinical information [67].

Regional mechanics also have clinical potential: quantifying the effects of medical therapies, measuring damage based on loss of mechanical function, minimizing injury to regions by selecting ablation patterns, and monitoring reginal function and remodeling following catheter ablation [37]. Currently there are several techniques for measuring regional mechanics, such as echocardiographic speckle tracking, cardiac magnetic resonance (CMR) tagging, and cine displacement encoding stimulated echo (DENSE) CMR. However, those techniques are limited in the atrium due to their thin walls [37]. Patient-specific heart surface shows promise for improving the interpretation of clinical data from patients [39]. Therefore, the need for generating patient-specific computational 4D heart surface has clinical significance.

Hence, function analysis combined with mechanics analysis may provide more information in clinical investigation and has the potential for improving clinical procedural planning [75]. The analysis all four chambers simultaneously compared with separate analysis of each chamber may offer more comprehensive information regarding the optimal timing of surgery and monitoring after surgery.

3.2 Motivation

In chapter 2, we summarized the current methods in surface fitting from medical images. Currently used surface modeling techniques for high resolution data suffer from tiling or terracing problem when applied to highly anisotropic MRI data [40] [121-123], and shape assumptions limit the application of those techniques on irregular shapes. Statistical modeling limits the application to datasets which are similar to the training set [42]. Therefore, the main issues with the current methods for heart reconstruction from MRI-based images are shape assumptions, long computation times and terracing.

In order to resolve those problems mentioned, we proposed a novel 4D heart surface fitting algorithm from highly anisotropic cardiac MRI data, preserving the advantage of no shape assumption and reducing the terracing problem within reasonable time. The basic idea of this algorithm was inspired by the idea from Skrinjar, et al. [43]. In [43], Skrinjar developed a mesh generation algorithm by mapping a pre-meshed sphere to segmented data along the gradient field of the Laplacian equation solution. This method is not model-based and has no shape assumption. However, it takes nearly 2 hours to generate a surface and the terracing effect still exits. We were inspired by the idea of mapping a pre-meshed sphere to segmented data, since all shapes of heart chambers are topologically equal to a sphere [37]. Instead of solving the Laplacian equation, we mapped the sphere using a method called radial shrinking, which will be described in the following section. By using radial shrinking, the interpolated surface is rough and coarse. Because heart surface is smooth and of uniform texture, the triangle normals in the constructed surface should have similar magnitudes and slowly varying directions along the heart wall. Therefore, we modified the Laplacian method [105] to smooth the surface, which aims at smoothing the surface while regularizing the vertex density and reducing the fitting error to the segmented data. To avoid over-smoothing, a cost function proposed in [52] was used to monitor the smoothness and fitting error. For each subject, a subject-specific template was first constructed near the largest volume phase, then deformed to the remaining phases. Moreover, assigning a whole slice into atrium or ventricle will introduce over- or under-estimate in volume and size. We approximated mitral valve (MV) and tricuspid valve (TV) planes and annuli at each phase to handle the obstacles caused by the large inter-slice distance in the passageways between ventricles and atria [38].

The proposed algorithm treats each chamber separately, which enabled the ability to analyze each chamber independently and the whole heart, including LA, LV, RA and RV, as a comprehensive model. This reconstructed surface provides spatial-temporal evolution of cardiac structures (ventricles and atria), from which quantitative measurements of volume, geometry and wall motion were taken. The reconstructed 4D heart surface provides a comprehensive understanding of the interaction among both ventricles and atria. The pathologies that are considered in this research include, but are not limited to, mitral regurgitation.

3.3 Main Workflow

In this section, a novel mesh generation algorithm is proposed using a triangulation technique that can be applied to all four chambers of the heart, including LV, RV, LA and RA, across the whole cardiac cycle from 2D cardiac MRI data. The main workflow of the fitting algorithm is demonstrated in the scheme in Figure 3.1.

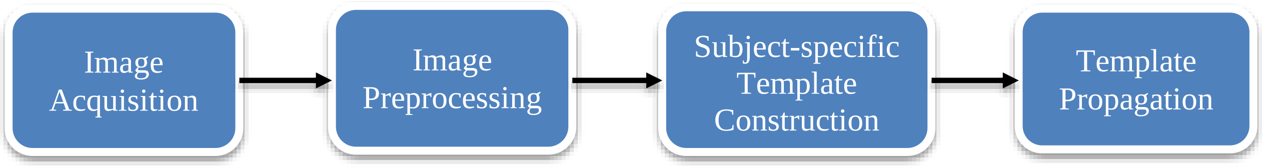

Figure 3.1 The main workflow of the mesh generation system

3.4 Image Acquisition

3.4.1 MRI Protocols

Cardiac MRI was performed on all participants with a standard cine MRI protocol described in Section 1.4 augmented with a right two chamber view and a stack of atrial short axis views. Figure 3.2 shows the entire imaging views in the MRI protocols. Protocols used in this research were reviewed and approved by the Auburn University and University of Alabama at Birmingham (UAB) Institutional Review Board (IRB).

For the healthy group, all magnetic resonance imaging (MRI) scans were acquired from a Siemens 3 Tesla (T) Verio scanner (Siemens Healthcare, Germany) at the Auburn University MRI Research Center. For the patient group, all MRI scans were performed on a 1.5T scanner (Signa, GE Healthcare, Milwaukee, Wisconsin) at UAB. For cine MRI, data was acquired with an ECG-gated, breath-hold steady state free precision (SSFP) technique in standard two-chamber, four-chamber, and short axis (SA) imaging orientations. To enable surface reconstructions in all four chambers, two additional scans were acquired. A right two chamber view imaged the right-sided atrium and ventricle with 1 extra breath-hold. An atrial short axis view was acquired so that images cover from LV apex to LA apex, and RV apex to RA apex. This view usually required 4-8 slices with 2-4 extra breath-holds. Note that this protocol only requires 3-5 extra breath holds relative to a standard cine cardiac MRI protocol. The imaging parameters for these scans are shown in Table 1-1 in Chapter 1. Figure 3.2 shows the images at different views from cine MRI with projections from other views.

To determine the right two-chamber orientation, four-chamber view was used for the slice prescription. A plane that transects the RV apex and the middle of tricuspid valve annulus was acquired. The atrial short axis view was also prescribed on the four-chamber view. The orientation was set to parallel to both MV and TV annuli, or as close to parallel to both as possible. The slices of atrial short axis covered from LA apex to the TV annulus or MV annulus, depending on which one is further to the respective apex. Usually, to acquire enough slices and less overlapping, right two-chamber, standard left two-chamber and four-chamber views were used as references for the SA view as shown in Figure 3.2 A, B and E.

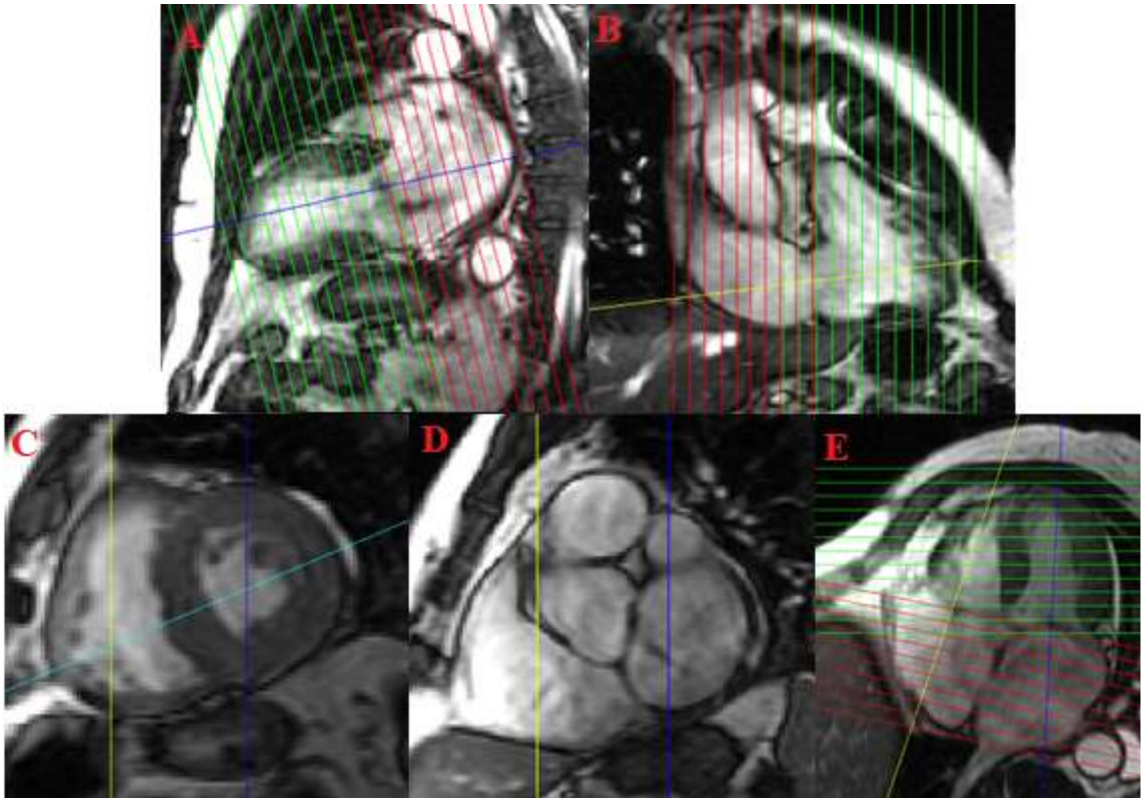

Figure 3.2 MRI imaging orientations and projections. A, C, E: standard two chamber, short axis and four chamber views respectively. B: extra right 2 chamber view. D: extra atrial short axis view. Projection lines, green- short axis view, red-atrial short axis view, yellow-right 2 chamber view, cyan-four chamber view, blue-left 2 chamber view.

3.4.2 Image Population

Eight mitral regurgitation patients (n=8), aged from 48 to 82, before surgery were imaged in this study. Eight normal volunteers (n=8) without clinical or anatomical evidence of cardiovascular disease, aged from 19 to 24, were imaged as a healthy group.

3.5 Image Preprocessing

3.5.1 Image Segmentation

Delimitation of the endocardial boundaries of heart chambers is a prerequisite for heart surface reconstruction. In chapter 2, we reviewed the current methods and issues on segmentation. Grey level intensity variation and inhomogeneity, artifacts in images and difficulties in papillary muscles distinguish are the main issues preventing automatic segmentation. To our best knowledge, there are no methods that have successfully solved the problems or provided accurate automatic segmentations over a broad range of imaging studies. In this dissertation, we used a semi-auto method on a house-built software called “set myo contours” (SMC) to segment four heart chambers on MRI images [77]. This method has been successfully applied and verified in many clinical studies [5] [24] [42] [62] [63].

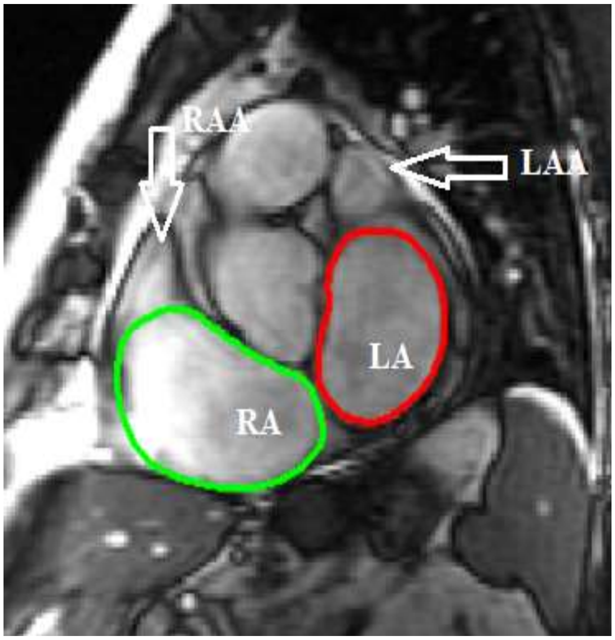

Figure 3.3 LA and RA contours in the short axis view with LAA and RAA excluded

In short axis and atrial short axis views, left and right endocardial contours were manually drawn continuously from the atrium apex to the ventricle apex without regard to atrioventricular or arterial boundaries at ventricular ES and ED. In our data sets, the ventricular ES phase mainly lies around phase 7 or 8 and ED around phase 1 or 20. While the atrial appendage is a part of the left atrium, its location may vary and the boundaries of the hooked and tube-shaped appendage is not always easy to identify from 2D slices. Since reliable assessment of the left atrial appendage was not always possible in the present study, its volume was usually excluded from the reported left atrial volumes [115]. Therefore, in the contouring, we excluded the atrial appendage. Figure 3.3 shows the LA and RA contours in the SA view with appendages excluded. Papillary muscles were included from the LV wall contours and were considered part of the chamber volume. In two-chamber, four-chamber and right two-chamber views, landmarks at intersections of the mitral valve (MV) and tricuspid valve (TV) leaflets with corresponding ventricle walls were defined at ventricular end-diastole (ED) and end-systole (ES). Figure 3.4 and Figure 3.5 shows the landmarks marked on the long axis views. All drawn contours and defined landmarks were propagated to remaining time frames using an automated algorithm [77].

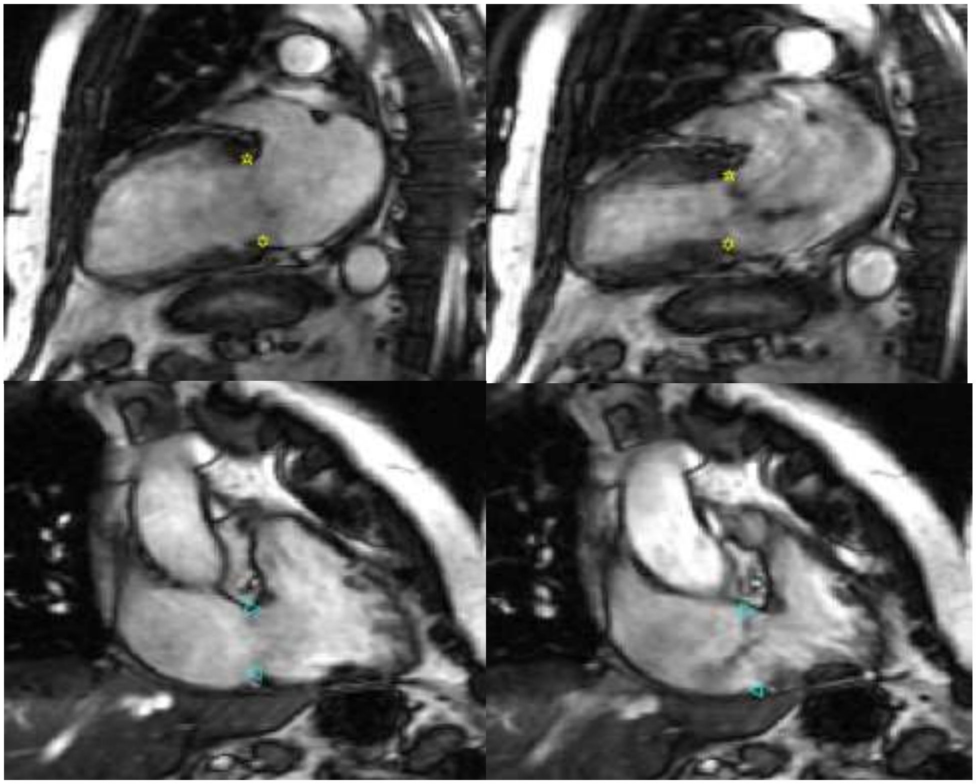

Figure 3.4 Landmarks for MV (yellow) and TV (blue) in the left 2 chamber (top) and the right 2 chamber (bottom) views at ventricular ED (left) and ES (right)

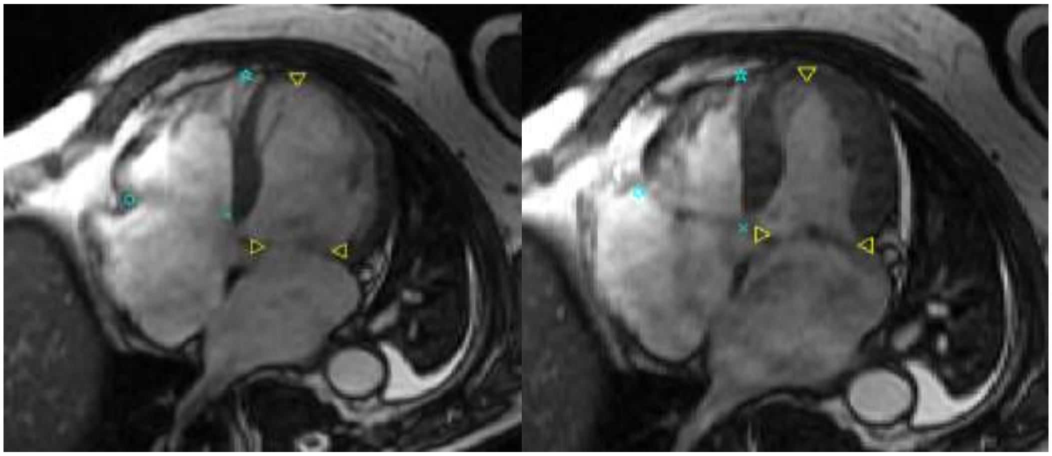

Figure 3.5 Landmarks for MV (yellow) and TV (blue) in the 4 chamber (bottom) views at ventricular ED (left) and ES (right)

In the surface fitting, we first constructed a template at the timeframe when the chamber has the largest volume, which will be explained and described in detail in Section 3.6. Long axis images provide comprehensive and more accurate information on the modeling of the basal and the apical levels [79]. Therefore, in addition to those endocardial contours in SA and atrial SA views, endocardial contours in long axis views were defined at ventricular ED and ES phases, which is shown in Figure 3.6. In two-chamber, four-chamber and right two-chamber long axis views, atrial endocardial contours were manually drawn at corresponding ventricular ES timeframe, and ventricular endocardial contours were drawn at corresponding ventricular ED timeframe. All contours and landmarks were double checked from different views and were corrected if needed. Surface modeling of the heart chambers were then applied to a set of points that were generated from the contours.

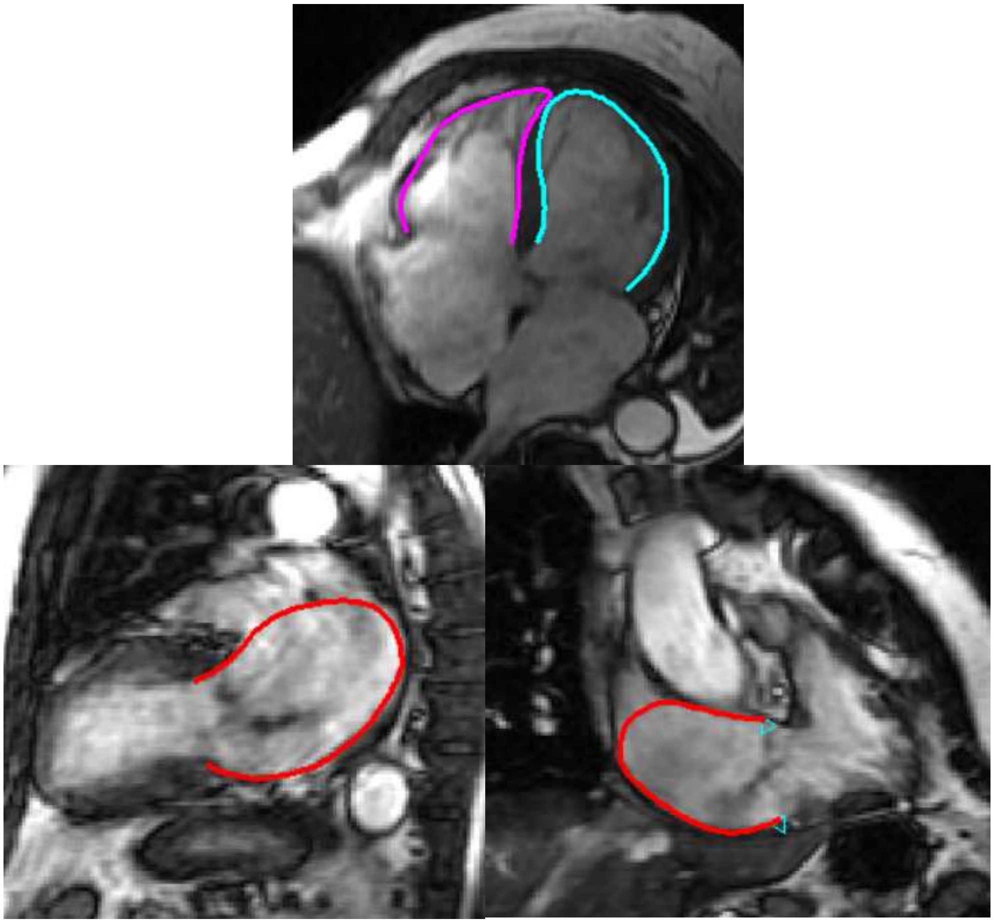

Figure 3.6 Contours in the long axis view. Top: 4 chamber view. Bottom left: left 2 chamber view. Bottom right: right 2 chamber view

3.5.2 Fitting Coordinate System

In surface fitting, a fitting coordinate system was used in the pre-alignment to account for rigid-body motion [37]. In [77], Patel found pulmonary vein ostia are minimally displaced and suggested the potential of pulmonary vein ostia In the LA registration or alignment in the future. However, in clinical cardiac MRI data, it is either hard to specify the luminary vein ostia due to the volume effect induced by the 8-mm slice thickness nor the imaging orientation, especially when the patient’s data is acquired under the pressure of minimizing scanning time and maximizing patient convenience. For the RA, it is hard to find reliable correspondence across images as well. Therefore, we used another fitting coordinate system that is popular in left ventricle. In this fitting coordinate system, the contours from ventricular short axis view are perpendicular to the z-axis running from the apex to base, and x-axis running through the anterior RV insertion into the LV wall [42]. All contours and valve landmarks were transformed to this fitting coordinate system before surface fitting. It is important to note that the above transformation is a rigid body transformation, which has no scaling or deforming effect on contour points and landmarks.

3.5.3 Valve Annulus and Plane Fitting

MV annulus is a saddle-shaped hyperbolic paraboloid [63-64], and TV annulus is also a non-planar structure with an elliptical saddle-shaped pattern [89]. Figure 3.7 shows the MV and annulus shape and the landmark positions we marked in the data sets. A representative TV annulus is shown in Figure 3.8. In standard clinical volume computation, one whole slice is assigned to either atrium or ventricle will introduce volume estimation errors. In this dissertation, instead of assigning an entire slice to a chamber, we used both valves to separate contours into

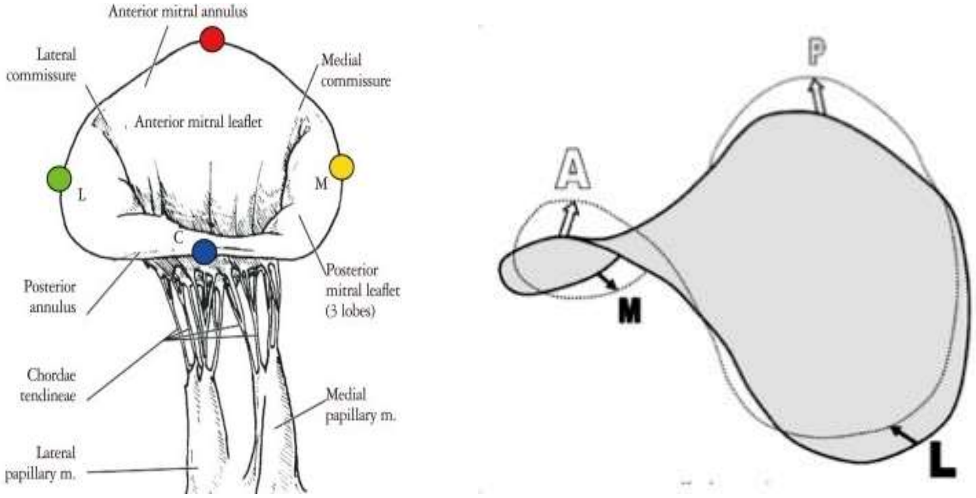

Figure 3.7 A schematic representative of the mitral valve and landmarks placement on the Mitral valve annulus, image source [65].

atrial and ventricular partial contours. Due to the difficulties and expense to simulate the exact annular and leaflets anatomy with limited landmarks from limited views, we approximated MV and TV with planes from the landmarks in long axis views using a least squares fit. The annuli were approximated by fitting ellipsoids to the marked landmarks [71] using least squares.

Based on the mitral valve (MV) and tricuspid valve (TV) landmarks defined in the long axis views, MV and TV planes were fit to those landmarks for each timeframe in the cardiac cycle [62-63]. These planes were used to split contours into atria and ventricles before the surface fitting as described below.

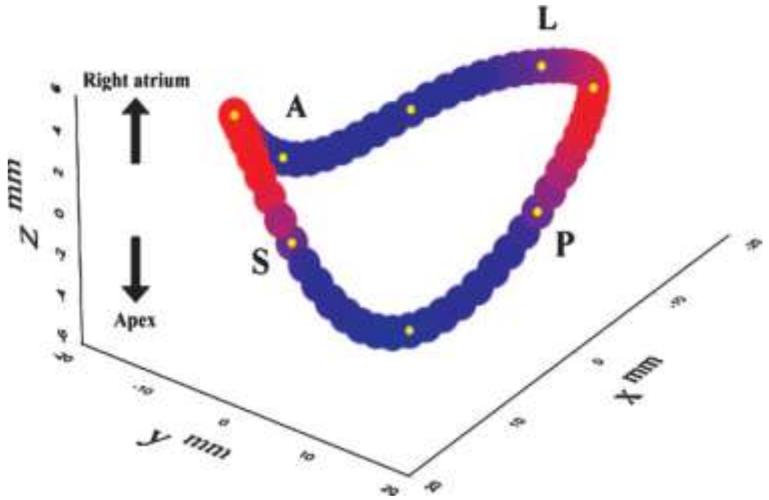

Figure 3.8 A schematic representative of the tricuspid valve annulus [90].

3.5.4 Contour Splitting

Short axis prescriptions are usually not parallel to the MV annulus nor TV annulus. As a result, volume calculated from short axis contours alone may be inaccurate. For example, in the atrioventricular region, if the whole slice is assigned to the ventricle, then the ventricle volume will be overestimated and atrium volume will be underestimated. If the whole slice is assigned to the atrium, then the overestimation and underestimation will be reversed. Therefore, we proposed a novel algorithm to separate the contours by employing the planes fitted to the MV and TV described above [63].

The approximated TV and MV planes were used to determine which part of each slice was in the atrium and which part was in the ventricle. This was realized by using the valve planes to separate contour points into LA and RA or LV and RV [63]. The separation was computed by the intersection of all the contours and the MV and TV planes. The portion of each slice in the atrium or ventricle was between 0 and 1 and the sum of atrial and ventricular portions in each slice sum to 1. Figure 3.9 illustrates the separation of the left-sided contours and right-sided contours by valve planes. In the figure, the left-sided contour points above MV plane are assigned to LA and those below are assigned to LV. The right-sided contour points above TV are assigned to RA and those below are assigned to RV.

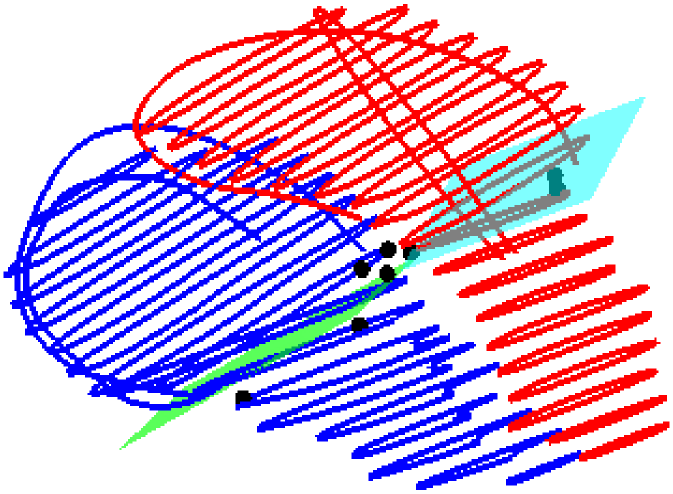

Figure 3.9 Contour splitting illustration of a MR patient at ES. Planes: TV (green), MV(cyan). Black dots: valve landmarks. Contours: Right-sided (blue); left-sided (red).

3.6 Surface Fitting Algorithm

3.6.1 Rough Mesh Surface Construction

In order to fit a smooth surface to the strongly anisotropic segmentation, we fitted a rough surface to the contour points first, and this rough surface was used as the initial input into a smoothing procedure. Since all shapes of heart chambers are topologically equal to a sphere [37] [43], we built a triangulated mesh sphere to contain the chamber data points, as shown in Figure 3.10, and shrank the sphere to fit a rough surface on the data points.

The pre-meshed sphere was nearly uniformly sampled with 1000 vertices and meshed with Delaunay triangulations [42] [65] [66]. Since this pre-meshed sphere is sampled with nearly uniformed distributed vertices, it is almost a perfect mesh with isosceles triangles. The sphere was centered at the centroid of the contour data points. The radius of the pre-meshed sphere was set to be the largest distance from the contour points to the centroid. By constructing a pre-meshed sphere in this way, all contour points of the chamber were inside of the sphere. An example of the constructed sphere is shown in Figure 3.10.

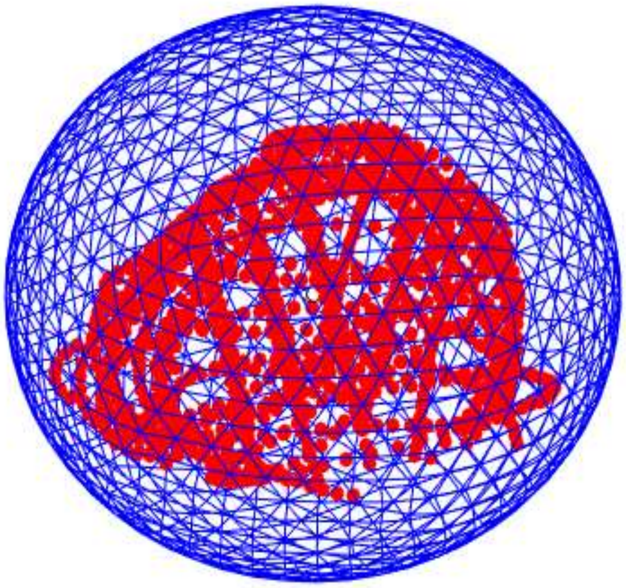

Figure 3.10 A pre-meshed sphere (blue mesh) wrapping contours (red points) of an atrium at ventricular ED.

To shrink the surface to the contour points, we moved each vertex along a radial line from the center of the sphere to the vertex on the sphere. This procedure is similar to the one in [37]. On the radial line, we centered a spherical neighborhood with a radius equal to the slice (8-mm in our data) and moved it along the radial line toward the center with a step size of 1/30 of the distance between the vertex and the chamber center. The neighborhood sphere stopped moving when the number of contour points inside the neighborhood was maximized. The vertex was then placed at the center of the spherical neighborhood. This procedure was repeated for all vertices on the sphere. This process is demonstrated in Figure 3.11.

Inside the valve annuli, there may be vertices with no contour points in the spherical neighborhood along the radial line from the vertex to the centroid. These vertices on the rough surface were placed at the intersection of the radial line and the MV or TV planes. This procedure was displayed in the Figure 3.12. The approximated annuli were employed as the connecting points in the atrioventricular region between atrium and ventricle in the smoothing procedure.

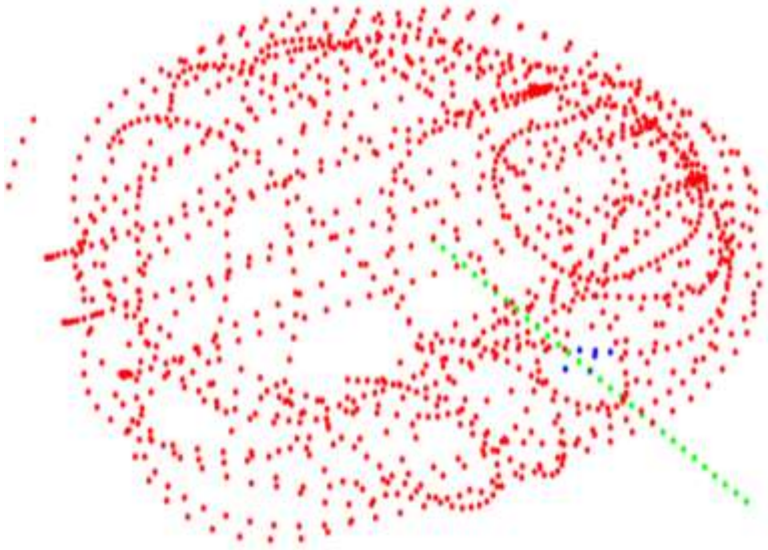

Figure 3.11 Red: Contour points. Blue: contour points in a spherical neighborhood along a radial line (green)

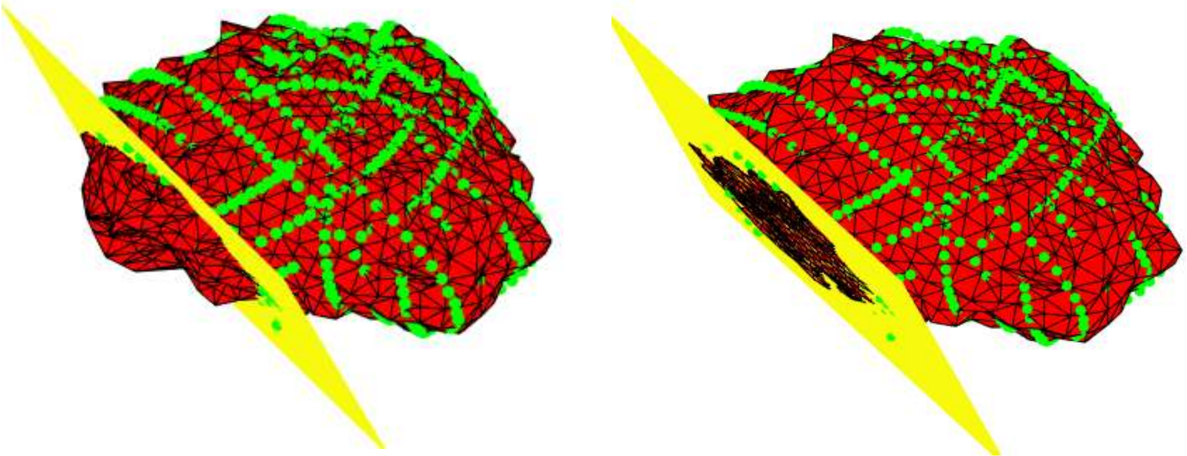

Figure 3.12 Left: rough surface (red) of an atrium with mitral valve plane (yellow). Right: The same surface (red) after being cut by the mitral valve plane (yellow)

3.6.2 Mesh Smoothing

The heart surface is smooth and of uniform texture [42], therefore, it is important to map the vertices from the pre-meshed sphere to an object with a smooth surface. The rough mesh surface created from the contour points and valve planes is coarse and has strongly irregular triangles, as shown in Figure 3.13. Hence, we smoothed the rough surface to obtain a surface with small fitting error and smooth curvature.

3.6.2.1 Laplacian Smoothing

Laplacian smoothing is a common technique in mesh smoothing [100] because it is easy to implement and offers many opportunities in modifications and improvements based on application [100]. In the Laplacian smoothing, the mesh connectivity is not changed but the vertex positions are optimized in each iteration to approximate prescribed Laplacians. In its general form, vertices are repeatedly moved by a scaled difference between the average of the neighboring vertices and the corresponding vertices [83] [84] [101] [102]. Laplacian smoothing arises from finding the function $p(x,y)$ that minimizes the following energy function:

$$E = \iint \frac{1}{2} \left|\left|\nabla p\right|\right|^2 dxdy \ , \tag{3.1}$$

The function *p* that minimizes 3.1 is given by the Euler-Larange equation:

$$-p_{xx} - p_{yy} = -\Delta p = \ 0 \ , \tag{3.2}$$

where the left-hand side is the function derivative δ*E*/δ*p*, and Δ is the Laplacian operator.

For a triangular mesh, the Laplacian Δp is defined as the following:

$$U(p_i) = \frac{1}{J} \sum_{j=1}^{J} p_{ij} - p_i \, , \mathrm{i} = 1 \cdots \mathrm{M} \, , \tag{3.3}$$

where p_i and p_{ij} are vertex coordinates in 3D, *M* is the total number of vertices on the mesh, and p_{ij} is the neighbor vertices in the one-ring neighborhood, which share edge with vertex p_i. *J* is the number of neighboring vertices. $U(p_i)$ is called the Laplacian operator or umbrella operator. Figure 3.14 shows the umbrella operator of a vertex with its first order neighbors.

For triangular meshes, Equation 3.2 is not solved directly. Instead, E in Equation 3.1 is minimized by gradient descent using the functional derivative defined by the left-hand side of Equation 3.2. This yields the Laplacian smoothing updated rule:

$$p^{n+1} = p^n - \lambda\big(-U(p^n)\big)$$

$$p^{n+1} \ = p^n + \lambda U(p^n) \, , \tag{3.4}$$

where λ is a step size.

3.6.2.2 Modified Laplacian Smoothing

Equation 3.3 is the most basic form of the Laplacian operator. The more general form of it is shown in Equation 3.5, which reduces to Equation 3.3 when $w_{ij} = 1$.

$$U(p_i) = \frac{1}{\sum_{j=1}^{J} w_{ij}} \sum_{j=1}^{J} w_{ij} p_{ij} - p_i, i = 1 \cdots M \, , \tag{3.5}$$

Though the Laplacian mesh smoothing method provides a fast and simple mesh smoothing method while increasing mesh regularity, it can cause the shape to shrink to a point when the mesh is closed and without boundary conditions. Another drawback of Laplacian method is that it develops unnatural deformation when applied to irregular mesh [100] [106]. Therefore, there has been a lot of work in the optimization of Laplacian mesh smoothing. One modification, called inverse distance weighting (IDW), that produces good results is to use inverse distances between a vertex and its neighbors as the coefficient w_{ij}in Equation 3.6 [103]:

$$w_{ij} = \frac{1}{d_j}, d_j = ||p_{ij} - p_i|| \ , \qquad 3.6$$

This modification can also shrink to a point in a closed mesh if there is no boundary condition, and it can worsen the triangle quality [100] as well because more weight is given to neighboring points, p_{ij}, closer to the central point, p_i.

To prevent shrinkage of the Laplacian method, Taubin [103] proposed a two-step Laplacian operator to inflate the mesh after smoothing, which is also called λ|μ method. It is realized by set $\lambda > 0$ in the Equation 3.4 in the first step then followed by an inflated step by setting $\lambda < 0$ in the Equation 3.4, which is usually denoted as μ for the negative λ. The λ and μ should satisfy the following constraints:

$$\frac{1}{\lambda} + \frac{1}{\mu} > 0 \, , \qquad 3.7$$

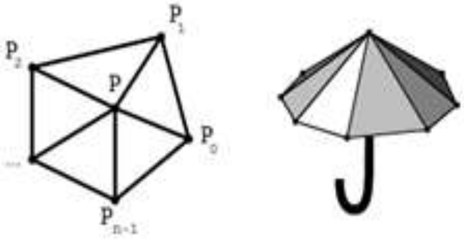

Figure 3.13 First order neighbors of a vertex p in the umbrella-operator

Desbrun et al. [102] proposed cotangent weights for scale-dependent and the weight in Equation 3.5 is defined as the following, and it is shown in Figure3.14.

$$w_{ij} = -\frac{1}{2(\cot \alpha_{ij} + \cot \beta_{ij})} , \qquad 3.8$$

For the cotangent weights, one drawback is the weights can be negative if $\alpha_{ij}+\beta_{ij}>0$, which results in flipped triangles. Another drawback of cotangent weights is that it leaves triangle shapes and sizes mostly unchanged, which only smooth the curvature but not improve the triangle quality and density [103].

There are other modifications from the basic Laplacian smoothing based on the application, but those modifications above are the most common ones.

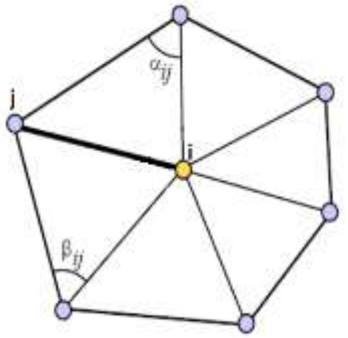

Figure 3.14 Illustration of cotangent weights in the Umbrella Operator

3.6.2.3 Proposed Modification with Density Regularizing

In mesh smoothing, we are aiming at moving vertices to generate approximate equilateral triangles while smoothing the surface. As pointed out in the previous section, using inverse distance weighting (IDW) in the Laplacian operator will worsen the triangle quality [100], which result in worse density regularity with iterations. Therefore, to prevent degradation of triangle quality, in this dissertation, we propose to use distance weighting instead of inverse distance weighting in the Laplacian operator:

$$w_{ij} = d_j, d_j = ||p_{ij} - p_i|| \,, \qquad 3.9$$

By using the distance as the weight, we can move a vertex p to make the triangle edges towards approximately the same length in each iteration. We will compare the relative performance of the distance weighting versus inverse distance weighting and other methods in Section 3.6.3.

3.6.2.4 Proposed Modification with Contour Points Constraint

As pointed out, when the Laplacian smoothing methods are applied without boundary constraints, it can result in shape shrinkage, i.e. an object shrinks to a point when the iteration is large enough [107]. Besides the Taubin method (λ|μ method) [103], another solution to address the shrinkage is to label the vertex as internal vertices or boundary vertices, then use the boundary vertices as constraints and smooth them independently with internal vertices [84] [106]. In [106], the author divided the mesh vertices into movable vertices and fixed vertices, then those fixed vertices were employed as boundaries to constraint the shape.

However, in our application to fit surfaces to segmented contour points from cardiac MRI data, the surface is a closed surface and has no boundaries. Due to the breath-hold shifts between slice acquisitions and user variability in contouring, the contour points may not be located on the mesh and we cannot use them as fixed vertices directly as well. Therefore, in this dissertation, with the application to fit surfaces to segmented data from cine MRI, we propose to modify the Laplacian method by adding nearby contour points of each vertex as local soft constraint.

We defined the nearby contour points of a vertex point to be all contour points within a sphere of radius *r* centered at the vertex. The radius *r* was set to the slice thickness, which is 8 mm in our datasets. In the smoothing procedure, only the nearby contour points have effect on that vertex. To find the contour point constraint, we started with the following cost function, which combines and fitting error term and a smoothness term:

$$E_1 = \iint \frac{1}{2}(c-p)^2 + \tfrac{1}{2}\left|\left|\nabla p\right|\right|^2 dxdy \quad , \tag{3.10}$$

where c is a function representing a surface from the measured contour points. The corresponding Euler-Lagrange equation is:

$$-(c-p) - \lambda\Delta\mu = 0 \quad , \tag{3.11}$$

For a triangular mesh with fixed, non-uniformly-spaced contour points, implementing the difference c-p is not trivial. Following the example of the umbrella operator, we could define c-p as the average distance between a vertex pi and neighboring contour points. Then, the iteration would be:

$$p_i^{n+1} = p_i^n + \lambda U(p_i^n) + \frac{1}{Q}\sum_{q=1}^{Q}\left(c_q - p_i^n\right), i = 1 \ldots\ldots M \tag{3.12}$$

where Q is the number of nearby contour points for vertex p_i^n, c_q is the *qth* nearby contour point to vertex p_i^n, Q is the total number of nearby contour points for vertex p_i^n. *M* is the total number of vertices on the mesh. To control the weight of the contour points constraint term, we use tuning term ω_2, and to avoid confusion with the λ|μ (Taubin) method in the comparion in Section 3.6.3, we replaced λ with ω_1, which yields:

$$p_i^{n+1} = p_i^n + \omega_1 U(p_i^n) + \frac{\omega_2}{Q}\sum_{q=1}^{Q}(c_q - p_i^n) \ , \tag{3.13}$$

This modification preserves the shape by the averaged difference between the nearby contour points and the corresponded vertex, which assigns equal weight to each nearby contour points. However, we want to enhance the effect of contour points closer to the vertex and diminish the effect of contour points further away from the vertex, this can be done by using the inverse distance weighting, which yields

$$p_i^{n+1} = p_i^n + \omega_1 U(p_i^n) + \frac{\omega_2}{\sum_{q=1}^{Q} \frac{1}{||c_q - p_i^n||}} \sum_{j=1}^{Q} \frac{c_q - p_i^n}{||c_q - p_i^n||} , \qquad 3.14$$

We will compare the relative performance of both proposed contour points constraint term with Taubin method and other methods in Section 3.6.3.

3.6.2.5 Summary of Alternatives

At this point we have the three alternatives for implentation of the Laplacian, U(p), listed in Table 3-1 and two alternatives for the shape control term listed in Table 3-2, which yields a total of 6 possible combinations. In the final disseration, we will optimize the weights, ω_1 and ω_2, for each combination using the sixteen subjects, including 8 normal subjects and 8 MR patients, described in Section 3.4.2 and compare them based on the fitting error, smoothness, and triangle quality criteria defined below.We will also study the sensitiviy of these criteria to weights and other parameters.

Table 3-1 Laplacian and modified Laplacian smoothing operator

Laplacian Operator	$U(p_i) = \frac{1}{J} \sum_{j=1}^{J} p_{ij} - p_i$
IDW Laplacian Operator	$U(p_i) = \frac{1}{\sum_{j=1}^{J} \frac{1}{\|\|p_{ij} - p_i\|\|}} \sum_{j=1}^{J} \frac{1}{\|\|p_{ij} - p_i\|\|} p_{ij} - p_i$
DW Laplacian Operator	$U(p_i) = \frac{1}{\sum_{j=1}^{J} \|\|p_{ij} - p_i\|\|} \sum_{j=1}^{J} \|\|p_{ij} - p_i\|\| p_{ij} - p_i$

Table 3-2 Different types of fitting contour points constraint

Average Difference	$\frac{1}{Q}\sum_{q=1}^{Q}\left(c_q - p_i^n\right), i = 1 \ldots . . M$
IDW Difference	$\frac{\omega_2}{\sum_{q=1}^{Q}\frac{1}{\lvert\lvert c_q - p_i^n \rvert\rvert}}\sum_{j=1}^{Q}\frac{c_q - p_i^n}{\lvert\lvert c_q - p_i^n \rvert\rvert}$

In the following sections, we will define the fitting error, smoothness and triangle quality criteria and present preliminary performance comparison results from a subset of the 6 combinations described above. In the comparison, in addition to 6 combinations from the 3 alternatives of the Laplacian operator and the two types of the contour points constraint, Taubin method, which is know to address the shrinkage problem, is also compared with the 6 combinations.

3.6.3 Performance Criterions

We aimed at reconstructing a surface to the contour points from the segmentation of cardiac MRI data with high accuracy and high triangle quality. Therefore, we will explore the performance of the smoothing algorithm based on the fitting error, surface smoothness and triangle quality aspects.

3.6.3.1 Fitting Error Criterion

We aimed at reconstructing the surface from the segmented data with high conformity to the segmented data. In order to measure how well it conforms, we estimated the fitting errors, which is defined as the ‘point-to-surface’ distance [46], i.e. the distance between the contour points and the corresponded projected points on the fitting surface. In here, we measured the normalized fitting errors:

$$E_e = \frac{1}{K}\sum_{k=1}^{K}(c_k - p_k)\,, \qquad 3.15$$

where c_k is the qth contour point, and P_k is the projection on the surface of C_k. K is the total number of contour points of the targeted chamber, and $\frac{1}{Q}$ is the term that normalizes the error in order to avoid the dependency of the number of contour points.

3.6.3.2 Smoothness Criterion

We aimed at reconstructing a surface with smooth curvature since the heart surface of human is smooth and of uniform texture. The change of surface normal on each vertex reflects the smoothness of the surface. The smaller the normal change is, the smoother the surface is. In [41], Schiros defined the normal change as the normalized normal difference between the vertex normal and the normals of its neighboring vertices:

$$Ec = \frac{1}{M}\sum_{i=1}^{M}\left(\frac{1}{J}\sum_{j=1}^{J}(1 - n_i \cdot n_j)\right), \qquad 3.16$$

where M is the total number of vertices on the surface, n_i is the unit normal vector of the ith vertex, and n_j is the unit normal vector of the jth vertex in the umbrella neighborhood of the ith vertex. The umbrella neighborhood a vertex is the set of all vertices that are connected to the vertex in the surface mesh, as shown in Figure 3.14. The term $\frac{1}{M}$ normalizes the normal change in order to avoid the dependency of the number of vertices on the surface.

The normal of each vertex is a unit vector, which is computed as the weighted sum of the unit normal of the triangles in its one-ring neighborhood. Figure 3.16 shows the i^{th} vertex and the normal of its neighbor triangles. The weights are set to be the inverse of the distance (d) from the vertex to its neighborhood triangle centers. The calculation of the vertex normal is shown as:

$$n_v = \frac{\sum_{i=1}^{I}(w_i n_i)}{||\sum_{i=1}^{I}(w_i n_i)\,||}\,, w_i = \frac{1}{d_i}, \qquad 3.17$$

where I is the number of neighbor triangles for vth vertex, w_i is the weight of ith neighbor triangle, where d_i is the distance between vth vertex and ith triangle center. This calculation is denoted in Figure 3.16 in which I = 5.

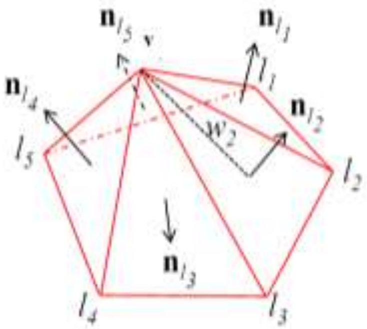

Figure 3.16 Normal vector of the vth vertex, and normal of its neighbor triangles

3.6.3.3 Triangle Quality Criterion

Besides the conformity and smoothness, we aimed at reconstructing the segmented data with high mesh quality, which can be detected by the quality of the triangle. One guideline is to measure the degree of the angles in the mesh, which indicates the quality of the triangular mesh. In the literature [38], the author pointed out that the range of 40 degrees to 80 degrees is typically considered to be good quality of triangles. To estimate the mesh quality of the fitted triangular mesh, we computed the percentage of good triangle angles.

3.6.4 Comparison Results

In the comparison, ω_1 and ω_2 were set to be 0.6 and 0.3, the parameter sensitivity will be conducted in the following section. The six combinations described in Section 3.6.2.5 were compared for the performance based on the criterions described in Section 3.6.3. Since Taubin method is known to address the shrinkage drawback of the Laplacian method, so we used it to compare with all the combinations as well with $\lambda = 0.5$ and $\mu = -0.53$. We conducted the comparison on 8 subjects, including 4 MR patients and 4 normal subjects for the preliminary experiments. In the final dissertation, all 16 subjects described in Section 3.4.2 will be compared.

3.6.4.1 Fitting Error

Figure 3.17 shows the normalized fitting error of all 6 combinations and the Taubin method over iterations for the LV surfaces. From it, we can see that the Taubin method has obvious increasing fitting error over the 100 iterations continuously and has increasing trending after 100 iterations too. The fitting error of other 6 combinations with the contour points constraint term decrease first and then will reach a stable value. Because the rough surface is built by interpolating vertices at points with largest number of contour points, therefore, the constraint term will first drag the vertices towards the contour points resulting in the decreasing fitting error, but the Laplacian-based term will smooth the vertices controlled by neighboring contour points resulting in the increasing distance to the contour points, therefore the error will increase after the decrease. In this data set, the performance of the Taubin method in the interpolated point is close to the contour points. In the smoothing procedure, the contour points fitting error is the worst compared to the other 6 combinations, which have the contour points constraint. This shows that the contour points constraint term performs better than the Taubin method in addressing the shrinkage problem of the Laplacian method. Among all the 6 combinations, The DW Laplacian and IDW Difference combination has the smallest stable value at 1.3 mm, which is smaller than the pixel size (1.56 mmx1.56mm). Therefore, we can conclude that, in this data set, the contour points constraint addresses the shrinkage problem better than the Taubin method, and the combination of the DW Laplacian operator and the IDW Difference type of contour points constraint has the best performance in reducing the fitting error.

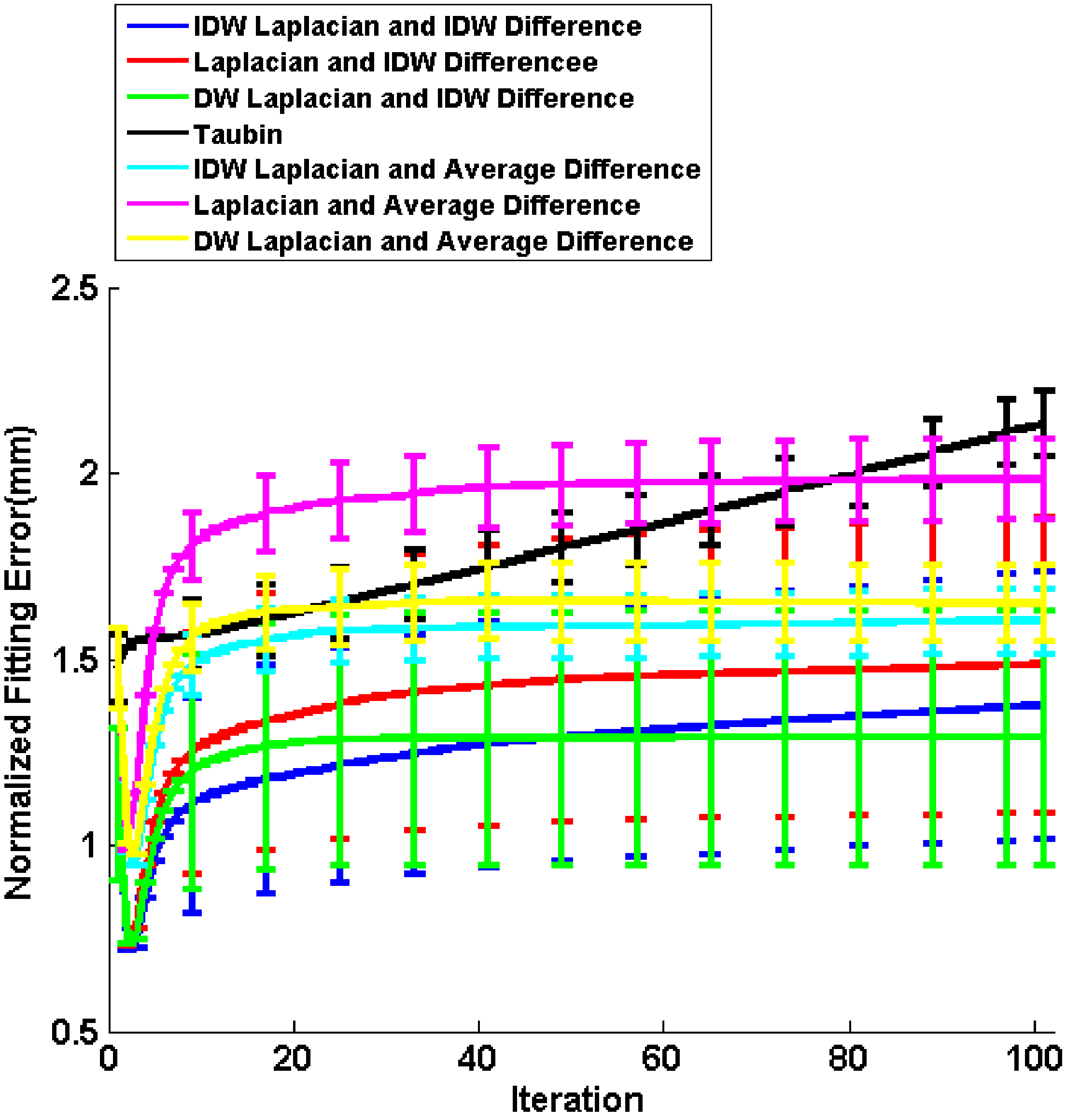

Figure 3.17 Avearged normalized fitting error of 4 normal subjects and 4 MR patients over iterations among the 6 combinations defined in Section 3.6.2.5 and the Taubin method. Mean±SD.

3.6.4.2 Smoothness

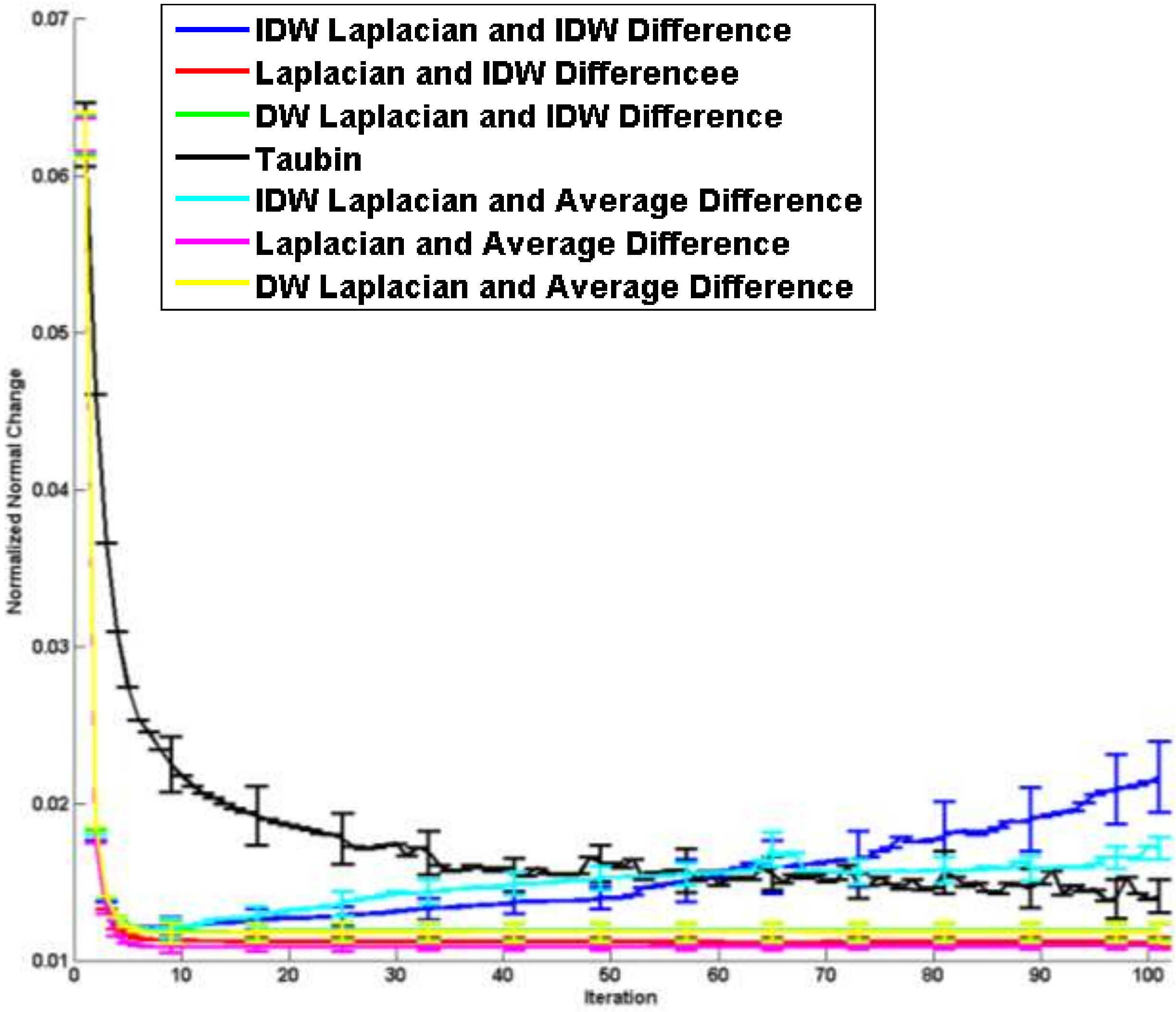

Figure 3.18 Averaged normalized surface normal change comparison of 4 normal subjects and 4 MR patients over iterations among the 6 combinations defined in Section 3.6.2.5 and the Taubin method. Mean±SD.

Figure 3.18 shows the averaged normalized surface normal change over iterations of the 8 subjects of the 6 combinations defined in Section 3.6.2.5 and the Taubin method. From the figure, we can see that the normal change curve of the Taubin method decreases at the slowest speed and the IDW Laplacian combinations decrease first then increase after 50 iterations. Both the Taubin method and the IDW Laplacian combinations have fluctuations over iterations. All combinations of the Laplacian and DW Laplacian decrease fast and have a stable value after 10 iterations. Therefore, in this data set, we can conclude that the performance of the combinations of the Laplacian operator and the DW Laplacian operator with both types of contour points constraint are good in the smoothness.

3.6.4.3 Triangle Quality

Figure 3.19 shows the averaged good angle percentage over iterations of the 8 subjects of the 6 combinations defined in Section 3.6.2.5 and the Taubin method. From the figure, we can see that, we can see that The IDW Laplacian operator and its combinations and the Laplacian operator and its combinations both have decreasing good triangle percentage over iterations. The curves of the good angle percentage of the Taubin method and the combination of the DW Laplacian operator with both types of contour points constraint have a stable value over iterations. In the DW Laplacian operator combinations, the IDW Difference type of contour points constraint has better performance that the Average Difference one. Therefore, in this dataset, we conclude that the Laplacian and IDW Laplacian operators have bad performance, and Taubin method has the best performance, the combination of DW Laplacian and IDW Difference has comparable good performance with Taubin method.

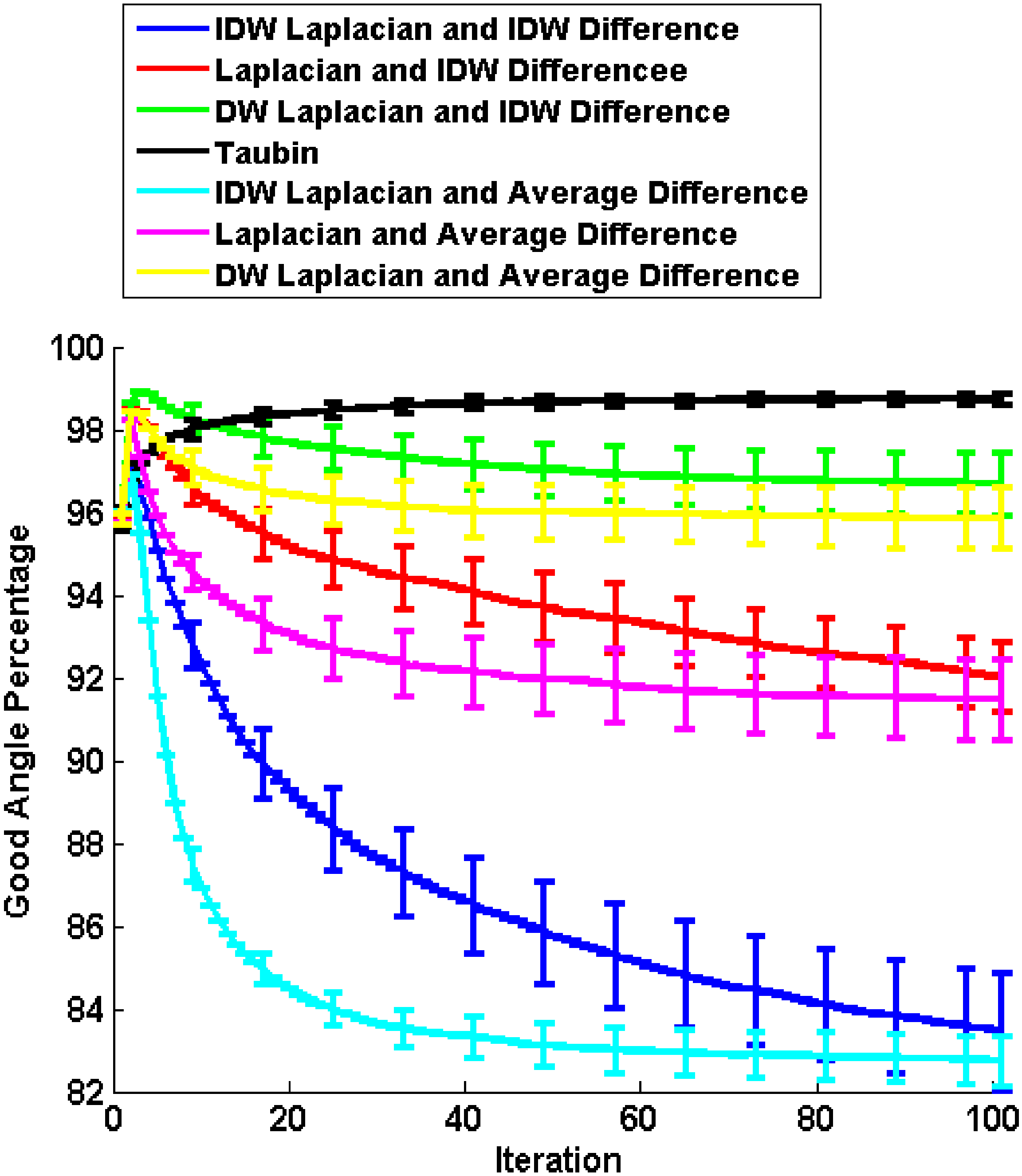

Figure 3.19 Averaged good angle percentage comparison of 4 normal subjects and 4 MR patients over iterations among the 6 combinations defined in Section 3.6.2.5 and the Taubin method. Mean±SD.

3.6.4.4 Conclusion

From performance of fitting error comparison, we can conclude that, we conclude that Taubin method has the worst performance and the combination of the DW Laplacian operator and the IDW Difference type of contour points constraint has the best performance in reducing the fitting error. From the smoothness performance comparison, we conclude that the performance of the combinations of the Laplacian operator and the DW Laplacian operator with both types of contour points constraint are good in the smoothness. From the triangle quality performance, we conclude that the Laplacian and IDW Laplacian operators have bad performance, and Taubin method has the best performance, the combination of DW Laplacian and IDW Difference has comparable good performance with Taubin method. Base on the conclusions from the comparison results, we found that the combination of the DW Laplacian operator and the IDW Difference type of contour points constraint have good performances in all of the fitting error, smoothness and the triangle quality aspects. However, since we only conducted performance comparison on the 8 representative subjects, therefore, we have no guarantee that it will follow the same trend in other studies. We used the combination of the DW Laplacian operator and the IDW difference type of contour points constraint in the smoothing for all the surfaces fitting in our dissertation. The iteration stops when the change of the vertex positions falls below a certain threshold.

3.6.5 Optimal Model Parameters

Based on the algorithm performance comparison in Section 3.6.4, we proposed to use the combination of the DW Laplacian operator and the IDW difference of contour points constraint term in the updating rule in the surface smoothing. In this section, we explored the effect of the parameters on the performances based on the criterions defined in Section 3.6.3. It is implemented by varying the following model parameters: the tuning parameter ω_1 for the DW Laplacian operator and the tuning parameter ω_2 for the IDW contour points constraint term in the updating rule as shown in Equation 3.14. The value of ω_1 in the updating rule controlled the vertex density and smoothness of the triangulated surface. The value of ω_2 in the updating rule controlled the fitting error of the triangulated surface. The optimal is explored by discretizing ω_1 and ω_2 in the interval from 0 to 1 with step size of 0.1 and conducting an exhaustive search.

Figure 3.20 shows the effects of different combinations of ω_1 and ω_2 on the normalized fitting error criterion, which reflects the fitting accuracy. It indicates that as long as $\omega_2 > 0.2$, the fitting error is less than a reasonable error (<2mm). Moreover, the top left triangle in the figure demonstrates a better performance in the fitting error. In the top left triangle, $\omega_2 > \omega_1$. Therefore, $\omega_2 > 0.2$ and $\omega_2 > \omega_1$ result a good performance in the fitting error, which reflects accurate fitting of the triangulated mesh to the surface.

Figure 3.21 shows the effects of the different combinations of ω_1 and ω_2 on the good angle percentage, which indicates the mesh quality. It shows that the good angle percentage increases while ω_2 decreases. For $\omega_2 > 0.6$, the good angle percentage increases then decreases along the increasing of ω_1. However, as long as ω_1 is between 0.2 and 0.8 and $\omega_2 < 0.7$, the good angle percentage is larger than 85%, which indicates good triangle quality and more generalized mesh density.

Figure 3.22 shows the effects of the different combinations on the normalized surface normal change, which reflects the goodness of the surface smoothness. It shows that when $\omega_2 < 0.7$ and $0.2 < \omega_1$, then the surface normal change lies at a small value (< 0.05).

From the performance analysis of the parameters in fitting accuracy, mesh quality and surface smoothness, we found the conditions for each aspect. Here we rewrite the findings: $\omega_2 >$

0.2 and $\omega_2 > \omega_1$ with fitting error < 1.5 mm, 0.2 < ω_1 < 0.8 and ω_2 <0.7 with good angle percentage > 85%, ω_2 < 0.7 and 0.2 < ω_1 with normal change < 0.05. Figure 3.22 shows the conditions for the three aspects. Therefore, to summarize all the conditions, we can conclude that the optimal parameter condition is $0.2 < \omega_2 < 0.7$ and $\omega_2 > \omega_1$, as the overlapped regions shown in Figure 3.23. When this condition is satisfied, the performance variations in fitting error, good angle percentage and the surface normal change are small, which demonstrates that the algorithm is relatively insensitive to parameters. In this dissertation, we set $\omega_1 = 0.4$ and $\omega_2 = 0.5$, which is marked as a red dot in Figure 3.20 to Figure 3.22. This combination has a small normalized fitting (<1.2 mm) and a small surface normal change (<0.02). Meanwhile, the good angle percentage is still high (around 90%). Therefore, using this parameter combination will generate a smooth surface with high accuracy and good mesh quality.

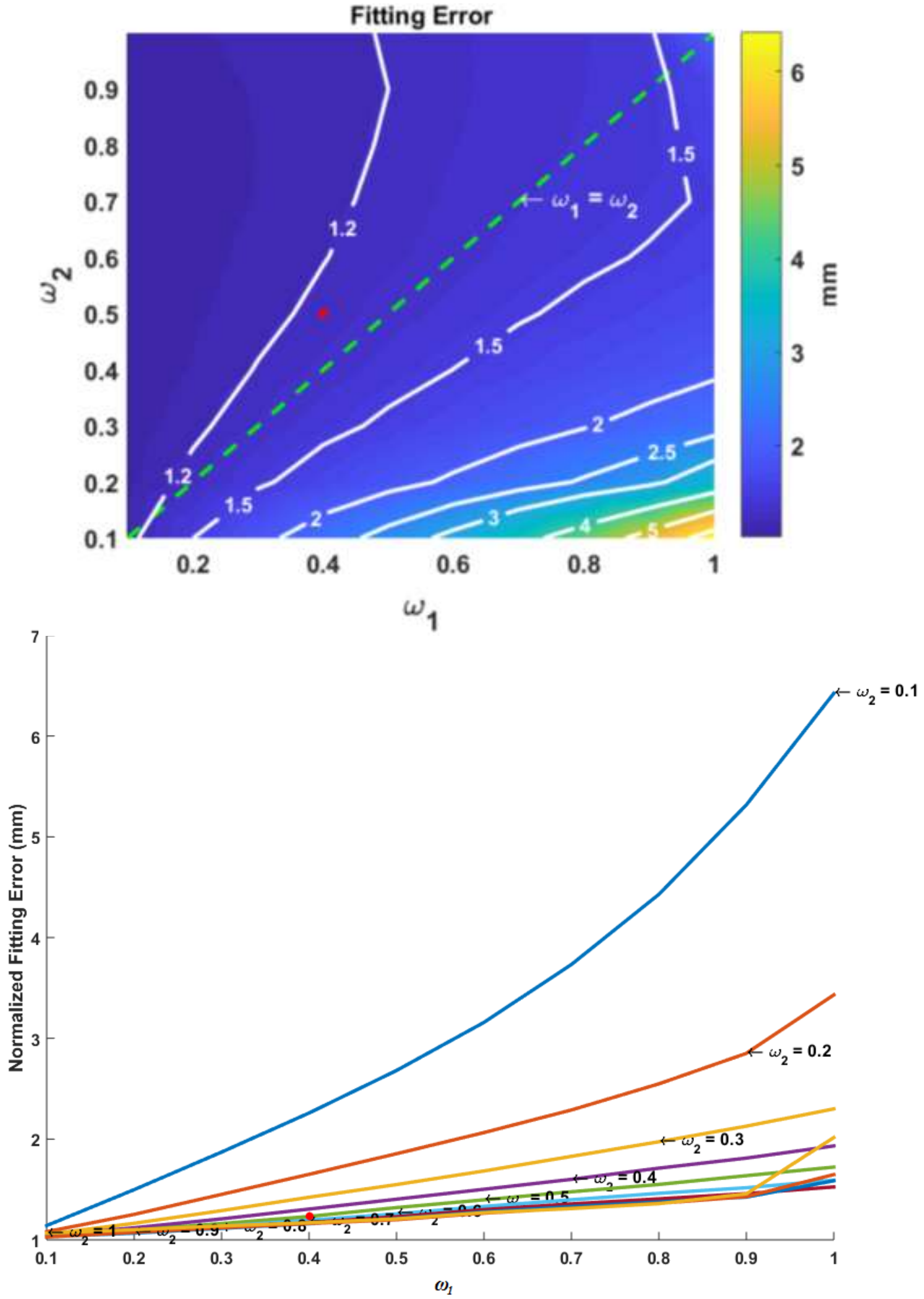

Figure 3.20 Fitting error vs. different ω1 and ω2 combinations. Red dot: the value used in this dissertation.

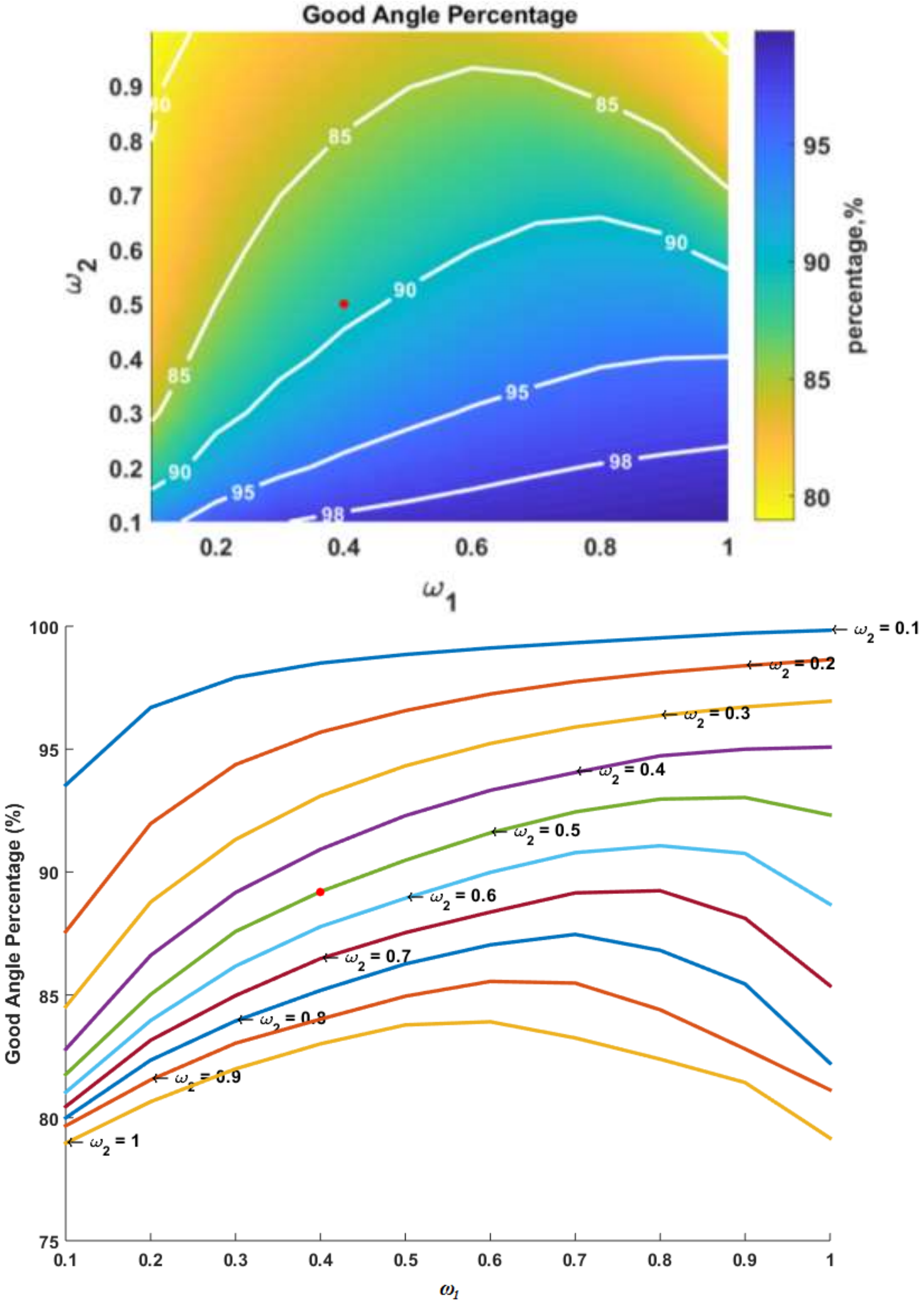

Figure 3.21 Good angle percentage versus different ω1 and ω2 combinations, red dot: the value used in this dissertation.

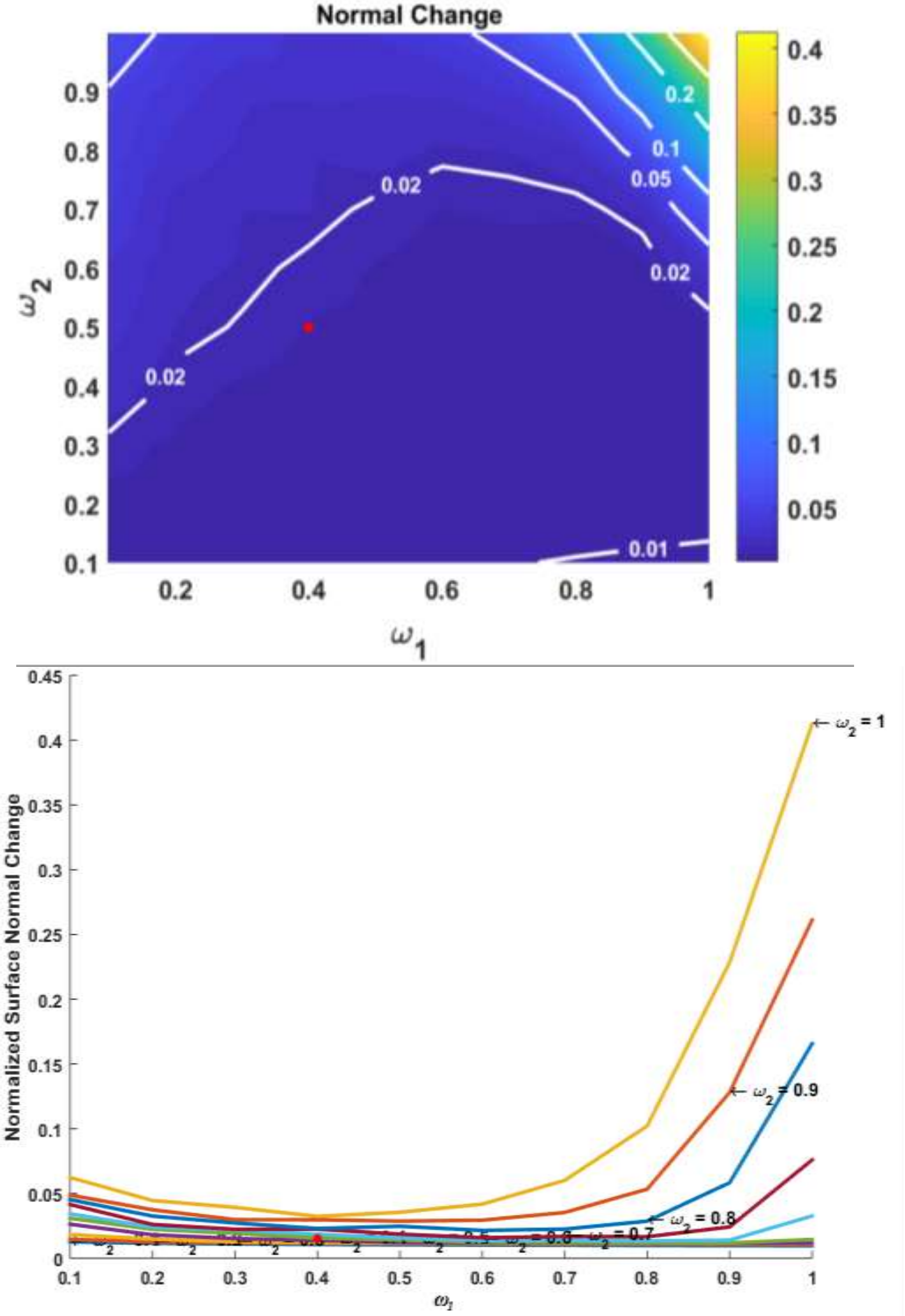

Figure 3.22 Normal change versus different ω1 and ω2 combinations, red dot: the value used in this dissertation.

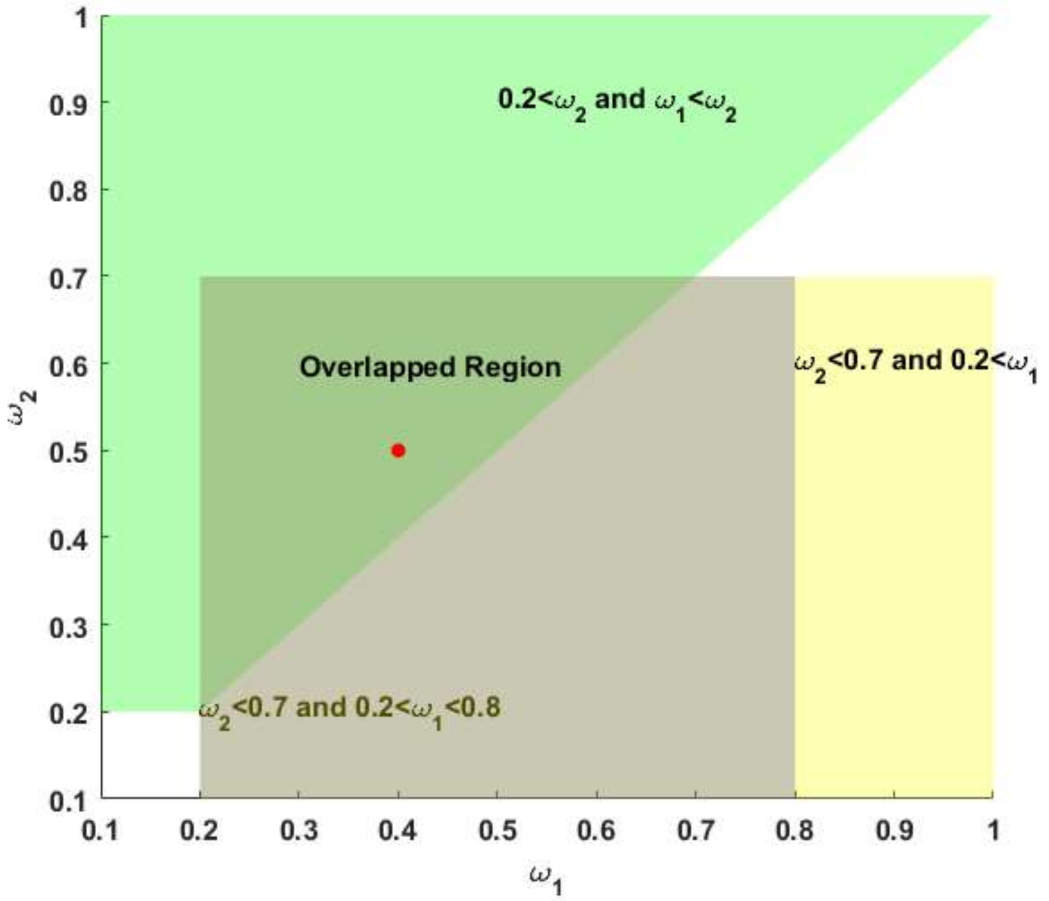

Figure 3.23 Regions of optimal parameters. Green region: optimal parameters for fitting error < 1.5 mm. Grey region: optimal parameters for good angle percentage > 85%, Yellow region and grey region: optimal parameters for normal change < 0.05. Greyed green region: the overlapped region of all three regions. Red dot: the value used in this dissertation.

3.7 4-D Endocardial Surface Fitting

3.7.1 Subject- Specific Template Construction

Generating subject-specific computational models of both atria and ventricles shows promise for improving the interpretation of clinical data from patients [39]. There is literature indicating that a personalized LA model is useful to provide specific anatomy guidance to some surgeries on LA, for example the catheter based ablation For the LA fibrillation, due to the large variation of LA structure [60]. A holistic or generic shaped model is not accurate enough to represent the whole shape population of the LA [72]. Therefore, instead of building a statistical template from large training data set and then adapting to the atria and ventricular anatomical MRI images [80], in this paper, we built a subject-specific template of each chamber for every subject in the 4D surface fitting procedure.

At the ventricular ED phase in the cardiac cycle, both left and right ventricles have the largest volume, therefore the geometry of the ventricle is less bent with a stretched wall compared to the geometry at the ES phase. For atria, at the ventricular ES phase, they tend to have the largest volume and same structure properties as the ventricles at ventricular ED. Hence, we built the template of each chamber at the phase when its volume was the largest during a cardiac cycle. Therefore, we built the LV and RV templates at ventricular ED, and LA and RA templates were built at ventricular ES by using the surface fitting algorithm described in Section 3.5.

3.7.2 Template Propagation

After the subject-specific template of each chamber was constructed for every subject, it was then deformed to the remaining phases in the cardiac cycle. The goal of the deformation process is to modify the heart model template of a frame to fit the contours of the next frame without changing the mesh connectivity [38]. Since the chamber template was constructed at the most dilated phase, which had the largest volume, we propagated it to the remaining phases forward and backward in time to the minimum volume phase of the chamber by deforming the time-adjacent surface. Note that, since the cardiac cycle is periodic, the first timeframe was considered to be adjacent to the last time frame. In our datasets, the heartbeat was divided into 20 timeframes, and the ventricular ED is around timeframe 1 or timeframe 20. For example, if we set the ventricular ED at 1 and ES at 8, the propagation time order was from timeframe 1 to 8 and from timeframe 1 to 20 to 9. For the atria, the propagation was from timeframe 8 to 1 and 9 to 20. Figure 3.24 shows the LV surface of a MR patient at ED phase and ES phase. Figure 3.25 illustrates the propagation directions on the volume time curves for atrium and ventricle. In the propagation process, we deformed the template to the contour points by following the same algorithm proposed in Section 3.6. Instead of using a pre-meshed sphere as the initial surface in the rough mesh surface construction, we used the reconstructed surface from the previous time frame in the expansion direction as the initial surface. Before the shrinking, the translational components between the current phase and the template was removed by translating the segmented data so that the mean of the contour points (i.e. its centroid) lies at the centroid of the

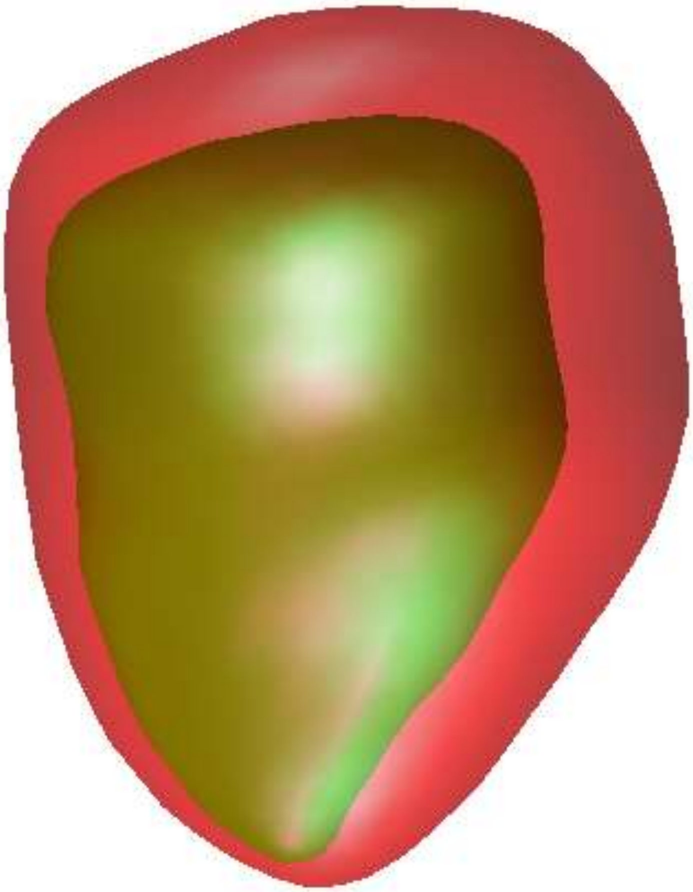

Figure 3.24 A LV surface at ED phase (red) and ES phase (green)

template. By choosing a template this way, the template has a larger volume than the volume of the current phase in most cases. In the propagation, our algorithm expands the template 10 mm in the radial direction to deal with the cases that the template volume is not large enough compared to the current phase. Due to the time adjacency, the template and the current phase should have similar volumes. In [132], the largest LV displacement documented is 8-10 mm, therefore, the 10 mm expansion is enough to cover the variation. First, the time-adjacent template of the current phase was shifted to the center of the contour data points of the current phase to construct a

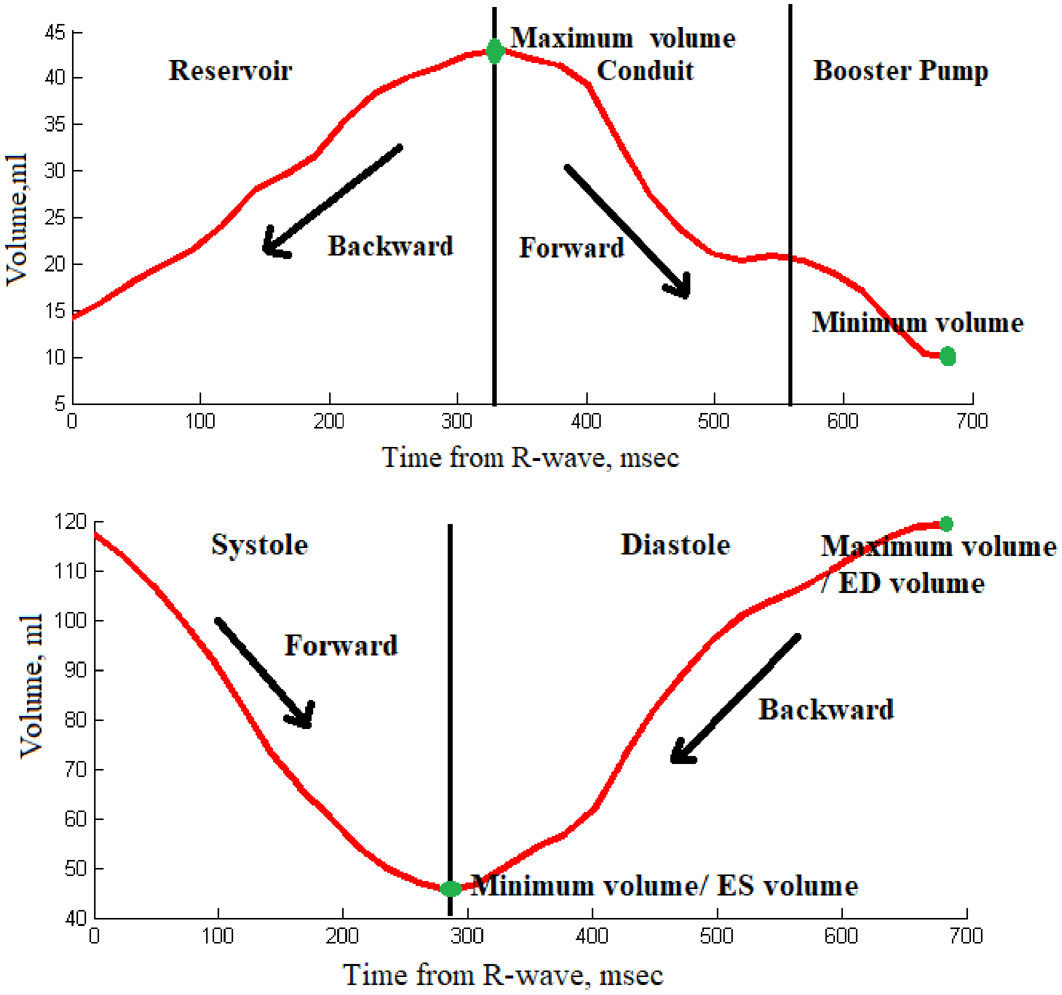

Figure 3.25 Illustration of propagation direction on the volume time curves. Top: atrium, bottom: ventricle.

rough mesh surface. Then the mesh was smoothed using the modified Laplacian method described in Section 3.5. Last, the template was replaced by the current phase and then deformed to the next timeframe.

There were two advantages by propagating from self-template for each chamber：(1) We preserved the geometry character of the chamber for the subject with less computation, since the ED geometry is the simplest in the whole cycle, and the rest is deformed from it. (2) By deforming the template surface to the contour points, the surfaces have one-to-one vertex correspondence during the whole cardiac cycle, which roughly follows the correspondence of material points on the chamber surface. Therefore, the local regional wall motion can be tracked and chamber functions can by analyzed at the same time while the surface geometry was measured.

3.8 Results

The fitted surface includes all four chambers during the whole cardiac cycle were reconstructed for all the subjects, including the normal group and MR patients group. In this dissertation, ω_1 and ω_2 were set to 0.4 and 0.5 empirically in the proposed algorithm. In Figure 3.26, a reconstructed heart with 4 chambers of a normal subject and a MR patient at ventricular ED and ES phase are displayed. From Figure 3.26, visually, we can see that the reconstructed surface is smooth and fit the contour points well, including the irregular shaped right ventricle and both atrium. We analyze the fitting result quantitatively in the following sections.

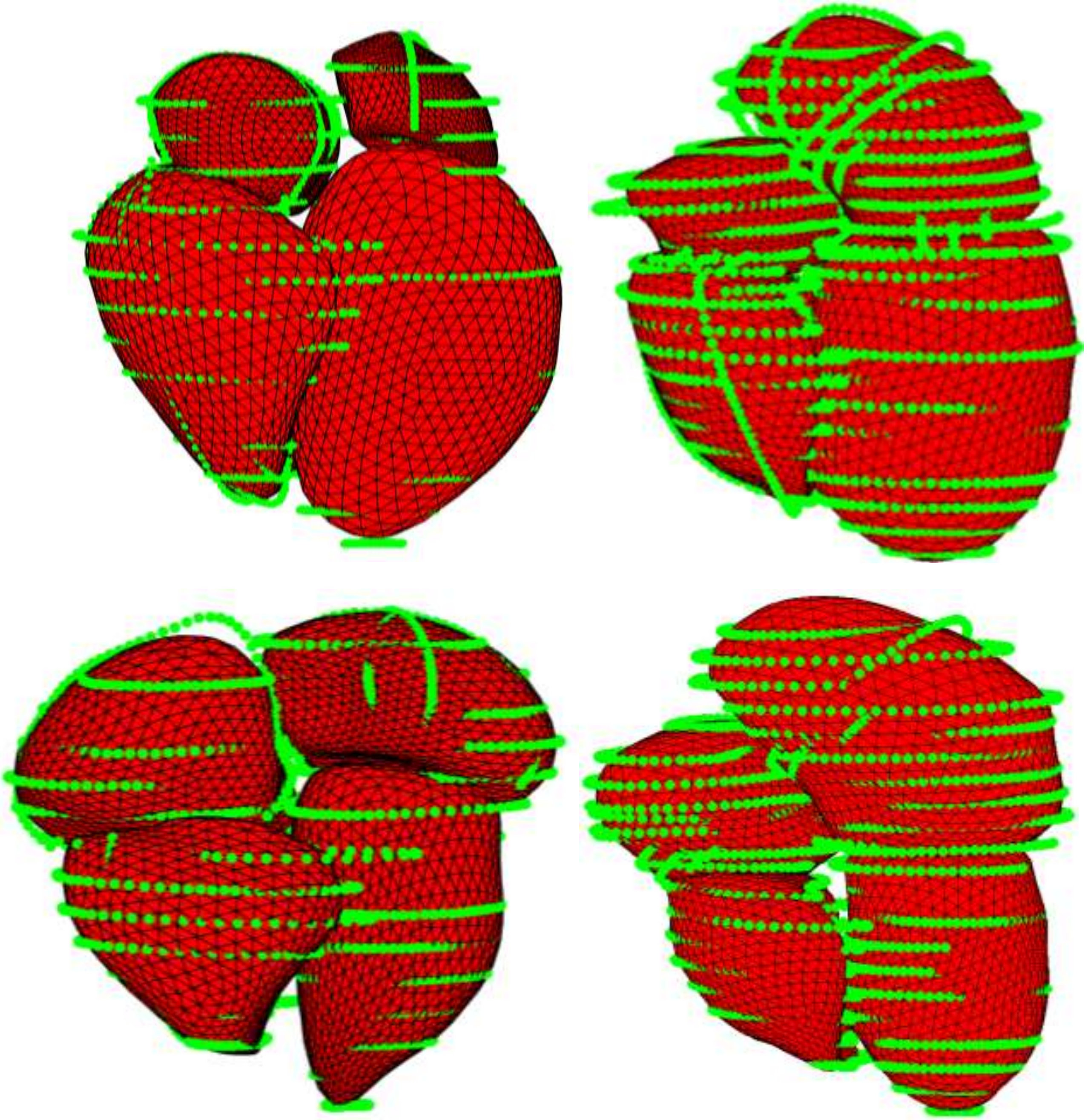

Figure 3.26 Fitted heart surfaces. Left: A normal Subject, Right: an MR patient; Top: Ventricular ED, Bottom: Ventricular ES. Green points: contour data points, Red surface: fitted surface, Black line: triangle edges.

3.8.1 Fitting Error

Table 3-3 shows the mean and standard deviation of the fitting error for normal and MR patients. From the table, we can see that the mean fitting error is small in both groups with small variations. The mitral regurgitation group has slightly higher value in the mean error in the fitting. In Figure 3.27 and Figure 3.28, the details of the fitting error for each subject in the normal subject group and the mitral regurgitation patient group are displayed respectively. From the figures, the same conclusion can be made as from the table. The fitting error for each participant is small, except that the error value of MR patient 8 is a slightly larger and more variation.

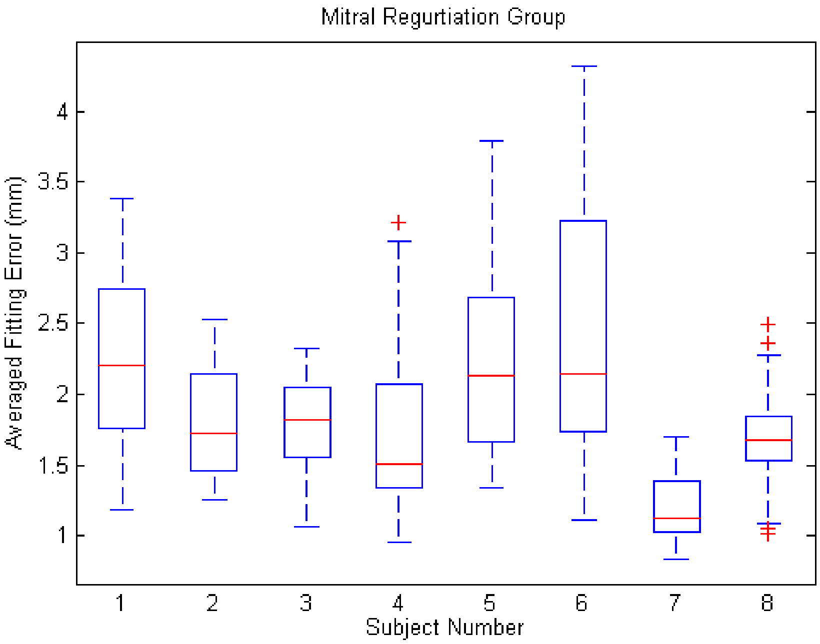

Figure 3.27 Box plots of averaged fitting error of each subject in the MR group. A box represents one subject with red line represents median of fitting error. The tops and bottoms of each box are the 25th and 75th percentiles of the fitting error. The dashed lines represent the upper and lower whiskers. Red cross represents outliers.

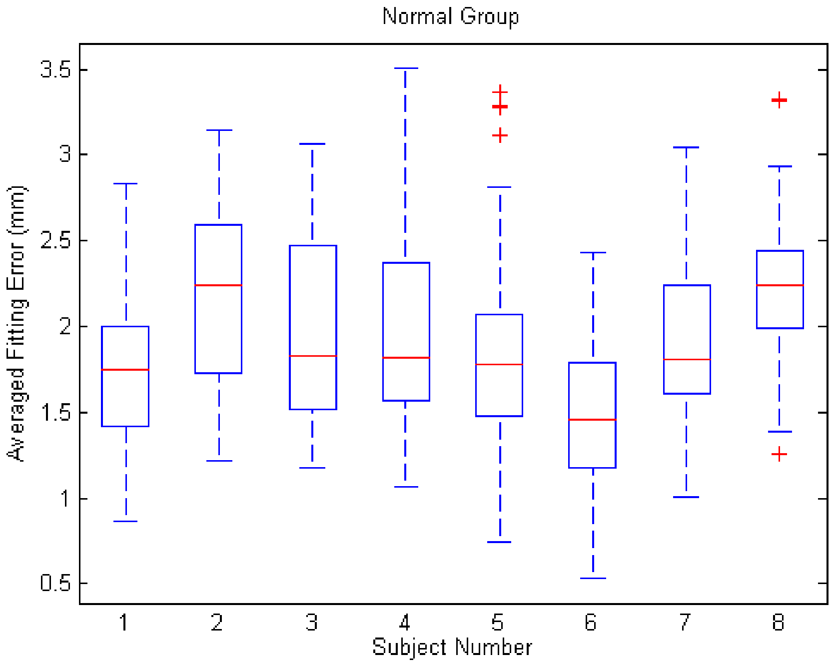

Figure 3.8 Box plots of averaged fitting error of each subject in the normal group. A box represents one subject with red line represents median of fitting error. The tops and bottoms of each box are the 25th and 75th percentiles of the fitting error. The dashed lines represent the upper and lower whiskers. Red cross represents outliers.

Table 3-3 Surface fitting error, mean±SD, mm

	LV	**LA**	**RV**	**RA**
MR	1.62±0.23	1.77±0.50	2.14±0.50	2.32±1.03
Normal	1.31±0.20	1.42±0.31	1.84±0.20	1.70±0.34

As observed in the table and figures, although the slice thickness for the datasets is 8mm, the averaged fitting error between all contour points and the mesh models across datasets are small and similar, which is around 1.62 mm to 2.32 mm. The in-plane resolution is 1.56 mm by 1.56 mm, from the table, we can see that the fitting error is around 1 to 2 pixels. Taking the heart motion and artifact into consideration, this disagreement between the contour points and the fitted surface is a very small value, and it shows that the 3D models fit very well to the 2D cardiac MRI data with 8 mm slice thickness and 1.56mm^2 pixel size.

3.8.2 Mesh Quality

Fitting error only reflects how accurate the fitting is, but the quality of the triangular surface needs to be analyzed as well. The percentages of good quality triangles (40 to 80 degree) are shown in Table 3-4 and Table 3-5. For all chambers, we observed from the table that the percentage of good quality angles mainly lies between 80% to 90% for both groups.

Table 3-4 Percentage of Good Triangle Angles for the Mitral Regurgitation group (%)

	LV	LA	RV	RA
MR01	95.36	97.72	85.45	84.26
MR02	91.52	97.1	87.25	95.56
MR03	88.1	90.87	82.65	85.75
MR04	94.15	92.74	85.12	80.4
MR05	98.59	89.74	89.35	83.18
MR06	98.08	92.59	77.69	87.58
MR07	91.67	93.63	85.91	91.19
MR08	90.67	91.20	78.51	93.50
TOTAL	93.52	93.20	83.99	87.68

Table 3-5 Percentage of Good Triangle Angles for the Normal group (%)

	LV	LA	RV	RA
NRM	93.10	82.71	90.55	93.76
NRM02	88.44	89.19	87.55	94.26
NRM03	90.74	90.23	73.39	90.89
NRM04	90.15	83.64	82.10	94.37
NRM05	96.84	91.78	82.70	85.57
NRM06	96.17	87.04	82.61	88.11
NRM07	93.25	87.07	81.86	93.71
NRM08	94.93	88.40	90.64	86.43
TOTAL	92.95	87.51	83.92	90.89

3.9 Discussion and Conclusions

In [36], the author used finite element method [38] to fit a surface on the LA by building a sphere inside the LA contour points and projecting contour points onto the inside sphere elements. In Skrinjar's method [42], he built a sphere outside the contour points and propagated to the boundary points by solving Laplace's equations. Motivated by the concept from those two papers and the propagation philosophy, we developed a novel algorithm, called radial shrinking, to propagate the vertex on the pre-meshed sphere towards the chamber contour points to fit a rough surface of the object. This method can handle noisy points cloud from different views or motion shift, and without parametrization or solving Laplace's equations. The averaged time to compute a surface on a personal laptop (Core, 2.2 GHz, 8GB RAM) is 68±4 minutes to generate all four chambers across a cardiac cycle with 20 timeframes, which is 51±3 seconds for a chamber at one timeframe. Compared to Skrinjar's method [42], which takes more than two hours to generate a surface of a chamber at one timeframe, the proposed algorithm reduces computation time tremendously. In Chun's method [51], it needs to generate statistical model first, the proposed method simplifies the computation in statistical model building. Compared to Lim's method [37], which takes about 30 minutes to generate surfaces of the left-sided of heart (LA and LV) for 20 timeframes, the proposed method computation time is comparable. We acknowledge that further optimization of the code can be explored to improve the performance, such as parallel programming in chamber fitting and two-direction propagation.

In this chapter, a novel surface fitting algorithm of 4D whole heart from cardiac MRI data is proposed. Chamber template is constructed for each chamber of every subject from a pre-meshed sphere by radial shrinking. The unique chamber template is then deformed to the next time-adjacent phase in the volume-contracting direction to generate a new surface. This technique can be applied to both ventricles and both atria. It enables the analysis of myocardium morphologic changes, such as curvature and wall motion for all segments in all four chambers of the heart. The proposed algorithm contributes in the following areas: (1) A comprehensive geometry modeling of human heart is built from 2D MRI, and to our knowledge, no previous work has been done before. Most research modeled the LV with less research on the RV surface modeling and LA modeling. Whole heart modeling was reconstructed from 3D CT data [74], or 3D cMRI data [45], and the common point of those studies is that the surface was fitted to data with isotropic or nearly isotropic resolution, usually less than 1 mm in three dimensions. Our surface model used the 2D MRI data, with 8 mm in the slice direction, which is popular in current clinical cardiac MRI imaging. (2) While building the model, the mitral valve annulus is approximated and used as the boundary for atrium and ventricle. (3) Instead of using a model from higher resolution or a statistic model as template, the proposed algorithm used self-template, which is constructed for each chamber of every subject. The self-template contributes in the morphologic properties preserving without regarding to pathology. (4) Surfaces constructed with the proposed algorithm have vertex-to-vertex correspondence across the heartbeat, which provides the access to wall motion analysis of all four chambers.

Chapter 4 VOLUMETRIC FUNCTION ANALYSIS AND VALIDATION

From the reconstructed surfaces, the volume can be obtained by summing up the volumes of the tetrahedrons formed by the triangles on the mesh. In this chapter, we will explore the volume functions and parameters derived from the fitted surfaces and compare with the disk summation method.

4.1 Volumetric Analysis

For the RV and RA, continuous measurements in size and mechanics are not widely available [11] [89]. Most current measurements are based on the 2 and/or 4 chamber views only, for example shortening of RV/RA long-axis size, which is the largest distance from base to apex, and RA short axis size, which is greatest distance from septal wall to free wall [89]. As pointed out previously, all measurements depending on single-slice long axis views are not accurate nor robust. There is research indicating that RA volume assessment would be more robust For the RA size than linear dimensions [69]. With the reconstructed surface, the volume of both all four chambers, including both atria and ventricles, can be obtained consistently in the time dimension.

4.1.1 Volume Computation from the Surface

For the volume computation, we followed the method Schiros developed in [42]. For each chamber, the volume is computed as the sum of the volumes of the tetrahedrons formed by the reconstructed triangulated mesh. A tetrahedron of the mesh is formed by a triangle on the mesh and the center of all vertices on the mesh. For the LA, RA and LV, the center of the mesh is commonly within the mesh, therefore, all formed tetrahedrons are enclosed by the mesh. However, the center of the RV mesh could be out of the mesh due to the concave region at the septal wall. If the center of the mesh lies out of the mesh, the tetrahedrons have to two cases of volumes. For tetrahedrons with triangles facing against the direction of the center will include both in-mesh and out-of-mesh volumes. For tetrahedrons with triangles facing towards the direction of the center, the volumes are completely out of the mesh. All volume out of the mesh should not be accounted for the volume of the mesh, therefore, signed tetrahedron volumes are computed employed [116]. If the triangle facing against the direction of the center, then, the tetrahedron form with this triangle has positive sign. If the triangle facing towards the direction of the center, then the tetrahedron has negative sign. For the illustration purpose, we displayed the 2D view of the volume computation and exaggerated it in Figure 4.1.

By summing all the tetrahedron volumes, the out-of-mesh volume of the positive tetrahedrons will be cancelled out by the volumes of the negative tetrahedrons. Denoted the *ith* triangle vertices as v_{i1}, v_{i2} and v_{i3} with center as v_o, then the volume of a reconstructed mesh is computed as:

$$V = \sum_{i=1}^{I} \frac{(v_{i1} - v_o) \cdot ((v_{i3} - v_{i1}) \times (v_{i2} - v_{i1}))}{6}, \qquad 4.1$$

where I is the number of triangles on the mesh.

4.1.2 Volumetric Parameters for Each Chamber

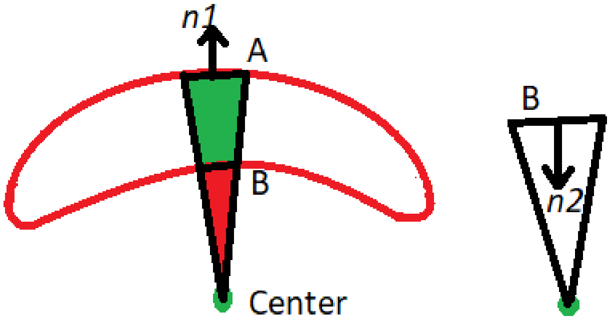

Figure 4.1 Volume sign illustraion. Triangle A and B with normal n1 and n2 respectively. Triangle A has facing aginst the center and triangle B facing towards the center. Volume in the green area should be included and red area should be excluded. The volume formed by triangle A and center has positive sign, and the volume formed by triangle B and center has negative sign. The the positive and negative in the red area is cancelled.

Standard ventricular volume parameters were computed at ED and ES timeframes, the stroke volume (SV) and ejection fraction (EF) were calculated as SV = EDV- ESV and EF = (EDV-ESV)/EDV [69].

For the LA volume parameters, except minimum and maximum volumes, there is no standard suggestions. As described in Section 1.1.1, LA has three phases. A normal LA volume time curve at rest is shown in Figure 4.2 [6]. LA passive emptying volume, LA active emptying volume, LA total emptying volume and LA conduit volume are the most common parameters to measure. Different literatures have a small variation in those definitions. All variations are due to the different determinations of the LA passive emptying volume. In [6], Ahtarovski defines: LA passive emptying volume = LA max – LA mdv, (LA mdv, volume after passive emptying but before mid-diastolic expansion). In [7], [87] and [117], LA passive emptying volume = LA max – LA bac, (LA bac, volume before atrial contraction). In most cases, the atrium volume-time curves of the normal group show a clear definition of all phases in normal subjects. However, in different pathologies, for example for MR patients, the diastasis (mid-diastolic expansion) is

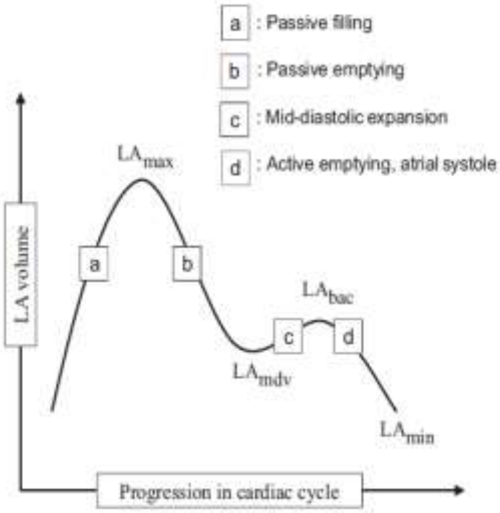

Figure 4.2 The normal left atrial volume-time curve [11].

difficult to identify. Therefore, we followed the definition in [7], [87] and [117], and the computation is displayed in Table 4-1.

For right atrium volume, less research and fewer clinical outcomes data are available on the quantification [69]. Right atrium still has reservoir, conduit and contraction phases as left atrium [88]; therefore, we computed the same volume parameters as left atrium in the right volume measurements.

Table 4-1 LA volume parameters definition

Parameter	Computation Formula
LA passive emptying volume	LA max -LA bac
LA active emptying volume	LA bac -LA min
LA total emptying volume	LA max – LA min
LA conduit volume	LVSV - LA total emptying volume
LA total emptying fraction	LA total emptying volume/LA max
LA passive emptying fraction	LA passive emptying volume/LA max
LA ejection fraction (LAEF)	LA active emptying volume/LA bac

Bac: before atrial contraction volume, min: minimum volume, max: maximum volume.

4.2 Surface Fitting Algorithm Validation

In this chapter, we will validate the reconstructed surface through volume comparison. With the reconstructed surface using the algorithm proposed in Chapter 3, the volume of all four chambers can be obtained consistently in the time dimension. Currently, disk summation, biplane method, area-length are popular and recommended methods in volume measurements from cardiac MRI data [69]. However, bi-plane and area-length method depends on the shape assumption, and slight orientation difference of long axis views result in immense variation in volume. Therefore, we used disk summation method as a gold standard for the volume computation in this study for the validation. In addition to the disk summation method, we employed valve plane-cutting techniques we developed to compute the volumes [62].

4.3 Image Acquisition and Population

Eight mitral regurgitation patients (n=8), aged from 48 to 82, before surgery were imaged in this study. Eight normal volunteers (n=8) without clinical or anatomical evidence of cardiovascular disease, aged from 19 to 24, were imaged as a healthy group. All studies were approved by the Auburn University Institutional Review Board (IRB). All subjects were scanned using the MRI protocols described in Section 3.4. Heart surfaces of all subjects were reconstructed using the proposed algorithm described in Chapter 3.

4.4 Volume Time Curves Comparison

To compare the volume, we first constructed the volume time curves by compute the volume using the volume computation method described in Section 4.1. From the volume-time curve in Figure 4.3, we can see that volumes computed by the proposed method have a high degree of agreement with the gold standard for both groups. The proposed method has a slightly higher value for both atria and ventricles near the respective ED phases. This is due to the different volume computation regions. For the proposed surface algorithm, it adds the whole volume, and the disk summation adds up stair-case like volumes, which introduce difference in volume on the edges.

4.5 Volume Function Analysis

In addition to the volume time curves comparison between the fitted surface method and the disk summation method, we also conducted comparison for volumetric parameters defined in Section 4.1 for all four chambers. In those tables, we compared the volume computed from the proposed surface fitting algorithm and the gold standard for all participants, including the normal subjects and MR patients. To measure the difference significance relationship between the two methods, we conducted Paired t-test to test mean differences among intra-subject volumes. Correlation coefficients between the volumes computed by the proposed triangulated surface

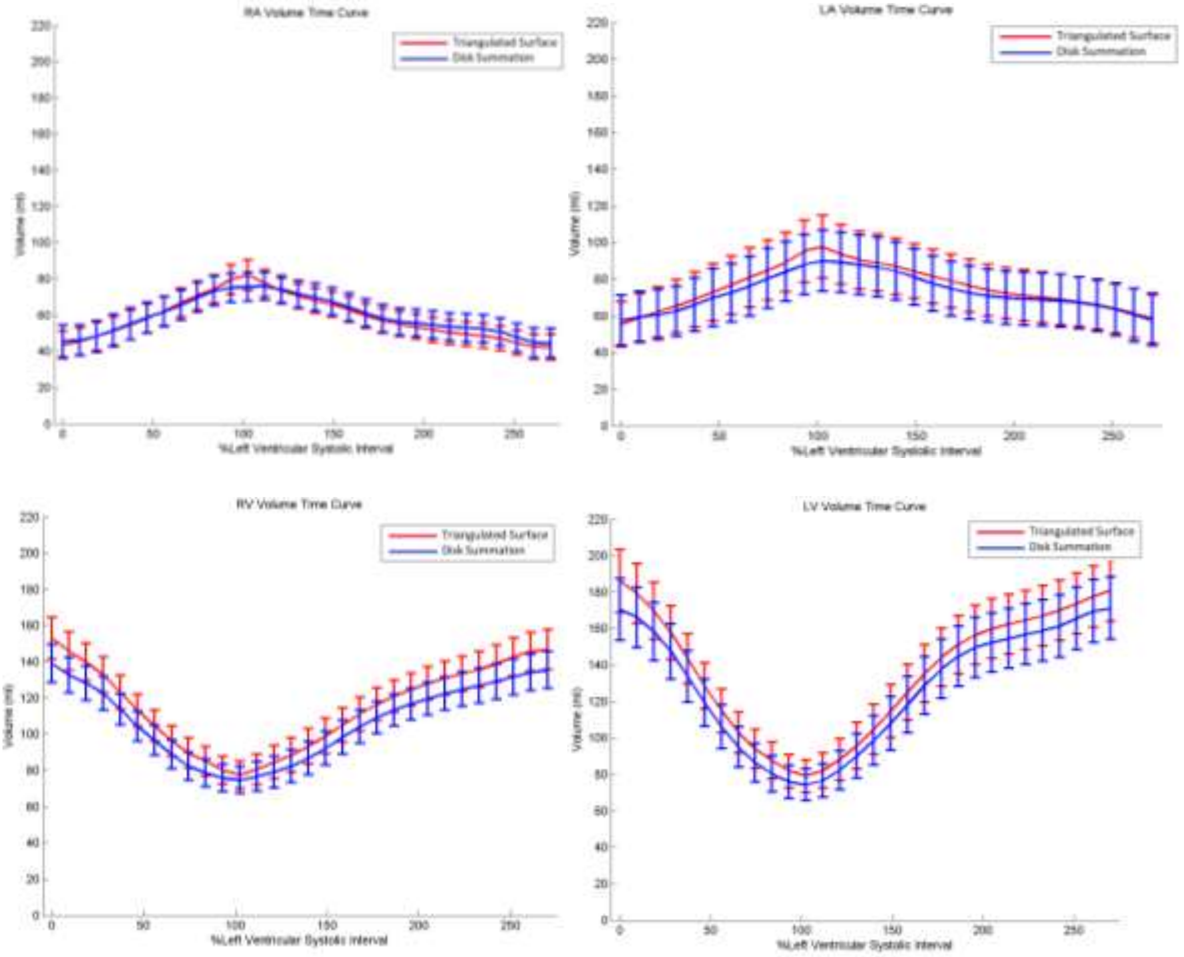

Figure 4.3 Averaged vomlome-time curves of all subjects (8 normals and 8 MR patiens) comparison between triangulated surface (TS) and disk summation (DS) algorithms of all four chambers. Mean ± standard error.

method and disk summation method were also assessed by simple linear regression analysis. All quantitative measurement were expressed as means±SE and for all statistical analyses, $p < 0.05$ was considered significant.

Table 4-2 Ventricular Volume Function Comparison, Triangulated Surface (TS) vs. Disk Summation (DS)

	Parameter	**TS**(mean±SE)	**DS**(mean±SE)	**P-Value**	**R**	**P-Value**
LV	**EDV(ML)**	184±17.0	173±17.0	0.6206	0.99	<0.01
	ESV(ML)	77±8.6	72±8.5	0.6352	0.99	<0.01
	SV(ML)	107±8.6	101±9.3	0.6303	0.98	<0.01
	EF (%)	59±1.3	59±1.4	0.8020	0.93	<0.01
RV	**EDV(ML)**	152±11.0	139±10.0	0.3972	0.98	<0.01
	ESV(ML)	76±7.5	73±7.4	0.7417	0.99	<0.01
	SV(ML)	75±5.0	66±4.8	0.1804	0.92	<0.01
	EF (%)	51±2.2	49±2.8	0.5619	0.98	<0.01

Volumes and Fractions Are Mean Se; SV: Stroke Volume; EF: Ejection Fraction; R: Correlation Coefficient. P1-Value: p-value of difference. P2-Value: p-value of correlation coefficient.

Table 4-3 Left Atrial volume function comparison, Triangulated Surface (TS) vs. Disk Summation (DS)

Parameter	**TS**(mean±SE)	**DS**(mean±SE)	**P-Value**	**R**	**P-Value**
EDV(ml)	98±17.0	92±17.0	0.8172	0.99	<0.01
ESV(ml)	56±12.0	57±14.0	0.9410	1.00	<0.01
BAC(ml)	71±14.0	69±14.0	0.9347	0.99	<0.01
Pas EV(ml)	27±4.1	23±3.2	0.4629	0.92	<0.01
Act EV(ml)	16±2.6	13±1.8	0.3423	0.60	0.0107
Total EV(ml)	42±5.6	35±3.6	0.3034	0.86	<0.01
Pas EF (%)	32±3.7	31±4.1	0.8285	0.95	<0.01
Act EF (%)	18±2.1	17±1.8	0.7482	0.64	<0.01
Total EF (%)	50±3.7	48±4.9	0.7315	0.93	<0.01
Con V(ml)	65±4.8	66±7.6	0.9309	0.83	<0.01

Volumes and fractions are mean ± SE; BAC: Before Atrial Contraction volume; V: Volume; Pas: Passive; Act: Active; E: Emptying; F: Fraction, Con: conduit. P1-Value: p-value of difference. P2-Value: p-value of correlation coefficient.

Tables 4-2 to 4-4 summarize the volume parameters of each chamber. We can see that both methods have a strong positive linear correlation, and there is no significant difference between the two methods for all volume parameters of all four chambers.

Table 4-2 Right Atrial Volume Function Comparison, Triangulated Surface (TS) vs. Disk Summation (DS)

Parameter	**TS**(mean±SE)	**DS**(mean±SE)	**P-Value**	**R**	**P-Value**
EDV(ml)	82±8.4	78±7.8	0.7301	0.99	<0.01
ESV(ml)	41±7.0	42±8.0	0.9476	0.99	<0.01
BAC(ml)	52±7.2	54±7.7	0.9442	0.96	<0.01
Pas EV(ml)	30±2.1	24±1.9	0.3136	0.61	0.3351
Act EV(ml)	11±1.3	12±2.1	0.6180	0.83	0.1751
Total EV(ml)	41±2.4	37±1.7	0.1211	0.57	0.0214
Pas EF (%)	40±2.8	35±3.7	0.8203	0.90	0.0178
Act EF (%)	14±1.5	17±2.9	0.8512	0.88	0.2201
Total EF (%)	54±3.0	52±4.0	0.7172	0.93	<0.01
Con V(ml)	34±3.7	29±4.1	0.3953	0.83	<0.01

Volumes and fractions are mean ± SE; BAC: Before Atrial Contraction volume; V: Volume; Pas: Passive; Act: Active; E: Emptying; F: Fraction, Con: conduit. P1-Value: p-value of difference. P2-Value: p-value of correlation coefficient.

In addition to the linear relationship and difference significance between the two methods, we conducted Bland-Altman analysis to demonstrate possible bias. It shows the overall bias as well as difference variation versus mean value of volume parameters. From the Bland-Altman plot, we can also observe the limits of agreement, which is the 2 times the SD of the difference. Figure 4.4 and Figure 4.5 show the Bland-Altman (BA) plots for ventricular ED and ES volume. Figure 4.6 and Figure 4.7 show the atrial minimum and maximum volume. In those figures, solid lines represent the mean (bias) and dotted lines represent the 95% limits of agreement, which is defined as the mean difference ± 1.96 SD of differences. The red dots are the difference of the normal subjects and green dots are the difference of the MR patients.

From ventricular volume comparison, we observed that there is a positive bias between the two methods, which indicates that the volume computed from the proposed surface fitting method is higher than that from the disk summation methods for ventricles. Besides that, we noticed that all differences are in the confidence limit, except one patient in the RV EDV. There is no trend between the difference and the mean value observed from the figures.

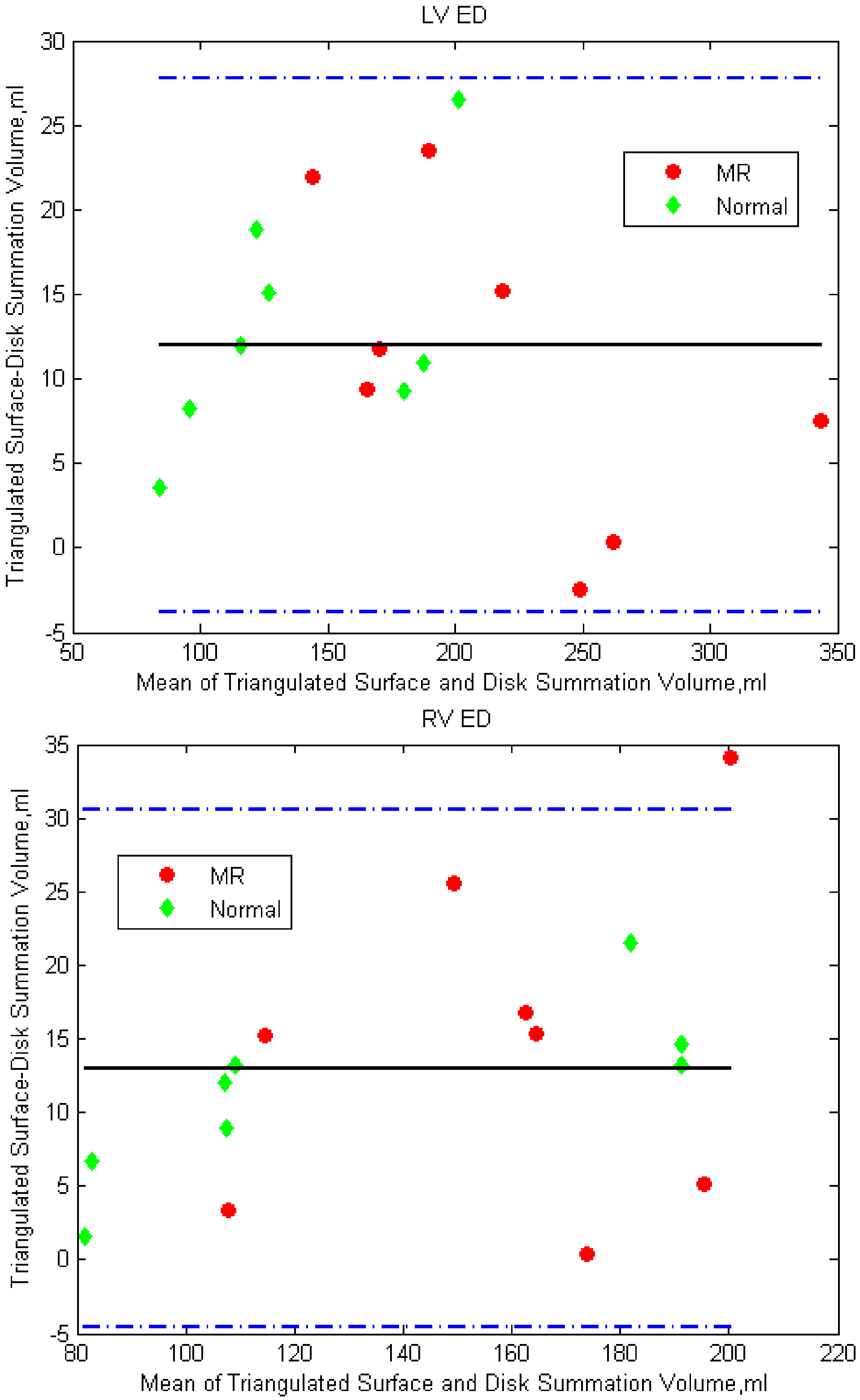

Figure 4.4 BA plot for ventricular EDV comparison between triangulated surface and disk summation methods. Dots represents difference. Solid lines represent the mean (bias) and dotted lines represent the 95% limits of agreement (mean ± 1.96 SD of differences)

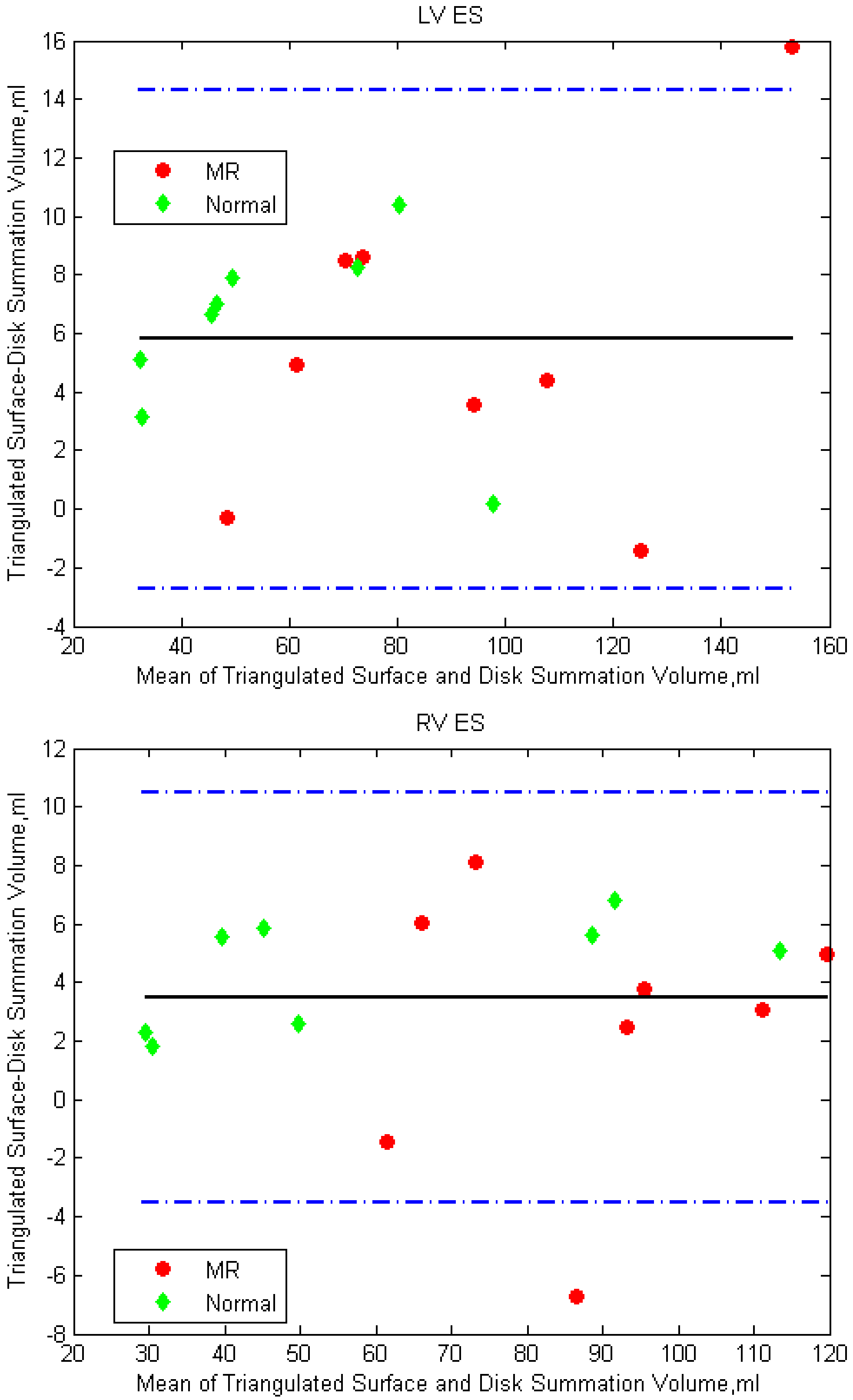

Figure 4.5 BA plot for ventricular ESV comparison between triangulated surface and disk summation methods. Dots represents difference. Solid lines represent the mean (bias) and dotted lines represent the 95% limits of agreement (mean ± 1.96 SD of differences)

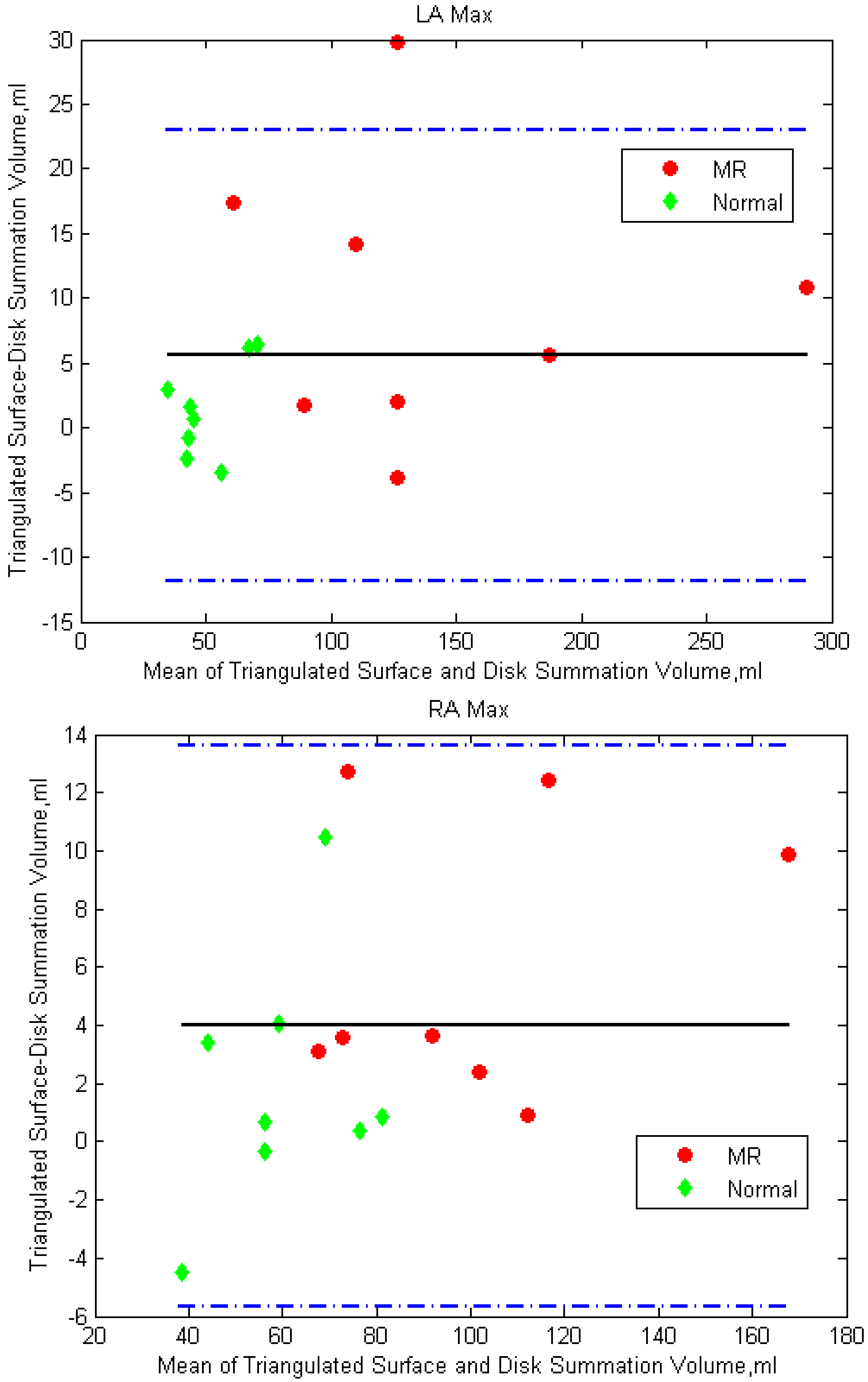

Figure 4.6 BA plot for atrial maximum volume comparison between triangulated surface and disk summation methods. Dots represents difference. Solid lines represent the mean (bias) and dotted lines represent the 95% limits of agreement (mean ± 1.96 SD of differences)

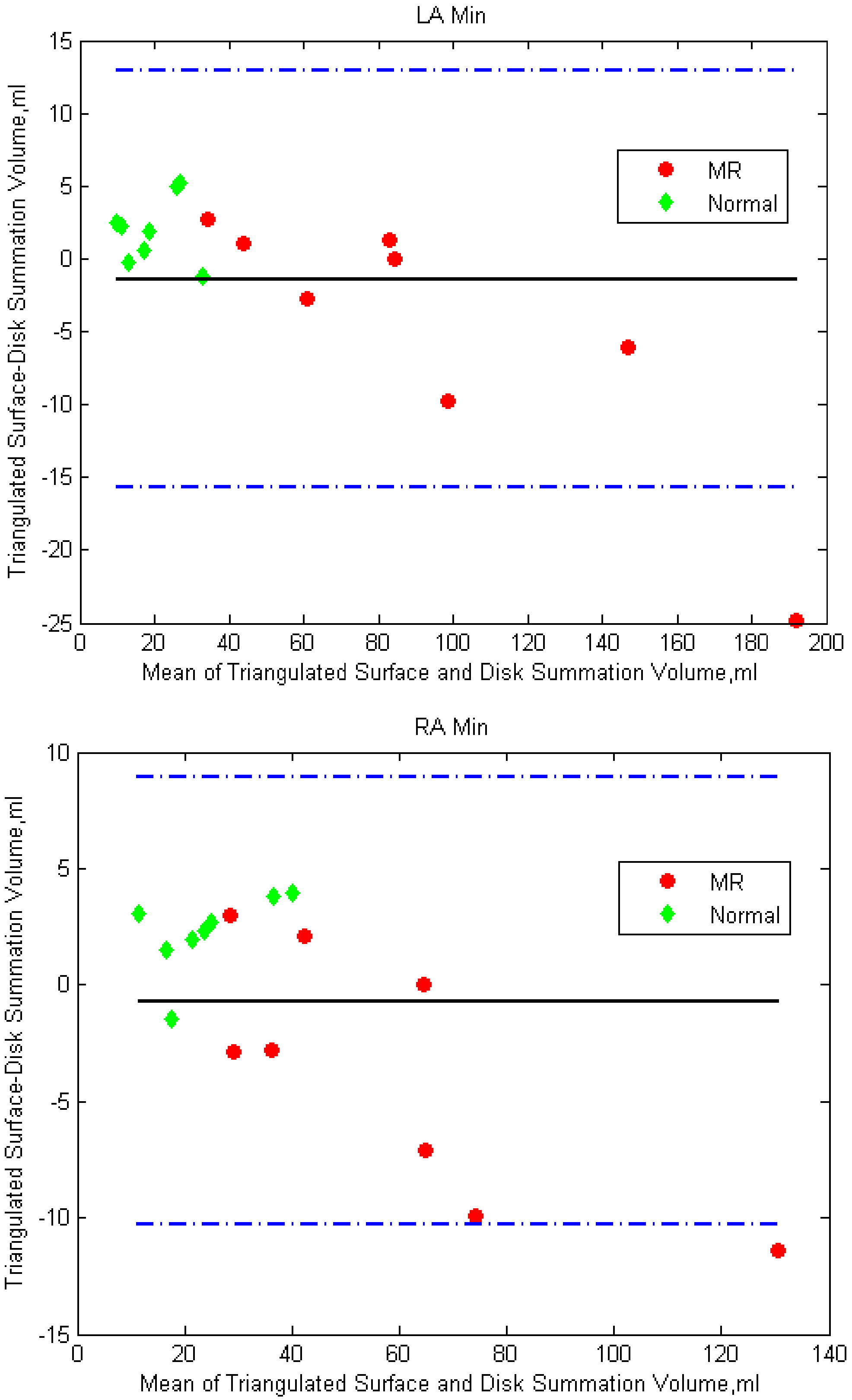

Figure 4.7 BA plot for atrial minimum volume comparison between triangulated surface and disk summation methods. Dots represents difference. Solid lines represent the mean (bias) and dotted lines represent the 95% limits of agreement (mean ± 1.96 SD of differences)

For the atrial volume parameters comparison in Figure 4.6 and Figure 4.7, obvious bias is only observed in the LA maximum volume, For the LA minimum and both of RA volumes were close to 0 in the mean difference. As the ventricular volume, most differences are within the confidence limit, and no trend is observed.

4.6 Conclusion

For the volume of all four chambers computed from the reconstructed surface and the disk summation methods, the volume time curves of all four chambers have a high degree of agreement and all volume parameters have a positive linear correlation without any significant difference. This observation between the comparisons from the volume computation validates the accuracy of the proposed surface fitting algorithm from the segmented MRI data.

Chapter 5 GEOMETRIC ANALYSIS FROM THE FITTED SURFACE AND VALIDATION

In this Chapter, we will explore the geometric parameters that can be derived from the fitted surface, then validate the proposed surface fitting algorithm curvatures through comparison with a prolate spheroid with known curvatures and LV curvatures computed from cubic B-spline surfaces.

5.1 Segment Models

For the studies in this dissertation, in order to analyze the regional properties of the endocardial wall, we need to divide each chamber into a segment model. For the LV, we divided it into a standard 16-segment model [69]. Based on a literature, we divided RV it into a 15-segment model, which is a 13-segment model from apex to base with RV outlet and inlet [61]. Figure 5.1 shows the standard segment-model of LV and RV. For the RA and LA, there is no standard suggestion, therefore, we divided both atria into 3 levels and 4 segments in each level, which sums up to 12 segments in total from atrial apex to atrial base, which is shown is Figure

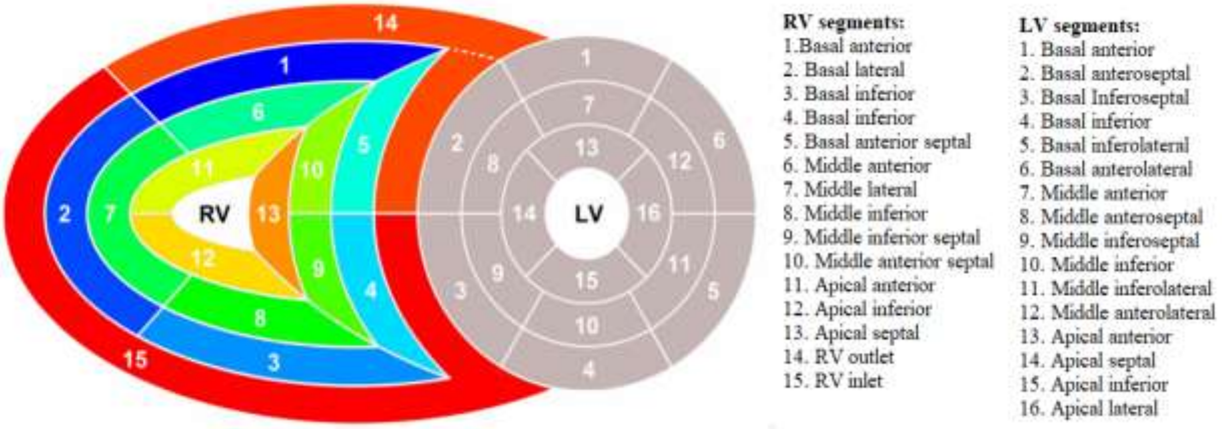

Figure 5.1 Standard LV myocardial segmentation of LV and RV [61].

5.2. All regional wall mechanics and motions, including surface curvature and displacement were measured based on this segment definitions.

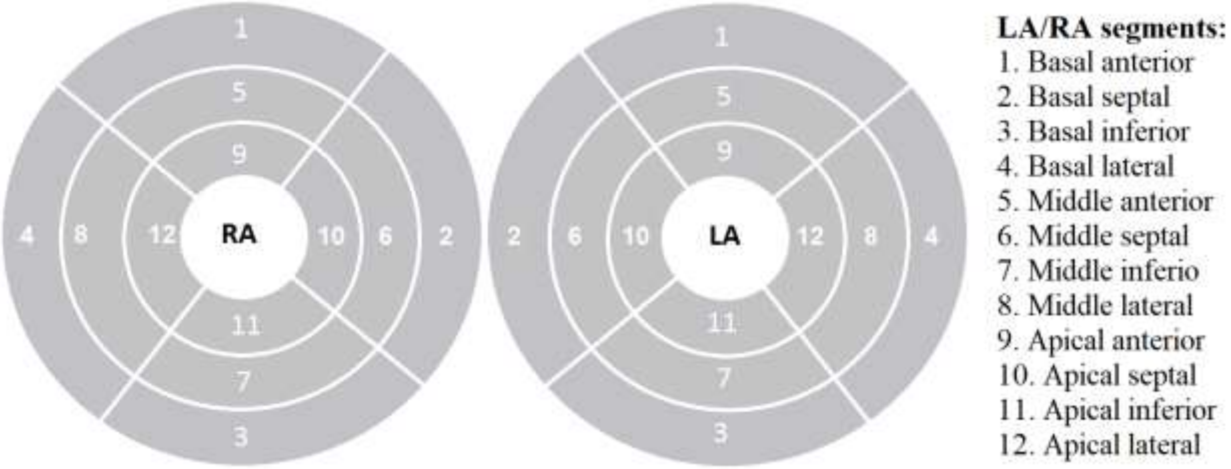

Figure 5.2 Myocardial segmentation of LA and RA.

5.2 Curvature Computation

Regional surface curvatures, including longitudinal curvature and circumferential curvature, are critical parameters in the analysis of heart remodeling [42]. In this section, the general curvature computation is presented, then, how longitudinal and circumferential curvatures of heart chambers are presented.

5.2.1 General curvature computation

The principle curvatures k_1, k_2, and principle curvature directions $\hat{\boldsymbol{e}}_1$ and $\hat{\boldsymbol{e}}_2$ were estimated by using Euler formula from the normal curvature [91] and solved by the least squares method. The maximum curvature, $k_1(v)$, and the minimum curvature $k_2(v)$ of a vertex v on a triangulated mesh are called the principle curvatures. The principle directions are the corresponding tangent directions $\hat{\boldsymbol{e}}_1$ and $\hat{\boldsymbol{e}}_2$. Let $k(v, \hat{\boldsymbol{t}})$ denote the curvature along any tangent direction, $\hat{\boldsymbol{t}}$, at v, and $k(\boldsymbol{v}, \hat{\boldsymbol{t}})$ can be calculated using the Euler formula,

$$\mathrm{k}(\mathrm{v}, \hat{\mathbf{t}}) = \mathrm{k}_1 \cos^2(\theta_{\hat{\mathbf{t}}}) + \mathrm{k}_2 \sin^2(\theta_{\hat{\mathbf{t}}}), \qquad \text{5-1}$$

where $\theta_{\hat{t}}$ is the angle between $\hat{\boldsymbol{t}}$ and $\hat{\boldsymbol{e}}_1$.

Assume v is a vertex on a triangulated mesh, to compute the principle curvatures and direction at vertex v, we first assume a random tangent direction $\hat{\boldsymbol{t}}_d$ and *e₁*, θ_0 is the angle between *e₁* and $\hat{\boldsymbol{e}}_1$, θ_d is the angle between $\hat{\boldsymbol{t}}_d$ and *e₁*, *k(v,* $\hat{\boldsymbol{t}}_d$*)* can be estimated using the following Equation:

$$\mathrm{k}(\mathrm{v}, \hat{\mathbf{t}}_\mathrm{d}) = \mathrm{k}_1(\mathrm{v}) \cos^2(\theta_\mathrm{d} - \theta_0) + \mathrm{k}_2 \sin^2(\theta_\mathrm{d} - \theta_0), \qquad 5\text{-}2$$

Which can be rewritten as

$$\mathrm{k}(\mathrm{v}, \hat{\mathbf{t}}_\mathrm{d}) = \mathrm{a} \cos^2(\theta_\mathrm{d}) + \mathrm{b} \cos\theta_\mathrm{d} \sin\theta_\mathrm{d} + \mathrm{c} \sin^2(\theta_\mathrm{d}), \qquad 5\text{-}3$$

Using least square method to calculate constants a, b and c, then the principle curvatures can be calculated as:

$$k_1(v) = \frac{(a+c)}{2} + \sqrt{\frac{(a+c)^2}{4} - ac + \frac{b^2}{4}}$$

$$\mathrm{k}_2(\mathrm{v}) = \frac{(\mathrm{a}+\mathrm{c})}{2} - \sqrt{\frac{(\mathrm{a}+\mathrm{c})^2}{4} - \mathrm{ac} + \frac{\mathrm{b}^2}{4}}\ , \qquad 5\text{-}4$$

5.2.2 Longitudinal and Circumferential Curvatures of Heart Chambers

To calculate the circumferential and longitudinal curvatures, the corresponding circumferential and longitudinal directions of each vertex need to be defined. All 4 chambers were transformed from the scanner coordinate (x,y,z) to the sphere coordinates (θ, φ, r). The longitudinal direction (t_l) and circumferential direction (t_c) were defined as the phi (φ) and theta (θ) directions in the sphere coordinate respectively, which is shown in Figure 5.3.

The angle between the maximum principle direction $\hat{\boldsymbol{e}}_1$ and the circumferential direction θ_c and the angle between the maximum principle direction and the longitudinal direction θ_l were then calculated. The circumferential curvature of a vertex was calculated as:

$$k_c(\mathbf{v}_p) = k_1 \cos^2(\theta_c) + k_2 \sin^2(\theta_c), p = 1 \dots P \qquad 5\text{-}5$$

The longitudinal curvature was calculated as:

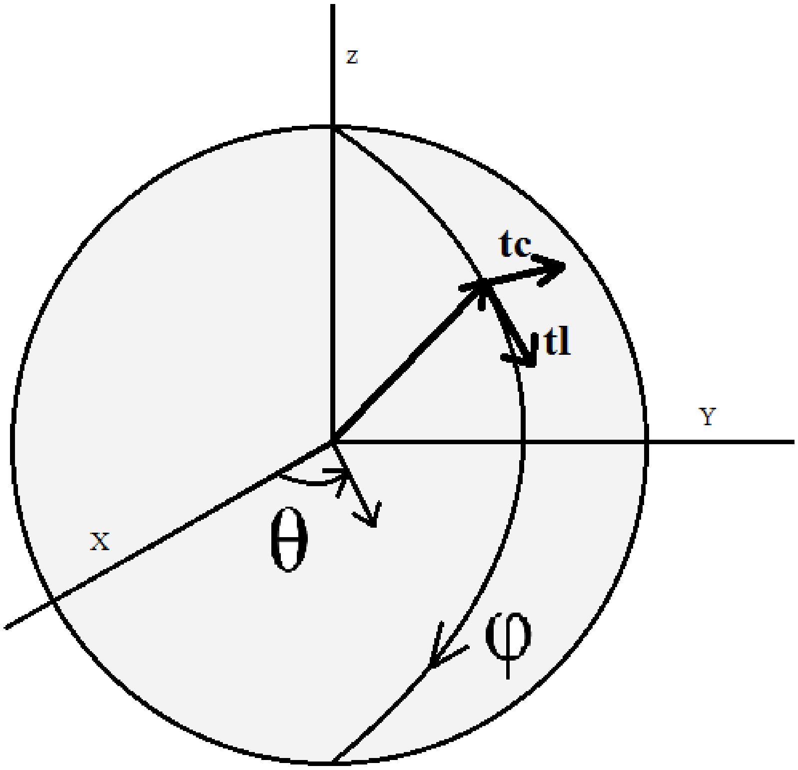

Figure 5.3 Longitudinal direction (tl) and circumferential direction (tc) in the sphere coordinate

$$k_l(\mathbf{v}_p) = k_1 \cos^2(\theta_l) + k_2 \sin^2(\theta_l), p = 1 \ldots P \qquad 5\text{-}6$$

For all the curvature analysis, we first transformed all 4 chambers into sphere coordinates and then further split into segments based on the segment-models described in the previous section, then computed using the methods defined in this section.

5.3 Validation on a Prolate Spheroid

The curvature computation was validated with two experiments. In the first experiment, triangulated surfaces were fit to contours simulated from a prolate spheroid and curvatures from the triangulated surfaces were compared to the known true curvatures. In the second experiment, triangulated surfaces were fit to a set of LV contours drawn on MRI data from a previous study and the triangulated surface curvatures were compared to curvatures computed from a B-spline surface [135] fit to the same contours. The B-spline surface curvatures have been validated through use in several clinical studies [138-144].

In the first validation experiment, a prolate spheroid was first generated. For a normal heart, the ratio of the short to long dimension is about 2/3 [52], therefore, we set the semi-major axis of the prolate spheroid equal to R and the semi-minor axis was set equal to $2R/3$ with R = 70mm. The Cartesian equation of the spheroid is:

$$\frac{x^2 + y^2}{a^2} + \frac{z^2}{c^2} = 1 \tag{5-7}$$

where $c = R$ =70 mm and $a = 2/3R$=46.7mm in our case.

The Gaussian curvature of the prolate spheroid is given by:

$$K(x,y,z) = \frac{c^6}{[c^4 + (a^2 - c^2)z^2]^2} \tag{5-8}$$

Figure 5.4 shows the prolate spheroid. For this spheroid, contours were simulated with chosen gap resembling slice thickness. Since the slice thickness in all the studies in this dissertation is 8 mm, we first simulated contours with 8 mm and fit a surface with difference

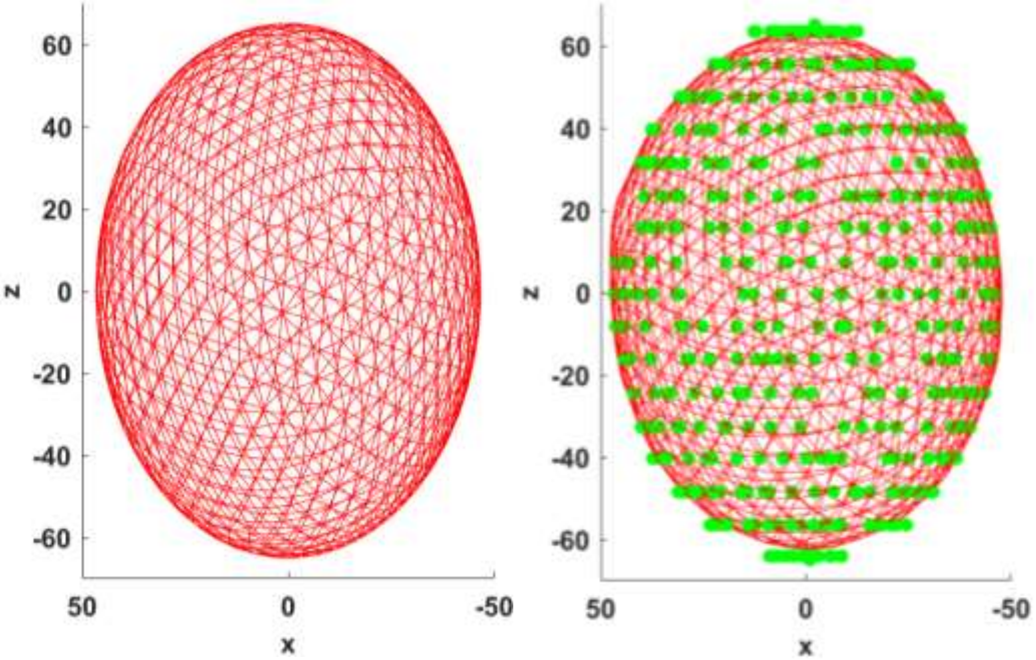

Figure 5.4 Illustration of a prolate spheroid (left) and a fitted prolate spheroid (right) from simulated contours (green) with gap = 8 mm.

number of vertex to find out the effect of that. In Figure 5.4, a fitted surface with 1000 vertices to the simulated contours with 8 mm gap is shown. For the fitted surfaces, the Gaussian curvature is obtained using Equation 1-4 with:

$$K = k_1 k_2 \qquad 5\text{-}9$$

Figure 5.5 shows Gaussian curvature error versus number of vertex on the fitted surface. From the figure, we can see that, when vertex number is larger than 1000, it doesn't change much for the mean error.

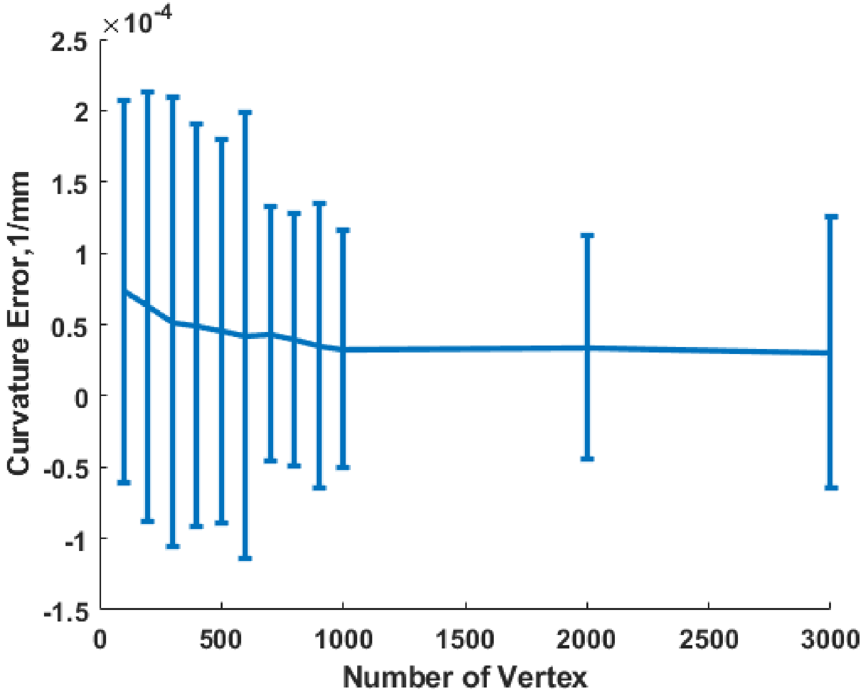

Figure 5.5 Gaussian curvature error versus number of vertex on the fitted surfaces, mean± SD

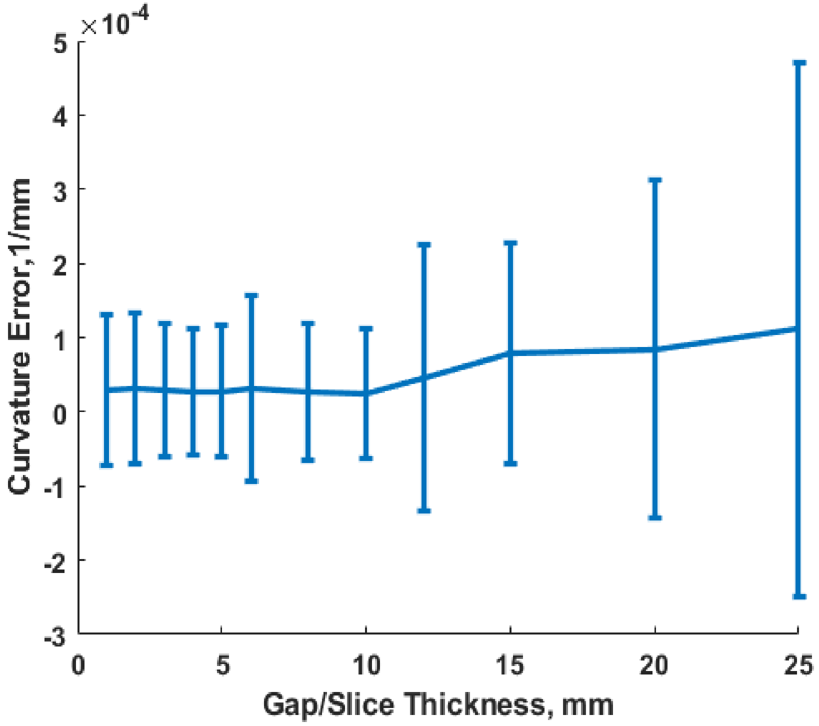

Figure 5.6 Gaussian curvature error versus simulated contour gap for fitted surfaces, mean± SD.

For our validation purpose on the slice thickness respect, we chose the gap of the simulated contours from 1mm to 25mm. Then fit surfaces to the simulated contours with 1000 vertices. The true curvature of the prolate spheroid is between 2.16×10^{-4} to 8.75×10^{-4} 1/mm. Figure 5.6 shows the averaged Gaussian curvature error of the fitted surfaces for different simulated contour gaps. As we can see from the figure, the averaged curvature error is on the order of 10^{-5}, which is one order less than the minimum true curvature. With smaller contour gap (slice thickness), the error is decreasing. When the gap is less than 10 mm, the error results in a stable value. Figure 5.7 shows mean and standard deviation Gaussian strain error for different gaps ranging from 1 mm to 25 mm. In the Figure, the prolate sphere is tilted a little to show the value near the apical region. From the figure we can see that, the minimum and maximum error are existing near the apex region. The ringing effects is due to the simulated contours.

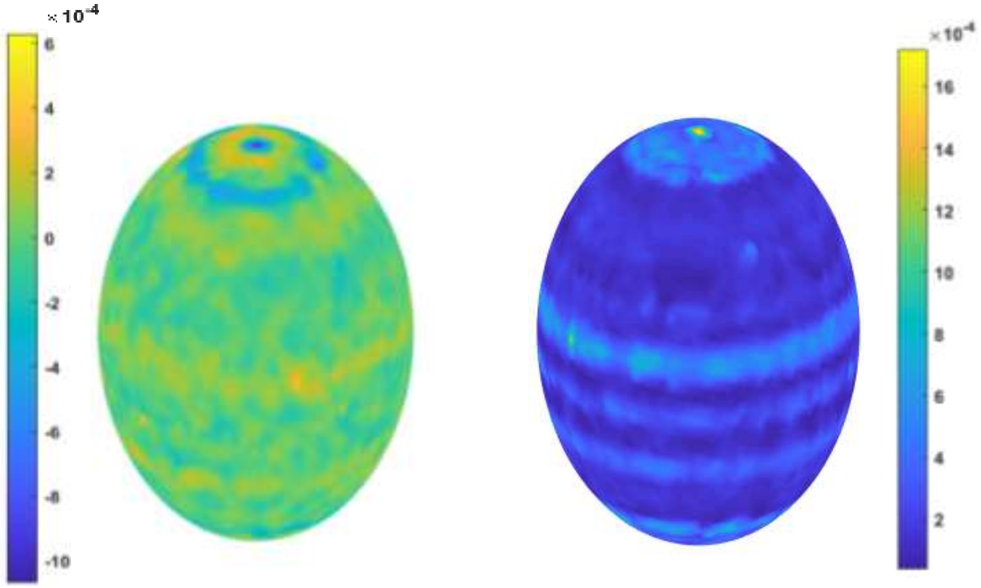

Figure 5.7 Prolate spheroid colored with Gaussian curvature mean error and standard deviation (SD) for surfaces with contour gaps ranging from 1 mm to 25mm. Left: mean of all gaps. Right: SD of all gaps. The ringing effects on the error surface is due to the simulated contours. The prolate spheroids are tilted to show the maximum and minimum values existing in the apical region.

5.3.1 Conclusion

From the fitted surface as shown in Figure 5.4, we can visually see the fitting is accurate and smooth. From the curvature comparison results, as shown in Figure 5.6, between the known curvature for the prolate and the computed curvature from the fitted surface, we can see the error is within a reasonable small error, which validates the fitting accuracy of the proposed algorithm.

5.4 Validation on LV curvatures

To further validate the proposed surface fitting algorithm, we fitted triangulated surfaces using the proposed algorithm described in Chapter 3 and cubic B-spline surfaces to the same set of LV contours drawn on MRI data from a previous study, then compared the longitudinal and circumferential curvatures from both surfaces. The cubic B-spline surface were fitted in the prolate spheroid coordinates (λ,μ,θ) , which contained 19 points in the μ direction and 24 points in the theta (θ) direction. The set of LV contours consisted contours from 16 subjects, including 8 normal and 8 MR subjects. They underwent MRI scanning in 1.5 T scanner using standard cine MRI protocols as described in Chapter 1. LV contours were manually drawn at ED and ES. Both LV surfaces were rotated to the same fitting coordinate as described in Section 3.5.2.

In the comparison, it was conducted based on each segment using the LV standard 16-segment model [69]. For each segment, the mean value and standard deviation were computed for all subjects. Paired T-test with Bonferroni correction was conducted to compare the curvatures between the B-spline surface and the proposed triangulated surface. Correlation coefficient was computed using simple linear regression as well. In the comparison, the apex is excluded in the apical layer due to the apex singularities in the LV B-spline surfaces [52].

Table 5-1 Circumferential Comparison at LVED, 1/mm.

Segment	B-spline	Proposed	P-value	R	P-value
Basal Anterior	0.042 ± 0.007	0.036 ± 0.008	0.0594	0.84	0.0012
Basal Anteroseptal	0.033 ± 0.009	0.039 ± 0.008	0.1320	0.73	0.0113
Basal Inferoseptal	0.039 ± 0.007	0.040 ± 0.005	0.4679	0.68	0.0209
Basal Inferior	0.045 ± 0.006	0.041 ± 0.006	0.0680	0.58	0.0617
Basal Inferolateral	0.036 ± 0.005	0.037 ± 0.005	0.6728	0.33	0.3204
Basal Anterolateral	0.040 ± 0.007	0.042 ± 0.007	0.3857	0.88	0.0004
Middle Anterior	0.027 ± 0.004	0.029 ± 0.006	0.4536	0.87	0.0006
Middle Anteroseptal	0.024 ± 0.004	0.032 ± 0.004	0.0008	0.77	0.0057
Middle Inferoseptal	0.023 ± 0.004	0.026 ± 0.005	0.0920	0.70	0.0154
Middle Inferior	0.028 ± 0.004	0.027 ± 0.005	0.4693	0.85	0.0008
Middle Inferolateral	0.024 ± 0.004	0.027 ± 0.005	0.1052	0.76	0.0071
Middle Anterolateral	0.023 ± 0.003	0.030 ± 0.005	0.0003	0.20	0.5584
Apical Anterior	0.040 ± 0.008	0.033 ± 0.006	0.0311	0.85	0.0009
Apical Septal	0.043 ± 0.006	0.043 ± 0.007	0.9085	0.88	0.0004
Apical Inferior	0.048 ± 0.005	0.039 ± 0.004	0.0002	0.60	0.0494
Apical Lateral	0.034 ± 0.007	0.029 ± 0.007	0.0661	0.72	0.0131

Mean±SD. R: correlation coefficient. Seg: segment

Table 5-2 Longitudinal Comparison at LVED, 1/mm

Segment	B-spline	Proposed	P-value	R	P-value
Basal Anterior	0.044 ± 0.005	0.048 ± 0.006	0.1249	0.62	0.0425
Basal Anteroseptal	0.042 ± 0.004	0.040 ± 0.008	0.3639	0.57	0.0678
Basal Inferoseptal	0.041 ± 0.008	0.042 ± 0.005	0.7052	0.68	0.0211
Basal Inferior	0.044 ± 0.008	0.047 ± 0.005	0.2638	0.86	0.0007
Basal Inferolateral	0.047 ± 0.006	0.041 ± 0.005	0.0167	0.66	0.0287
Basal Anterolateral	0.047 ± 0.006	0.047 ± 0.008	0.9075	0.64	0.0350
Middle Anterior	0.037 ± 0.006	0.037 ± 0.004	0.8354	0.68	0.0219
Middle Anteroseptal	0.034 ± 0.005	0.033 ± 0.004	0.5108	0.67	0.0234
Middle Inferoseptal	0.029 ± 0.005	0.030 ± 0.005	0.5863	0.84	0.0012
Middle Inferior	0.030 ± 0.006	0.038 ± 0.005	0.0099	0.64	0.0340
Middle Inferolateral	0.036 ± 0.007	0.034 ± 0.005	0.3717	0.83	0.0014
Middle Anterolateral	0.038 ± 0.005	0.035 ± 0.004	0.1194	0.69	0.0184
Apical Anterior	0.043 ± 0.005	0.042 ± 0.005	0.8784	0.62	0.0436
Apical Septal	0.048 ± 0.006	0.047 ± 0.008	0.7558	0.88	0.0004
Apical Inferior	0.047 ± 0.006	0.048 ± 0.006	0.9021	0.69	0.0179
Apical Lateral	0.041 ± 0.004	0.040 ± 0.006	0.9360	0.69	0.0176

Mean±SD. R: correlation coefficient. Seg: segment

Table 5-1 and Table 5-2 show the longitudinal and circumferential curvature comparison at LVED between the two methods. From the table we can see, in the longitudinal direction, most segments show no statistical significance between the two methods except segment 08, the middle inferoseptal. The correlation coefficient between the two methods is high for all segments. In the circumferential direction, segments 8, 12 and 15, i.e. the middle inferior, middle anterolateral inferior and apical inferior, have a statistical significance. The other 13 segments show no statistical significance with high correlation coefficients. Table 5-3 and Table 5-4 show the curvature comparison at LVES between the two methods. In the longitudinal direction, all segments have high correlation coefficients but no statistical significance. In the circumferential direction, except segments 8 and 12, i.e. middle inferior and middle anterolateral, all segments have no statistical significance but have high correlation coefficients.

Table 5-3 Longitudinal Curvature Comparison at LVES, 1/mm

Segment	B-spline	Proposed	P-value	R	P-value
Basal Anterior	0.065 ± 0.010	0.068 ± 0.017	0.5684	0.41	0.2156
Basal Anteroseptal	0.068 ± 0.011	0.059 ± 0.014	0.1261	0.73	0.0114
Basal Inferoseptal	0.069 ± 0.015	0.068 ± 0.016	0.9373	0.56	0.0740
Basal Inferior	0.071 ± 0.016	0.080 ± 0.017	0.2437	0.66	0.0277
Basal Inferolateral	0.073 ± 0.011	0.067 ± 0.014	0.2442	0.55	0.0771
Basal Anterolateral	0.070 ± 0.011	0.073 ± 0.017	0.5806	0.49	0.1245
Middle Anterior	0.055 ± 0.011	0.050 ± 0.007	0.2143	0.63	0.0373
Middle Anteroseptal	0.053 ± 0.011	0.043 ± 0.010	0.0509	0.50	0.1149
Middle Inferoseptal	0.043 ± 0.013	0.040 ± 0.021	0.7112	0.65	0.0316
Middle Inferior	0.042 ± 0.012	0.046 ± 0.011	0.4506	0.76	0.0062
Middle Inferolateral	0.048 ± 0.012	0.042 ± 0.009	0.2189	0.63	0.0388
Middle Anterolateral	0.052 ± 0.008	0.048 ± 0.007	0.2759	0.83	0.0017
Apical Anterior	0.063 ± 0.010	0.070 ± 0.014	0.2143	0.66	0.0263
Apical Septal	0.068 ± 0.011	0.079 ± 0.017	0.0935	0.95	0.0000
Apical Inferior	0.067 ± 0.009	0.075 ± 0.014	0.1638	0.78	0.0045
Apical Lateral	0.061 ± 0.008	0.059 ± 0.012	0.6272	0.57	0.0684

Mean±SD. R: correlation coefficient. Seg: segment

Table 5-4 Circumferential Curvature Comparison at LVES, 1/mm

Segment	B-spline	Proposed	P-value	R	P-value
Basal Anterior	0.066 ± 0.009	0.052 ± 0.013	0.0058	0.50	0.1141
Basal Anteroseptal	0.056 ± 0.010	0.057 ± 0.015	0.8445	0.66	0.0261
Basal Inferoseptal	0.062 ± 0.010	0.068 ± 0.014	0.2620	0.50	0.1131
Basal Inferior	0.066 ± 0.013	0.074 ± 0.017	0.2212	0.46	0.1544
Basal Inferolateral	0.058 ± 0.007	0.057 ± 0.011	0.8067	-0.27	0.4098
Basal Anterolateral	0.065 ± 0.009	0.065 ± 0.012	0.9267	0.51	0.1036
Middle Anterior	0.043 ± 0.009	0.042 ± 0.010	0.7673	0.56	0.0720
Middle Anteroseptal	0.037 ± 0.008	0.045 ± 0.009	0.0309	0.60	0.0492
Middle Inferoseptal	0.037 ± 0.011	0.039 ± 0.018	0.7333	0.75	0.0071
Middle Inferior	0.041 ± 0.005	0.039 ± 0.009	0.4846	0.67	0.0230
Middle Inferolateral	0.038 ± 0.008	0.038 ± 0.009	0.9785	0.90	0.0001
Middle Anterolateral	0.035 ± 0.008	0.046 ± 0.009	0.0050	0.40	0.2180
Apical Anterior	0.064 ± 0.018	0.054 ± 0.014	0.1730	0.86	0.0006
Apical Septal	0.066 ± 0.015	0.074 ± 0.018	0.3172	0.79	0.0033
Apical Inferior	0.068 ± 0.008	0.065 ± 0.014	0.5268	0.56	0.0714
Apical Lateral	0.055 ± 0.016	0.043 ± 0.015	0.0845	0.52	0.0944

Mean±SD. R: correlation coefficient. Seg: segment

Figure 5.8 and Figure 5.9 display the curvature comparison for the two methods in both directions for all segments. From the figures, the same conclusion can be made that LV curvatures in the longitudinal and circumferential directions from both methods have same trend with small difference for all layers at LVED and LVES.

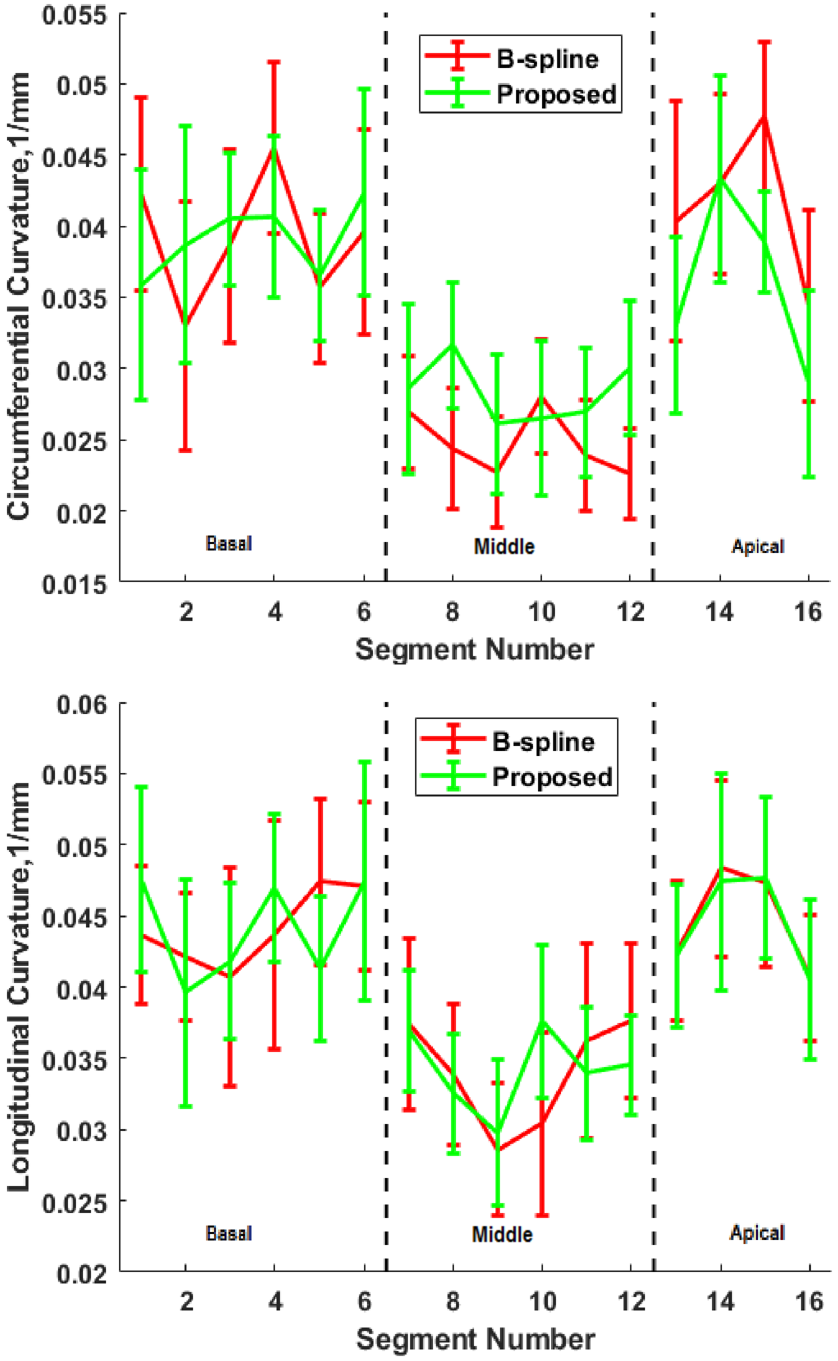

Figure 5.8 LV circumferential (top) and longitudinal (bottom) curvature versus segments at LVED. Mean±SD., 1/mm.

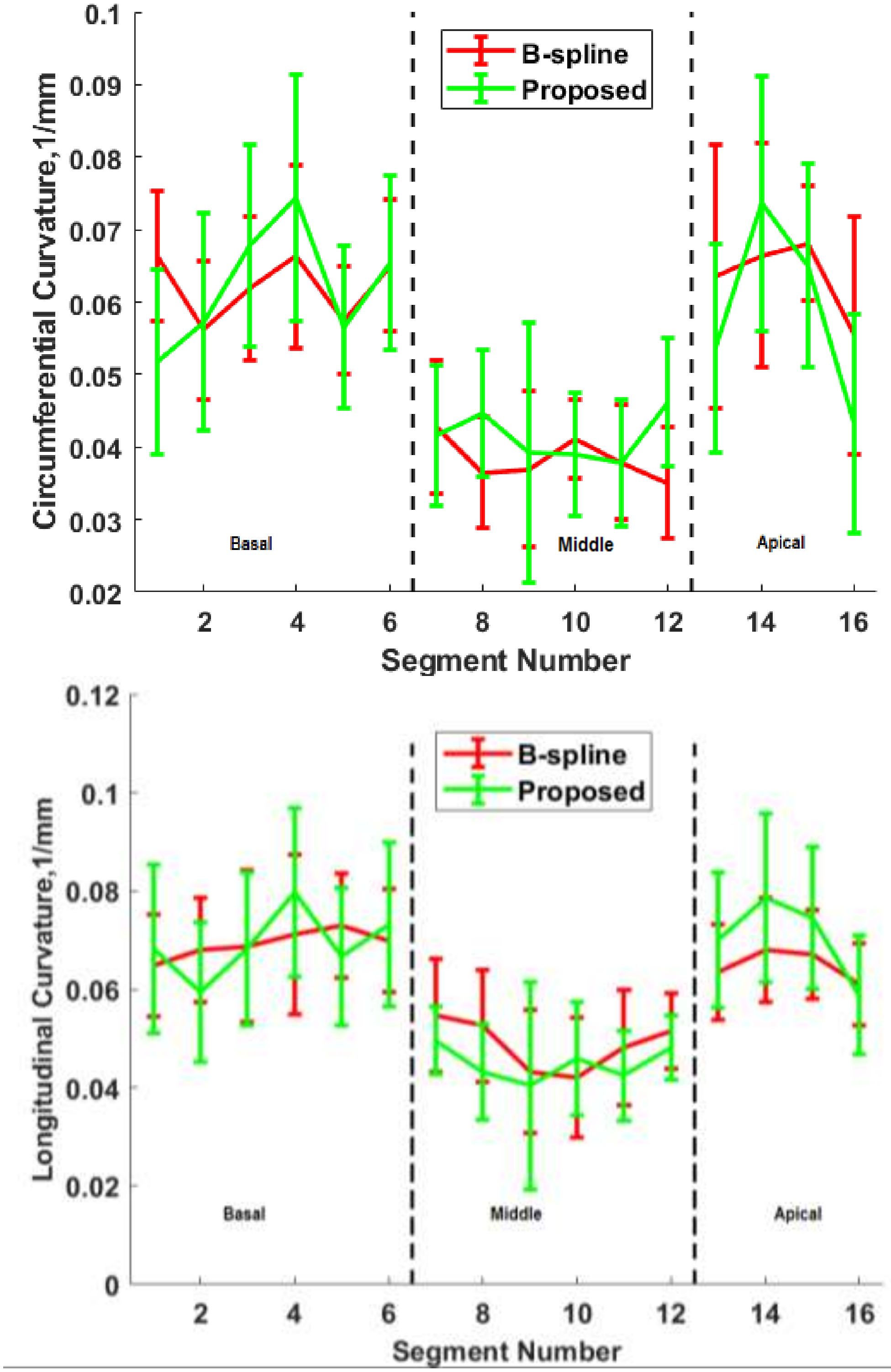

Figure 5.9 LV circumferential (top) and longitudinal (bottom) curvature versus segments at LVES. Mean±SD, 1/mm.

5.4.1 Discussion and Conclusion on the LV curvatures

From the comparison curves and tables, we can that the curvatures of most segments in both directions are not statistically significant for both methods. The difference in the two or three segments could be introduced by the smoothing functions are different in the two methods, especially when the contours have motion error or are not perfectly aligned. Figure 5.10 shows the difference of B-spline surface and the triangulated surface result in from mis-aligned contours for a subject. However, most segments have high agreement and this validates the fitting accuracy of the proposed algorithm.

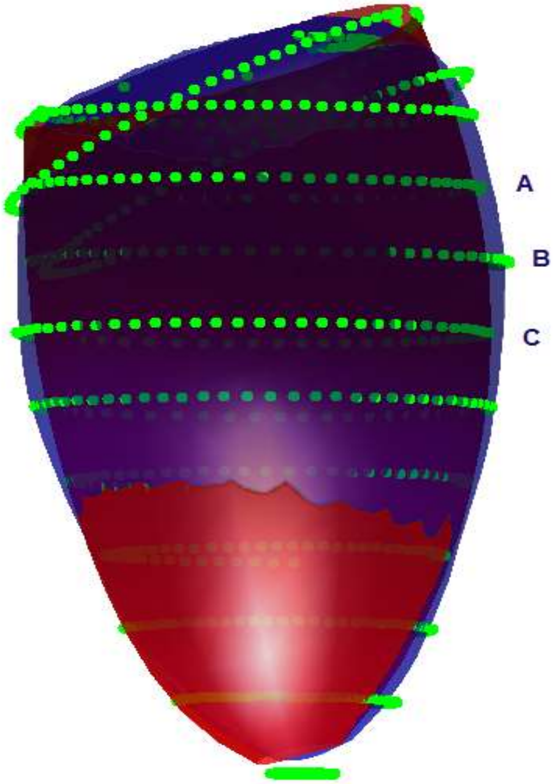

Figure 5.10 Illustration of B-spline surface (red) and triangulated surface (blue) difference. Slices A, B and C are not perfectly aligned, the smoothing functions of the two surfaces result in differences in the surfaces.

5.5 Conclusion

From the curvature comparison on a perfect prolate spheroid and B-spline LV mesh, we found the curvatures in both directions have large linear correlation without any significant difference. This observation in the comparisons validates the accuracy of the curvature computation and accuracy of the proposed surface fitting algorithm from the segmented MRI data.

Chapter 6 MECHANICS ANALYSIS AND VALIDATION

Quantifying ventricular and atrial mechanical function is important for diagnosing and managing patients with heart disease over time. However, LA and RA have thin walls, which limit the application of the tMRI-based methods in strain measurement [14]. The surfaces of each heart chamber reconstructed from the endocardial contour points using the proposed algorithm has one to one vertex correspondence, which allows the access to track local myocardial motion. In this chapter, we develop a technique for measuring myocardial wall strain from an approximate correspondence between mesh vertices in different time frames, then, we validated this technique with tMRI strains in the LV.

6.1 Wall Motion Tracking

The surface reconstructed by the proposed algorithm has vertex-to-vertex correspondence across the whole cardiac cycle, therefore, the wall motion can be analyzed. To track the wall motion of all 4 chambers, we measured the displacement of each vertex in the radius direction across a whole cardiac cycle [37]. In Section 4.2, the segment-models of all four chambers were described. In the wall motion analysis, the vertex displacements were then averaged based on segments defined in those segment-models.

6.2 Strain Computation

Tagging MRI (tMRI) and displacement encoding with stimulated-echoes (DENSE) are well-established imaging methods for evaluating regional mechanical function of the heart, but cine MRI is more commonly used in clinical environments. In this dissertation, we propose a new method for quantifying the 2D strain of the endocardial surface reconstructed from cine MRI data. In the strain computation, all corresponded triangles were transformed to the same plane with z = 0, then, the 2D displacement and strain tensor were computed using the constant strain triangle. The computation will be illustrated using a transformed triangle as the constant strain triangle element as shown in Figure 6.1 [147].

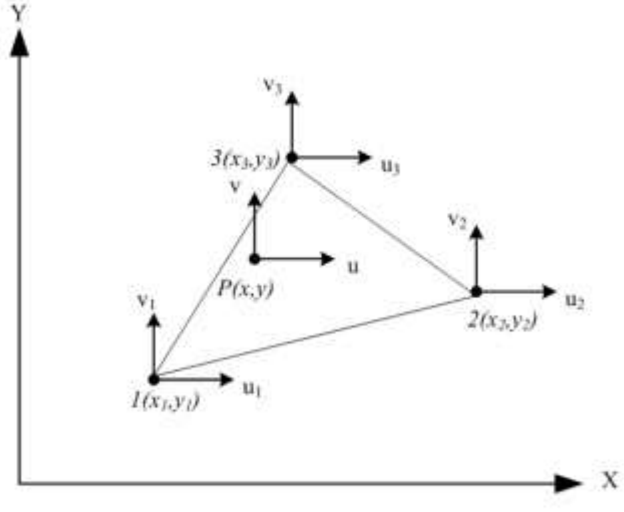

Figure 6.1 Constant strain triangle element for plane strain [147]

The displacement can be expressed as:

$$\begin{Bmatrix} u \\ v \end{Bmatrix} = \begin{bmatrix} N_1 & 0 & N_2 & 0 & N_3 & 0 \\ 0 & N_1 & 0 & N_2 & 0 & N_3 \end{bmatrix} \begin{Bmatrix} u_1 \\ v_1 \\ u_2 \\ v_2 \\ u_3 \\ v_3 \end{Bmatrix} \qquad 6\text{-}1$$

where the shape functions (N_1 N_2 N_3) are:

$$N_1 = \frac{1}{2A}\{(x_2y_3 - x_3y_2) + (y_2 - y_3)x + (x_3 - x_2)y\}$$

$$N_2 = \frac{1}{2A}\{(x_3y_1 - x_1y_3) + (y_3 - y_1)x + (x_1 - x_3)y\}$$

$$N_3 = \frac{1}{2A}\{(x_1y_2 - x_2y_1) + (y_1 - y_2)x + (x_2 - x_1)y\} \qquad 6\text{-}2$$

and A is the area of the triangle.

Then, the gradient of the displacement is given by:

$$\nabla u = \frac{1}{2A}\begin{bmatrix} y_{23}u_1 + y_{31}u_2 + y_{12}u_3 & x_{32}u_1 + x_{13}u_2 + x_{21}u_3 \\ y_{23}v_1 + y_{31}v_2 + y_{12}v_3 & x_{32}v_1 + x_{13}v_2 + x_{21}v_3 \end{bmatrix} \qquad 6\text{-}3$$

The strain tensor is given by:

$$E = \frac{1}{2}[\nabla u^T + \nabla u + \nabla u^T \nabla u] \qquad 6\text{-}4$$

The principle strains, i.e., the maximum and minimum strain, are the eigenvalues of the strain tensor. In the strain computation, the timeframe with the largest volume of the chamber is used as the reference phase. This strain computation will be validated through comparison to tMRI based methods in the following section.

6.3 Strain Analysis Validation

In this section, we will validate the fitting algorithm through LV endocardial 2D strains by comparing the strains from the fitted triangulated surface with strains from the following tMRI-based methods: HARP [136], DMF [137], and PSB [135]. We performed Repeated Measures ANOVA using univariate approach in R (https://www.r-project.org) for the comparison. The comparison is followed by pairwise comparison between the proposed method and the t-MRI based methods.

6.3.1 Imaging Acquisition and Method

To validate the proposed surface fitting algorithm through strain computation with in-vivo data,a total of 30 human studies were used, including images from 10 normal subjects (NL) and patients with pathologies including 5 with diabetes with infarction (DMI), 8 with resistant hypertension (HTN) and 7 with pulmonary arterial hypertension (PAH). All participants were imaged on a 1.5T scanner (GE Healthcare, Milwaukee, WI) with standard cine MRI protocol and standard tagging MRI (tMRI) protocol. Both protocols consist of 2-chamber view, 4-chamber view and a short-axis view (SA) with parameters as follows: FOV: 360-400mm, 8mm slice thickness, no gap, and 256*256 matrix. LV triangulated surfaces were fitted to the 30 studies using the proposed surface fitting algorithm described in Chapter 3. The minimum principal strain at the centroid of each triangle was computed from the displacements of the corresponded triangle vertices. All strains were averaged based on the near basal, middle and apical layers. Then the strains of each layer were compared with the strains computed from the tMRI-based methods, i.e. HARP [136], DMF [137], and PSB [135], using Repeated Measured ANOVA followed by pairwise comparison.

6.3.2 Results

Figure 6.2 displays the averaged LV endocardial principal minimum surface strains and strains from tMRI-based methods. From the figure, we can see that the surface strains are larger in magnitude relative to the tMRI-based strains, especially for the basal and middle layers. However, the strain curves have similar shapes across the heart cycle.

To further test the curvature measurements with different methods, we conducted Repeated Measurements ANOVA for strains at the ES timeframe based on the three layers. The p-value from the test of the Repeated Measurements ANOVA of all three layers are less than 0.05, which means there are statistically significant differences in the methods. To further compare the surface strains with the t-MRI based methods, we conducted paired pairwise comparison with Bonferroni correction. Table 7-1 shows the pairwise comparison p-value and correlation coefficient between the surface strain and tMRI-based strains. From Figure 8.2 we can see that, the strain difference is small near LV ED (1%-30% LVES interval) and is increasing while approaching LVES (100% LVES interval).

From Figure 6.2 and Table 6-1, we find the curve shapes are similar with moderate correlation between the surface wall strain and the strains from the tMRI-based methods. However, the p-values between the methods show significant difference. To further understanding the difference, we display the Bland-Altman plots of the differences, and show the scatter plots with regression line between the endocardial surface strain and the tMRI-based strains.

Table 6-1 Comparison of LV endocardial minimum principal surface strain computed from cine MRI with 3D mid-wall strains from tMRI at ventricular ES.

		HARP		
	Diff. (Mean±SE)	p	R	p
Base	0.081±0.006	<0.01	0.48	0.0218
Mid-Ventricle	0.062±0.006	<0.01	0.44	0.0373
Near Apex	0.032±0.006	<0.01	0.47	0.0317

		PSB		
	Diff. (Mean±SE)	p	R	p
Base	0.049±0.007	<0.01	0.40	0.1652
Mid-Ventricle	0.058±0.007	<0.01	0.39	0.0839
Near Apex	0.023±0.008	0.012	0.43	0.3511

		DMF		
	Diff. (Mean±SE)	p	R	p
Base	0.061±0.005	<0.01	0.41	0.0511
Mid-Ventricle	0.054±0.005	<0.01	0.46	0.0471
Near Apex	0.038±0.006	<0.01	0.42	0.1720

Diff: difference. R: correlation coefficient

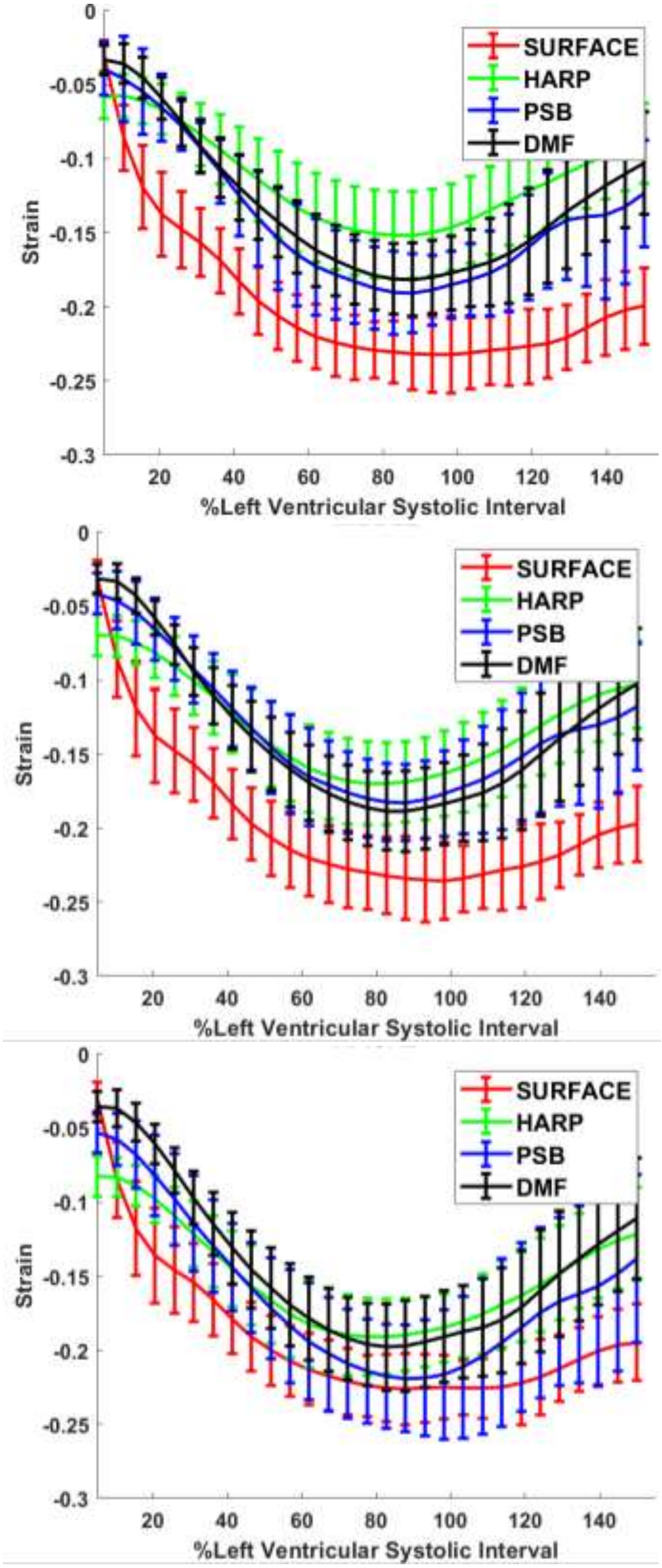

Figure 6.2 Plots of LV endocardial minimum principal strain (red) computed from cine MRI compared with 3D mid-wall strains (green, blue, black) averaged over a layer near the basal (top), middle (middle) and apical (bottom). Mean ± SD.

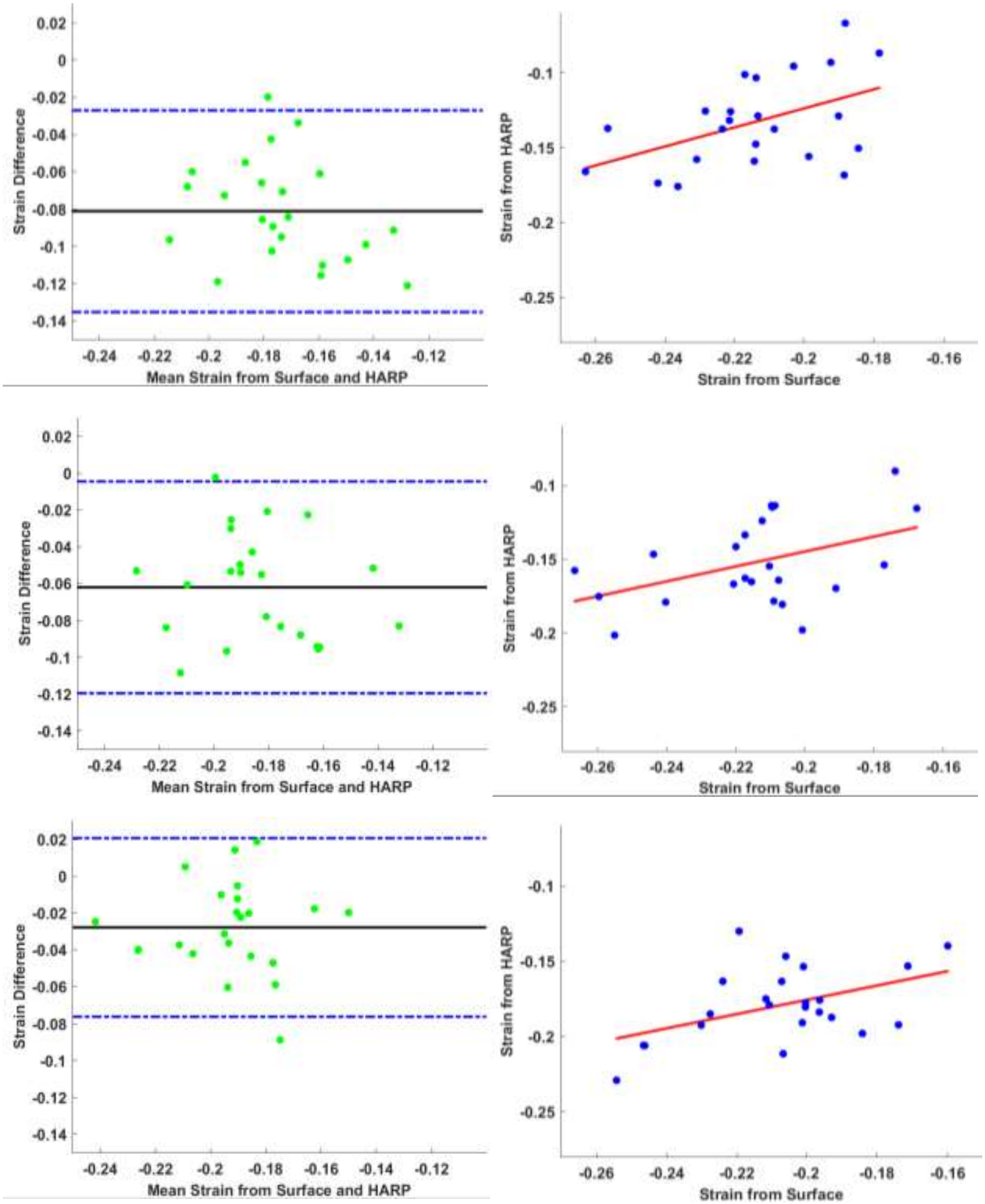

Figure 6.3 BA plot (left) and scatter plot (right) of strains from surface and HARP. Top: basal layer. Middle: middle layer. Bottom: apical layer.

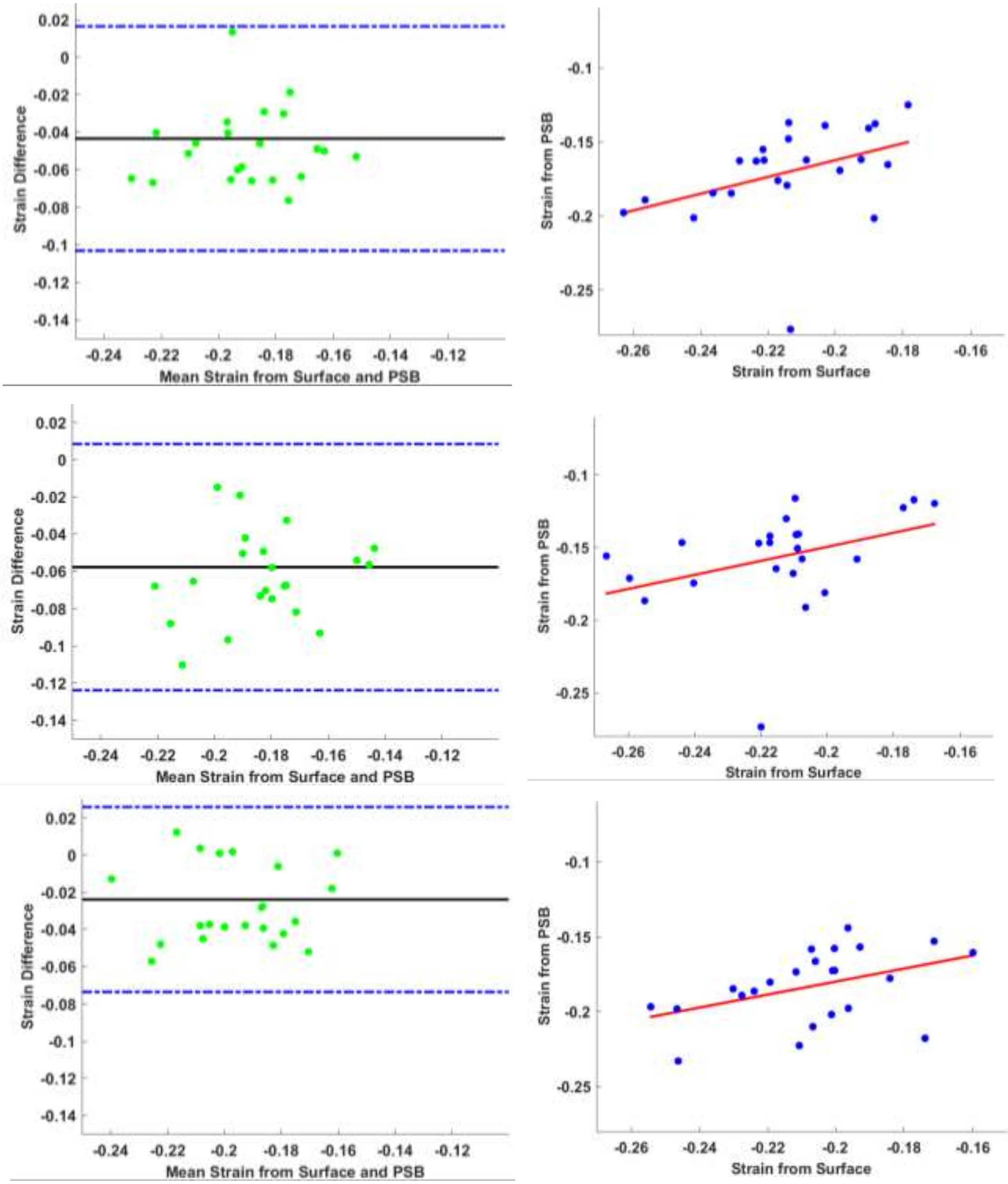

Figure 6.4 BA plot (left) and scatter plot (right) of strains from surface and PSB. Top: basal layer. Middle: middle layer. Bottom: apical layer.

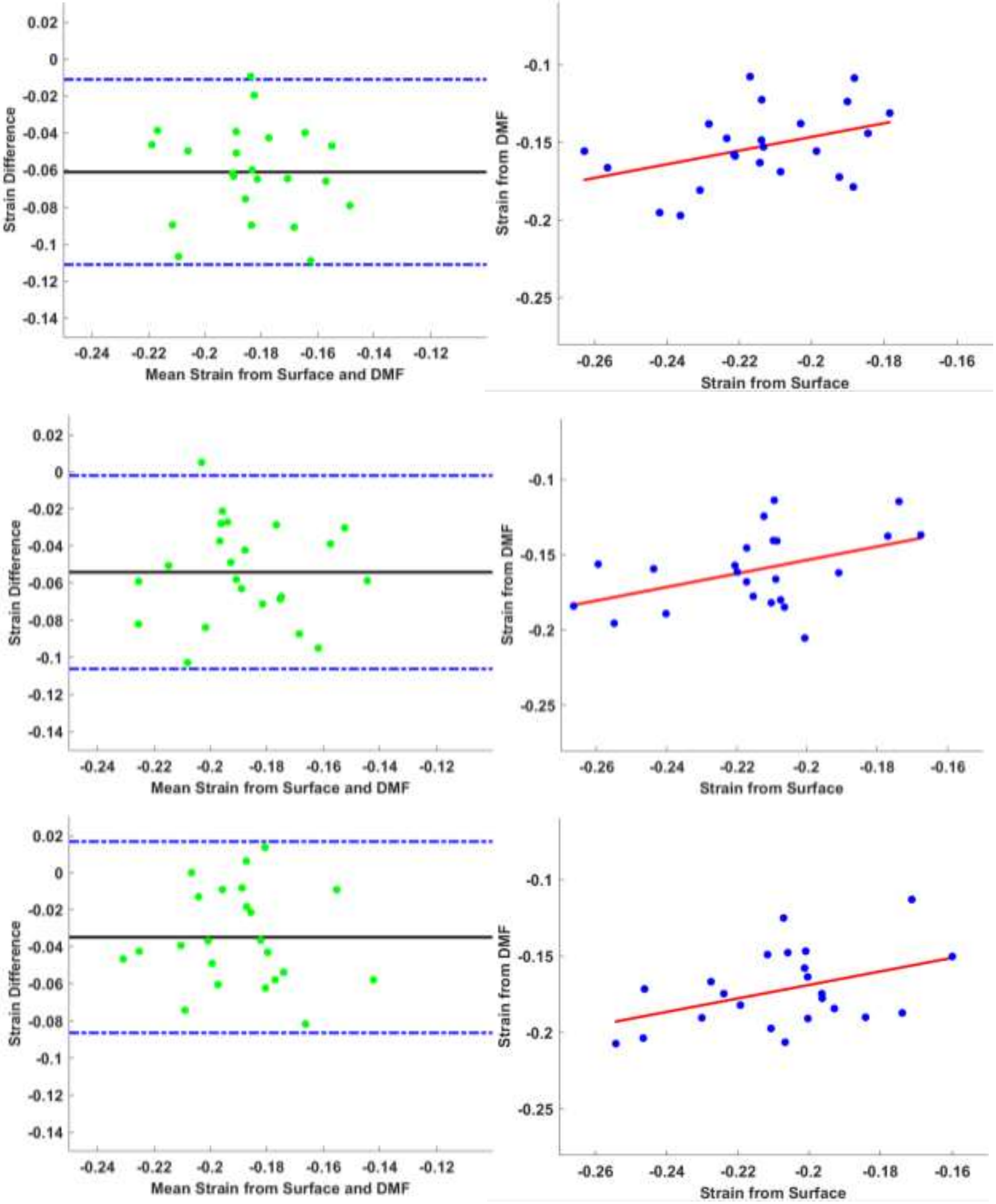

Figure 6.5 BA plot (left) and scatter plot (right) of strains from surface and DMF. Top: basal layer. Middle: middle layer. Bottom: apical layer.

From Figure 6.3, we can see that, the mean difference between the surface strain and the strain from HARP lies around -0.08 in the basal layer, -0.06 at the middle layer and -0.02 at the apical layer. Except one subject, all difference lies between the ±2SD and no obvious trend in the differences for all three layers. From Figure 6.4, we can see that, the mean difference between the surface strain and the strain from PSB lies around-0.05 in the basal and middle layers, and -0.02 at the apical layer. Except one subject, all difference lies between the ±2SD and no obvious trend in the differences for all three layers. From the scatter plot, we can see there is an outlier, which explains the smaller correlation in Table 6-1 for the PSB at the basal and middle layers. From Figure 6.5, we can see that, the mean difference between the surface strain and the strain from DMF lies around -0.06 in the basal and middle layers, and -0.04 at the apical layer. Except one subject, all difference lies between the ±2SD and no obvious trend in the differences for all three layers.

6.4 Conclusion

From the strain time curves, we can see the curve shapes of the endocardial surface strain are very similar to that of the strains from the tMRI-based methods with moderate correlations. From the Bland-Altman plots and scatter plots, we can see that, the surface strain is larger in amplitude than the tMRI-based methods.

The comparison between the surface strain and tMRI-based strain shows a difference in the strain computation. There are mainly two reasons for that: 1). The surface strain was measured from the endocardial surface, while the HARP strain was measured as average of the epicardial and endocardial walls and PSB and DMF strains were measured on the mid-wall of the myocardium. 2) The surface strain was based on vertex correspondences that are only approximately true, while the tMRI-based methods were based on the material points. However, the curve shapes are similar and our finding that the endocardial surface strain is larger in magnitude than the mid-wall strains is consistent with previous work [146]. In which, the author finds the endocardial wall has larger strain magnitude than the middle and epicardial walls at LVES [146]. Therefore, this validation through LV strain computation shows the potential to derive accurate myocardium deformation information despite that there is not a strict correspondence between surface vertices over time from cine MRI data. The method is not dependent on chamber geometry or wall thickness and can also be used to quantify strains in the relatively thin-walled left and right atria and right ventricle. In a clinical setting, contours are often drawn at ED and ES to measure volumes and ejection fraction. These contours can be automatically propagated to the remaining [77] and used to compute surface strain across a complete cardiac cycle.

Chapter 7 CHARACTERIZATION OF GEOMETRY, VOLUME AND WALL MOTION VERSUS AGE ON HEALTHY SUBJECTS WITH MRI

This study was conducted to explore novel techniques in geometry evaluation and wall mechanics measurement along with volume function analysis from cine MRI data. The main purpose of this study is to characterize the atrial functions and mechanics along with ventricular analysis in both young and old healthy groups. In the same time, we explored the remodeling with aging. The abstract of this work was accepted to the 2017 ISMRM.

7.1 Introduction

LA and RA volume functions have been recognized as important predictors of heart failure and have association with congenital heart disease and reoccurrence, such as pulmonary hypertension, valvular disease, atrial fibrillation and myocardial infarction [4] [33] [38] [59] [70] [92-94]. LA volume function along with size reflects LA performance and is considered as a predictor of cardiovascular morbidity and mortality [10-13] [22] [92]. In addition, they play an important role in optimizing overall cardiac function and pathologic conditions. RA volume assessment has the potential to be an early marker of RV dysfunction [33] [48]. LA volumes are widely employed in clinical protocols [38], however, less research and fewer clinical outcomes are available on the quantification of RA.

In addition to the clinical importance of atrial size and volume, atrial myocardial deformation analysis and regional mechanics have clinical potential in quantifying medical therapies, damage measurements, minimizing injuries, monitoring reginal functions and remodeling [14] [93]. Many techniques for measuring regional mechanics, such as tagging MRI, and cine displacement encoding stimulated echo (DENSE) CMR, are limited in both atria by their thin walls [14]. Speckle tracking is a popular method in the atrial deformation measurement [93] [95], especially in the RA. However, the limitation of speckle tracking includes variability in quality related to operator experience and limited acoustic windows often related to body habitus [94]. Another limitation in current RA and LA deformation analysis is that they require LV-specific software, because no vendor-independent commercial software is available for dedicated atrial analysis [93]. Currently, RA mechanics have been less explored [95].

Besides the atrial clinical importance and potentials, both ventricles have demonstrated clinical potential. RV volume function is a major marker in a variety of cardiovascular disease, including pulmonary hypertension, ventricular ischemia or infarction, pulmonary or tricuspid valvular heart disease [9]. It has mutual influence with LV on each other via the pulmonary circulation and through the septal wall [12], while the influence of these coupling mechanisms are incompletely understood [9]. The complexity in the RV geometry is not easily described or modeled and limited the analysis of RV function and true wall motion analysis [11-12] [68-69]. Instead, simpler assessments of RV volume, such as ejection fraction or fractional area shortening, are more commonly calculated, which are measured mostly rely on linear dimensions from 2-chamber or 4-chamber views. Those measurements have the same drawback as in atrial measurements with angle dependency [69]. Plus, those simpler assessments do not reflect the underlying RV performance and are not sufficient in diagnosis guiding [11]. Moreover, the evaluation of RV is also insufficient compared to numerous LV analysis.

There is literature indicating that the combination of volume function, structure analysis and regional motion might provide more supplementary information before diagnostic and surgery [39] [14]. With the current situation, i.e., continuous RA volume measurements and mechanics analysis are lacking [94], and RV and LA measurements are insufficient, we are motivated by the clinical need for simultaneous analysis of both atria and ventricles [95] to conduct this study. In this study, we combined geometry analysis, wall mechanics estimation with volume function analysis for both atrial and ventricles on both young and old healthy subjects using the proposed surface fitting algorithm, which has no shape assumption nor angle-dependency. From the fitted surfaces, we measured the volume across the whole cardiac cycle. With the one-to-one vertex correspondence of the fitted surfaces, we estimated wall motions and strains along with geometries of all four chambers separately and simultaneously. In addition to the characterization of the atrial and ventricular functions and mechanics on young and old healthy subjects, we also conducted comparison between the two groups with the purpose to explore the remodeling of heart with aging.

7.2 Material and Methods

7.2.1 Imaging Acquisition

In this study, eight young normal subjects (n=8, mean age, 22±2 years; range, 19-24 years) and eleven old normal subjects (m=11, mean age, 61±6 years; range, 59-67 years) without clinical or anatomical evidence of cardiovascular disease were recruited. All participants underwent cine MRI using standard MRI protocols described in chapter 1 and the additional protocols described in chapter 3. The short summary of the MRI protocols are as follows: Using a Siemens 3 Tesla (T) Verio scanner (Siemens Healthcare, Germany), all participants were imaged with a triggered-gated breath-hold balanced SSFP sequence. An extra atrial SA orientation with 6 to 8 slices and 2 to 3 extra breath-holds was acquired. An extra right two-chamber orientation was imaged with one extra breath-hold. The study protocol was approved by the Institutional Review Boards at the University of Alabama at Birmingham and Auburn University. All participants gave written informed consent. For each subject, the analysis in this study contains two-chamber, four-chamber, right two-chamber, short axis and atrial short axis views.

7.2.2 Image Segmentation and Surface Reconstruction

All cardiac MRI images were contoured and tracked using a semi-auto method on a house-built software SMC [77]. As described in the image preprocessing section in the previous chapter, all endocardial contours were manually drawn at ED and ES in atrial short axis, short axis views and long axis views, then propagated to the remaining timeframes [77]. MV and TV landmarks were manually marked in the long axis views at ED and ES, then propagate to the remaining timeframes [77]. All propagated landmarks and contours were double checked from different views and were corrected as needed, then transformed to a fitting coordinate system. From the image segmentations in fitting coordinates, surfaces were fitted to all four chambers by using the novel surface fitting algorithm that we developed and described in Chapter 3.

7.2.3 Parameters Computation

From the reconstructed surfaces, parameters for geometry, wall mechanics and volume functions were estimated for each chamber. In the geometry estimation, the volume was computed by summing up the volumes of the tetrahedrons formed by the triangulated mesh, which was elaborated in Section 4.1.1. The volume parameters for each chamber were computed by following the definition in Section 4.1.2. Besides the volume, the surface area also reflects some fact of the size of the chamber and it was computed by summing up all the triangle areas on the surface mesh. In Section 5.1, segment-models were described for all four chambers. In the curvature computation, the principal curvatures were first computed, then the longitudinal curvature and circumferential curvature were obtained by following the curvature computation algorithm described in Section 5.2. With the vertex-to-vertex correspondence on the surface of each chamber in the cardiac cycle, we could track the motion on the endocardial wall by computing the radial displacement [37] of each vertex to the corresponded vertex at the first timeframe. The myocardial wall strain was computed by transferring corresponded 3D triangles to 2D planes then using the constant strain triangle element method [147], which was described in Section 6.2.

7.2.4 Statistical Analysis

In this study, the longitudinal and circumferential curvatures, radial displacement and strain were calculated and averaged for all subjects based on segments, which were described in the segment-models in Section 5.1. Student's two sample t test were conducted to compare the young group (n=8) and the old group (n=11) in volume, geometry and mechanics parameters. To avoid inflating the probability of a Type I error, the Bonferroni test procedure was utilized to adjust the significance level accordingly. All data are presented as mean ± standard deviation (SD). A $P<0.05$ was considered statistically significant.

7.3 Results

7.3.1 Geometry Evaluation

7.3.1.1 Surface Area

Table 7-1 shows summary and comparison of the surface area between the two groups. From the table, we can see that LA is significantly increased in the old group at both LVED and LVES phases. Figure 7.1 shows the averaged 3D surface area time curves of the four chambers with the same axis range for the young and old groups. From the figure, we can see the increase In the LA as well. Therefore, we expect the volume of LA to have statistical significance as well.

Table 7-1 Surface area (cm3) at corresponded volume phase for the young group and the old group.

Phase	Young		Old	
	Mean±SD	Range	Mean±SD	Range
LA Min V	3.9±1.2	2.7-5.8	5.4±0.9*	4.2-6.8
LVED V	14.0± 3.0	9.7-18.4	13.2± 1.3	16.5-16.1
RA Min V	4.3±1.3	6.5-2.7	5.8±1.5	3.10-8.6
RVED V	14.6±3.5	10.5-19.0	15.1±2.4	12.2-19.9
LA Max V	7.2±1.4	9.6-5.8	8.9±1.2*	7.6-11.4
LVED V	7.9±2.1	5.3-10.9	6.7±0.7	8.1-5.9
RA Max V	7.8±1.4	9.8-5.5	9.5±2.6	4.9-13.5
RVED V	8.6±2.9	5.3-12.7	8.7±1.2	7.5-11.3

Min: minimum. Max: maximum. V: volume. *: P<0.05 vs. Young

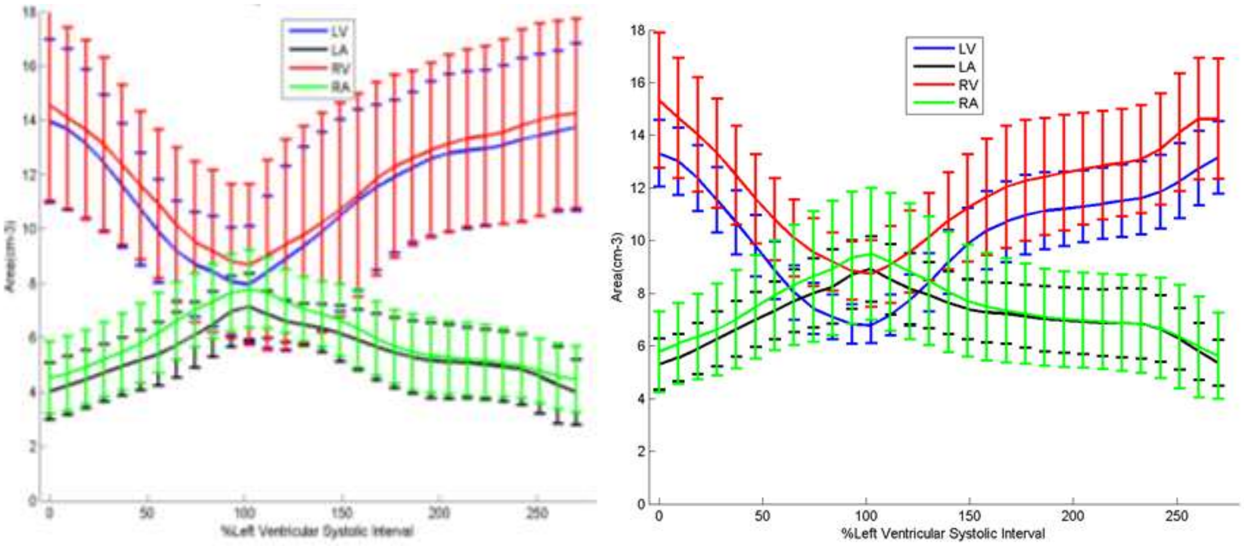

Figure 7.1 3D surface area vs. time of the young group (left) and the old group (right) with the same y-axis range. Mean±SD.

7.3.1.2 Curvatures

Table 7-2 to Table 7-5 show the statistical summary of the circumferential and longitudinal curvatures between the two groups at LVES and LVED. For the LV, there was no statistical difference for curvatures. For the RV, the circumferential curvature had statistical difference in the middle and basal regions. The longitudinal curvature statistical difference occurred at the middle lateral segments. In the longitudinal direction, LA had statistical difference in the middle and apical segments. In the circumferential direction, statistical difference occurred in the middle and apical segments. There was more difference in the circumferential direction and all curvature happened in the middle and apical layers. For the RA, circumferential curvature had statistical difference in the apical anterior segment, and the basal lateral segment had longitudinal curvature statistically significant difference.

Table 7-2 LV curvature (1/mm) analysis in the young and old normal subjects at LVES and LVED. Mean ± SD.

	LVES		**LVED**	
	Young	Old	Young	Old
	Circumferential			
Basal Anterior	0.05±0.010	0.05±0.024	0.04±0.005	0.03±0.013
Basal Anteroseptal	0.05±0.009	0.06±0.028	0.03±0.005	0.04±0.015
Basal Inferoseptal	0.05±0.008	0.07±0.028	0.04±0.004	0.04±0.015
Basal Inferior	0.06±0.010	0.07±0.031	0.04±0.006	0.04±0.016
Basal Inferolateral	0.05±0.011	0.06±0.028	0.03±0.006	0.04±0.014
Basal Anterolateral	0.06±0.011	0.07±0.024	0.04±0.006	0.04±0.015
Middle Anterior	0.04±0.006	0.04±0.016	0.03±0.003	0.03±0.011
Middle Anteroseptal	0.04±0.005	0.05±0.018	0.03±0.005	0.03±0.011
Middle Inferoseptal	0.04±0.007	0.04±0.024	0.03±0.006	0.03±0.012
Middle Inferior	0.04±0.009	0.04±0.016	0.03±0.008	0.02±0.009*
Middle Inferolateral	0.04±0.010	0.04±0.013	0.03±0.006	0.03±0.010
Middle Anterolateral	0.05±0.008	0.04±0.017	0.03±0.004	0.03±0.011
Apical Anterior	0.05±0.010	0.06±0.021	0.03±0.005	0.04±0.013
Apical Septal	0.07±0.013	0.08±0.030	0.04±0.006	0.04±0.017
Apical Inferior	0.06±0.007	0.07±0.035	0.04±0.004	0.04±0.015
Apical Lateral	0.05±0.012	0.04±0.021	0.03±0.007	0.03±0.011
	Longitudinal			
Basal Anterior	0.06± 0.010	0.07± 0.032	0.05±0.006	0.04±0.016
Basal Anteroseptal	0.05± 0.008	0.07± 0.034	0.04±0.003	0.04±0.016
Basal Inferoseptal	0.06± 0.008	0.07± 0.030	0.04±0.004	0.04±0.016
Basal Inferior	0.07± 0.009	0.08± 0.032	0.04±0.005	0.04±0.016
Basal Inferolateral	0.05± 0.011	0.07± 0.032	0.04±0.004	0.04±0.014
Basal Anterolateral	0.06± 0.013	0.08± 0.030	0.04±0.006	0.05±0.017
Middle Anterior	0.05± 0.006	0.05± 0.017	0.04±0.004	0.03±0.013
Middle Anteroseptal	0.05± 0.009	0.04± 0.018	0.03±0.006	0.03±0.012
Middle Inferoseptal	0.05± 0.013	0.04± 0.026	0.03±0.008	0.03±0.012
Middle Inferior	0.06± 0.012	0.04± 0.019	0.04±0.009	0.03±0.013
Middle Inferolateral	0.05± 0.006	0.04± 0.019	0.04±0.005	0.03±0.012
Middle Anterolateral	0.05± 0.008	0.05± 0.019	0.04±0.005	0.03±0.012
Apical Anterior	0.07± 0.009	0.07± 0.025	0.04±0.006	0.04±0.014
Apical Septal	0.08± 0.019	0.08± 0.029	0.05±0.009	0.05±0.018
Apical Inferior	0.08± 0.016	0.08± 0.034	0.05±0.007	0.05±0.017
Apical Lateral	0.06± 0.007	0.06± 0.025	0.04±0.004	0.04±0.014

*: $p<0.05$ vs. Young

Table 7-3 RV curvature (1/mm) analysis in the young and old normal subjects at LVES and LVED. Mean ± SD.

	LVES		**LVED**	
	Young	Old	Young	Old
	Circumferential			
Basal Anterior	0.08±0.023	0.07±0.030	0.05±0.010	0.05±0.026
Basal Lateral	0.04±0.010	0.04±0.024	0.03±0.005	0.02±0.018
Basal Inferior	0.04±0.010	0.05±0.020	0.03±0.008	0.04±0.014
Basal Inferoseptal	0.08±0.019	0.05±0.021*	0.05±0.013	0.04±0.017
Basal Anteroseptal	0.02±0.007	0.01±0.016	0.01±0.007	0.02±0.016
Middle Anterior	0.06±0.019	0.02±0.041*	0.04±0.016	0.03±0.013*
Middle Lateral	0.03±0.009	0.02±0.011	0.02±0.007	0.02±0.008
Middle Inferior	0.04±0.010	0.04±0.018	0.03±0.008	0.03±0.013
Middle Inferoseptal	0.07±0.021	0.06±0.024	0.04±0.010	0.03±0.014
Middle Anterorseptal	0.02±0.015	0.00±0.011*	0.01±0.013	0.00±0.011
Apical Anterior	0.04±0.029	0.01±0.043*	0.03±0.013	0.02±0.019
Apical Inferior	0.07±0.017	0.06±0.025	0.05±0.011	0.04±0.017
Apical Septal	0.13±0.047	0.07±0.056	0.08±0.014	0.05±0.020*
Outlet	0.08±0.016	0.06±0.023	0.06±0.008	0.04±0.016*
Inlet	0.07±0.010	0.07±0.026	0.05±0.008	0.05±0.020
	Longitudinal			
Basal Anterior	0.07± 0.016	0.07± 0.032	0.05±0.007	0.05±0.019
Basal Lateral	0.04± 0.009	0.03± 0.017	0.03±0.006	0.02±0.012
Basal Inferior	0.05± 0.012	0.04± 0.018	0.04±0.009	0.03±0.012
Basal Inferoseptal	0.05± 0.013	0.07± 0.029	0.04±0.009	0.05±0.019
Basal Anteroseptal	0.01± 0.012	0.01± 0.012	0.01±0.012	0.01±0.018
Middle Anterior	0.04± 0.020	0.03± 0.090	0.04±0.011	0.05±0.022*
Middle Lateral	0.04± 0.010	0.02± 0.009*	0.02±0.007	0.01±0.007*
Middle Inferior	0.05± 0.007	0.04± 0.016	0.04±0.006	0.03±0.013
Middle Inferoseptal	0.06± 0.015	0.08± 0.038*	0.04±0.008	0.05±0.023
Middle Anterorseptal	0.01± 0.018	0.00± 0.014	-0.00±0.020	0.00±0.011
Apical Anterior	0.05± 0.046	0.03± 0.124	0.05±0.017	0.05±0.035
Apical Inferior	0.10± 0.026	0.07± 0.034	0.06±0.009	0.05±0.021
Apical Septal	0.12± 0.039	0.12± 0.083	0.07±0.015	0.08±0.029
Outlet	0.06± 0.014	0.06± 0.026	0.04±0.008	0.05±0.018
Inlet	0.06± 0.010	0.06± 0.024	0.04±0.007	0.04±0.017

*: $p<0.05$ vs. Young

Figures 7.2 to 7.5 display the longitudinal and circumferential curvatures of all four chambers for both the young group and the old group. For the LV, curvatures in the longitudinal and circumferential of the old group increase in the apical segments. In the basal layer, only the circumferential curvature increased, while there was no significant difference in the middle layer.

Table 7-4 LA curvature (1/mm) analysis in the young and old normal subjects at LVES and LVED. Mean ± SD.

	Maximum Volume Phase		**Minimum Volume Phase**	
	Young	Old	Young	Old
	Circumferential			
Basal Anterior	0.06±0.010	0.05±0.020	0.09±0.017	0.07±0.033
Basal Septal	0.07±0.005	0.07±0.031	0.11±0.015	0.10±0.045
Basal Inferior	0.06±0.009	0.05±0.023	0.09±0.018	0.08±0.035
Basal Lateral	0.04±0.009	0.03±0.016	0.05±0.010	0.04±0.025
Middle Anterior	0.05±0.013	0.04±0.021	0.07±0.019	0.05±0.020
Middle Septal	0.04±0.021	0.02±0.011*	0.06±0.028	0.02±0.011*
Middle Inferior	0.05±0.006	0.04±0.016	0.08±0.011	0.05±0.019*
Middle Lateral	0.02±0.011	0.02±0.013	0.04±0.013	0.02±0.011
Apical Anterior	0.07±0.008	0.05±0.018*	0.11±0.014	0.07±0.030*
Apical Septal	0.06±0.022	0.05±0.036	0.07±0.023	0.07±0.047
Apical Inferior	0.06±0.009	0.06±0.025	0.09±0.017	0.10±0.054
Apical Lateral	0.06±0.009	0.07±0.031	0.09±0.020	0.13±0.081
	Longitudinal			
Basal Anterior	0.07± 0.010	0.06± 0.023	0.10±0.020	0.08±0.036
Basal Septal	0.06± 0.015	0.07± 0.028	0.10±0.027	0.10±0.038
Basal Inferior	0.06± 0.010	0.06± 0.026	0.09±0.016	0.09±0.036
Basal Lateral	0.04± 0.012	0.03± 0.017	0.05±0.012	0.04±0.024
Middle Anterior	0.07± 0.012	0.05± 0.018*	0.08±0.014	0.07±0.026
Middle Septal	0.04± 0.020	0.02± 0.014*	0.05±0.026	0.02±0.011*
Middle Inferior	0.06± 0.007	0.04± 0.018	0.08±0.012	0.04±0.027*
Middle Lateral	0.03± 0.009	0.03± 0.014	0.04±0.009	0.03±0.015
Apical Anterior	0.07± 0.013	0.05± 0.018	0.11±0.026	0.07±0.027
Apical Septal	0.06± 0.017	0.04± 0.022	0.07±0.023	0.06±0.038
Apical Inferior	0.07± 0.012	0.05± 0.018*	0.09±0.015	0.07±0.029
Apical Lateral	0.07± 0.011	0.04± 0.018*	0.11±0.014	0.07±0.049*

*: p<0.05 vs. Young

The circumferential curvature of the old group increased in the basal and apical layers for most segments. The longitudinal curvature of the old group in the apical layer increased for all the segments in the basal layer. There was few difference in the middle and apical layer. For the RV, only the lateral and inferior-septal in the basal and middle layers showed small differences in both directions, and in the apical there were some difference in the circumferential direction. For the LA, the curvature in both directions were smaller in the middle segments and most basal segments in the old group. The circumferential curvature of the old group showed a slight change in the basal layer and the most difference exited in the middle and apical layers. The longitudinal curvature of the old group decreased in the middle and basal layers. For the RA, most segments changed in both directions in the basal and middle layers between the two groups. In the middle layer, there were some difference in the circumferential direction for most segments in the middle and apical layers

Table 7-5 RA curvature (1/mm) analysis in the young and old normal subjects at LVES and LVED. Mean ± SD.

	Maximum Volume Phase		**Minimum Volume Phase**	
	Young	Old	Young	Old
	Circumferential			
Basal Anterior	0.06±0.006	0.06±0.027	0.09±0.010	0.10±0.044
Basal Septal	0.04±0.013	0.04±0.019	0.07±0.023	0.06±0.028
Basal Inferior	0.04±0.016	0.04±0.017	0.04±0.017	0.06±0.025
Basal Lateral	0.06±0.012	0.05±0.019	0.09±0.031	0.07±0.028
Middle Anterior	0.05±0.015	0.04±0.023	0.06±0.009	0.05±0.036
Middle Septal	0.05±0.010	0.04±0.021	0.08±0.014	0.05±0.021*
Middle Inferior	0.05±0.009	0.04±0.030	0.07±0.020	0.04±0.029*
Middle Lateral	0.05±0.015	0.03±0.020*	0.06±0.022	0.04±0.022*
Apical Anterior	0.03±0.007	0.05±0.021*	0.06±0.028	0.08±0.034
Apical Septal	0.06±0.008	0.05±0.021	0.08±0.020	0.06±0.034
Apical Inferior	0.06±0.010	0.05±0.021	0.10±0.031	0.07±0.037
Apical Lateral	0.06±0.010	0.06±0.025	0.08±0.017	0.08±0.037
	Longitudinal			
Basal Anterior	0.06± 0.011	0.06± 0.022	0.09±0.013	0.08±0.031
Basal Septal	0.05± 0.012	0.05± 0.023	0.07±0.019	0.07±0.032
Basal Inferior	0.04± 0.015	0.05± 0.019	0.05±0.018	0.06±0.027
Basal Lateral	0.06± 0.019	0.03± 0.020*	0.09±0.035	0.04±0.022*
Middle Anterior	0.05± 0.004	0.04± 0.023	0.06±0.005	0.04±0.029
Middle Septal	0.05± 0.008	0.04± 0.020	0.07±0.011	0.05±0.023
Middle Inferior	0.04± 0.014	0.04± 0.026	0.05±0.021	0.05±0.026
Middle Lateral	0.04± 0.013	0.04± 0.018	0.05±0.021	0.05±0.021
Apical Anterior	0.04± 0.005	0.05± 0.022	0.07±0.020	0.07±0.032
Apical Septal	0.05± 0.012	0.05± 0.020	0.08±0.021	0.06±0.026
Apical Inferior	0.06± 0.009	0.04± 0.022	0.10±0.029	0.06±0.033*
Apical Lateral	0.05± 0.013	0.06± 0.026	0.07±0.016	0.08±0.036

*: p<0.05 vs. Young

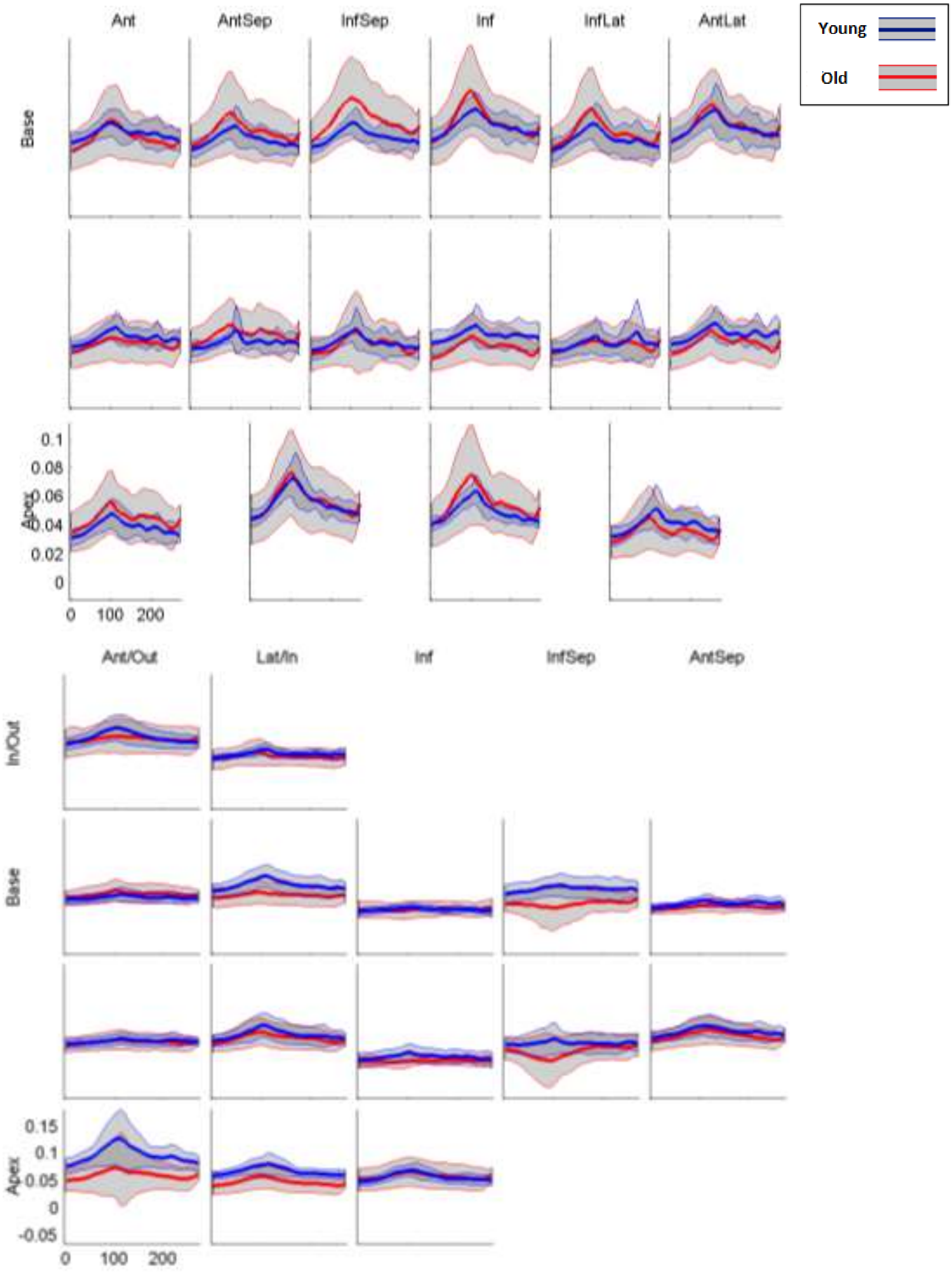

Figure 7.2 Averaged circumferential curvature (1/mm) of LV (top) and RV (bottom), mean±SD

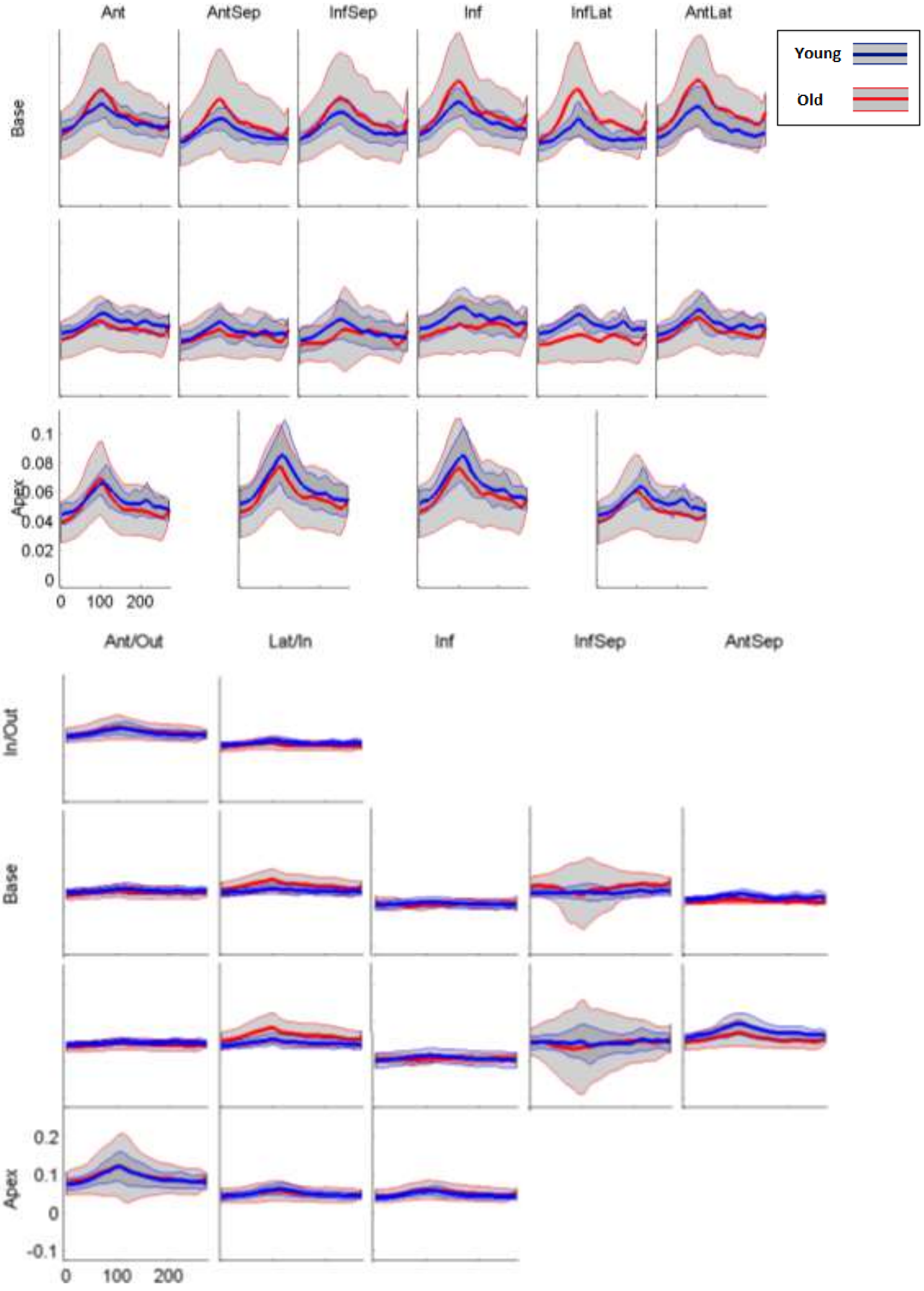

Figure 7.3 Averaged longitudinal curvature (1/mm) of LV (top) and RV (bottom), mean±SD.

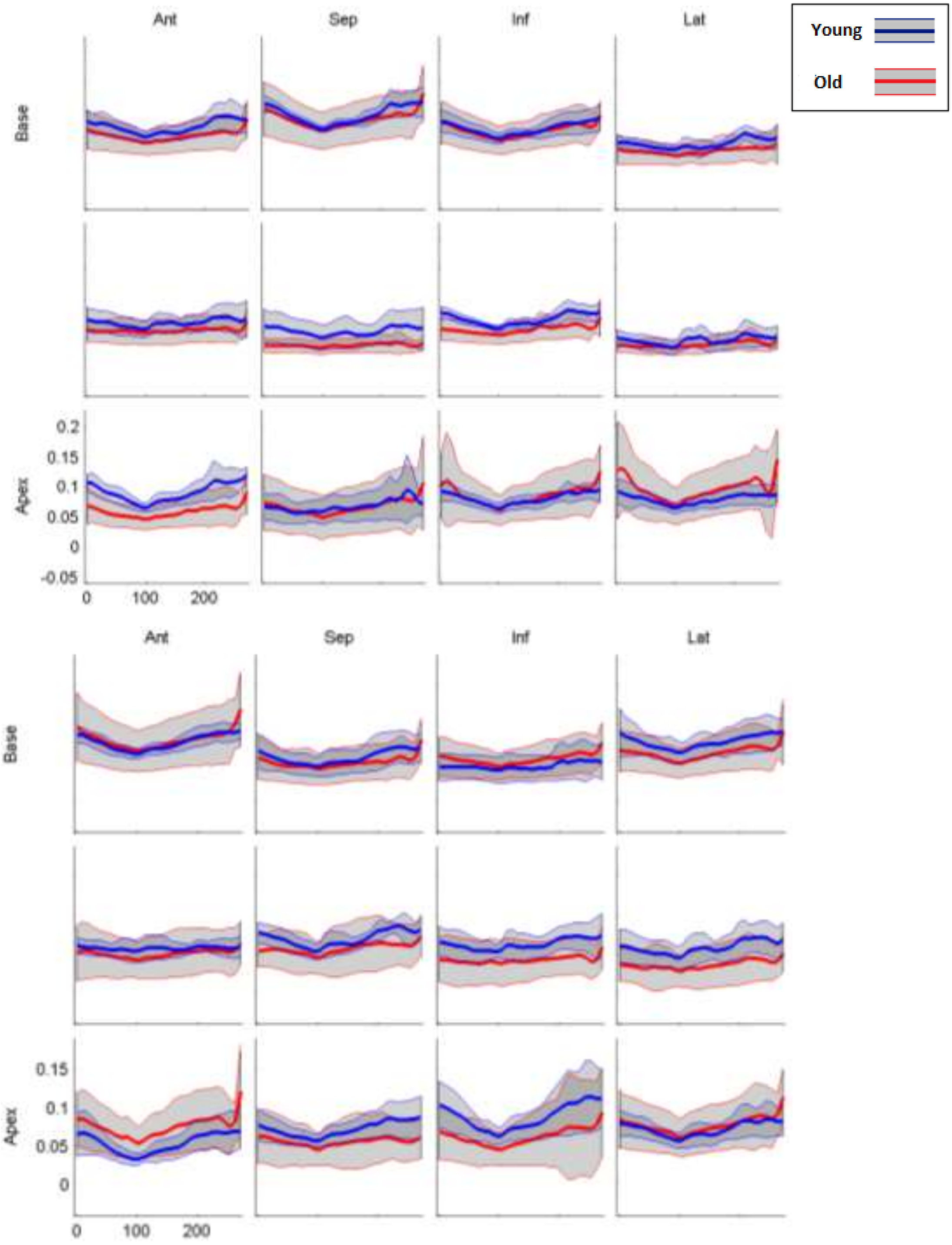

Figure 7.4 Averaged circumferential curvature (1/mm) of LA (top) and RA (bottom), mean±SD.

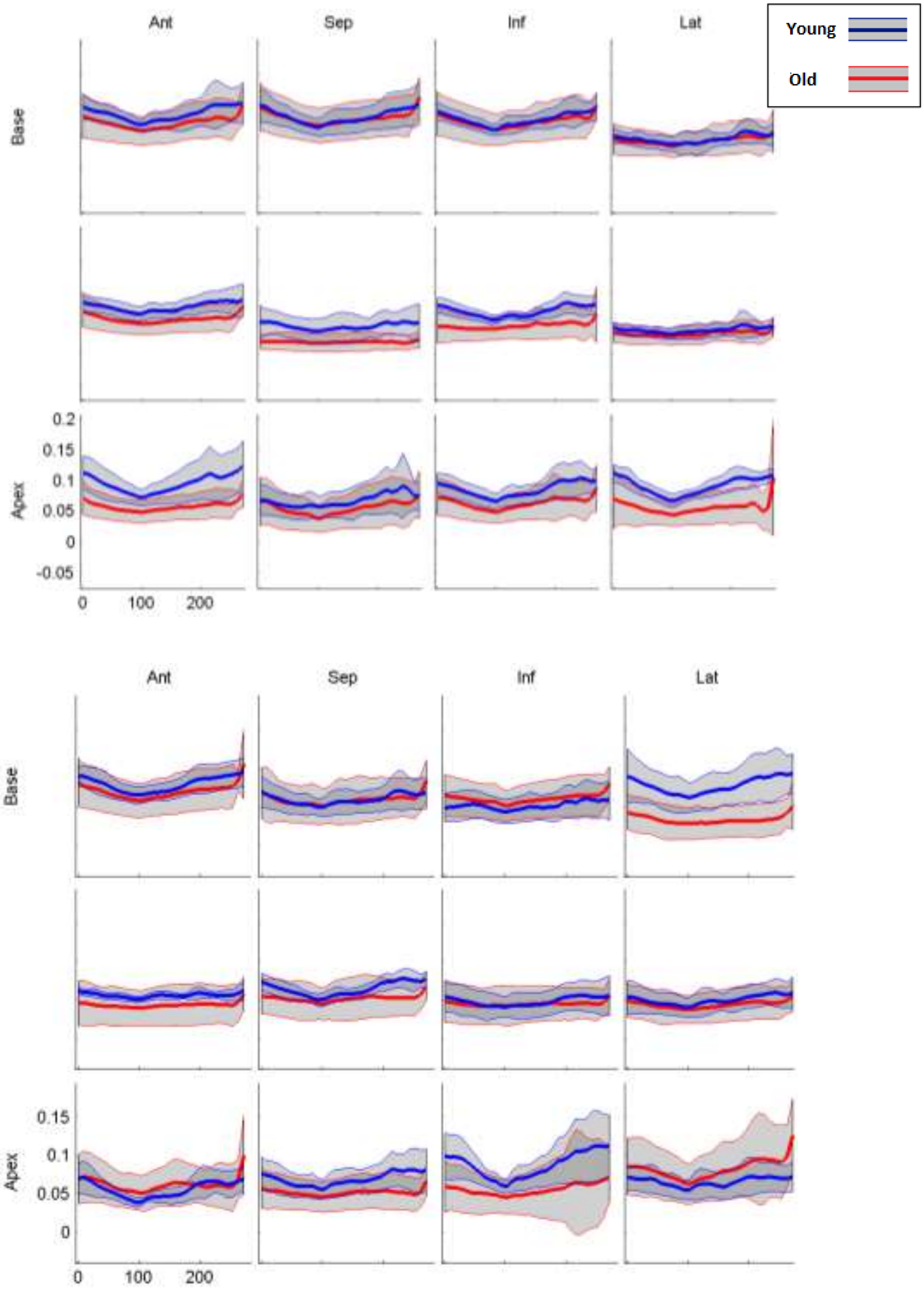

Figure 7.5 Averaged longitudinal curvature (1/mm) of LA (top) and RA (bottom), mean±SD.

7.3.2 Volume Function Analysis

Table 7-6 and Table 7-7 display the statistical summary of the volume parameters of the two groups. LV had a small decrease in the ED and ES volumes in the old group. The stroke volume was preserved while the ejection fraction had a statistically significant increase in the old group. For the RV, it had increased ED and ES volumes without statistical significance. The ejection fraction was slightly decreased while the stroke volume was increased. The LA had increased in the maximum and minimum volumes with statistical significance in the old group. The total ejection volume was increased and ejection fraction was decreased without statistical significance in the old group. RA had an increase in the maximum volume and minimum volume

Table 7-6 Ventricular Volume Function in the young and old normal subjects, mean ± SD

	LV		**RV**	
Parameter	Young	Old	Young	Old
EDV(ml)	146±46.0	131 ±20.0	137±51.0	165 ±48.0
ESV(ml)	60±24.0	44 ±8.0	63±33.0	78 ±52.0
SV(ml)	85±25.0	86 ±15.0	74±20.0	87 ±38.0
EF (%)	59±4.6	66 ±4.0*	56±7.5	54 ±17.0

Volumes and fractions are mean ± SE; BAC: Before Atrial Contraction volume; V: Volume; SV: stroke volume; EF: ejection fraction. *: P<0.05 vs. Young.

Table 7-7 Atrial Volume Function in the young and old normal subjects, mean ± SD

	LA		**RA**	
Parameter	Young	Old	Young	Old
Max V(ml)	51±14.0	70 ±17.0*	61±16.0	83 ±33.0
Min V(ml)	20±8.5	31 ±7.8*	25±10.0	37 ±18.0
BAC V(ml)	32±13.0	48 ±13.0*	35±14.0	53 ±22.0
Pas EV(ml)	19±6.9	23 ±9.3	26±8.0	30 ±14.0
Act EV(ml)	12±5.4	17 ±7.3	10±4.9	16 ±6.0*
Total EV(ml)	31±7.5	39 ±12.0	36±8.0	46 ±18.0
Pas EF (%)	38±12.0	32 ±11.0	44±11.0	36 ±7.9
Act EF (%)	36±10.0	35 ±7.6	28±8.9	31 ±8.2
Total EF (%)	61±9.1	56 ±8.4	60±8.0	56 ±8.2
Con V(ml)	55±19.0	47 ±7.9	38±15.0	41 ±32.0

Volumes and fractions are mean ± SE; BAC: Before Atrial Contraction volume; V: Volume; Pas: Passive; Act: Active; E: Emptying; F: Fraction, Con: conduit. *: P<0.05 vs. Young.

in the old group, but the increase was not statistically significant. The total RA ejection volume increased, while the ejection fraction had a decrease without statistical significance.

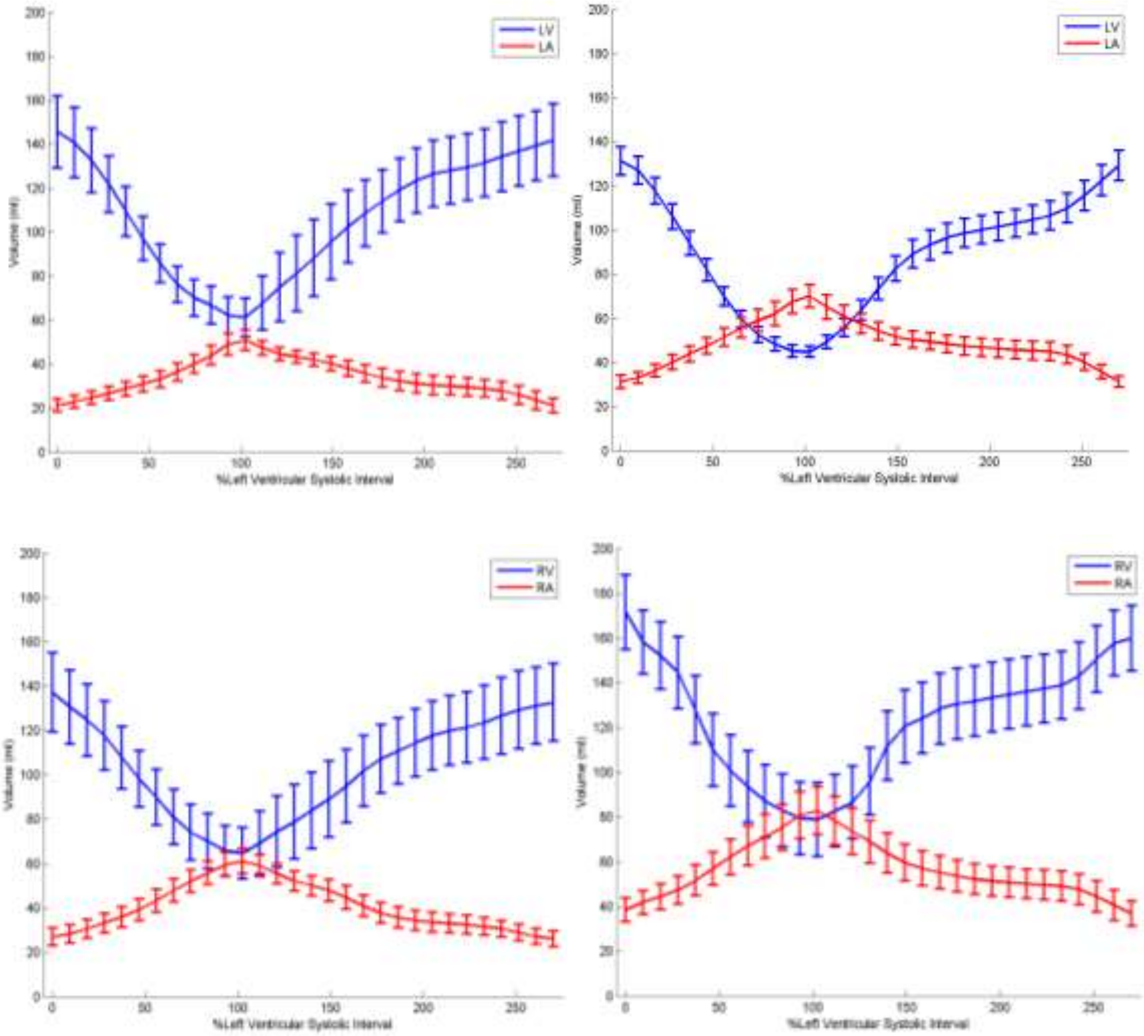

Figure 7.6 Volume time curves in the young healthy (left) group and the old healthy (right) group with the same y-axis range, mean ± SD, ml.

Figure 7.6 displays the volume time curves of all four chambers of the young and the old healthy groups. The mean volume of the left-sided and right-sided heart of the young healthy group was less than 180 ml. The old group had a lower LV volume curve with smaller standard deviation as well. The LA, RA and RV volume time curves were slightly higher in the old group.

From the volume parameters and volume time curves, we can see that LV was the only chamber that showed a decrease in volume for the old group and the epiendocardial contour of LV at LVED was clear to define. Therefore, to futher understand the geometry and volume remodeling of LV, we computed the mass and mass-to-volume ratio of LV at LVED. Table 7-8 showed the summary of the mass and mass-to-volume ratio for the two groups. The mass of LV at LVED decreases without statistical significance, but the mass-to-volume ratio increased in the old group with statistical significance. This statistically increased mass-to-volume ratio of the old group was consistent with prviouse work [145]. Figure 7.7 showed the boxplot of the mass-to-volume ratio of the two groups.

Table 7-8 Statistical summary of LV mass and LV mass to volume ratio of the young and old group and LVED. Mean±SD.

	Young	Old
Mass	66.67 ±26.95	80.32±21.62
Mass to Volume	0.45±0.06	0.61±0.12*

*: P<0.05 vs. Young.

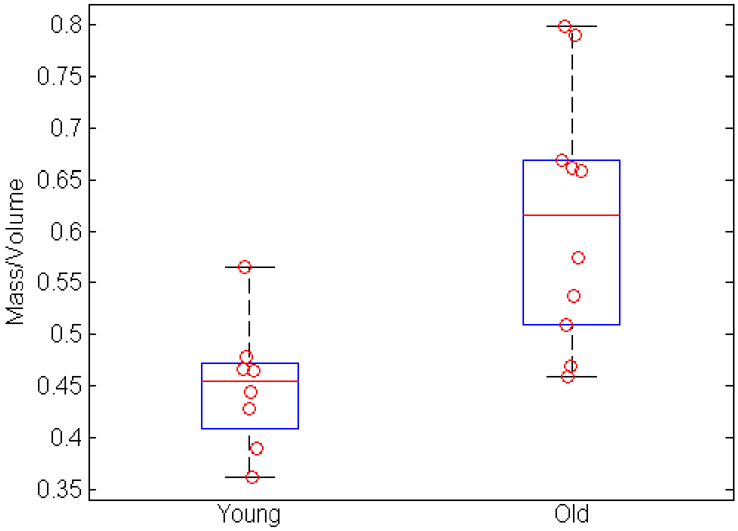

Figure 7.7 Mass-to-volume ratio of LV for the young group and the old group at LVED

In order to understand the mutual relationship among the volumes of all four chambers, we computed the volume ratio between the volumes. Figure 7.8 shows the volume ratios for the two groups. The ratio of LA/LV and RV/LV of the young group was higher than the old group across the whole cardiac cycle. For most phases, the RA/RV was higher too. The ratio of RA/LA was very close with a slight difference for the two groups. The deviation of the RV/LV ratio was much larger in the old group than the young group.

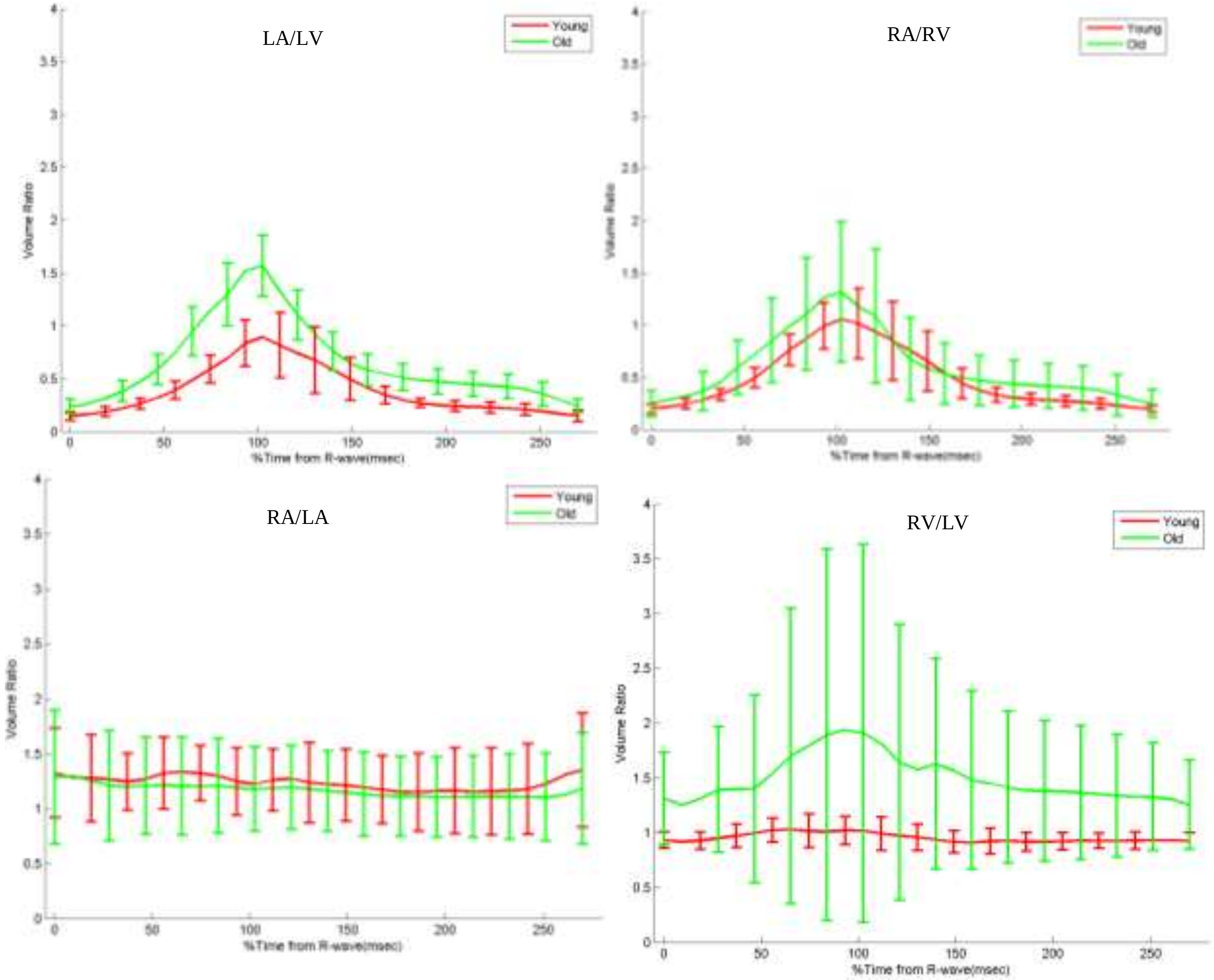

Figure 7.8 Chamber volume ratios of the young (red) and old (green) groups. Mean±SD.

7.3.3 Wall Motion Tracking

Table 7-9 and Table 7-10 display the statistical summary of the displacement in the radial direction for each segment at LVES. From the tables, we can see that only the basal anterior segment of LA, the basal inferior segment of RA and the middle lateral segment of RV showed statistical difference between the young and old groups. Except that, all segments had no statistical difference. Figure 7.9 and Figure 7.10 show the heart motion in the radial direction of

Table 7-9 Ventricular displacement analysis (mm) in healthy subjects at LVES mean ± SD.

	Young	**Old**
	LV	
Basal Anterior	-13.27±2.008	-11.71±4.546
Basal Anteroseptal	-11.07±1.910	-8.61±3.955
Basal Inferoseptal	-9.61±1.794	-7.81±3.373
Basal Inferior	-10.13±1.631	-9.37±3.241
Basal Inferolateral	-11.46±1.785	-11.57±3.757
Basal Anterolateral	-13.11±1.845	-13.04±4.753
Middle Anterior	-8.94±1.103	-8.73±1.826
Middle Anteroseptal	-6.38±1.184	-6.44±1.280
Middle Inferoseptal	-5.36±1.300	-5.84±1.554
Middle Inferior	-6.83±1.155	-7.89±1.921
Middle Inferolateral	-8.48±1.079	-9.93±2.039
Middle Anterolateral	-9.31±1.329	-10.18±1.977
Apical Anterior	-3.88±1.282	-5.66±3.078
Apical Septal	-3.23±2.118	-5.61±3.305
Apical Inferior	-3.78±1.904	-6.40±4.098
Apical Lateral	-4.52±1.014	-6.81±3.977
	RV	
Basal Anterior	-9.26±1.731	-8.83±2.387
Basal Lateral	-11.16±1.272	-11.11±3.099
Basal Inferior	-12.40±1.983	-12.30±2.864
Basal Inferoseptal	-7.33±1.687	-7.06±2.018
Basal Anteroseptal	-4.52±1.237	-4.36±2.010
Basal Anterior	-2.09±2.078	-3.70±1.808
Middle Lateral	-3.18±1.482	-5.32±1.953*
Middle Inferior	-5.71±1.639	-7.10±2.203
Middle Inferoseptal	0.16±1.230	-1.07±2.848
Middle Anterorseptal	4.33±1.884	4.02±3.469
Apical Anterior	2.14±1.279	-0.23±3.222
Apical Inferior	0.04±0.914	-1.89±3.271
Apical Septal	2.54±1.242	0.92±3.729
Outlet	-14.54±1.901	-12.69±3.906
Inlet	-15.32±0.999	-13.84±3.953

*: $P<0.05$ vs. Young.

all four chambers. We can see that, with the exception of a few isolated segment, the displacement in all four chambers between the young and old group were not statistically significant. However, there were some interesting trends. In the LA, most displacement existed in the middle and apical layers for both groups. In addition to that, the young group had slightly larger displacement in the middle and apical segments. In the RA, most displacement happened at the anterior and septal segments in the middle layer and all segments in the apical layers. As in the LA displacement, the young group had slightly larger displacement than the old group in the middle and apical layer. In the LV, all three layers had large displacement and the young group had slightly smaller displacement in the apical layer. In the RV, the anterior and lateral segments

Table 7-10 Atrial displacement (mm) analysis in healthy subjects at LA minimum volume phase, mean ± SD,

	Young	**Old**
	LA	
Basal Anterior	-0.21±1.470	1.32±2.063*
Basal Septal	2.05±1.577	2.44±0.939
Basal Inferior	2.40±1.144	2.14±0.935
Basal Lateral	-0.91±1.116	0.25±1.288
Middle Anterior	2.79±1.779	4.13±2.651
Middle Septal	4.80±1.951	3.87±1.618
Middle Inferior	6.80±1.360	5.54±1.644
Middle Lateral	3.20±1.235	3.80±1.843
Apical Anterior	7.31±2.626	7.29±2.697
Apical Septal	9.10±2.651	7.17±2.223
Apical Inferior	11.13±1.728	8.92±2.574
Apical Lateral	9.93±2.210	9.10±2.838
	RA	
Basal Anterior	1.39±1.476	1.33±2.112
Basal Septal	2.96±1.424	3.08±1.683
Basal Inferior	-2.06±1.002	-0.03±1.625*
Basal Lateral	-5.24±1.059	-4.19±1.665
Middle Anterior	7.10±3.014	5.92±2.861
Middle Septal	10.42±1.766	8.69±2.031
Middle Inferior	2.80±1.392	3.99±2.106
Middle Lateral	-2.68±0.992	-1.53±1.886
Apical Anterior	12.63±3.125	10.42±3.951
Apical Septal	16.01±2.300	13.42±3.820
Apical Inferior	10.74±2.580	10.35±3.079
Apical Lateral	7.73±2.146	6.19±2.619

*: P<0.05 vs. Young.

and the apical segments showed larger displacement than other segments for both groups. The findings from the figures were consistent with displacement parameter comparison in the tables.

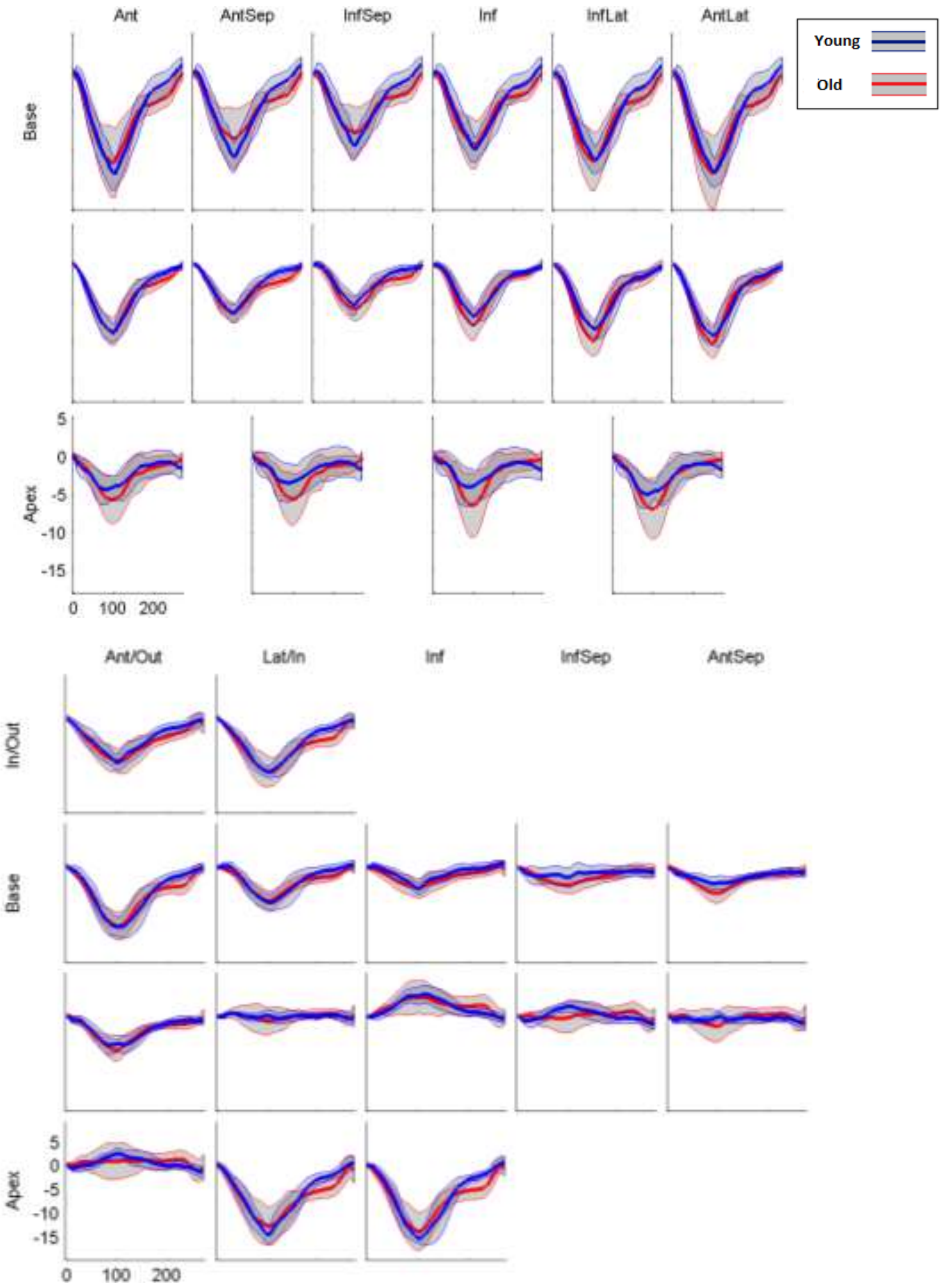

Figure 7.9 Averaged displacement (mm) of LV (top) and RV (bottom), mean±SD

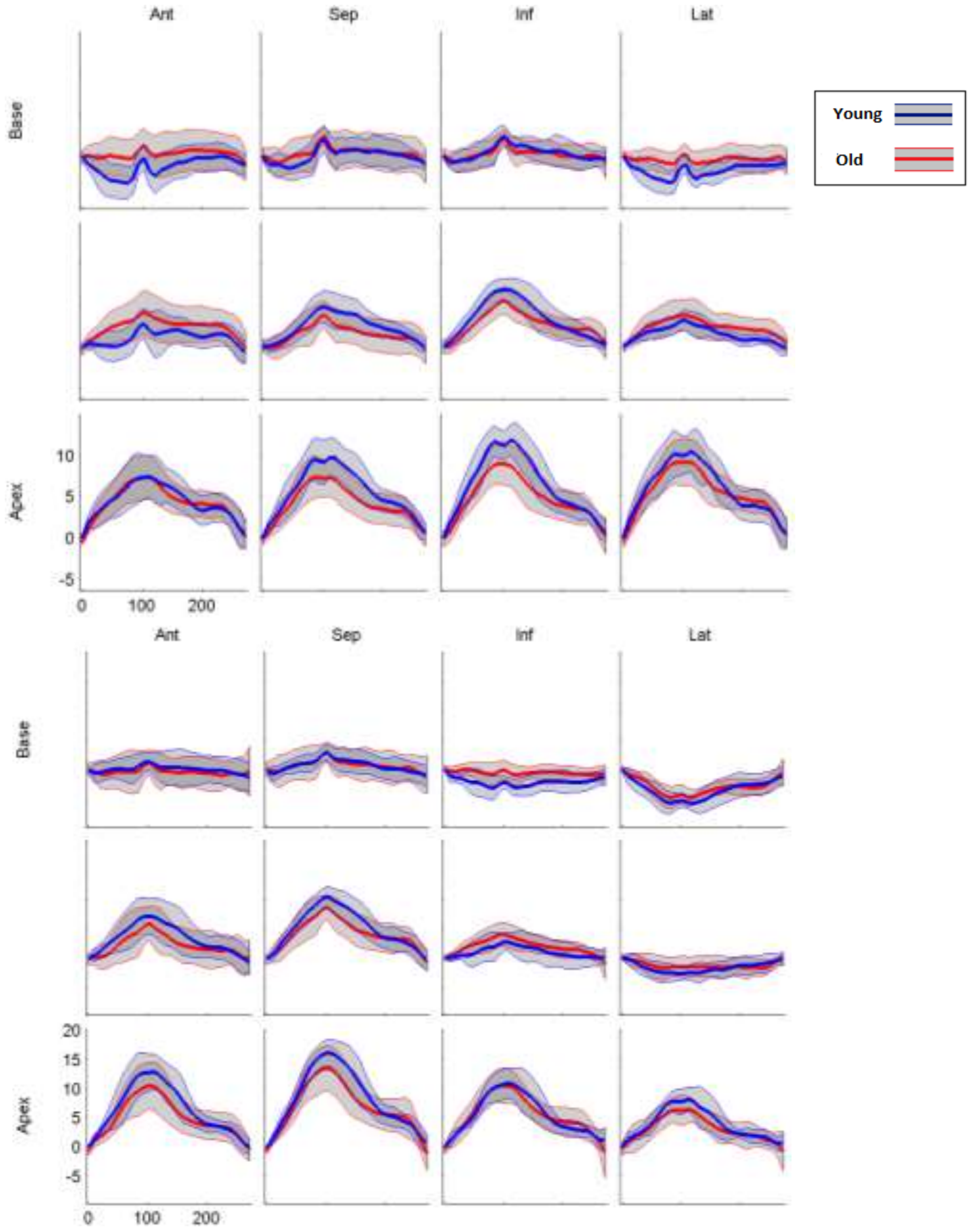

Figure 7.10 Averaged displacement (mm) of LA (top) and RA (bottom), mean±SD

7.3.4 Strain Analysis

For the strain computation, the largest volume phase was used as the reference timeframe, which was LVED for ventricles and LA maximum volume phase for atria. Table 7-11 and Table 7-12 show the statistical summary of the principal minimum strain of the two groups near the corresponded minimum volume phase, which was LVES for ventricles, and LA minimum phase (near LVED) for atria. For the LV, all segments had statistical difference. For the RV, most segments of the three layers had statistical difference. The statistical difference of

Table 7-11 Ventricular minimum strain analysis in the young and old normal subject at LVES.

	Young	**Old**
	LV	
Basal Anterior	-0.29±0.022	-0.24±0.026*
Basal Anteroseptal	-0.28±0.021	-0.23±0.029*
Basal Inferoseptal	-0.29±0.027	-0.24±0.025*
Basal Inferior	-0.29±0.019	-0.25±0.035*
Basal Inferolateral	-0.29±0.022	-0.24±0.039*
Basal Anterolateral	-0.30±0.027	-0.25±0.023*
Middle Anterior	-0.29±0.025	-0.23±0.035*
Middle Anteroseptal	-0.29±0.029	-0.25±0.025*
Middle Inferoseptal	-0.30±0.028	-0.25±0.028*
Middle Inferior	-0.29±0.024	-0.25±0.023*
Middle Inferolateral	-0.28±0.026	-0.24±0.024*
Middle Anterolateral	-0.29±0.030	-0.24±0.020*
Apical Anterior	-0.28±0.022	-0.22±0.021*
Apical Septal	-0.29±0.023	-0.23±0.020*
Apical Inferior	-0.28±0.014	-0.24±0.022*
Apical Lateral	-0.29±0.024	-0.22±0.033*
	RV	
Basal Anterior	-0.33±0.042	-0.24±0.075*
Basal Lateral	-0.26±0.047	-0.26±0.053
Basal Inferior	-0.30±0.041	-0.29±0.043
Basal Inferoseptal	-0.27±0.068	-0.17±0.041*
Basal Anteroseptal	-0.24±0.050	-0.22±0.057
Middle Anterior	-0.25±0.045	-0.29±0.030*
Middle Lateral	-0.15±0.038	-0.16±0.052
Middle Inferior	-0.26±0.036	-0.26±0.044
Middle Inferoseptal	-0.33±0.020	-0.23±0.046*
Middle Anterorseptal	-0.29±0.038	-0.21±0.035*
Apical Anterior	-0.28±0.072	-0.29±0.032
Apical Inferior	-0.32±0.065	-0.29±0.044
Apical Septal	-0.35±0.055	-0.30±0.024*
Outlet	-0.04±0.017	-0.08±0.025*
Inlet	-0.09±0.024	-0.10±0.015

*: P<0.05 vs. Young.

LA strain occurred at middle and apical layers. For the RA, statistical difference occurred at several segments in all three layers.

Table 7-12 Atrial minimum strain analysis in the young and old normal subject at LA minimum volume phase (near LVED)

	Young	**Old**
	LA	
Basal Anterior	-0.09±0.048	-0.09±0.034
Basal Septal	-0.16±0.049	-0.15±0.013
Basal Inferior	-0.07±0.044	-0.09±0.036
Basal Lateral	-0.10±0.041	-0.13±0.051
Middle Anterior	-0.23±0.040	-0.21±0.035
Middle Septal	-0.26±0.094	-0.21±0.044
Middle Inferior	-0.29±0.044	-0.20±0.043*
Middle Lateral	-0.12±0.020	-0.13±0.030
Apical Anterior	-0.28±0.045	-0.27±0.042
Apical Septal	-0.20±0.049	-0.24±0.033
Apical Inferior	-0.32±0.046	-0.27±0.027*
Apical Lateral	-0.30±0.042	-0.25±0.032*
	RA	
Basal Anterior	-0.08±0.037	-0.14±0.037*
Basal Septal	-0.05±0.031	-0.13±0.034*
Basal Inferior	-0.09±0.063	-0.10±0.037
Basal Lateral	-0.09±0.033	-0.12±0.026*
Middle Anterior	-0.29±0.082	-0.28±0.050
Middle Septal	-0.26±0.058	-0.24±0.045
Middle Inferior	-0.15±0.102	-0.18±0.062
Middle Lateral	-0.21±0.053	-0.15±0.029*
Apical Anterior	-0.25±0.043	-0.29±0.023*
Apical Septal	-0.26±0.055	-0.29±0.030
Apical Inferior	-0.30±0.053	-0.29±0.010
Apical Lateral	-0.30±0.043	-0.26±0.029*

*: $P<0.05$ vs. Young.

Figure 7.11 and Figure 7.12 showed the curvature time curves of all four chambers. The negative strain indicates the contraction and positive indicates dilation. In the computation, since the largest volume was used as reference, then the strain should theoretically be negative or close to 0. We can see that both groups had very similar strain curves in all four chambers. LA strain of the old group as slightly larger for most segments, which was the same as in the RA. But the difference between the two groups was larger in the RA. For the LV, the strain of the old group was slightly larger for most segments in the basal and middle layers. For the RV, the curves of the two group were very close.

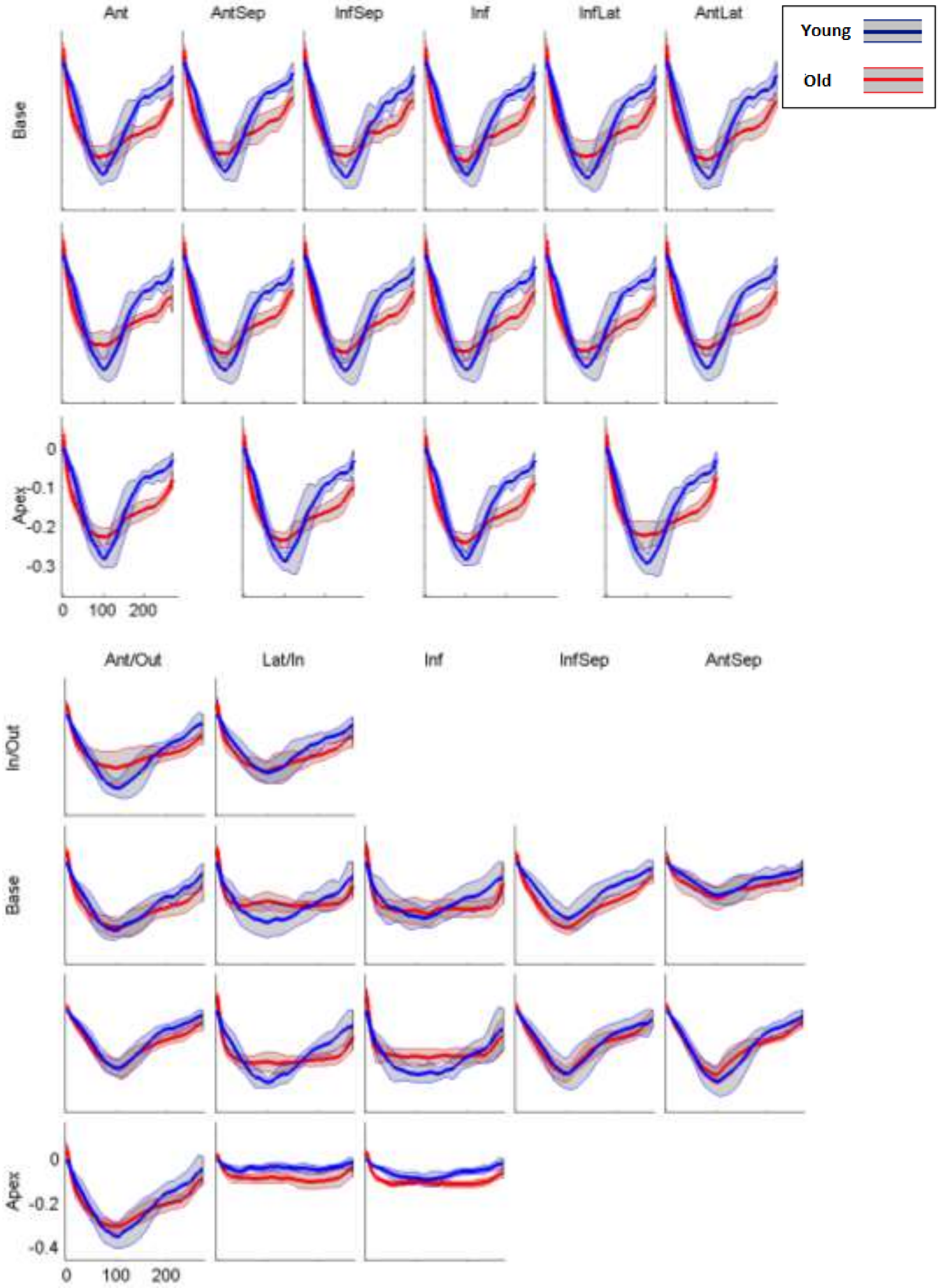

Figure 7.11 Averaged principal minimum strain of LV (top) and RV (bottom), mean±SD, 1/mm.

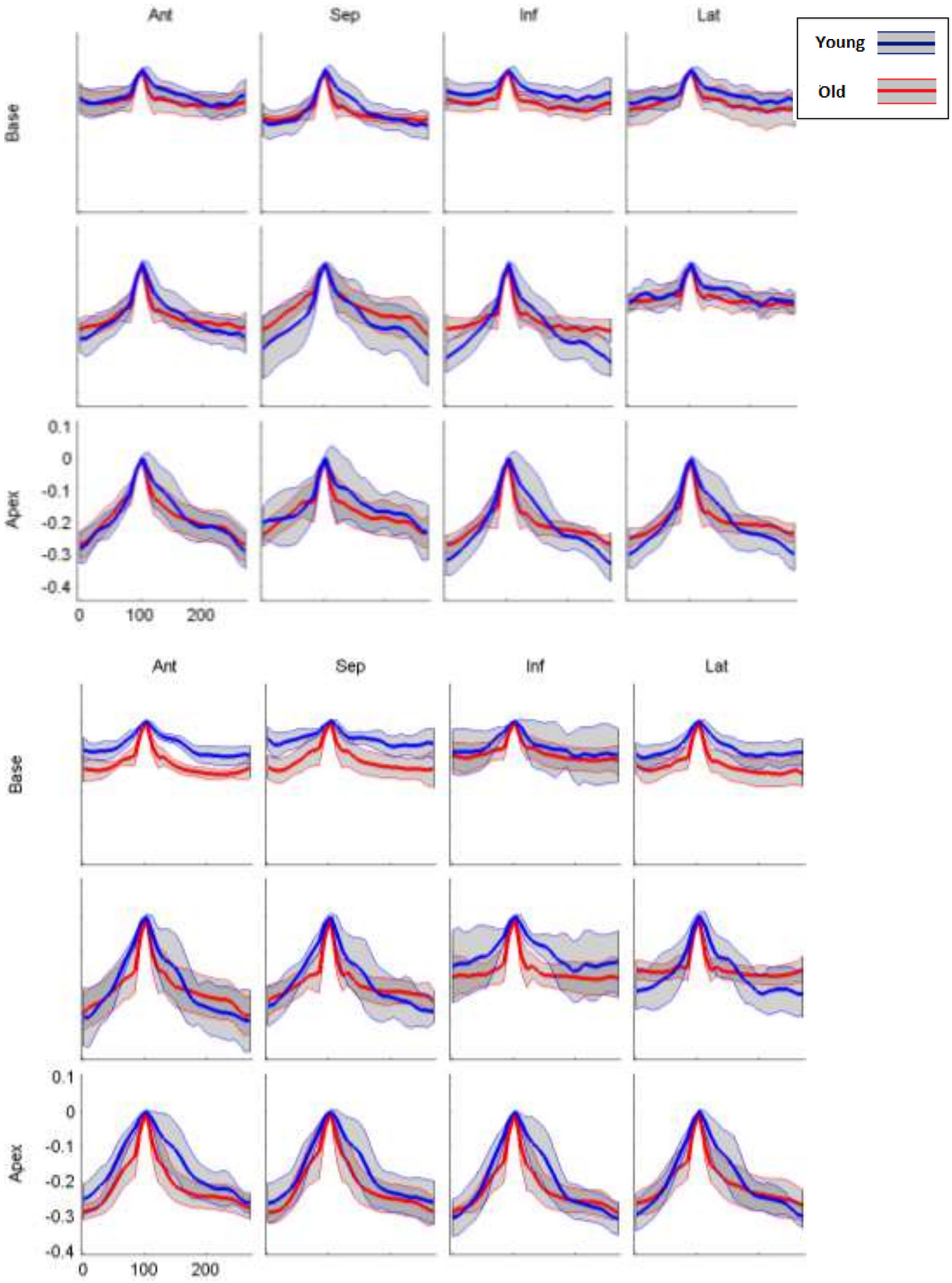

Figure 7.12 Averaged principal minimum strain of LA (top) and RA(bottom), mean±SD, 1/mm.

7.4 Discussion and Conclusion

This work represents the first study to combine the 3D geometries and wall motions with volume functions for all four chambers versus age across a whole cardiac cycle from cine MRI data. We characterized the continuous volume functions, geometries and mechanics of the young and old healthy subjects. In the same time, we explored age-associated differences in structures and functions of all four chambers.

Currently, for atrial geometry analysis, it is always limited to the linear dimension or area computed from four-chamber or two-chamber views. From those long axis views, longitudinal diameter is obtained by the distance between the posterior wall of the RA/LA to the center of the TV/MV plane, and the transverse diameter is obtained by the distance between the lateral RA/LA wall and interatrial septum at the mid-atrial level [69-70]. Figure 7.15 shows the dimensions and area measurements of RA from the long axis views. LA dimension measured form long axis views has been used extensively in clinical practice and research. However, as mentioned before, those long axes views have disadvantage with angle-dependency and it has become clear that it may not represent an accurate picture of atrial size [69]. In this study, instead of computing the linear dimension or surface area from one single slice, we computed the surface area by summing up the triangle areas on the mesh. By computing this way, the area reflected the 3D size character of the chamber without the angle dependency. Moreover, we reported volumes by summing up the tetrahedron volumes formed by the triangles on the mesh for all four chambers. By computing in this way, the 3D geometry of the chamber was considered in the volume computation. Therefore, it also reflected the 3D geometry and showed potential in better understanding of the chamber geometry.

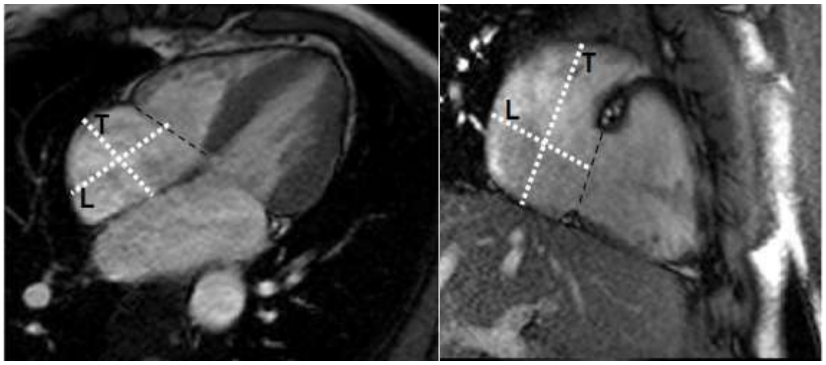

Figure 7.13 Linear dimension of RA. Left: apical 4-chamber view. Right: apical right 2-chamber view. L: longitudinal diameter; T: transverse diameter. Image source [69].

From this study, we found that age is associated with remodeling in geometries and volume functions of all four chambers. In the old group, without any pathology conditions, we found LA developed significant enlargement and decreased LA ejection fraction, which was consistent with previous work. In [149], the author reported that aging was associated with increased LA volume and decreased LA function. In our findings, the LA enlargement consisted of being lengthened and rounded. The LA functions had a decrease in ejection fraction and an increase in total ejection volume associated with aging. LV had a slight decrease in the size and volume but increased mass to volume ratio, consistent with age-related remodeling [148] [150] [151]. In our study, we confirmed prior suggestion [148] [150] that the mass to volume ratio increase is also driven by the decrease in the LV volumes. RA and RV developed a small amount of enlargement with aging. RA showed the same increase in ejection volume and decrease in ejection fraction as in the LA. RV showed a small increase in stroke volume, while a slight decrease in ejection fraction with age. For the right-sided of heart, there is few study reports the geometry and function remodeling with aging.

Besides the size and volume functions, we also explored methods to analyze the regional mechanics of the myocardial walls from cine MRI data. In which, we found the regional motion had no age-associated effect, while the strain was decreasing in magnitude in the contraction direction with aging. The decrease of strain magnitude was due to the enlargement of the chambers with preserved myocardial wall displacement. Our finding was consistent in [152] with speckle-tracking in terms of age-dependency in the LV strain. Therefore, the proposed method on strain measurement from cine MRI data has the potential to estimate the atrial mechanics and explore the age-dependency effects in the future. In addition to the remodeling of each chamber separately, we explored the age-dependency in mutual relationship by computing the volume ratios, which showed decrease in the LA/LV, RV/LV and RA/RV ratios with aging. It is noted that in the motion measurement, we were not marking the cardiac tissue in the imaging, but deform a vertex from a time-adjacent surface based on contour points. By deforming this way, we can’t guarantee the correspondence on the tissue, but it is close to true vertex. Considering the thin wall and complex geometry of both atrial and RV, this is a simple but efficient way to measure motion within reasonable error.

As a conclusion of this study, we summarize that we provided comprehensive analysis on geometry, volume functions and mechanism of heart on the young and old healthy subjects. The proposed methods in continuous atrial volume measurement and mechanism analysis from cine MRI data has the potential in clinical environment. The age-associated findings in mechanism, volume function and chamber size and with volume ratios are from a relatively small study size, which may make generalization of the inference of this study less compelling but may provide a basis For the larger study, especially for those uncommonly computed parameters.

Chapter 8 FUNCTIONAL AND MECHANICAL REMODELING IN SEVERE ISOLATED MITRAL REGURGITATION WITH PRESERVED LEFT VENTRICULAR EJECTION FRACTION PRE- AND POST-SURGERY

In this study, we compared volumes, curvatures, displacements and strains in severe mitral regurgitation patients with preserved left ventricular ejection fraction with age-matched controls to evaluate atrial and ventricular remodeling, changes in function and mechanics, and the link between the four heart chambers. We also explored the effect of mitral valve surgery on the heart by performing a similar comparison between patients at baseline and six-month after surgery. The abstract of this work was presented at ISMRM 2017 [5].

8.1 Introduction

Mitral regurgitation (MR) is the most frequent form of valvular disease, and its prevalence increases with age [2] [97]. Isolated MR from myxomatous degeneration of the mitral valve represents a low-pressure volume overload because excess volume is ejected into the low-pressure left atrium. Thus, the decrease in forward cardiac output in MR is compensated by an increase in left ventricular (LV) stroke volume that is mediated by augmentation of LV preload (end-diastolic volume) and an increase in adrenergic drive. These compensatory mechanisms preserve LV ejection fraction (EF), even in the face of increasing LV end-systolic (ES) dimension (D)/volume over time. Correct identification of surgical candidates and optimizing the timing of surgery are key in patient management. The most common guidelines recommend surgical intervention when LVEF < 60% and/or an LV end-systolic dimension > 40 mm [22]. However, despite LVEF >60% prior to surgery, post-operative LV dysfunction is common and is associated with increased morbidity and mortality [99]. Moreover, there are studies reporting that patients with MR are not receiving timely surgery due to the subtle symptoms of heart failure [100]. In [96], the data showed that worse outcomes may result from waiting 2 or more months after development of symptoms or achievement of accepted guidelines (LVEF<60% and/or LV end-systolic dimension >40 mm). As a result, the 2017 AHA/ACC update of 2014 AHA/ACC valvular heart disease guidelines state that MV surgery is reasonable for patients with chronic severe MR with preserved LV function (LVEF>60% and LVESD<40 mm) [22]. Therefore, the challenge of surgery lies in the timing of surgery between early surgery and delayed intervention.

Besides enlargement and remodeling of the LV, LA enlarges as MR proceeds and the enlargement may contribute to the development of MR as well [97] [113]. LA volume at diagnosis predicts long-term outcome [2] and LA remodeling is proved to be a pivotal in guiding patient-tailored therapy and improve their survival in MR patients [113]. Previous studies have demonstrated the prognostic importance of LA size in isolated MR. However, the combination between the LA size and mechanics have not been studied. Current research is “LV centric,” though the circulatory system is closed, and all four chambers are interdependent. In particular, the role of RA size and mechanics related to MR has not been well studied [154].

Therefore, to find additional parameters for surgery guidelines, we conducted a comprehensive analysis on the LA, RA, RV and LV to explore the mutual relationship and the MR-associated remodeling in the 4-chambers. We also conducted a similar analysis to explore the effect of mitral valve (MV) surgery with the purpose of further understanding MR-associated remodeling.

8.2 Methods

8.2.1 Study Population

Sixteen patients (n=16, mean age: 61.1±11.9 years; range: 38-82 years) with severe isolated mitral regurgitation secondary to degenerative mitral valve disease were recruited from 2016 to 2017 at the University of Alabama at Birmingham and were referred for corrective mitral valve surgery. Patients were excluded who had evidence of aortic valve disease, coronary artery disease or concomitant mitral stenosis. All patients underwent cine MRI before surgery. Among those patients who had surgery, only 6 datasets (n = 6, mean age, 61.2±9.8 years; range, 50-74 years) of 6-month post-surgery patients were available at the date this dissertation was submitted. Eleven age-matched normal subjects (n=11, mean age, 61±6 years; range, 59-67 years) without clinical or anatomical evidence of cardiovascular disease were recruited as the control group. All age-matched control underwent cine MRI with the same protocol as the patient group. The study protocol was approved by the Institutional Review Boards of University of Alabama at Birmingham and Auburn University. All participants gave written informed content.

For clarification, in this chapter, the MR patient group (n=16) refers to all the sixteen patients, the post-surgery group (n=6) refers to the six datasets of the 6-month follow-ups and the pre-surgery group 9 (n=6) refers to the same patients in the post-surgery group before the surgery.

8.2.2 Surgery

MV repair was performed through a median ternotomy and employed standard hypothermic cardiopulmonary bypass and cold blood cardioplegia. A variety of methods were used to repair the MV including leaflet resection, chordal replacement, or a combination of each, and these patients had implantation of a flexible annuloplasty ring. The adequacy of repair was assessed by intraoperative transesophageal echocardiography.

8.2.3 Image Acquisition and Processing

MRI was performed on a 1.5-T MRI scanner (Signa GE Healthcare, Milwaukee, Wisconsin) optimized for cardiac imaging. The same standard MRI protocols with the additional two orientations described in Section 3.4 were used. The protocols were summarized as: Electrocardiographically gated breath-hold SSFP technique was used to obtain standard two-chamber, four-chamber and short axis views, and an extra right two-chamber and atrial short axis views covering the whole left and right atria using the following parameters: slice thickness of the imaging planes 8 mm, 20 phases, scan matrix 256 × 256, flip angle 45°, repetition/echo times 3.8/1.6 ms).

Endocardial contours of both atria were contoured and tracked in atrial short axis, short axis, two-chamber, four-chamber and right two-chamber views using a semi-auto method on a house-built software SMC [77]. In those long axis views, landmarks of MV and TV were also defined and tracked. All propagated landmarks and contours were double checked from different views and were corrected as needed by experienced personnel on a personal computer. From the contours and valve landmarks, surfaces of both atria were reconstructed from endocardial contours by using the surface fitting algorithm described in Chapter 3.

8.2.4 Parameter Computation

For the volume parameters, we followed the same parameters defined in Section 4.1. With the one-to-one vertex correspondence of the reconstructed surfaces, the curvatures, regional wall motion and strains of the endocardial wall can be estimated based on the segment models defined in Section 5.1. The longitudinal and circumferential curvatures were calculated using the definition described in Section 5.2. The strain was computed using the definition described in Section 6.2 and the largest volume phase was used as reference, which was LVED for ventricles and LA maximum volume phase for atria. In the displacement calculation of each vertex at LVES, the first timeframe was used as reference. In the volume computation, all volume related parameters were

8.2.5 Statistical Analysis

The Student 2-sample t test for continuous variables was conducted to compare the control group (n=11) and the MR group (n = 16) in terms of geometric, volumetric and mechanical variables. Comparisons of the MRI variables among control subjects and MR patients before and 6 months after surgery were performed with 2-way ANOVA with repeated measures followed by group comparison. For the post-surgery group, we only had 6 datasets available, therefore, in this comparison, only the pre-surgery datasets of the same patients were used. All data are presented as mean ± one standard deviation. A P value less than 0.05 was considered statistically significant. All statistical analyses were performed with R version 3.4.3.

8.3 Results

8.3.1 Volume Function Analysis

Table 8-1 and Table 8-2 display a statistical summary of the volumes in each chamber for the two groups. The LVED and LVES volumes have increased significantly in the MR patient

Table 8-1 Ventricular volume function analysis, Control vs. MR

	LV		**RV**	
Parameter	Control (n=11)	MR (n=16)	Control (n=11)	MR (n=16)
EDVI(ml/cm^2)	73±10.0	107±26.0*	90±18.0	83±21.0
ESVI(ml/cm^2)	25±4.4	46±15.0*	42±22.0	44±11.0
SVI(ml/cm^2)	48±7.2	61±13.0*	48±20.0	38±12.0
EF (%)	66±4.0	58±6.7*	54±17.0	46±6.4

Mean ± SD; V: Volume; SV: stroke volume; EF: ejection fraction. *: P<0.05 vs. controls;

group with a significant decrease in EF. The EF, however, was still within the normal range (55% to 70% [22]). For the RV, there was a slight decrease at the EDV, a slight increase in the ESV, and a slight decrease in EF. However, none of those changes in the RV were statistically significant. For the LA, the volumes and EFs all significantly increase, with the exception of the ejection volumes, which are not significantly different. In the RA, statistical significance was only observed in the passive EF.

Table 8-2 Atrial volume function analysis, Control vs. MR

Parameter	LA		RA	
	Control (n=11)	MR (n=16)	Control (n=11)	MR (n=16)
Max VI(ml/cm^2)	39±9.4	72±32.0*	47±19.0	50±18.0
Min VI(ml/cm^2)	17±4.8	45±24.0*	21±9.7	27±16.0
BAC VI(ml/cm^2)	26±6.8	58±27.0*	29±12.0	36±14.0
Pas EVI(ml/cm^2)	13±5.6	14±7.8	17±8.1	14±6.5
Act EVI(ml/cm^2)	9±3.5	13±5.6	9±3.5	9±4.2
Total EVI(ml/cm^2)	22±6.7	28±11.0	26±11.0	23±6.2
Pas EF (%)	32±11.0	21±7.8*	36±7.9	28±9.2*
Act EF (%)	35±7.6	25±9.4*	31±8.2	29±15.0
Total EF (%)	56±8.4	40±9.3*	56±8.2	49±13.0
Con VI(ml/cm^2)	26±3.4	34±11.0	22±16.0	15±7.0

Mean ± SD; BAC: Before Atrial Contraction volume; V: Volume; I: Index; Pas: Passive; Act: Active; E: Emptying; F: Fraction, Con: conduit. *: $P<0.05$ vs. controls.

Figure 8.1 shows the-volume-difference and-volume-difference-percentage time curves between the control group (n =11) and the MR patient group (n=16). The mean volume difference in the left-sided heart was much higher than the right-sided. The enlargement of LV and LA in the MR patients were between 40 to 82 ml, and 20 ml in the RA. On the contrary, the RV difference between the two groups was not consistent across the cardiac cycle. RV volume of the MR group was larger during the contraction while smaller during diastole. From the mean-volume-difference-percentage time curves, we can see that, the percentage increase of LA was higher than 100%, LV is between 50% to 120%, RA was between 0% to 50%.

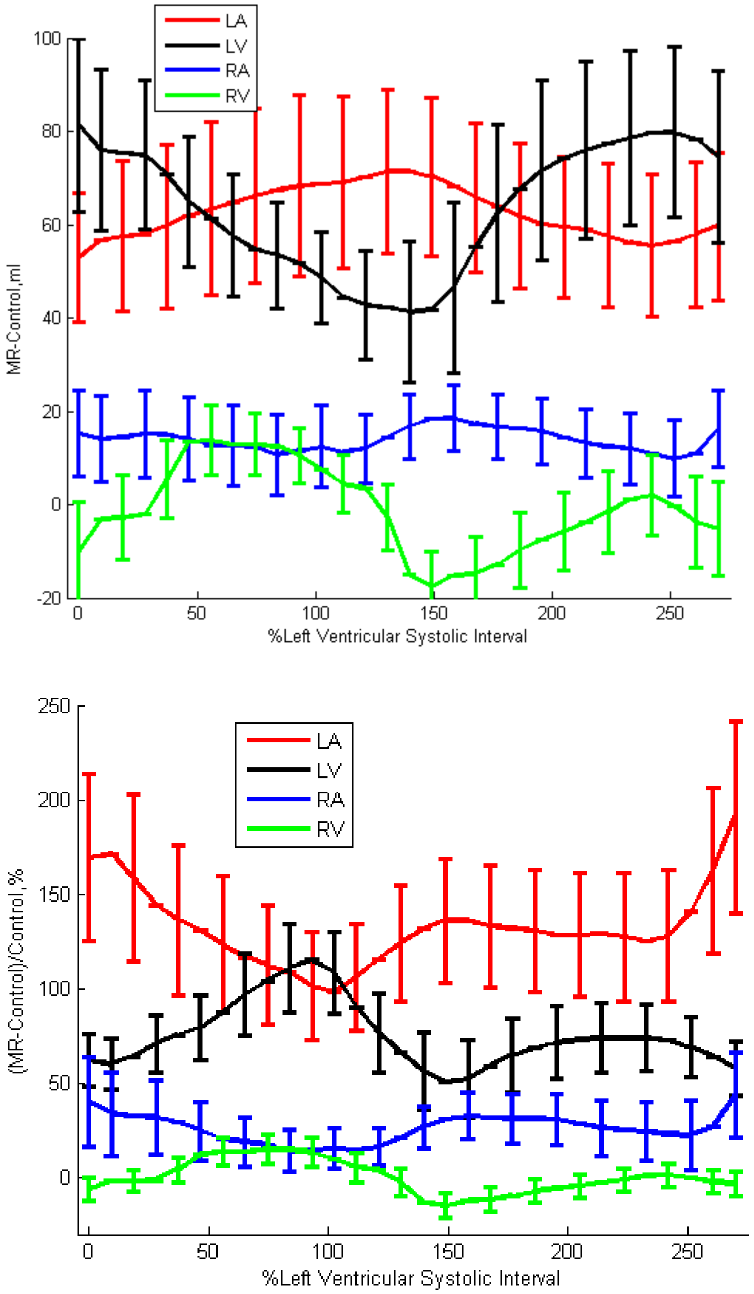

Figure 8.1 Volume-difference (top) and Volume-difference-percentage (bottom) time curves in the MR group compared to the age-matched control group. Mean±SE.

Tables 8-3 to 8-4 show a statistical summary of volumes in the control group (n=11), the pre-surgery group (n=6), and 6 months post-surgery group (n=6). We observed no significant changes in ventricular function between the pre-surgery and post-surgery group. In the LV, no parameters were significantly changed after surgery compared to the pre-surgery group. The LV EDV normalized post-surgery. This decrease, accompanied with a smaller decrease in the LV ESV, resulted in a decrease in stroke volume, which was consistent with previous work [108], the decrease in EF after surgery was not significant, and it remained lower than the control group. In the RV, no volume parameters were significantly different from the control and pre-surgery groups. In the atrial function analysis, both atria had changes after surgery. In the LA, only the active ejection volume had a significant decrease after surgery relative to the pre-

Table 8-3 Atrial volume function parameters analysis on surgical MR patients.

Parameter	LV Control (n=11)	LV Pre (n=6)	LV Post (n=6)	RV Control (n=11)	RV Pre (n=6)	RV Post (n=6)
EDVI(ml/cm^2)	73±10.0	96±33.0	82±15.0	90±18.0	74±24.0	72±8.6
ESVI(ml/cm^2)	25±4.4	39±15.0*	40±11.0*	42±22.0	39±11.0	40±7.5
SVI(ml/cm^2)	48±7.2	57±20.0	42±7.7	48±20.0	35±15.0	31±4.4
EF (%)	66±4.0	59±8.9	52±7.2*	54±17.0	47±5.7	44±5.4

Mean ± SD; V: Volume; SV: stroke volume; EF: ejection fraction. I:index; * $P<0.05$ vs. Control; †: $P <0.05$ vs. Pre.

Table 8-3 Ventricular volume function parameters analysis on surgical MR patients

Parameter	LA Control (n=11)	LA Pre (n=6)	LA Post (n=6)	RA Control (n=11)	RA Pre (n=6)	RA Post (n=6)
Max VI(ml/cm^2)	39±9.4	57±21.0*	50±19.0	47±19.0	46±18.0	46±13.0
Min VI(ml/cm^2)	17±4.8	36±17.0*	34±20.0*	21±9.7	22±10.0	31±12.0†
BAC VI(ml/cm^2)	26±6.8	48±18.0*	40±18.0	29±12.0	34±8.3	35±12.0
Pas EVI(ml/cm^2)	13±5.6	9±3.4	10±3.1	17±8.1	12±11.0	11±4.6
Act EVI(ml/cm^2)	9±3.5	12±5.1	6±2.6†	9±3.5	12±5.0	4±1.5*†
Total EVI(ml/cm^2)	22±6.7	21±5.9	16±3.7	26±11.0	24±9.2	15±3.5
Pas EF (%)	32±11.0	16±3.2*	21±6.7	36±7.9	24±10.0*	25±9.3*
Act EF (%)	35±7.6	27±12.0	17±12.0*	31±8.2	36±16.0	12±6.2*†
Total EF (%)	56±8.4	39±9.3*	34±13.0*	56±8.2	52±7.4	34±8.9*
Con VI(ml/cm^2)	26±3.4	36±16.0	27±4.0	22±16.0	11±5.7	16±1.9

Mean ± SD; BAC: Before Atrial Contraction volume; V: Volume; Pas: Passive; Act: Active; E: Emptying; F: Fraction, Con: conduit. * $P<0.05$ vs. Control; †: $P <0.05$ vs. Pre.

surgery group. Most parameters, including maximum and minimum volumes, tended to return to the control group. In the RA, the active ejection volume and active EF had statistically significant changes compared to the pre-surgery group

Figure 8.2 shows the volume time curves of each chamber for the control group (n = 11), MR patient group (n =16) and post-surgery MR patient group (n =6). The LA and LV had enlargement across the whole cardiac cycle in the MR patient group, which were consistent with previous studies [5]. We also observed increased variability in the LV and LA curves in MR patients relative to controls, which indicated the large variability in the LV and LA enlargement. For the RA, we observed consistent increase of the MR patient group relative to the control group, though no statistically significance in volume values were observed as displayed in Table 8-2. After surgery, the RA, LA and LV volume time curves were returning to the control group.

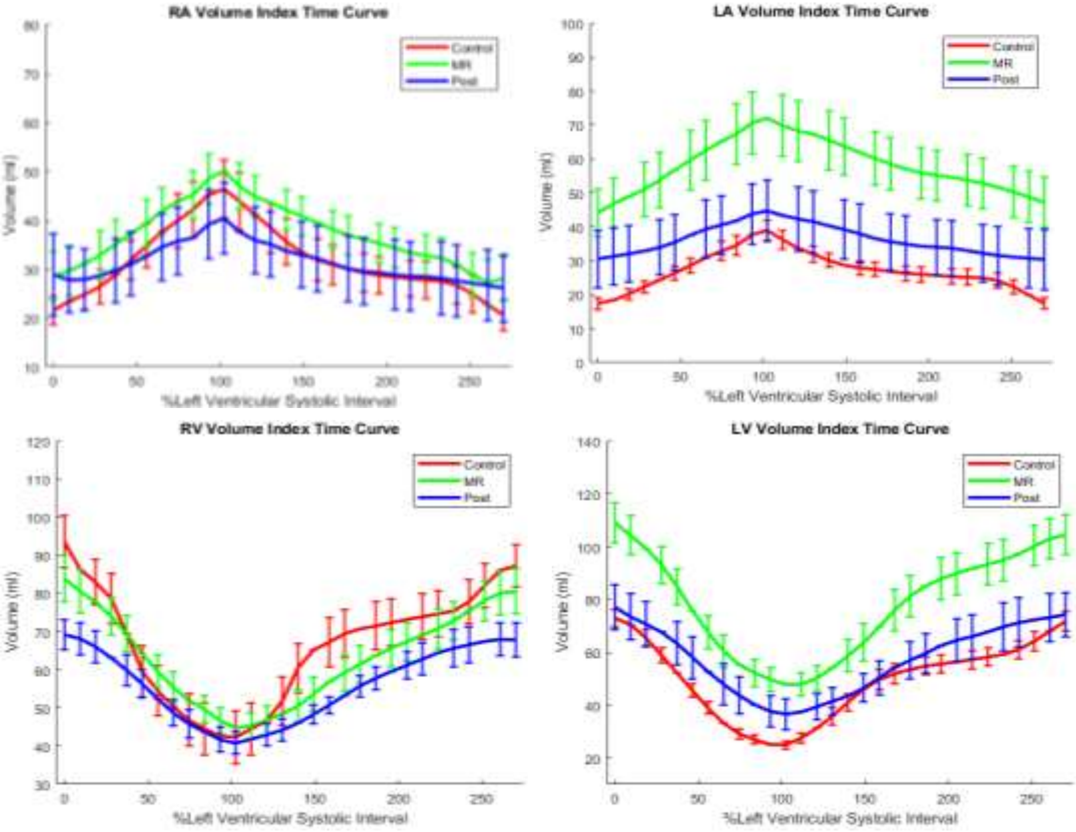

Figure 8.2 Indexed Volume time curves of the control group (n=11), MR patient group (n =16), and post-surgery MR patient (n=6) group. Mean±SD.

To study the mutual relationship among chambers, we computed the chamber volume ratios. Table 8-5 shows the comparison between the control group (n=6) and the MR patient group (n =16). The ratios of RV/LV, RA/LA and LA/LV had significant changes at LVED and RA/LA had significant change at LVES. The surgery normalized the RV/LV and RA/LA ratios. Figure 8.3 showed the ratios across the cardiac cyle. The ratios of RV/LV and RA/RV in the MR patient group had a consistent decrease across the cardiac cycle, while the ratio of LA/LV had an obvioius increase during ventricular diastole.After surgery, the ratios of RV/LV and RA/LA had an increase and returned to the control group as shown in Table 8-6.

Table 8-5 Volume ratio analysis, control vs. MR

	LVES		**LVED**	
	Control (n=11)	MR (n=16)	Control (n=11)	MR (n=16)
RV/LV	1.57 ±0.29	1.52±0.51	1.31±0.42	0.78±0.14*
RA/LA	1.18 ±0.38	0.75±0.22*	1.29 ±0.61	0.69±0.25*
RA/RV	1.32 ±0.67	1.14±0.39	0.25 ±0.13	0.35±0.19
LA/LV	1.57 ±0.29	1.52±0.51	0.24±0.07	0.4±0.18*

Mean ± SD; * P<0.05 vs. Control.

Table 8-4 Volume ratio analysis on surgical MR patients

	LVES			**LVED**		
	Control (n=11)	Pre (n=6)	Post (n=6)	Control (n=11)	Pre (n=6)	Post (n=6)
RV/LV	1.57 ±0.29	1.01±0.13	1.26±25.0	1.31±0.42	0.81±0.17*	0.93±0.19
RA/LA	1.18 ±0.38	1.13±0.31	0.91±0.13	1.29 ±0.61	0.40±0.10	0.94±0.22
RA/RV	1.32 ±0.67	0.88±0.21	1.04±0.55	0.25 ±0.13	0.81±0.28	0.43±0.31
LA/LV	1.57 ±0.29	1.31±0.29	1.26±0.42	0.24±0.07	0.33±0.16	0.39±0.21*

Mean ± SD; * P<0.05 vs. Control; †: P <0.05 vs. Pre.

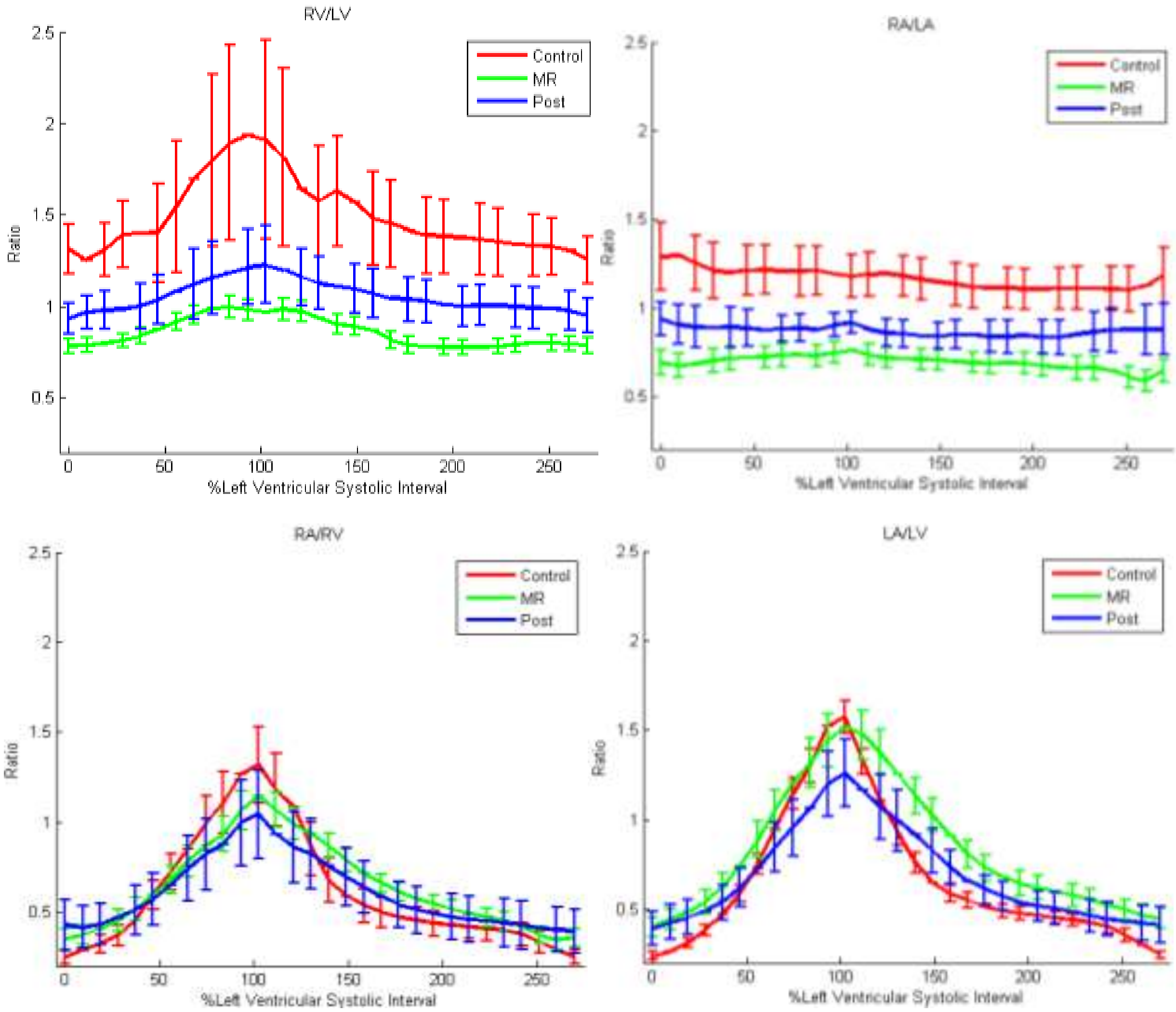

Figure 8.3 Chamber volume ratio of the control group (n=11), MR patient group (n= 16) and post-surgery MR patient group (n 6). Mean±SD.

8.3.2 Endocardial Surface Curvature

Tables 8-7 to 8-10 describe curvatures in the control group and the MR patient group in the longitudinal and circumferential directions at LVES and LVED. For the LV, a statistically significant decrease occurred in the apical segments for both directions at LVES, while no significant change in the LVED phase. This indicates the enlargement in both directions of LV at apical region, which was consistent with previous work [41]. In the RV, several segments showed statistically decrease in the MR patient group. In the LA, more segments showed statistically difference in the curvatures of both directions, and the difference most occurred in the basal and middle regions. For the RA, no MR-associated curvature differences were observed in both directions.

Table 8-6 LV curvature (1/mm) analysis in the MR patients at LVES and LVED

	LVES		**LVED**	
	Control (n=11)	MR (n=16)	Control (n=11)	MR (n=16)
	Circumferential			
Basal Anterior	0.05±0.024	0.04±0.019	0.03±0.013	0.03±0.012
Basal Anteroseptal	0.06±0.028	0.05±0.019	0.04±0.015	0.04±0.013
Basal Inferoseptal	0.07±0.028	0.05±0.020	0.04±0.015	0.03±0.013
Basal Inferior	0.07±0.031	0.06±0.022	0.04±0.016	0.03±0.012
Basal Inferolateral	0.06±0.028	0.04±0.017	0.040.014	0.03±0.010
Basal Anterolateral	0.07±0.024	0.05±0.019	0.04±0.015	0.04±0.013
Middle Anterior	0.04±0.016	0.03±0.015	0.03±0.011	0.03±0.011
Middle Anteroseptal	0.05±0.018	0.03±0.012	0.03±0.011	0.02±0.011
Middle Inferoseptal	0.04±0.024	0.03±0.012	0.03±0.012	0.02±0.010
Middle Inferior	0.04±0.016	0.03±0.012	0.02±0.009	0.02±0.008
Middle Inferolateral	0.04±0.013	0.03±0.014	0.03±0.010	0.02±0.007
Middle Anterolateral	0.04±0.017	0.04±0.016	0.03±0.011	0.03±0.010
Apical Anterior	0.06±0.021	0.04±0.016	0.04±0.013	0.03±0.011
Apical Septal	0.08±0.030	0.05±0.020*	0.04±0.017	0.04±0.013
Apical Inferior	0.07±0.035	0.05±0.016*	0.04±0.015	0.03±0.011
Apical Lateral	0.04±0.021	0.03±0.013	0.03±0.011	0.02±0.009
	Longitudinal			
Basal Anterior	0.07±0.032	0.06±0.024	0.04±0.016	0.04±0.019
Basal Anteroseptal	0.07±0.034	0.06±0.022	0.04±0.016	0.04±0.014
Basal Inferoseptal	0.07±0.030	0.06±0.022	0.04±0.016	0.04±0.014
Basal Inferior	0.08±0.032	0.06±0.022	0.04±0.016	0.04±0.013
Basal Inferolateral	0.07±0.032	0.06±0.020	0.04±0.014	0.04±0.012
Basal Anterolateral	0.08±0.030	0.06±0.023	0.05±0.017	0.04±0.014
Middle Anterior	0.05±0.017	0.04±0.016	0.03±0.013	0.03±0.012
Middle Anteroseptal	0.04±0.018	0.03±0.014	0.03±0.012	0.03±0.011
Middle Inferoseptal	0.04±0.026	0.04±0.017	0.03±0.012	0.03±0.011
Middle Inferior	0.04±0.019	0.04±0.017	0.03±0.013	0.03±0.010
Middle Inferolateral	0.04±0.019	0.04±0.015	0.03±0.012	0.03±0.010
Middle Anterolateral	0.05±0.019	0.04±0.015	0.03±0.012	0.03±0.010
Apical Anterior	0.07±0.025	0.05±0.017*	0.04±0.014	0.03±0.011
Apical Septal	0.08±0.029	0.05±0.020*	0.05±0.018	0.04±0.014
Apical Inferior	0.08±0.034	0.06±0.023	0.05±0.017	0.04±0.014
Apical Lateral	0.06±0.025	0.05±0.017	0.04±0.014	0.03±0.012

Values are Mean ± SD. *: P<0.05 vs. Control.

Table 8-7 RV curvature (1/mm) analysis in the MR patients at LVES and LVED.

	LVES		**LVED**	
	Control (n=11)	MR (n=16)	Control (n=11)	MR (n=16)
	Circumferential			
Basal Anterior	0.07±0.030	0.06±0.027	0.05±0.026	0.05±0.022
Basal Lateral	0.04±0.024	0.03±0.014	0.02±0.018	0.02±0.010
Basal Inferior	0.05±0.020	0.04±0.024	0.04±0.014	0.03±0.016
Basal Inferoseptal	0.05±0.021	0.03±0.015	0.04±0.017	0.02±0.011*
Basal Anteroseptal	0.01±0.016	0.03±0.023	0.02±0.016	0.03±0.021
Basal Anterior	0.02±0.041	0.03±0.010	0.03±0.013	0.02±0.008
Middle Lateral	0.02±0.011	0.02±0.011	0.02±0.008	0.02±0.010
Middle Inferior	0.04±0.018	0.04±0.014	0.03±0.013	0.03±0.012
Middle Inferoseptal	0.06±0.024	0.04±0.018	0.03±0.014	0.03±0.011
Middle Anterorseptal	0.00±0.011	0.01±0.022	0.00±0.011	0.02±0.019*
Apical Anterior	0.01±0.043	0.02±0.011	0.02±0.019	0.02±0.010
Apical Inferior	0.06±0.025	0.05±0.021	0.04±0.017	0.04±0.016
Apical Septal	0.07±0.056	0.04±0.031	0.05±0.020	0.05±0.021
Outlet	0.06±0.023	0.05±0.019	0.04±0.016	0.04±0.016
Inlet	0.07±0.026	0.06±0.021	0.05±0.020	0.05±0.016
	Longitudinal			
Basal Anterior	0.07±0.032	0.05±0.024	0.05±0.019	0.04±0.020
Basal Lateral	0.03±0.017	0.03±0.013	0.02±0.012	0.02±0.012
Basal Inferior	0.04±0.018	0.04±0.018	0.03±0.012	0.03±0.015
Basal Inferoseptal	0.07±0.029	0.05±0.021*	0.05±0.019	0.03±0.017
Basal Anteroseptal	0.01±0.012	0.02±0.021*	0.01±0.018	0.02±0.020
Basal Anterior	0.03±0.090	0.03±0.021	0.05±0.022	0.02±0.014*
Middle Lateral	0.02±0.09	0.02±0.011	0.01±0.007	0.02±0.014
Middle Inferior	0.04±0.016	0.04±0.016	0.03±0.013	0.04±0.013
Middle Inferoseptal	0.08±0.038	0.06±0.033	0.05±0.023	0.04±0.025
Middle Anterorseptal	0.00±0.014	0.04±0.032*	0.00±0.011	0.05±0.027*
Apical Anterior	0.03±0.124	0.03±0.023	0.05±0.035	0.03±0.023
Apical Inferior	0.07±0.034	0.07±0.028	0.05±0.021	0.05±0.019
Apical Septal	0.12±0.083	0.08±0.048	0.08±0.029	0.08±0.028
Outlet	0.06±0.026	0.06±0.020	0.05±0.018	0.05±0.017
Inlet	0.06±0.024	0.05±0.018	0.04±0.017	0.04±0.014

Values are Mean ± SD. *: P<0.05 vs. Control.

Table 8-8 LA curvature (1/mm) analysis in the MR patients at LVES and LVED.

	LVES		**LVED**	
	Control (n=11)	MR (n=16)	Control (n=11)	MR (n=16)
	Circumferential			
Basal Anterior	0.05±0.020	0.04±0.014	0.07±0.033	0.05±0.020
Basal Septal	0.07±0.031	0.05±0.016*	0.10±0.045	0.06±0.025*
Basal Inferior	0.05±0.023	0.03±0.013*	0.08±0.035	0.04±0.019
Basal Lateral	0.03±0.016	0.03±0.015	0.04±0.025	0.03±0.015
Middle Anterior	0.04±0.021	0.04±0.013	0.05±0.020	0.04±0.015
Middle Septal	0.02±0.011	0.03±0.013*	0.02±0.011	0.04±0.014*
Middle Inferior	0.04±0.016	0.03±0.012	0.05±0.019	0.04±0.017
Middle Lateral	0.02±0.013	0.02±0.010	0.02±0.011	0.03±0.013
Apical Anterior	0.05±0.018	0.04±0.017	0.07±0.030	0.05±0.022
Apical Septal	0.05±0.036	0.03±0.014	0.07±0.047	0.05±0.024
Apical Inferior	0.06±0.025	0.05±0.017	0.10±0.054	0.06±0.025
Apical Lateral	0.07±0.031	0.05±0.020	0.13±0.081	0.08±0.039
	Longitudinal			
Basal Anterior	0.06±0.023	0.04±0.015	0.08±0.036	0.05±0.021*
Basal Septal	0.07±0.028	0.05±0.018	0.10±0.038	0.06±0.023*
Basal Inferior	0.06±0.026	0.04±0.014*	0.09±0.036	0.04±0.017*
Basal Lateral	0.03±0.017	0.03±0.014	0.04±0.024	0.04±0.019
Middle Anterior	0.05±0.018	0.04±0.014	0.07±0.026	0.05±0.018*
Middle Septal	0.02±0.014	0.03±0.012	0.02±0.011	0.03±0.015
Middle Inferior	0.04±0.018	0.04±0.014	0.04±0.027	0.05±0.019
Middle Lateral	0.03±0.014	0.03±0.010	0.03±0.015	0.03±0.013
Apical Anterior	0.05±0.018	0.04±0.013	0.07±0.027	0.05±0.018*
Apical Septal	0.04±0.022	0.03±0.013	0.06±0.038	0.04±0.025
Apical Inferior	0.05±0.018	0.04±0.013	0.07±0.029	0.06±0.021
Apical Lateral	0.04±0.018	0.04±0.013	0.07±0.049	0.05±0.024

Values are Mean ± SD. *: $P<0.05$ vs. Control.

Table 8-9 RA curvature (1/mm) analysis in the MR patients at LVES and LVED.

	LVES		**LVED**	
	Control (n=11)	MR (n=16)	Control (n=11)	MR (n=16)
	Circumferential			
Basal Anterior	0.06±0.027	0.06±0.020	0.10±0.044	0.07±0.029
Basal Septal	0.04±0.019	0.04±0.018	0.06±0.028	0.05±0.023
Basal Inferior	0.04±0.017	0.04±0.016	0.06±0.025	0.05±0.026
Basal Lateral	0.05±0.019	0.04±0.018	0.07±0.028	0.06±0.024
Middle Anterior	0.04±0.023	0.05±0.017	0.05±0.036	0.07±0.029
Middle Septal	0.04±0.021	0.03±0.016	0.05±0.021	0.05±0.023
Middle Inferior	0.04±0.030	0.04±0.015	0.04±0.029	0.04±0.017
Middle Lateral	0.03±0.020	0.03±0.017	0.04±0.022	0.03±0.016
Apical Anterior	0.05±0.021	0.05±0.016	0.08±0.034	0.06±0.025
Apical Septal	0.05±0.021	0.05±0.017	0.06±0.034	0.08±0.037
Apical Inferior	0.05±0.021	0.05±0.019	0.07±0.037	0.08±0.041
Apical Lateral	0.06±0.025	0.06±0.022	0.08±0.037	0.08±0.030
	Longitudinal			
Basal Anterior	0.06±0.022	0.05±0.021	0.08±0.031	0.06±0.023
Basal Septal	0.05±0.023	0.05±0.018	0.07±0.032	0.05±0.021
Basal Inferior	0.05±0.019	0.05±0.019	0.06±0.027	0.06±0.026
Basal Lateral	0.03±0.020	0.03±0.021	0.04±0.022	0.04±0.023
Middle Anterior	0.04±0.023	0.04±0.013	0.04±0.029	0.05±0.017
Middle Septal	0.04±0.020	0.03±0.014	0.05±0.023	0.05±0.021
Middle Inferior	0.04±0.026	0.04±0.014	0.05±0.026	0.05±0.021
Middle Lateral	0.04±0.018	0.03±0.016	0.05±0.021	0.04±0.022
Apical Anterior	0.05±0.022	0.04±0.014	0.07±0.032	0.06±0.023
Apical Septal	0.05±0.020	0.04±0.012	0.06±0.026	0.05±0.029
Apical Inferior	0.04±0.022	0.04±0.016	0.06±0.033	0.06±0.040
Apical Lateral	0.06±0.026	0.05±0.023	0.08±0.036	0.08±0.035

Values are Mean ± SD. *: $P<0.05$ vs. Control.

Tables 8-11 to 8-14 describe curvatures in the control group (n=11), the pre-surgery MR group (n =6) and the post-surgery MR group (n=6). After surgery, no statistical significance in curvatures were observed compare to the pre-surgery group.

Table 8-10 LV curvature (1/mm) analysis in the surgical MR patients at LVES and LVED.

	LVES			LVED		
	Control (n=11)	Pre (n=6)	Post (n=6)	Control (n=11)	Pre (n=6)	Post (n=6)
	Circumferential					
B. Anterior	0.05±0.024	0.04±0.027	0.03±0.019	0.03±0.013	0.03±0.017	0.03±0.016
B. AnSep	0.06±0.028	0.05±0.029	0.05±0.025	0.04±0.015	0.03±0.021	0.03±0.019
B. InfSep	0.07±0.028	0.05±0.030	0.05±0.029	0.04±0.015	0.03±0.019	0.04±0.021
B.Inferior	0.07±0.031	0.05±0.030	0.06±0.031	0.04±0.016	0.03±0.018	0.04±0.021
B. InfLa	0.06±0.028	0.04±0.022	0.04±0.029	0.04±0.014	0.03±0.014	0.03±0.016
B. AnLa	0.07±0.024	0.05±0.030	0.05±0.027	0.04±0.015	0.04±0.021	0.03±0.017
M. Anterior	0.04±0.016	0.03±0.018	0.03±0.019	0.03±0.011	0.02±0.015	0.02±0.014
M. AnSep	0.05±0.018	0.03±0.018	0.03±0.021	0.03±0.011	0.02±0.017	0.02±0.014
M. InfSep	0.04±0.024	0.02±0.015	0.02±0.017	0.03±0.012	0.02±0.012	0.02±0.010
M. Inferior	0.04±0.016	0.03±0.015	0.03±0.018	0.02±0.009	0.02±0.011	0.02±0.012
M. InfLa	0.04±0.013	0.02±0.017	0.03±0.016	0.03±0.010	0.02±0.011	0.02±0.012
M. AnLa	0.04±0.017	0.04±0.022	0.03±0.020	0.03±0.011	0.03±0.016	0.03±0.014
A. Anterior	0.06±0.021	0.04±0.023	0.04±0.022	0.04±0.013	0.03±0.018	0.03±0.017
A. Septal	0.08±0.030	0.04±0.027	0.06±0.037	0.04±0.017	0.03±0.020	0.04±0.024
A. Inferior	0.07±0.035	0.04±0.025	0.04±0.023	0.04±0.015	0.03±0.016	0.03±0.018
A. Lateral	0.04±0.021	0.03±0.020	0.03±0.018	0.03±0.011	0.02±0.014	0.02±0.012
	Longitudinal					
B. Anterior	0.07±0.032	0.06±0.037	0.05±0.027	0.04±0.016	0.04±0.031	0.03±0.020
B. AnSep	0.07±0.034	0.05±0.031	0.05±0.026	0.04±0.016	0.03±0.022	0.03±0.020
B. InfSep	0.07±0.030	0.05±0.031	0.05±0.031	0.04±0.016	0.03±0.020	0.04±0.024
B.Inferior	0.08±0.032	0.06±0.034	0.06±0.036	0.04±0.016	0.04±0.021	0.04±0.023
B. InfLa	0.07±0.032	0.05±0.030	0.06±0.036	0.04±0.014	0.03±0.019	0.03±0.019
B. AnLa	0.08±0.030	0.06±0.034	0.05±0.033	0.05±0.017	0.04±0.023	0.03±0.019
M. Anterior	0.05±0.017	0.04±0.021	0.04±0.020	0.03±0.013	0.03±0.020	0.03±0.016
M. AnSep	0.04±0.018	0.03±0.017	0.03±0.016	0.03±0.012	0.02±0.015	0.02±0.011
M. InfSep	0.04±0.026	0.02±0.018	0.03±0.019	0.03±0.012	0.02±0.013	0.03±0.015
M. Inferior	0.04±0.019	0.03±0.020	0.04±0.023	0.03±0.013	0.03±0.015	0.02±0.013
M. InfLa	0.04±0.019	0.03±0.019	0.03±0.020	0.03±0.012	0.03±0.014	0.03±0.017
M. AnLa	0.05±0.019	0.04±0.022	0.04±0.020	0.03±0.012	0.03±0.016	0.03±0.016
A. Anterior	0.07±0.025	0.04±0.024	0.04±0.025	0.04±0.014	0.03±0.018	0.03±0.019
A. Septal	0.08±0.029	0.05±0.027	0.06±0.038	0.05±0.018	0.03±0.020	0.04±0.025
A. Inferior	0.08±0.034	0.05±0.031	0.05±0.029	0.05±0.017	0.04±0.021	0.04±0.022
A. Lateral	0.06±0.025	0.04±0.025	0.04±0.023	0.04±0.014	0.03±0.017	0.03±0.017

Values are Mean ± SD. *: P<0.05 vs. Control. B.: basal, M,: Middle, A,: Apical. InfSep:Inferoseptal. AnSep: Anterorseptal. InfLA:Inferolateral: InfLa, AnLa: Anterolateral

Table 8-11 RV curvature (1/mm) analysis in the surgical MR patients at LVES and LVED.

	LVES			LVED		
	Control (n=11)	Pre (n=6)	Post (n=6)	Control (n=11)	Pre (n=6)	Post (n=6)
	Circumferential					
B. Anterior	0.07±0.030	0.06±0.039	0.06±0.040	0.05±0.026	0.05±0.032	0.05±0.033
B. Lateral	0.04±0.024	0.03±0.018	0.03±0.017	0.02±0.018	0.02±0.013	0.02±0.013
B. Inferior	0.05±0.020	0.03±0.021	0.03±0.023	0.04±0.014	0.03±0.016	0.03±0.018
B. InfSep	0.05±0.021	0.03±0.020	0.04±0.025	0.04±0.017	0.02±0.014	0.04±0.022
B. AnSep	0.01±0.016	0.02±0.018	0.02±0.019	0.02±0.016	0.02±0.017	0.02±0.018
B. Anterior	0.02±0.041	0.03±0.015	0.03±0.020	0.03±0.013	0.02±0.012	0.02±0.017
M. Lateral	0.02±0.011	0.02±0.012	0.02±0.013	0.02±0.008	0.01±0.011	0.01±0.009
M. Inferior	0.04±0.018	0.03±0.020	0.04±0.023	0.03±0.013	0.03±0.016	0.03±0.020
M. InfSep	0.06±0.024	0.03±0.025	0.05±0.028	0.03±0.014	0.02±0.014	0.04±0.023
M. AnSep	0.00±0.011	0.01±0.015	0.01±0.014	0.00±0.011	0.01±0.008	0.00±0.008
A. Anterior	0.01±0.043	0.02±0.015	0.02±0.014	0.02±0.019	0.02±0.013	0.02±0.014
A. Inferior	0.06±0.025	0.05±0.027	0.05±0.032	0.04±0.017	0.04±0.021	0.04±0.026
A. Septal	0.07±0.056	0.03±0.043	0.04±0.043	0.05±0.020	0.04±0.027	0.04±0.026
Outlet	0.06±0.023	0.05±0.028	0.05±0.035	0.04±0.016	0.04±0.022	0.04±0.035
Inlet	0.07±0.026	0.06±0.033	0.06±0.033	0.05±0.020	0.04±0.025	0.05±0.030
	Longitudinal					
B. Anterior	0.07±0.032	0.05±0.034	0.06±0.044	0.05±0.019	0.04±0.029	0.05±0.041
B. Lateral	0.03±0.017	0.03±0.018	0.02±0.014	0.02±0.012	0.02±0.016	0.02±0.014
B. Inferior	0.04±0.018	0.03±0.020	0.04±0.026	0.03±0.012	0.02±0.015	0.03±0.019
B. InfSep	0.07±0.029	0.05±0.026	0.05±0.029	0.05±0.019	0.03±0.019	0.04±0.024
B. AnSep	0.01±0.012	0.02±0.018	0.02±0.028	0.01±0.018	0.01±0.016	0.01±0.021
B. Anterior	0.03±0.090	0.03±0.026	0.06±0.063	0.05±0.022	0.02±0.016	0.04±0.042
M. Lateral	0.02±0.09	0.02±0.014	0.02±0.012	0.01±0.007	0.01±0.012	0.02±0.013
M. Inferior	0.04±0.016	0.04±0.024	0.04±0.023	0.03±0.013	0.03±0.018	0.03±0.020
M. InfSep	0.08±0.038	0.05±0.033	0.05±0.038	0.05±0.023	0.03±0.019	0.04±0.028
M. AnSep	0.00±0.014	0.05±0.038*	0.02±0.033	0.00±0.011	0.05±0.028*	0.02±0.030
A. Anterior	0.03±0.124	0.02±0.015	0.04±0.029	0.05±0.035	0.02±0.013	0.04±0.047
A. Inferior	0.07±0.034	0.06±0.036	0.06±0.044	0.05±0.021	0.05±0.026	0.05±0.031
A. Septal	0.12±0.083	0.08±0.064	0.07±0.050	0.08±0.029	0.07±0.038	0.06±0.038
Outlet	0.06±0.026	0.05±0.027	0.05±0.038	0.05±0.018	0.04±0.023	0.05±0.038
Inlet	0.06±0.024	0.05±0.027	0.05±0.028	0.04±0.017	0.04±0.021	0.04±0.026

Values are Mean ± SD. *: P<0.05 vs. Control. B.: basal, M,: Middle, A,: Apical. InfSep:Inferoseptal. AnSep: Anterorseptal.

Table 8-12 LA curvature (1/mm) analysis in the surgical MR patients at LVES and LVED.

	Maximum Volume Phase			**Minimum Volume Phase**		
	Control (n=11)	Pre (n=6)	Post (n=6)	Control (n=11)	Pre (n=6)	Post (n=6)
			Circumferential			
B. Anterior	0.05±0.020	0.03±0.021	0.04±0.020	0.07±0.033	0.05±0.030	0.04±0.027
B. Septal	0.07±0.031	0.04±0.025	0.05±0.027	0.10±0.045	0.06±0.035	0.06±0.033
B. Inferior	0.05±0.023	0.03±0.017	0.04±0.022	0.08±0.035	0.04±0.022*	0.04±0.026*
B. Lateral	0.03±0.016	0.02±0.012	0.02±0.020	0.04±0.025	0.03±0.021	0.02±0.024
M. Anterior	0.04±0.021	0.03±0.020	0.03±0.020	0.05±0.020	0.04±0.022	0.04±0.021
M. Septal	0.02±0.011	0.03±0.017	0.03±0.020	0.02±0.011	0.03±0.020	0.03±0.018
M. Inferior	0.04±0.016	0.03±0.018	0.03±0.019	0.05±0.019	0.04±0.024	0.04±0.023
M. Lateral	0.02±0.013	0.02±0.012	0.02±0.012	0.02±0.011	0.02±0.015	0.02±0.013
A. Anterior	0.05±0.018	0.03±0.019	0.04±0.023	0.07±0.030	0.05±0.026	0.05±0.029
A. Septal	0.05±0.036	0.03±0.021	0.03±0.023	0.07±0.047	0.04±0.032	0.04±0.029
A. Inferior	0.06±0.025	0.04±0.026	0.05±0.029	0.10±0.054	0.06±0.040	0.06±0.039
A. Lateral	0.07±0.031	0.05±0.031	0.05±0.030	0.13±0.081	0.08±0.057	0.07±0.044
			Longitudinal			
B. Anterior	0.06±0.023	0.04±0.024	0.04±0.024	0.08±0.036	0.05±0.032	0.06±0.035
B. Septal	0.07±0.028	0.05±0.027	0.05±0.028	0.10±0.038	0.06±0.034	0.06±0.033
B. Inferior	0.06±0.026	0.03±0.019	0.04±0.026	0.09±0.036	0.04±0.024	0.05±0.029
B. Lateral	0.03±0.017	0.02±0.018	0.03±0.024	0.04±0.024	0.04±0.029	0.03±0.023
M. Anterior	0.05±0.018	0.03±0.020	0.04±0.024	0.07±0.026	0.05±0.026	0.05±0.028
M. Septal	0.02±0.014	0.02±0.017	0.03±0.018	0.02±0.011	0.03±0.022	0.03±0.019
M. Inferior	0.04±0.018	0.04±0.022	0.03±0.022	0.04±0.027	0.05±0.030	0.04±0.025
M. Lateral	0.03±0.014	0.02±0.015	0.03±0.016	0.03±0.015	0.03±0.019	0.03±0.017
A. Anterior	0.05±0.018	0.03±0.020	0.04±0.023	0.07±0.027	0.05±0.026	0.05±0.028
A. Septal	0.04±0.022	0.03±0.020	0.03±0.019	0.06±0.038	0.04±0.033	0.03±0.022
A. Inferior	0.05±0.018	0.03±0.020	0.04±0.024	0.07±0.029	0.05±0.030	0.05±0.029
A. Lateral	0.04±0.018	0.04±0.021	0.03±0.021	0.07±0.049	0.06±0.038	0.04±0.028

Values are Mean ± SD. *: $P<0.05$ vs. Control. B.: basal, M,: Middle, A,: Apical.

Table 8-13 RA curvature (1/mm) analysis in the surgical MR patients at LVES and LVED.

	Maximum Volume Phase			**Minimum Volume Phase**		
	Control (n=11)	Pre (n=6)	Post (n=6)	Control (n=11)	Pre (n=6)	Post (n=6)
	Circumferential					
B. Anterior	0.06±0.027	0.05±0.031	0.05±0.028	0.10±0.044	0.07±0.043	0.06±0.033
B. Septal	0.04±0.019	0.04±0.021	0.04±0.022	0.06±0.028	0.04±0.028	0.04±0.025
B. Inferior	0.04±0.017	0.04±0.024	0.03±0.018	0.06±0.025	0.05±0.035	0.03±0.021
B. Lateral	0.05±0.019	0.04±0.022	0.04±0.026	0.07±0.028	0.05±0.028	0.05±0.028
M. Anterior	0.04±0.023	0.04±0.024	0.04±0.021	0.05±0.036	0.05±0.032	0.04±0.026
M. Septal	0.04±0.021	0.03±0.021	0.03±0.018	0.05±0.021	0.04±0.024	0.04±0.022
M. Inferior	0.04±0.030	0.03±0.019	0.03±0.017	0.04±0.029	0.04±0.026	0.03±0.018
M. Lateral	0.03±0.020	0.03±0.020	0.04±0.021	0.04±0.022	0.03±0.020	0.04±0.024
A. Anterior	0.05±0.021	0.05±0.025	0.06±0.034	0.08±0.034	0.06±0.039	0.08±0.048
A. Septal	0.05±0.021	0.04±0.024	0.04±0.022	0.06±0.034	0.07±0.044	0.05±0.028
A. Inferior	0.05±0.021	0.04±0.024	0.04±0.024	0.07±0.037	0.07±0.047	0.05±0.029
A. Lateral	0.06±0.025	0.05±0.030	0.06±0.034	0.08±0.037	0.08±0.047	0.06±0.036
	Longitudinal					
B. Anterior	0.06±0.022	0.05±0.028	0.05±0.026	0.08±0.031	0.06±0.034	0.05±0.032
B. Septal	0.05±0.023	0.05±0.027	0.04±0.025	0.07±0.032	0.05±0.030	0.05±0.028
B. Inferior	0.05±0.019	0.05±0.027	0.04±0.022	0.06±0.027	0.05±0.034	0.04±0.025
B. Lateral	0.03±0.020	0.03±0.022	0.04±0.022	0.04±0.022	0.04±0.029	0.04±0.024
M. Anterior	0.04±0.023	0.03±0.019	0.04±0.023	0.04±0.029	0.04±0.023	0.05±0.027
M. Septal	0.04±0.020	0.03±0.019	0.03±0.018	0.05±0.023	0.04±0.025	0.04±0.021
M. Inferior	0.04±0.026	0.03±0.021	0.04±0.021	0.05±0.026	0.05±0.032	0.04±0.023
M. Lateral	0.04±0.018	0.03±0.015	0.03±0.017	0.05±0.021	0.03±0.018	0.04±0.021
A. Anterior	0.05±0.022	0.04±0.021	0.05±0.032	0.07±0.032	0.05±0.031	0.07±0.048
A. Septal	0.05±0.020	0.03±0.019	0.04±0.022	0.06±0.026	0.05±0.032	0.04±0.027
A. Inferior	0.04±0.022	0.03±0.020	0.04±0.021	0.06±0.033	0.06±0.049	0.05±0.027
A. Lateral	0.06±0.026	0.05±0.029	0.06±0.032	0.08±0.036	0.08±0.048	0.06±0.040

Values are Mean ± SD. *: $P<0.05$ vs. Control. B.: basal, M,: Middle, A,: Apical.

Figures 8.4 to 8.7 show curvatures in the control group (n =11), the MR patient group (n =16) and post-surgery MR patient group (n =6). For the LV, the curvatures were relatively low in the middle layer. For most segments, the curvature of the MR group was smaller than the control group due to the enlargement. There was a trend that the curvatures returned to the control group in the apical region after surgery. For the RV, curvatures were low for almost all segments without any difference among the groups. For the LA, the same observations were found as in the LV due to the LA enlargement. For the RA, the curvatures were very low in the middle and basal layers for both groups. After surgery, the lateral wall had a large variation. For all four chambers, the curvatures had less variations in the time dimension in the MR patient group and the post-surgery group than in the control group.

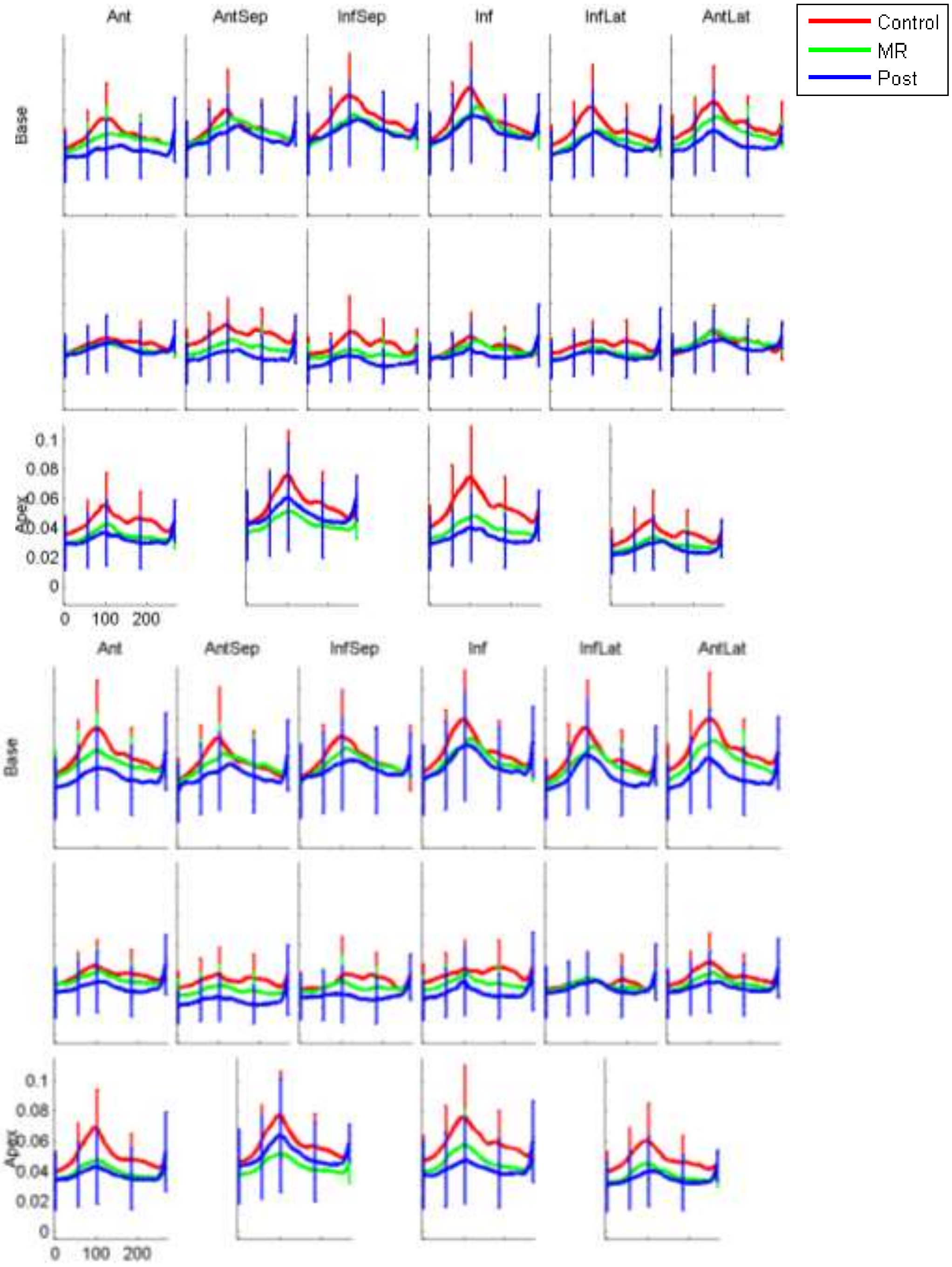

Figure 8.4 Averaged LV circumferential (top) and longitudinal (bottom) curvatures. Mean±SD, 1/mm.

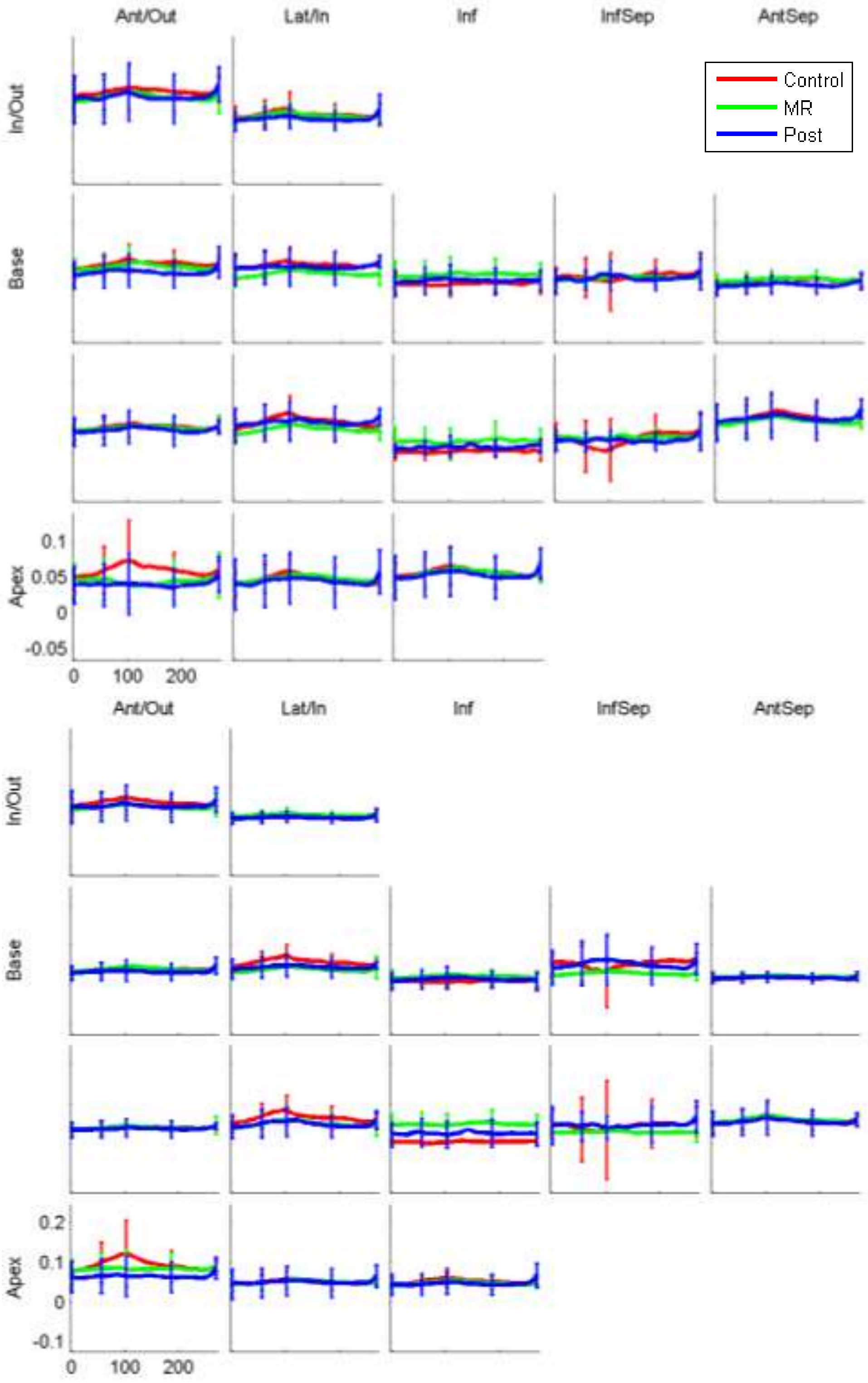

Figure 8.5 Averaged RV circumferential (top) and longitudinal (bottom) curvatures. Mean±SD, 1/mm.

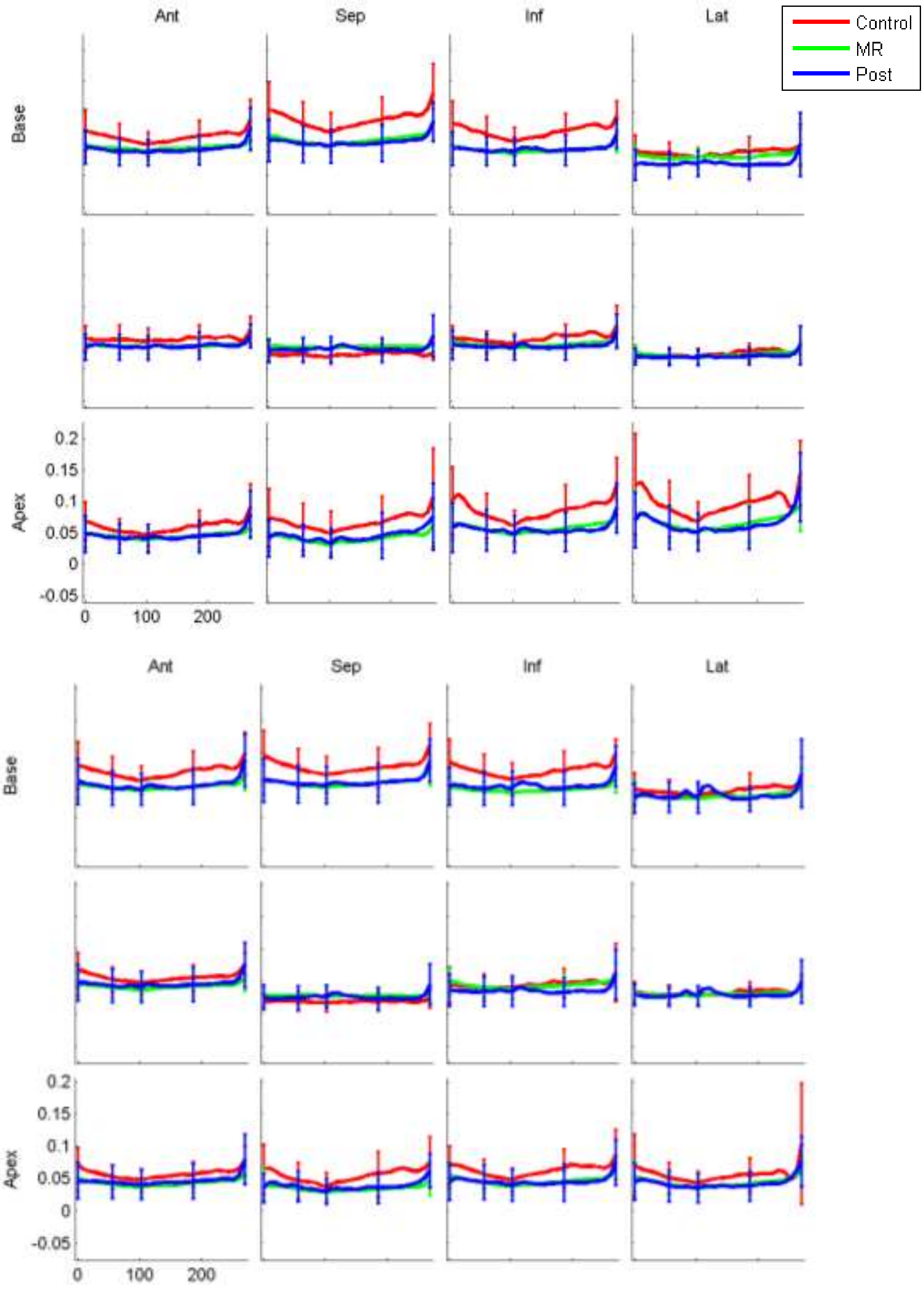

Figure 8.6 Averaged LA circumferential (top) and longitudinal (bottom) curvatures. Mean±SD, 1/mm.

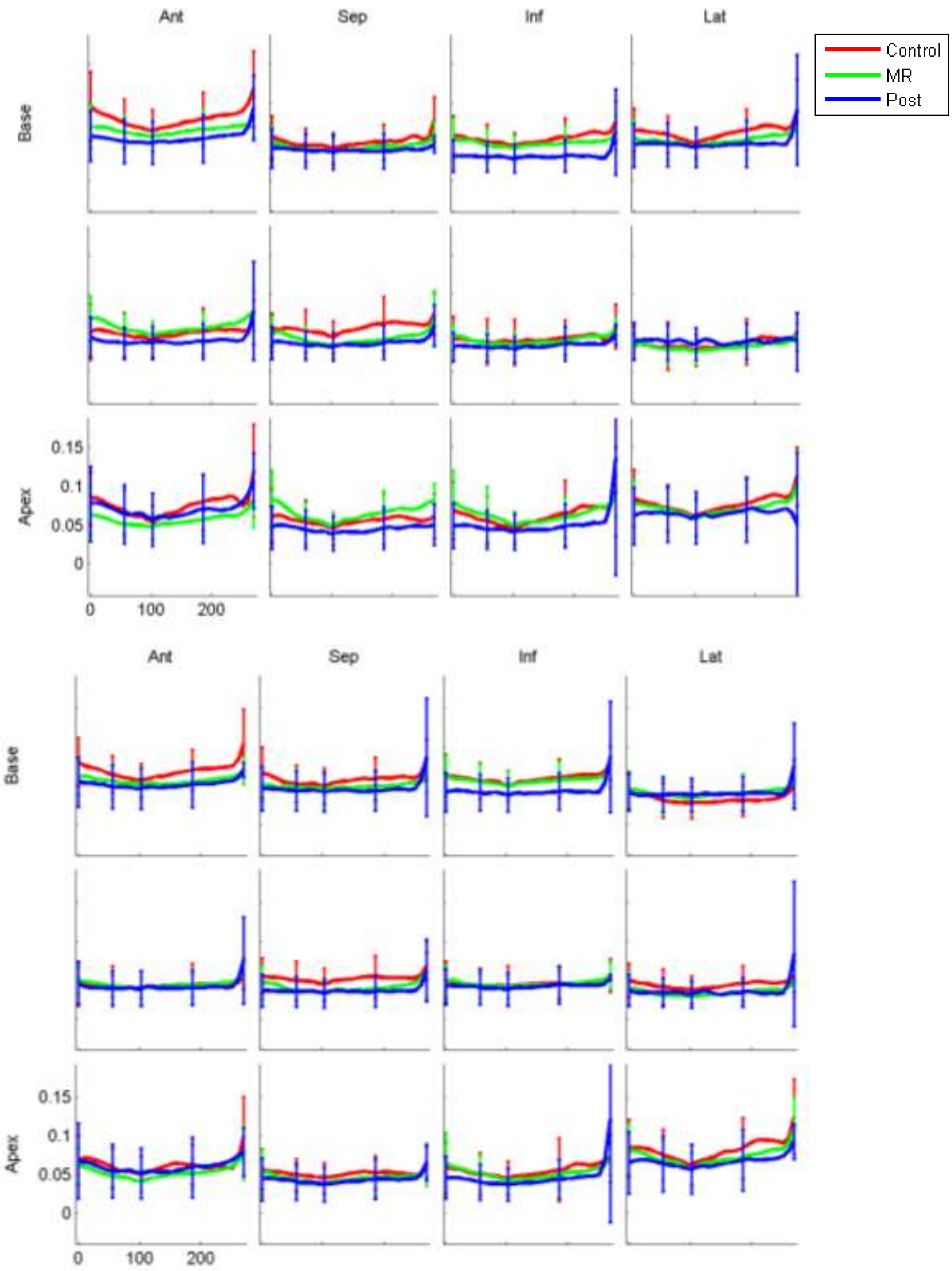

Figure 8.7 Averaged RA circumferential (top) and longitudinal (bottom) curvatures. Mean±SD, 1/mm.

8.3.3 Wall motion tracking

Table 8-15 and Table 8-18 display the statistical summary of the displacement in the radial direction of each segment at LVES for the control group (n=11) and MR patient group (n=16). The displacements of LV had no statistical difference for all segments. For the RV, the

Table 8-14 Ventricular radial displacement (mm) analysis in the control group and MR patient group, mean ± SD.

	Control (n=11)	**MR (n=16)**
	LV	
Basal Anterior	-11.7±4.5	-11.6±2.3
Basal Anteroseptal	-8.6±4.0	-8.7±2.4
Basal Inferoseptal	-7.8±3.4	-8.2±2.9
Basal Inferior	-9.4±3.2	-9.5±3.2
Basal Inferolateral	-11.6±3.8	-11.9±2.5
Basal Anterolateral	-13.0±4.7	-12.8±2.6
Middle Anterior	-8.7±1.8	-9.1±2.5
Middle Anteroseptal	-6.4±1.3	-5.9±3.3
Middle Inferoseptal	-5.8±1.5	-5.6±3.2
Middle Inferior	-7.9±1.9	-7.6±2.2
Middle Inferolateral	-9.9±2.1	-10.2±3.0
Middle Anterolateral	-10.2±2.0	-11.0±3.0
Apical Anterior	-5.7±3.1	-5.2±22
Apical Septal	-5.6±3.3	-4.2±2.7
Apical Inferior	-6.4±4.1	-5.5±2.3
Apical Lateral	-6.8±3.9	-6.7±3.4
	RV	
Basal Anterior	-8.8±2.4	-8.2±3.5
Basal Lateral	-11.1±3.1	-9.9±4.4
Basal Inferior	-12.3±2.8	-8.5±2.9*
Basal Inferoseptal	-7.1±2.0	-2.3±2.5*
Basal Anteroseptal	-4.4±2.0	-2.8±3.6
Basal Anterior	-3.7±1.8	-3.0±2.4
Middle Lateral	-5.3±1.9	-5.1±3.2
Middle Inferior	-7.1±2.2	-4.9±2.5*
Middle Inferoseptal	-1.1±2.8	2.0±4.0
Middle Anterorseptal	4.0±3.4	1.5±4.7
Apical Anterior	-0.2±3.2	0.3±3.7
Apical Inferior	-1.9±3.3	-1.1±3.9
Apical Septal	0.9±3.7	0.9±4.5
Outlet	-12.7±3.9	-11.0±4.4
Inlet	-13.8±3.9	-11.0±4.2

Values are Mean ± SD. *: P<0.05 vs. Control.

MR group had statistically significant decrease in three segments located in the middle and basal segments. The LA had a statistically decreased displacement only in the middle anterior segment. For the RA, most basal segments and one middle septal segment had statistically significant difference with less displacement in the MR group.

Table 8-15 Atrial radial displacement (mm) analysis in the control group and MR patient group at LVES, mean ± SD

	Control (n=11)	**MR (n=16)**
	LA	
Basal Anterior	1.32±2.063	-0.23±1.740
Basal Septal	2.44±0.939	1.50±1.669
Basal Inferior	2.14±0.935	1.05±1.553
Basal Lateral	0.25±1.288	-0.04±0.877
Middle Anterior	4.13±2.651	2.20±1.640*
Middle Septal	3.87±1.618	3.83±2.450
Middle Inferior	5.54±1.644	5.03±2.504
Middle Lateral	3.80±1.843	3.80±1.613
Apical Anterior	7.29±2.697	6.34±1.560
Apical Septal	7.17±2.223	7.18±1.988
Apical Inferior	8.92±2.574	9.41±2.851
Apical Lateral	9.10±2.838	9.19±2.629
	RA	
Basal Anterior	1.33±2.112	-1.43±2.004*
Basal Septal	3.08±1.683	-0.39±1.460*
Basal Inferior	-0.03±1.625	-2.19±1.824*
Basal Lateral	-4.19±1.665	-4.78±2.245
Middle Anterior	5.92±2.861	4.10±2.395
Middle Septal	8.69±2.031	6.01±3.117*
Middle Inferior	3.99±2.106	3.14±2.667
Middle Lateral	-1.53±1.886	-0.88±2.539
Apical Anterior	10.42±3.951	10.13±3.100
Apical Septal	13.42±3.820	13.57±4.711
Apical Inferior	10.35±3.079	10.89±4.864
Apical Lateral	6.19±2.619	7.01±2.258

Values are Mean ± SD. *: P<0.05 vs. Control.

Table 8-15 to Table 8-16 show the radial displacement statistical summary of the control group (n=11), the pre-surgery MR patient group (n=6) and the post-surgery MR patient group (n =6). Compared to the pre-surgery group, the post-surgery group changed significantly in the middle segments in the LV, in most segments in the RV, in two segments in the middle and apical layers in the LA and most segments in the RA. After surgery, all four chambers had more significant differences with the controls before they had the surgery.

Table 8-16 Ventricular radial displacement (1/mm) analysis in the surgical MR patients at LVES.

	Control (n=11)	**Pre (n=6)**	**Post (n=6)**
		LV	
Basal Anterior	-11.7±4.5	-11.8±3.3	-7.8±4.9
Basal Anteroseptal	-8.6±3.9	-8.5±2.5	-4.7±3.7
Basal Inferoseptal	-7.8±3.4	-7.8±2.7	-4.6±3.5
Basal Inferior	-9.4±3.2	-9.3±2.8	-6.6±2.8
Basal Inferolateral	-11.6±3.7	-11.0±2.8	-8.9±3.6
Basal Anterolateral	-13.0±4.7	-12.3±3.2	-10.0±4.9
Middle Anterior	-8.7±1.8	-9.5±2.4	-6.5±2.7†
Middle Anteroseptal	-6.4±1.3	-6.4±2.3	-1.2±1.6†*
Middle Inferoseptal	-5.8±1.5	-5.6±1.9	-1.1±0.9*
Middle Inferior	-7.9±1.9	-7.4±2.3	-5.9±1.6
Middle Inferolateral	-9.9±2.1	-9.9±2.6	-10.6±1.9
Middle Anterolateral	-10.2±2.0	-10.8±3.3	-10.7±3.7
Apical Anterior	-5.7±3.1	-5.3±2.4	-5.5±2.2
Apical Septal	-5.6±3.3	-4.2±2.1	-2.7±2.9
Apical Inferior	-6.4±4.1	-5.1±2.2	-5.7±3.5
Apical Lateral	-6.8±4.0	-6.1±3.5	-8.3±2.6
		RV	
Basal Anterior	-8.8±2.4	-8.5±3.3	-5.9±3.7
Basal Lateral	-11.1±31	-11.0±1.8	-4.6±3.1†*
Basal Inferior	-12.3±2.8	-8.8±1.5*	-5.7±1.6†*
Basal Inferoseptal	-7.1±2.0	-2.4±1.6*	-4.3±0.8†*
Basal Anteroseptal	-4.4±2.0	-2.5±3.2	-3.7±1.6
Basal Anterior	-3.7±1.8	-2.7±3.3	-3.6±2.1
Middle Lateral	-5.3±1.9	-4.6±2.2	-2.7±1.6*
Middle Inferior	-7.1±2.2	-4.1±0.9*	-4.5±2.1*
Middle Inferoseptal	-1.1±2.8	2.2±2.7	-2.9±2.6†
Middle Anterorseptal	4.0±3.4	2.6±4.1	-1.8±2.2*
Apical Anterior	-0.2±3.2	1.4±4.7	-2.5±1.8†
Apical Inferior	-1.9±3.3	-0.02±3.3	-3.2±2.6†
Apical Septal	0.9±3.7	2.1±3.8	-3.2±2.8†*
Outlet	-12.7±3.9	-11.4±3.8	-5.6±2.7*
Inlet	-13.8±3.9	-11.6±2.1	-6.1±2.8†*

Values are Mean ± SD. *: $P<0.05$ vs. Control. †: $P<0.05$ vs. Pre.

Table 8-17 Atrial radial displacement (1/mm) analysis in the surgical MR patients at LVES.

	Control (n=11)	**Pre (n=6)**	**Post (n=6)**
		LA	
Basal Anterior	1.32±2.063	-0.51±1.571	0.43±1.360
Basal Septal	2.44±0.939	0.62±1.407*	0.84±1.481*
Basal Inferior	2.14±0.935	0.59±1.178*	0.27±2.177*
Basal Lateral	0.25±1.288	-0.09±0.666	-0.17±1.624
Middle Anterior	4.13±2.651	2.14±0.920	3.30±1.649
Middle Septal	3.87±1.618	2.64±2.086	2.45±1.487
Middle Inferior	5.54±1.644	5.06±1.965	1.75±1.147†*
Middle Lateral	3.80±1.843	4.62±1.797	2.61±1.496
Apical Anterior	7.29±2.697	5.87±0.924	5.88±1.452
Apical Septal	7.17±2.223	6.21±1.199	5.28±0.620
Apical Inferior	8.92±2.574	9.11±2.394	5.32±1.279†*
Apical Lateral	9.10±2.838	9.67±3.170	5.74±1.988*
		RA	
Basal Anterior	1.33±2.112	-2.41±1.834*	0.52±1.447†
Basal Septal	3.08±1.683	-1.13±1.138*	2.70±2.752†
Basal Inferior	-0.03±1.625	-2.45±2.503*	1.58±3.448
Basal Lateral	-4.19±1.665	-5.18±2.411	0.71±2.984*
Middle Anterior	5.92±2.861	3.90±2.988	2.90±2.327
Middle Septal	8.69±2.031	5.19±2.517*	3.45±2.264†*
Middle Inferior	3.99±2.106	3.17±3.353	1.61±1.219*
Middle Lateral	-1.53±1.886	0.57±2.951	0.13±1.186
Apical Anterior	10.42±3.951	11.35±3.305	5.64±2.857†*
Apical Septal	13.42±3.820	14.20±2.866	5.96±2.703†*
Apical Inferior	10.35±3.079	11.63±3.398	4.52±1.712†*
Apical Lateral	6.19±2.619	8.08±1.683	3.40±1.409†*

Values are Mean ± SD. *: $P<0.05$ vs. Control. †: $P < 0.05$ vs. Pre.

Figure 8.8 and Figure 8.9 show the displacement of the control group (n=11), the MR patient group (n =16) and the post-surgery group (n =6) across the cardiac cycle. For most segments of all four chambers in the post-surgery group had less displacement in magnitude compared to MR patient group, and had more difference to the controls than the MR patient group.

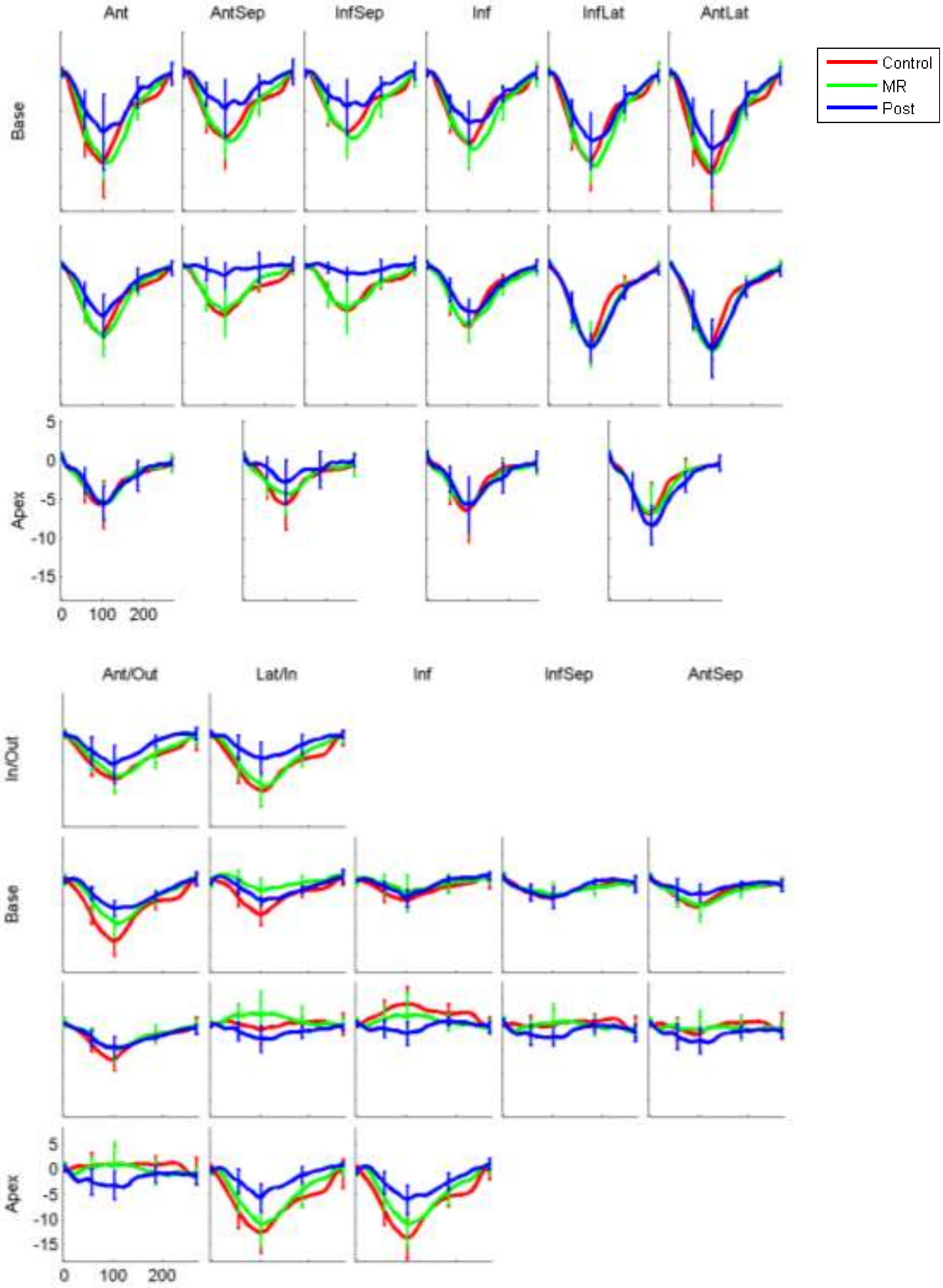

Figure 8.8 Averaged displacement (mm) corresponded to 1st timeframe of LV (top) and RV (bottom)

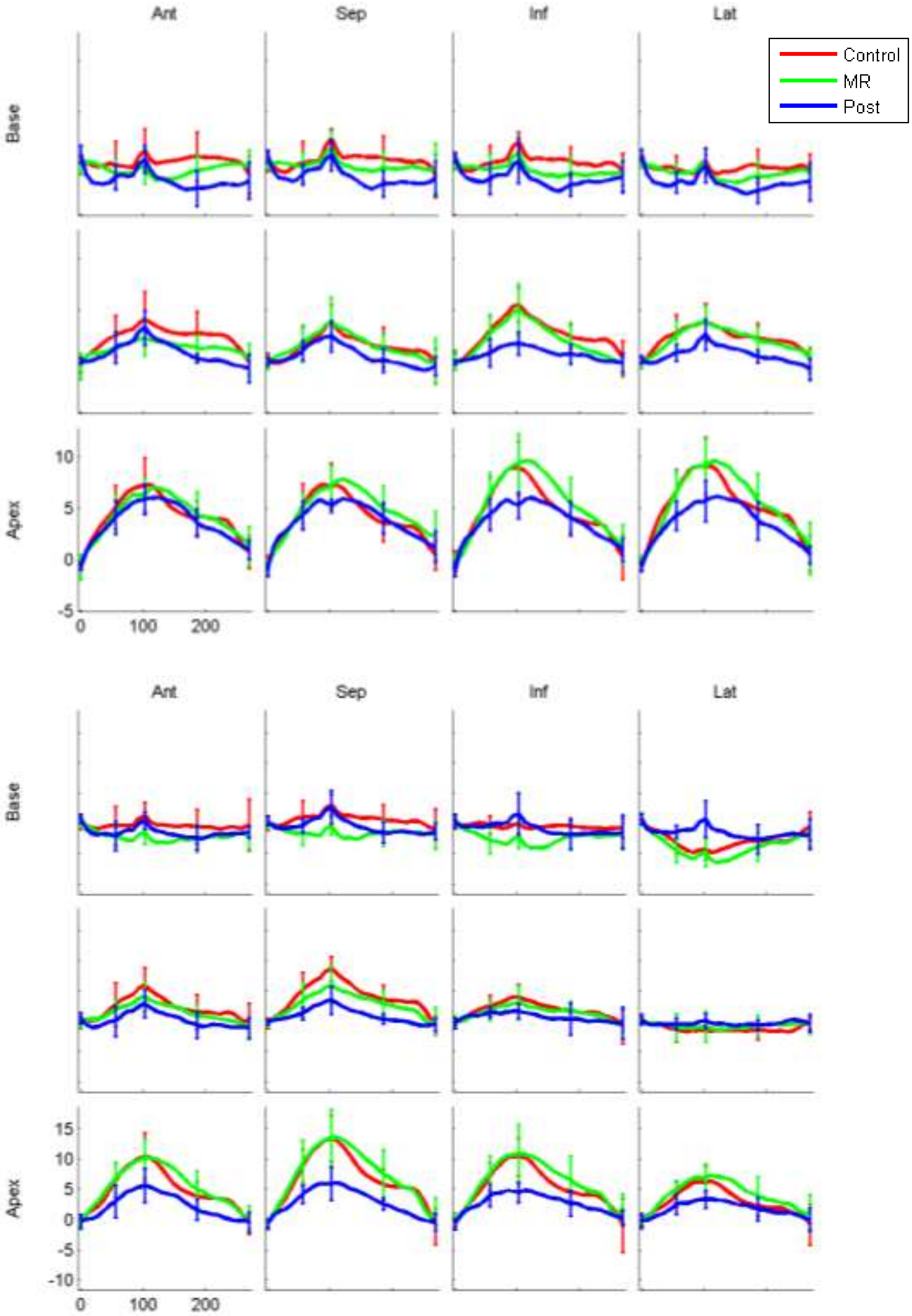

Figure 8.9 Averaged displacement (mm) corresponded to 1st timeframe of LA (top) and RA (bottom)

8.3.4 Strain Analysis

Table 8-19 and Table 8-20 show the statistical summary of the minimum principal strain of the control group and the MR group near the corresponded minimum volume phase, which

Table 8-18 Ventricular minimum strain analysis in the control and MR groups at LVES.

	Control (n=11)	**MR (n=16)**
	LV	
Basal Anterior	-0.24±0.026	-0.22±0.085
Basal Anteroseptal	-0.23±0.029	-0.21±0.070
Basal Inferoseptal	-0.24±0.025	-0.23±0.053
Basal Inferior	-0.25±0.035	-0.23±0.056
Basal Inferolateral	-0.24±0.039	-0.25±0.035
Basal Anterolateral	-0.25±0.023	-0.22±0.085
Middle Anterior	-0.23±0.035	-0.25±0.035
Middle Anteroseptal	-0.25±0.025	-0.23±0.052
Middle Inferoseptal	-0.25±0.028	-0.25±0.034
Middle Inferior	-0.25±0.023	-0.24±0.027
Middle Inferolateral	-0.24±0.024	-0.27±0.029
Middle Anterolateral	-0.24±0.020	-0.25±0.029
Apical Anterior	-0.22±0.021	-0.25±0.039
Apical Septal	-0.23±0.020	-0.26±0.040*
Apical Inferior	-0.24±0.022	-0.27±0.034*
Apical Lateral	-0.22±0.033	-0.25±0.042
	RV	
Basal Anterior	-0.24±0.075	-0.23±0.072
Basal Lateral	-0.26±0.053	-0.23±0.067
Basal Inferior	-0.29±0.043	-0.26±0.040
Basal Inferoseptal	-0.17±0.041	-0.19±0.036
Basal Anteroseptal	-0.22±0.057	-0.23±0.060
Basal Anterior	-0.29±0.030	-0.20±0.047
Middle Lateral	-0.16±0.052	-0.16±0.046
Middle Inferior	-0.26±0.044	-0.23±0.061
Middle Inferoseptal	-0.23±0.046	-0.25±0.067
Middle Anterorseptal	-0.21±0.035	-0.25±0.035*
Apical Anterior	-0.29±0.032	-0.19±0.053*
Apical Inferior	-0.29±0.044	-0.24±0.064*
Apical Septal	-0.30±0.024	-0.28±0.044
Outlet	-0.08±0.025	-0.09±0.023
Inlet	-0.10±0.015	-0.11±0.018

Values are Mean ± SD. *: P<0.05 vs. Control.

was LVES for ventricles and LA minimum phase (near LVED) for atria. The negative indicates the contraction of the myocardium. For the LV, the statistical decrease in magnitude only occurred in the apical region, which was consistent with previous work [42]. For the RV, statistically significant difference occurred in the middle and apical regions. For the LA and RA, most segments had a statistically significant decrease in magnitude in the MR group.

Table 8-19 Atrial minimum strain analysis in the control group and MR patient group at LA minimum volume phase.

	Control (n=11)	**MR (n=16)**
	LA	
Basal Anterior	-0.09±0.034	-0.04±0.053*
Basal Septal	-0.15±0.013	-0.07±0.071*
Basal Inferior	-0.09±0.036	-0.04±0.056*
Basal Lateral	-0.13±0.051	-0.05±0.048*
Middle Anterior	-0.21±0.035	-0.14±0.133
Middle Septal	-0.21±0.044	-0.11±0.093*
Middle Inferior	-0.20±0.043	-0.09±0.098*
Middle Lateral	-0.13±0.030	-0.07±0.068*
Apical Anterior	-0.27±0.042	-0.13±0.118*
Apical Septal	-0.24±0.033	-0.10±0.102*
Apical Inferior	-0.27±0.027	-0.15±0.122*
Apical Lateral	-0.25±0.032	-0.15±0.129*
	RA	
Basal Anterior	-0.14±0.037	-0.06±0.075*
Basal Septal	-0.13±0.034	-0.05±0.056*
Basal Inferior	-0.10±0.037	-0.05±0.072
Basal Lateral	-0.12±0.026	-0.07±0.082*
Middle Anterior	-0.28±0.050	-0.17±0.159
Middle Septal	-0.24±0.045	-0.13±0.135*
Middle Inferior	-0.18±0.062	-0.09±0.098*
Middle Lateral	-0.15±0.029	-0.11±0.125
Apical Anterior	-0.29±0.023	-0.17±0.142*
Apical Septal	-0.29±0.030	-0.19±0.155
Apical Inferior	-0.29±0.010	-0.17±0.140*
Apical Lateral	-0.26±0.029	-0.16±0.127*

Values are Mean ± SD. *: P<0.05 vs. Control.

Tables 8-21 to 8-22 show the minimum principal strain statistical summary of the control group (n=11), the pre-surgery group (n=6) and the post-surgery group (n=6). In the LV, strains tended to be elevated relative to controls before surgery and normalize after surgery. In the RV, strains, with the exception of two anterior segments, strains were not significantly different between controls and MR pre-surgery, but were lower than controls post-surgery. In the LA, strains were decreased in magnitude in the middle and apical levels relative to controls. Post-surgery, most of these segments returned to normal. The RA, in all but three segments, was not

Table 8-20 Ventricular minimum strain analysis in the surgical MR patients at LVES.

	Control (n=11)	**Pre (n=6)**	**Post (n=6)**
		LV	
Basal Anterior	-0.24±0.026	-0.26±0.034	-0.22±0.047
Basal Anteroseptal	-0.23±0.029	-0.25±0.032	-0.22±0.018
Basal Inferoseptal	-0.24±0.025	-0.26±0.008*	-0.23±0.029
Basal Inferior	-0.25±0.035	-0.25±0.021	-0.22±0.025
Basal Inferolateral	-0.24±0.039	-0.27±0.025	-0.24±0.025
Basal Anterolateral	-0.25±0.023	-0.25±0.041	-0.23±0.022
Middle Anterior	-0.23±0.035	-0.26±0.029	-0.22±0.016
Middle Anteroseptal	-0.25±0.025	-0.25±0.023	-0.23±0.032
Middle Inferoseptal	-0.25±0.028	-0.27±0.035	-0.22±0.022†
Middle Inferior	-0.25±0.023	-0.26±0.017	-0.22±0.034
Middle Inferolateral	-0.24±0.024	-0.28±0.038*	-0.23±0.028
Middle Anterolateral	-0.24±0.020	-0.26±0.031	-0.23±0.018
Apical Anterior	-0.22±0.021	-0.26±0.028*	-0.20±0.014†
Apical Septal	-0.23±0.020	-0.26±0.016*	-0.22±0.025†
Apical Inferior	-0.24±0.022	-0.27±0.019*	-0.21±0.019†*
Apical Lateral	0.22±0.033	-0.26±0.029	-0.22±0.018
		RV	
Basal Anterior	-0.24±0.075	-0.22±0.079	-0.19±0.034
Basal Lateral	-0.26±0.053	-0.23±0.080	-0.22±0.045
Basal Inferior	-0.29±0.043	-0.28±0.046	-0.27±0.073
Basal Inferoseptal	-0.17±0.041	-0.20±0.036	-0.16±0.023
Basal Anteroseptal	-0.22±0.057	-0.21±0.059	-0.22±0.020
Basal Anterior	-0.29±0.030	-0.21±0.064*	-0.19±0.074*
Middle Lateral	-0.16±0.052	-0.13±0.038	-0.14±0.043
Middle Inferior	-0.26±0.044	-0.21±0.074	-0.22±0.032
Middle Inferoseptal	-0.23±0.046	-0.28±0.062	-0.24±0.022
Middle Anterorseptal	-0.21±0.035	-0.24±0.035	-0.21±0.039
Apical Anterior	-0.29±0.032	-0.20±0.083*	-0.20±0.056*
Apical Inferior	-0.29±0.044	-0.25±0.051	-0.23±0.048*
Apical Septal	-0.30±0.024	-0.29±0.047	-0.26±0.037*
Outlet	-0.08±0.025	-0.09±0.027	-0.08±0.040
Inlet	-0.10±0.015	-0.11±0.021	-0.11±0.015

Values are Mean ± SD. *: P<0.05 vs. Control. †: P <0.05 vs. Pre.

statistically different than controls, but after surgery, RA strains were decreased in magnitude in the apical level relative to both pre-surgery and controls.

Table 8-21 Atrial minimum strain analysis in the surgical MR patients at LA minimum volume phase.

	Control (n=11)	Pre (n=6)	Post (n=6)
		LA	
Basal Anterior	-0.09±0.034	-0.09±0.016	-0.07±0.031
Basal Septal	-0.15±0.013	-0.11±0.035*	-0.12±0.012*
Basal Inferior	-0.09±0.036	-0.07±0.044	-0.10±0.041
Basal Lateral	-0.13±0.051	-0.08±0.026	-0.10±0.047
Middle Anterior	-0.21±0.035	-0.21±0.082	-0.23±0.027
Middle Septal	-0.21±0.044	-0.16±0.044	-0.19±0.042
Middle Inferior	-0.20±0.043	-0.13±0.028*	-0.14±0.026*
Middle Lateral	-0.13±0.030	-0.09±0.035*	-0.12±0.053
Apical Anterior	-0.27±0.042	-0.17±0.060*	-0.20±0.055*
Apical Septal	-0.24±0.033	-0.14±0.072*	-0.20±0.069
Apical Inferior	-0.27±0.027	-0.21±0.061*	-0.22±0.060
Apical Lateral	-0.25±0.032	-0.20±0.049*	-0.22±0.042
		RA	
Basal Anterior	-0.14±0.037	-0.12±0.040	-0.11±0.029
Basal Septal	-0.13±0.034	-0.08±0.039*	-0.10±0.062
Basal Inferior	-0.10±0.037	-0.09±0.046	-0.10±0.084
Basal Lateral	-0.12±0.026	-0.12±0.063	-0.11±0.043
Middle Anterior	-0.28±0.050	-0.29±0.031	-0.22±0.073
Middle Septal	-0.24±0.045	-0.21±0.040	-0.17±0.034*
Middle Inferior	-0.18±0.062	-0.13±0.058	-0.14±0.071
Middle Lateral	-0.15±0.029	-0.21±0.042*	-0.18±0.047†
Apical Anterior	-0.29±0.023	-0.27±0.033	-0.20±0.055†*
Apical Septal	-0.29±0.030	-0.28±0.020	-0.21±0.062*
Apical Inferior	-0.29±0.010	-0.26±0.020*	-0.19±0.069*
Apical Lateral	-0.26±0.029	-0.24±0.018	-0.21±0.026†*

Values are Mean ± SD. *: $P<0.05$ vs. Control. †: $P<0.05$ vs. Pre.

Figures 8.10 and 8.11 show the principal minimum strain of the control group (n=11), the MR patient group (n=16) and the post-surgery group (n=6). In the LV, the differences among the curves were small, except near LVES. In the RV, the control group strains were larger in magnitude only in several segments in the basal and middle regions. In the LA, the MR group had different shape compared to the control group in all layers. After surgery, the strain time curves were returning towards the control group. In the RA, the control group had smaller strains and surgery had a small effect on the strain curves.

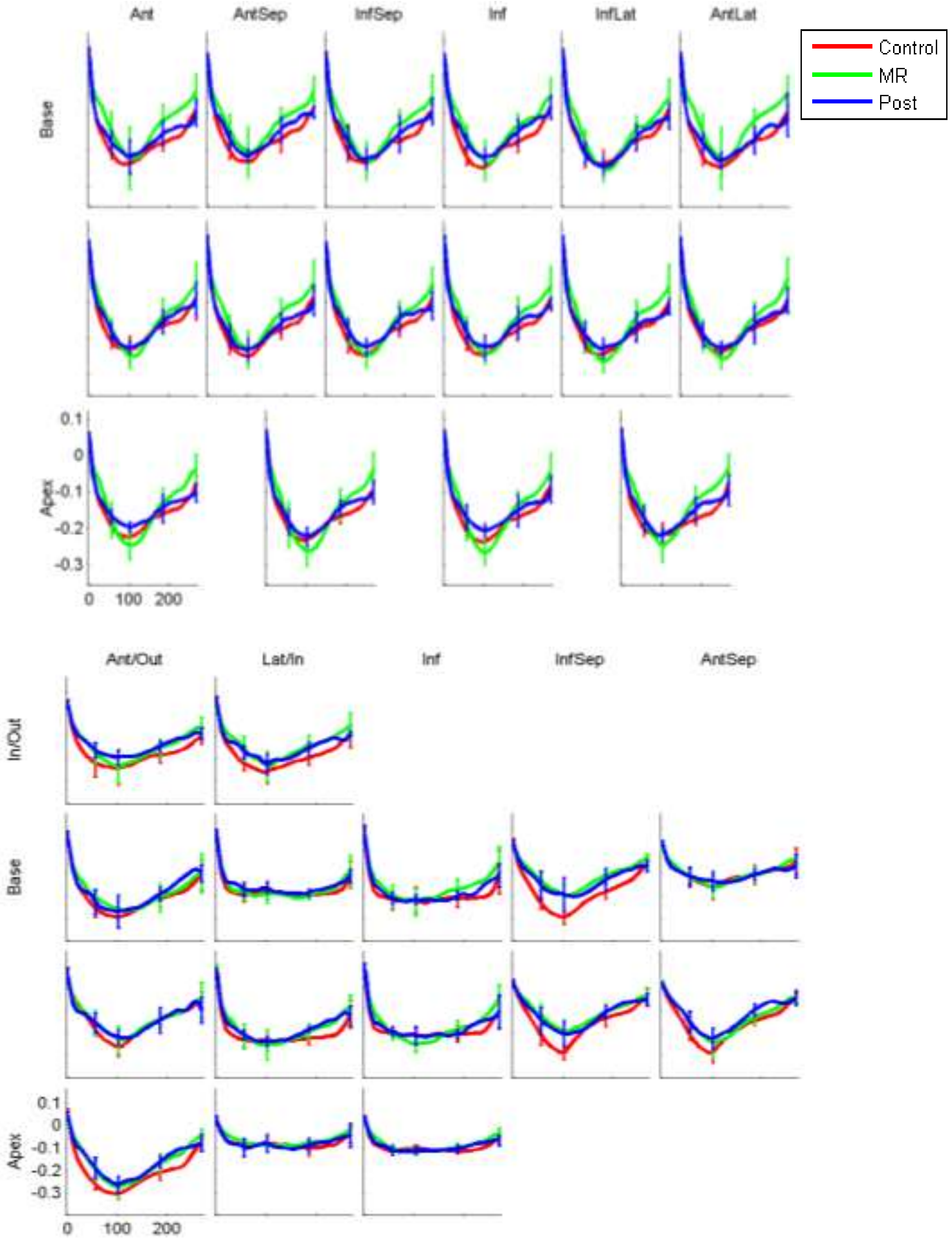

Figure 8.10 Averaged principal minimum strain of LV (top) and RV(bottom). Mean ± SD.

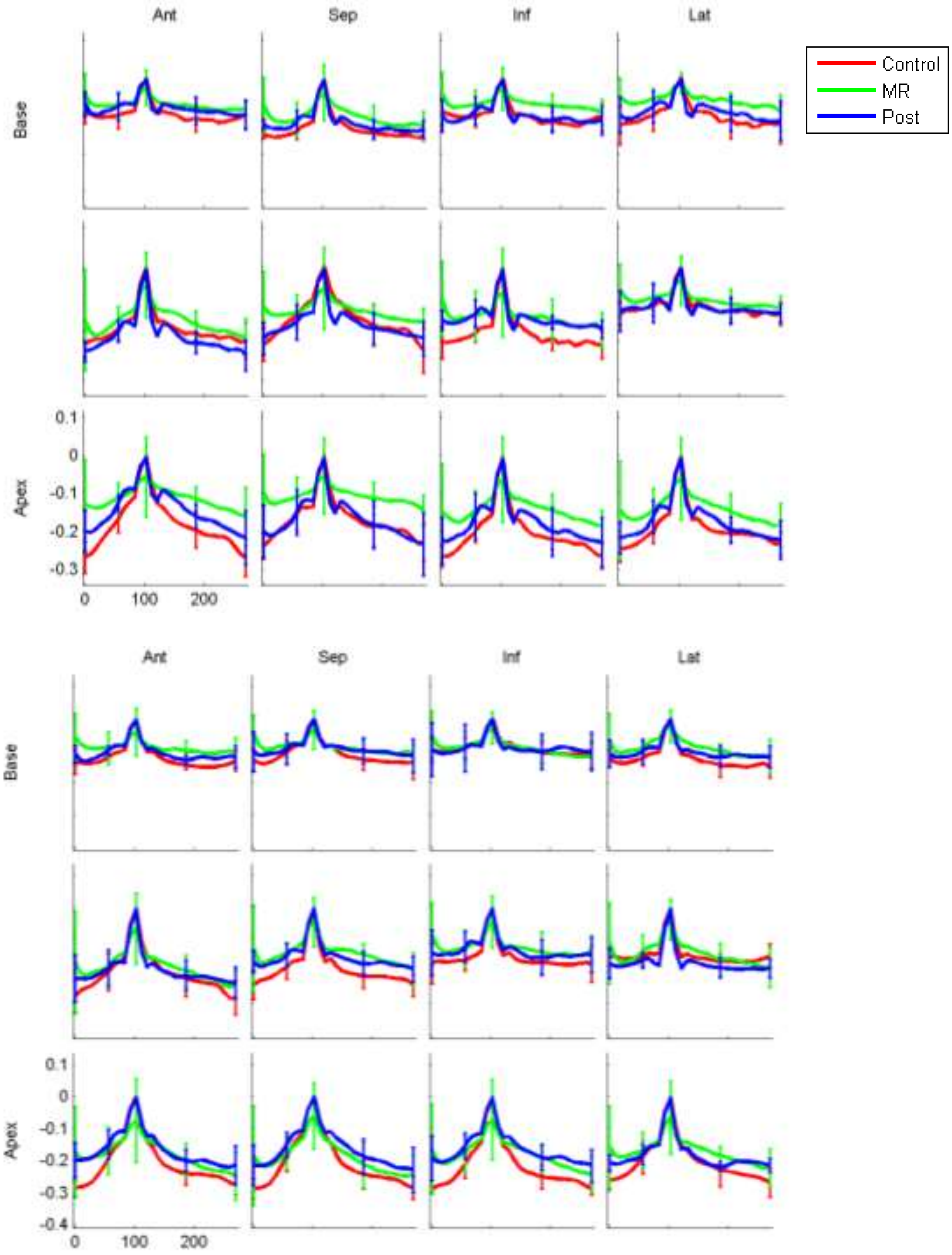

Figure 8.11 Averaged principal minimum strain of LA (top) and RA(bottom). Mean ± SD.

8.4 Discussion

This study demonstrates remodeling of MR patients in the size, volume function and mechanics of heart chambers. The MR-associated remodeling is marked by several size features companied with strain change as well as mutual relationship difference. Taken together these findings suggest that MR likely contribute to alterations in both structures and functions of other chambers in addition to LV and LA sizes. The major MR-associated remodeling and MV-surgery effect in this study are three-fold.

First, MR was associated with structure alternations In the LV, LA and RA [97] [113] [153]. In [42], the author reported the importance of LV apex remodeling in MR progression. In our study, we found the LV apex remodeling happened in both the longitudinal and circumferential directions based on the curvature assessment. In [153], the author proposed that LA volume has the potential in predicting heart failure, since LA volume is a sensitive barometer of LV filling pressure. In our study, we found the enlargement of LA is 50% to 120%, which has the potential to affect future surgery guidelines. In addition to the LA and LV enlargement as previous studies [97] [113] [153], this study also showed the MR-associated alternation in the RA size, which had consistent enlargement across the whole cardiac cycle, though the enlargement did not reach a significant level. The size of the LV, LA and RA returned to normal after surgery.

Current research mainly lies in the LA and LV, due to the direct connection of the 2-chambers to the mitral valve. The right side of the heart is thought to be relatively unaffected by MRI. To the best of our knowledge, the only study to investigate the RA with MR is [154], which reported no change in the RA volumes and function between MR patients and controls. While our results also showed no significant changes in volumes, we found differences in active and total EF as well as differences in wall displacement and strain. More work needs to be done in the effort to explain the RA changes in patients with MR. In addition to the volume of each chamber independently, we found MR-associated changes in mutual relationship among chambers. The volume ratio of LA/LV increased in MR patients, while the ratios of RA/LA and RV/LV decreased significantly. After surgery, the ratios of RV/LV and RA/LA returned to normal, but the LA/LV ratio increased at a larger degree.

Secondly, we found MR-associated changes in volume function. As expected, LV had a significant decrease in EF, though the LVEF was still within the normal range [144]. In addition to the LV volume function changes, we also found changes in the LA volume function – in particular, a significant decrease in total EF. Both LA passive EF and active EF decreased, while the author in [154] only found LA active EF decreases and unchanged LA passive EF in MR patients [154]. This difference may due to the different method used in [154], which utilized 3D echocardiography. Regardless of the LA passive EF, the total LAEF decreased, which suggests that LA volume and function could be utilized to determine surgical timing.

Thirdly, MR was associated with changes in chamber mechanics. Regional wall motion showed significant differences in the LA in the basal segments and in the RV and RA for several segments in the basal and middle regions. The LA and RA were most sensitive to strain changes and tended to normalize after surgery.

8.5 Conclusion

In an attempt to define the remodeling of heart chambers due to MR, we measured and compared the geometry, volume and mechanics with age-matched normal subjects. To estimate the MV surgery effect, we conducted the comparison analysis from the six-month follow-ups with the same pre-surgery patients. The main finding in this study was the remodeling of RA in addition to that of LV and LA in the MR patients. The remodeling was not limited to volumes, but also includes volume functions and mechanics. With a limited number of follow-ups, we found the MV surgery remodeled LV, LA, and RA in size, and significantly changed the motion of all 4-chambers. However, to further track the effect of valve surgery on hearts, more data from patients after surgery is needed.

Chapter 9 CONCLUSION AND FUTURE WORK

9.1 Conclusion

In this dissertation, the background of the research was first introduced, including heart anatomy, cardiac functions, mitral regurgitation and the cardiac imaging modalities. The standard MRI protocols used in this dissertation were also described in the first chapter. It was followed by the literature review on heart surface modeling, in which the current techniques were summarized and compared.

Motivated by clinical needs and with the pursuit to resolve some of the current issues in methods of heart fitting from MRI-based images, the first study in this dissertation was to develop a novel algorithm of fitting 4D heart surfaces from highly anisotropic 2D MRI data, which included the triangulated mesh generation, mesh smoothing, and propagation. This algorithm works well on both atria and ventricles without any shape assumption or prior-knowledge model. Several parameters of chamber shape and function can be computed from the meshes: volumes, surface area, curvatures, displacement, and strain. This algorithm was validated through three aspects: volume function analysis comparison with disk summation method, geometry comparison with perfect prolate spheroid and B-spline LV models, and strain comparison with tMRI-based methods.

To evaluate and characterize the continuous volumes, mechanics and geometries of all four chambers versus age, we presented a study on in-vivo data of both young and old healthy subjects using the proposed surface fitting algorithm. This study represents the first study to combine the analyses of 3D geometries and wall motions along with volume functions for all four chambers with continuous measurements across a cardiac cycle on the young and old healthy subjects from cine MRI data. In this study, we find the geometry and volume function remodeling in all four chambers. In addition to the findings in size enlargement and ejection fraction decrease in the LA, and increase in the LV mass to volume ratio, which are consistent with previous studies [148-150], we also find that RA and RV develop a small enlargement with aging. The RA function remodeling shows the similar behavior as in the LA, which has increase in ejection volume while decrease in ejection fraction. For the LA enlargement, we find it occurs in both longitudinal and circumferential directions. In the age-related remodeling in regional mechanics, we find the no age-associated effects on regional motion, while the strain is decreasing in magnitude in the contraction direction with aging [152]. Moreover, we explored the mutual relationship by computing the volume ratios, which shows decrease in the LA/LV, RV/LV and RA/RV ratios with aging.

The proposed surface fitting algorithm was further applied on a preliminary clinical study in an attempt to define the remodeling of heart chambers due to mitral regurgitation and MV surgery. The results were compared between the MR patients and age-matched controls, and between the same patients before they had surgery and six-month after surgery. We find that LV and LA sizes enlarge in MR and reduce after surgery as expected [97] [113], besides that, we also find that RA enlarges in MR as well. MR is associated with reduced volume functions in the LV as in prior studies [144], and LA. However, the displacement is not affected by MR pathology while the contraction strain is reduced in the MR patients. It seems RV is not alternated due to the MR and MV surgery. MV surgery reduced the wall motion of all four chambers consistently in the cardiac cycle.

This research has both clinical and technical significance, especially through analysis of chambers beyond left ventricle. The first study plays an important role in developing novel techniques in shape analysis of whole heart and provides more detailed information of all four chambers from cine MRI data. The second study helps the understanding of normal atria volumetric functions, geometries and mechanics along with ventricular analysis versus age. The third study provides a potential clinical application of the 4D heart surface fitting algorithm and analysis for evaluating the atria and ventricular remodeling in MR patients along with monitoring after surgery.

9.2 Directions for Future Work

Further tracking of the valve surgery effect on hearts can be done in the future. In this dissertation, the tracking was measured on a limited number of available follow-up datasets. In the future, more surgery follow-ups can be acquired for analysis to evaluate the surgery effect on heart remodeling. Another potential future work is to apply the proposed algorithm on different pathologies. In this dissertation, we explored the remodeling of heart in MR patients with preserved left ventricle ejection fraction. In the future, we can explore the remodeling the heart for different pathologies, such as high blood pressure, diabetes and other valvular heart disease.

REFERENCES

[1] “http://www.theheartfoundation.org/heart-disease-facts/heart-disease-statistics”.

[2] T. Le Tourneau, D. Messika-Zeitoun, A. Russo, D. Detaint, Y. Topilsky, DW. Mahoney. Impact of left atrial volume on clinical outcome in organicmitral regurgitation. J Am Coll Cardiol 2010; 56:570–8.

[3] L. Ling, M. Enriquez-Sarano, J. Seward, A. Tajik, H. Schaff, K. Bailey et al. Clinical outcome of mitral regurgitation due to fail leaflet. N Engl J Med 1996; 335:1417–23.

[4] A. Borg, K. Pearce, S. Williams, S. Ray. Left atrial function and deformation in chronic primary mitral regurgitation. Eur J Echocardiogr 2009; 10:833–40.

[5] X. Zhang, S, Llyod, et al. Left Atrial Enlargement and Systolic Failure Measured By Cardiac MRI In Severe Isolated Mitral Regurgitation With Preserved Left Ventricular Ejection Fraction, ISMRM, 2017, 2868.

[6] K.A. Ahtarovski, K.K. Iversen. Left atrial and ventricular function during dobutamine and glycopyrrolate stress in healthy young and elderly as evaluated by cardiac magnetic resonance. Am J Physiol Heart Circ Physiol. 2012.

[7] K. Posina, J. McLaughlin, et al. Relationship of phasic left atrial volume and emptying function to left ventricular filling pressure: a cardiovascular magnetic resonance study. Journal of Cardiovascular Magnetic Resonance, 2013.

[8] C. Dong, G. Wang. Curvatures estimation on triangular mesh. J Zhejing Univ SCI. 2005.

[9] N. Voelkel, R. Quaife; Report of a National Heart, Lung, and Blood Institute Working Group on Cellular and Molecular Mechanisms of Right Heart

[10] E. C. Lin, S. R. Klepac, and E. J. Samett, "Cardiac MRI–technical aspects primer," E-medicine [online].

[11] Clifford R. Greyson, Evaluation of Right Ventricular Function, Curr Cardiol Rep (2011) 13:194–202;

[12] E. Nagel, M. Stuber, O.M.Hess, Importance of the right ventricle in valvular heart disease. European Heart Jornal, 1996, 17,829-826.

[13] "http://www.texasheartinstitute.org/hic/anatomy/anatomy2.cfm"

[14] “www.aireurbano.com”, 2015. Human heart diagram labeled.

[15] R. E. Klabunde, Cardiovascular physiology concepts. Lippincott Williams & Wilkins, 2005.

[16] “http://www.phschool.com/science/biology_place/biocoach/cardio2/circuits.html”

[17] W.K., Purves, D. Sadava and G.H. Orians, Life: The Science of Biology: Volume III: Plants and Animals. Vol. 3. 2004: WH Freeman & Co.

[18] "http://www.cvphysiology.com"

[19] McMurray, J.J.V. and M.A. Pfeffer, Heart failure. The Lancet, 2005. 365(9474): 1877-1889.

[20] B Liu, N. Edwards, et al. Timing surgery in mitral regurgitation: defining risk and optimising intervention using stress echocardiography, echoresearch and prctices.

[21] Markwick A, Lee L, Horsfall M, Sinhal A, Chew D. TCT-784 Prognostic implications of moderate and severe mitral regurgitation in contemporary clinical care. J Am Coll Cardiol. 2012.

[22] Nishimura RA, Otto CM, et al. 2017 AHA/ACC focused update of the 2014 AHA/ACC guideline for the management of patients with valvular heart disease: a report of the American College of Cardiology/American Heart Association Task Force on Clinical Practice Guidelines. Circulation. 2017;

[23] X. Zhang, S. Lloyd, Four Chamber Endocardial Surface Reconstruction from Cardiac MRI Data, ISMRM, 2017, 3156.

[24] Q. Duan, E. D. Angelini, and A. F. Laine, "Real-time segmentation by Active Geometric Functions," Computer methods and programs in biomedicine, vol. 98, pp. 223-230, 2010.

[25] Q. Tao, E. Ipek, et al. Fully automatic segmentation of left atrium and pulmonary veins in the LAte gadolinium-enhanced MRI: Towards objective atrial scar assessment. J Magn Reson Imaging, 2016 Aug;44(2):346-54.

[26] J. K. Udupa, L. Wei, S. Samarasekera, Y. Miki, M. Van Buchem, and R. I. Grossman, "Multiple sclerosis lesion quantification using fuzzy-connectedness principles," Medical Imaging, IEEE Transactions on, vol. 16, pp. 598-609, 1997.

[27] M. Kass, A. Witkin, and D. Terzopoulos, "Snakes: Active contour models," International journal of computer vision, vol. 1, pp. 321-331, 1988.

[28] J. A. Sethian, Level set methods and fast marching methods. Cambridge Cambridge Univeristy Press, 1999.

[29] S. Osher and R. P. Fedkiw, Level set methods and dynamic implicit surfaces. vol. 153 Springer Verlag, 2003.

[30] T. F. Chan and L. A. Vese, "Active contours without edges," Image Processing, IEEE Transactions on, vol. 10, pp. 266-277, 2001.

[31] E. D. Angelini, S. Homma, G. Pearson, J. W. Holmes, and A. F. Laine, "Segmentation of real-time three-dimensional ultrasound for quantification of ventricular function: a clinical study on right and left ventricles," Ultrasound in medicine & biology, vol. 31, pp. 1143-1158, 2005.

[32] T. Cootes, C. Taylor, D. Cooper, J. Graham, and A. Lanitis, "Active shape models," Computer vision and image understanding, vol. 61, pp. 38-59, 1995.

[33] T. F. Cootes, G. J. Edwards, and C. J. Taylor, "Active appearance models," Pattern Analysis and Machine Intelligence, IEEE Transactions on, vol. 23, pp. 681-685, 2001.

[34] T. F. Cootes, C. J. Taylor, D. H. Cooper, and J. Graham, "Active shape models-their training and application," Computer vision and image understanding, vol. 61, pp. 38-59, 1995.

[35] C. Petitjean and J. N. Dacher, "A review of segmentation methods in short axis cardiac MR images," Medical Image Analysis, vol. 15, pp. 169-184, 2011.

[36] C. Moyer, P. Helm, et al. Wall-motion Based analysis of global and regional left atrial mechanics, IEEE Transactions on medical imaging, vol.32, 2013.

[37] C.W. Lim, Y. Su, et al. Automatic 4D reconstruction of patient-specific cardiac mesh with 1-to-1 vertex correspondence from segmented contours lines. PLOS ONE, 2014.

[38] M. Gonzales, G. Sturgeon, A three-dimensional finite element model of human atrial anatomy: New methods for cubic Hermite meshes with extraordinary vertices. Medical Image Analysis, 2013, 525-537.

[39] W. E. Lorensen and H. E. Cline, "Marching cubes: A high resolution 3D surface construction algorithm," ACM Siggraph Computer Graphics, vol. 21, pp. 163-169, 1987.

[40] R. Manzke, C. Meyer, et al. Automatic Segmentation of Rotational X-Ray Images for Anatomic Intra-Procedural Surface Generation in Atrial Fibrillation Ablation Procedures. IEEE Transactions on Medical Imaging. 2010.

[41] Chun G. Schiros. Biventricular Active Mesh Model of the Heart and Analysis of Morphologic Changes Toward Physiology and Pathologies. Auburn University dissertation, 2012.

[42] Skrinjar, and A. Bistoquet. Generation of Myocardial Wall Surface Meshes from Segmente dMRI. International Journal of Biomedical Imaging Volume 2009, Article ID 313517.

[43] B.Delhay, J. Lotjonen, Dynamic 3-D Cardiac Surface Model from MR Images. IEEE, 2005.

[44] R. Karim et al, Surface flattening of the human left atrium and proof-of-concept clinical applications, 2014, Computerized Medical Imaging and Graphics 38 (2014) 251–266.

[45] Ecabert, J. Peters, et al. Automatic whole heart segmentation in static magnetic resonance image volumes. In Medical image computing and computer-assisted intervention – MICCAI 2007. p. 402–10.

[46] D. Suna, M.E. Rettmanna et al, Simulated evaluation of an intraoperative surface modeling method for catheter ablation by a real phantom simulation experiment, 2015, Proc SPIE Int Soc Opt Eng. 9415: doi:10.1117/12.2082478

[47] P. Jiamsripong, T. Honda,et al.Three methods for evaluation of left atrial volume. European Journal of Echocardiography (2008) 9, 351–355.

[48] Q. Tao, E. Ipek. Fully automatic left atrium and pulmonary veins segmentation For the LAte gadolinium enhanced MRI combining contrast enhanced MRA. ISMRM, 2016, 0137

[49] E. Bardinet, L. D. Cohen, and N. Ayache, "A parametric deformable model to fit unstructured 3D data," Computer vision and image understanding, vol. 71

[50] H. Huang, L. Shen, R. Zhang, F. Makedon, B. Hettleman, and J. Pearlman, "Surface alignment of 3D spherical harmonic models: Application to cardiac MRI analysis," Medical Image Computing and Computer-Assisted Intervention–MICCAI 2005, pp. 67-74, 2005.

[51] L. H. Staib and J. S. Duncan, "Model-based deformable surface finding for medical images," Medical Imaging, IEEE Transactions on, vol. 15, pp. 720-731, 1996.

[52] Goshtasby and D. A. Turner, "Segmentation of cardiac cine MR images for extraction of right and left ventricular chambers," Medical Imaging, IEEE Transactions on, vol. 14, pp. 56-64, 1995.

[53] P. Hunter and B. Smaill, "The analysis of cardiac function: a continuum approach," in Progress in biophysics and molecular biology, 1988, p. 101.

[54] B. Vallet, E. Angelini, and A. Laine, "Variational segmentation framework in prolate spheroidal coordinates for 3D real-time echocardiography," in Medical Imaging 2006: Image Processing, 2006, pp. 1370-1380.

[55] Matheny and D. B. Goldgof, "The use of three-and four-dimensional surface harmonics for rigid and nonrigid shape recovery and representation," Pattern Analysis and Machine Intelligence, IEEE Transactions on, vol. 17, pp. 967-981, 1995.

[56] V. D. Liseikin, Grid generation methods. Springer Verlag, 2009.

[57] Ekoule, F. Peyrin, and C. Odet, "A triangulation algorithm from arbitrary shaped multiple planar contours," ACM Transactions on Graphics (TOG), vol. 10, pp. 182-199, 1991.

[58] Vijarnsorn, K.Myers, et al, Evaluation of single right atrial volume and function with magnetic resonance imaging in children with hypoplastic left heart, Pediatr Radiol (2016) 46:991–1002

[59] Y. Zheng, T. Wang et al, Multi-part left atrium modeling and segmentation in C-Arm CT Volumes for Atrial Fibrillation Ablation.

[60] L. Zhong, L. Gobeawan, et al. Right ventricular regional wall curvedness and area strain in patients with repaired tetralogy of Fallot. Am J Physiol Heart Circ Physiol, 2012.

[61] X. Zhang, G. C. Schiros, et al. Mitral Annular Kinetics in Mitral Regurgitation, Journal of Cardiovascular Magnetic Resonance, J Cardiovasc Magn Reson (2014) 16(Suppl 1): P269. doi:10.1186/1532-429X-16-S1-P269

[62] X. Zhang, N. Jha, et al. A Novel Aprroach to Comprehensive Atrio-ventricular Functional Analysis, ISMRM, 2015,5630.

[63] F. Mahmood, B. Subramaniam. Three-Dimensional Echocardiographic Assessment of Changes in Mitral Valve Geometry After Valve Repair. Ann Thorac Surg. 2009 December; 88(6): 1838–1844. D

[64] Assessment of Mitral Valve Complex by Three-Dimensional Echocardiography: Therapeutic Strategy for Functional Mitral Regurgitation

[65] Andrew B, Kelly W, et al. Modeling left atrial volume, shape, and contraction patterns in normal subjects by cardiac magnetic resonance imaging, International J of Cardiology, 2013

[66] Saul G Myerson, Heart valve disease: investigation by cardiovascular magnetic resonance, Journal of Cardiovascular Magnetic Resonance 2012, 14:7

[67] John A.Sallach, W.H.Wilson Tang, et al, Right Atrial Volume Index in Chronic Systolic Heart Failure and Prognosis, JACC: cardiovascular imaging, 2009.

[68] Roberto M. Lang, Luigi P, et al. Recommendations for Cardiac Chamber Quantification by Echocardiography in Adults: An Update from the American Society of Echocardiography and the European Association of Cardiovascular Imaging. J Am Soc Echocardiogr 2015; 28:1-39

[69] Maceira, J. Cosin-Sales, et al. Reference right atrial dimensions and volume estimation by steady state free precession cardiovascular magnetic resonance. Maceira et al. Journal of Cardiovascular Magnetic Resonance 2013, 15:29.

[70] David Messika-Zeitoun, Michael Bellamy, et al. Left atrial remodelling in mitral regurgitation—methodologic approach, physiological determinants, and outcome implications: a prospective quantitativeDoppler-echocardiographic and electron beam-computed tomographic study.Eurn Heart J 2007 28, 1773–1781.

[71] L. Ring, B. Ranna et al, Dynamics of the tricuspid valve annulus in normal and dilated right hearts: a three-dimensional transoesophageal echocardiography study. European Hear Jornal-cardiovascular Imaging, 756-762, 2012.

[72] Sherif M, Mohsen A. et al. Global left atrial dysfunction and regionalheterogeneity in primary chronic mitral insufficiency. European Journal of Echocardiography (2011) 12, 384–393 doi:10.1093/ejechocard/jer033

[73] Y. Takagi, S Ehara, et al. Comparison of determinations of left atrial volume by the biplane area-length and Simpson’s methods using 64-slice computed tomography.Journal of Cardiology (2009) 53, 257—264.

[74] Y. Zheng, A. Barbu, Four-Chamber Heart Modeling and automatic segmentation for 3-D cardiac CT volumes using marginal space learning and steerable features, IEEE Transcation on medical imaging, vol.27, 2008.

[75] S.P. Raya, J.K.Udupa,Shape-Based Interpolation of Multidimensional Objects. IEEE TRANSACTIONS ON MEDICAL IMAGING, VOL. 9, NO. I, MARCH 1990.

[76] A.R.Patel, O.Fatemi et al, Cardiac Cycle Dependent Left Atrial Dynamics: Implications for Catheter Ablation of Atrial Fibrillation.Heart Rhythm. 2008 June; 5(6): 787–793. 2008.03.003

[77] W. Feng, H. Nagaraj, H. Gupta, S. G. Lloyd, I. Aban, G. J. Perry, D. A. Calhoun, L. J. Dell'Italia, and T. S. Denney, "A dual propagation contours technique for semi-automated assessment of systolic and diastolic cardiac function by CMR," J Cardiovasc Magn Reson, vol. 11, pp. 11-30, 2009.

[78] J. Lotjonen, S. Kivisto, et al. Statistical shape model of atria, ventricles and epicardium from short- and long-axis MR images, Medical Image Analysis 8 (2004) 371–386

[79] Ecabert O, Peters J, et al. Whole heart segmentation in static magnetic resonance image volumes. Medical image computing and computer-assisted intervention-MICCAI 2007.

[80] T. Erber and G. Hockney, "Equilibrium configurations of N equal charges on a sphere,"Journal of Physics A: Mathematical and General, vol. 24, p. L1369, 1991.

[81] E. W. Weisstein, "Delaunay triangulation," From MathWorld–A wolfram Web Resource.

[82] L. Kobbelt, S. Campagna, J. Vorsatz, and H.-P. Seidel, Interactive multi-resolution modeling on arbitrary meshes. In ACM Computer Graphics (SIGGRAPH ’98 Pro-ceedings), pp. 105–114, 1998.

[83] M. Enriquez-Sarano, A. J. Tajik, H. V. Schaff, T. A. Orszulak, M. D. McGoon, K. R.Bailey, and R. L. Frye, "Echocardiographic prediction of left ventricular function after correction of mitral regurgitation: results and clinical implications," Journal of the American College of Cardiology, vol. 24, pp. 1536-1543, 1994.

[84] K. Hormann, U. Labsik, and G. Greiner. Remeshing triangulated surfaces with optimal parametrizations. Computer-Aided Design, 33(11):779–788, 2001

[85] X. Wang, T. Chen, Meshless deformable models for 3D cardiac motion and strain analysis from tagged MRI. Magnetic Resonance Imaging 33, 2015, 146-160.

[86] R. Leischik, H. Littwitz. Echocardiographic Evaluation of Left Atrial Mechanics: Function, History, Novel Techniques, Advantages, and Pitfalls. BioMed Research International. 2015.

[87] G.Q. Roca, P. Campbell, et al. Right Atrial Function in Pulmonary Arterial Hypertension. Circ Cardiovasc Imaging. 2015.

[88] W. Bommer, L. Weinert, el l. Determination of right atrial and right ventricular size by Two-Dimensional Echocardiography.Circulation. 1979;60:91-100.

[89] S.Fukuda, G. Saracino, et al. Three-Dimensional Geometry of the Tricuspid Annulus in Healthy Subjects and in Patients with Functional Tricuspid Regurgitation A Real-Time, 3-Dimensional Echocardiographic Study. Circulation, 2006, 114: I-492-I498.

[90] X. Chen and F. Schmitt, "Intrinsic surface properties from surface triangulation," 1992, pp. 739-743.

[91] J. Zhu, J. Chen, et al. Comparison of left atrial function in healthy individuals versus patients with non-ST-segment elevation myocardial infarction using two-dimensional speckle tracking echocardiography. CARDIOVASCULAR JOURNAL OF AFRICA, 2013, Vol 24, No 5.

[92] G. Roca; P. Campbell, Right Atrial Function in Pulmonary Arterial Hypertension. Circ Cardiovasc Imaging. 2015.

[93] S. Malik, D. Kwan, The Right Atrium: Gateway to the Heart—Anatomic and Pathologic Imaging Findings. RadioGraphics 2015; 35:14–31.

[94] Rai; E. Lima E. Speckle Tracking Echocardiography of the Right Atrium: The Neglected Chamber. Clin. Cardiol. 2015. 38, 11, 692–697.

[95] Z. Samad, P. Kaul, L. K. Shaw, D. D. Glower, E. J. Velazquez, P. S. Douglas, and J. G. Jollis, "Impact of early surgery on survival of patients with severe mitral regurgitation," Heart, vol. 97, p. 221, 2011.

[96] B.D. Hoit. Atrial Functional Mitral Regurgitation, Jornal of the American College of Cardiology, 2011, Vol. 58, No. 14.

[97] M. Maiello, R. Sharman, et al. Differential Left Atrial Remodeling in the LV Diastolic Dysfunction and Mitral Regurgitation. 2009, Journal Compilation.

[98] M. I. Ahmed, J. D. Gladden, S. H. Litovsky, S. G. Lloyd, H. Gupta, S. Inusah, T. S. Denney, P. Powell, D. C. McGiffin, and L. J. Dell'Italia, "Increased oxidative stress and cardiomyocyte myofibrillar degeneration in patients with chronic isolated mitral regurgitation and ejection fraction> 60%," J Am Coll Cardiol, vol. 55, pp. 671-679, 2010.

[99] D. H. Adams, R. Rosenhek, and V. Falk, "Degenerative mitral valve regurgitation: best practice revolution," European heart journal, vol. 31, p. 1958, 2010.

[100] Y. Ohtake, A. Belyaev at al. Mesh regularization and adaptive smoothing. Computer-Aided Design. 2001.

[101] Nealen, T. Igarashi, et al. Laplacian Mesh Optimization. Proceedings of the 4th International Conference on Computer Graphics and Interactive Techniques in Australasia and Southeast Asia 2006, Kuala Lumpur, Malaysia, November 29 - December 2, 2006

[102] M. Desbrun, M. Meyer, et al. Implicit fairing of irregular meshes using diffusion and curvature flow. Proceedings of Siggraph, 1999.

[103] G. Taubin. A signal processing approach to fair surface design. Computer Graphics SIGGRAPH 95 Proceedings. 1995.

[104] G. Taubin. Curve and surface smoothing without shrinkage. International Conference on Computer Vision, 1995.

[105] Sorkine, Laplacian Mesh Processing. EUROGRAPHICS 2005.

[106] J. Vollmer, R. Mencl, and H. Müller Improved Laplacian Smoothing of Noisy Surface Meshes, EUROGRAPHICS ’99 / P. Brunet and R. Scopigno,199

[107] M. Enriquez-Sarano, Timing of mitral valve surgery, Heart 2002, 79-85.

[108] Enriquez-Sarano M, Suri RM, Clavel MA, Mantovani F, Michelena HI, Pislaru S, Mahoney DW & Schaff HV 2015 Is there an outcome penalty linked to guideline-based indications for valvular surgery? Early and long-term analysis of patients with organic mitral regurgitation. Journal of Thoracic and Cardiovascular Surgery 150 50–58.

[109] M. Enriquez-Sarano, R. Suri, et al. Is there an outcome penalty linked to guideline-based indications for valvular surgery? Early and long-term analysis of patients with organic mitral regurgitation. The Journal of Thoracic and Cardiovascular Surgery. Volume 150, Issue 1, July 2015, Pages 4-5.

[110] David TE, Armstrong S, McCrindle BW & Manlhiot C 2013 Late outcomes of mitral valve repair for mitral regurgitation due to degenerative disease. Circulation 127 1485–1492.

[111] Biner S, Rafique A, Rafii F, Tolstrup K, Noorani O, Shiota T,Gurudevan S & Siegel RJ 2010 Reproducibility of proximal isovelocitysurface area, vena contracta, and regurgitant jet area for assessment ofmitral regurgitation severity. JACC: Cardiovascular Imaging 3 235–243.

[112] . Yang, W. Tsai, et al. Role of Left Atrial Reservoir Strain the RAte in Left Atrial Remodeling in Severe Mitral Regurgitation. Jornal of Medical Ultrasound, 2016.

[113] B.S. Ibrahim, Right ventricular failure, European society of cardiology, 2016, volume 14.

[114] T Poutanen, A Ikonen, et al. Left atrial volume assessed by transthoracic three-dimensional echocardiography and magnetic resonance imaging: dynamic changes during the heart cycle in children. Heart 2000.

[115] B. Pat, C. Killingsworth, T. Denney, J. Zheng, P. Powell, M. Tillson, A. R. Dillon, and L. J. Dell'Italia, "Dissociation between cardiomyocyte function and remodeling with -adrenergic receptor blockade in isolated canine mitral regurgitation," Am J Physiol Heart Circ Physiol, vol. 295, pp. H2321-7, 2008.

[116] G. Blume, C. Mcleod, Left atrial function: physiology, assessment, and clinical implications. European Journal of Echocardiography (2011) 12, 421–430.

[117] H. Kasban, M. A. M. El-Bendary and D. H. Salama. A Comparative Study of Medical Imaging Techniques. International Journal of Information Science and Intelligent System, 4(2): 37-58,2015.

[118] G. Wahba, "Spline interpolation and smoothing on the sphere," SIAM Journal on Scientific and Statistical Computing, vol. 2, p. 5, 1981.

[119] G. Wahba, "Spline interpolation and smoothing on the sphere," SIAM Journal on Scientific and Statistical Computing, vol. 2, p. 5, 1981.

[120] P. Hunter, P. Nielsen, B. H. Smaill, and I. LeGrice, "An anatomical heart model with applications to myocardial activation and ventricular mechanics," Critical reviews in biomedical engineering, vol. 20, p. 403, 1992.

[121] J. Lotjonen, P. J. Reissman, I. E. Magnin, J. Nenonen, and T. Katila, "A triangulation method of an arbitrary point set for biomagnetic problems," Magnetics, IEEE Transactions on, vol. 34, pp. 2228-2233, 1998.

[122] MICHAEL KAZHDAN Johns Hopkins University and HUGUES HOPPE. P. J. Frey and P. L. George, Mesh generation. Wiley Online Library, 2000.

[123] S. Gibson, "Constrained elastic surface nets: Generating smooth surfaces from binary segmented data," Medical Image Computing and Computer-Assisted Interventation—MICCAI'98, pp. 888-898, 1998.

[124] D. Sun, M. Rettmann, et al. Anatomic surface reconstruction from sampled point cloud data and prior models, Stud Health Technol Inform. 2014; 16:387-393.

[125] M. Kazhdan , M. Bolitho, and H. Hoppe. Poisson Surface Reconstruction Eurographics Symposium on Geometry Processing. 2006.

[126] D. Pace, P. Golland, Creating 3D heart models of children with congenital heart disease using magnetic resonance imaging, Proc. Intl. Mag. Reson. Med 23, 2015.

[127] T. Cootes, C. Taylor, D. Cooper, J. Graham, and A. Lanitis, Active shape models, Computer vision and image understanding, vol. 61, pp. 38-59, 1995.

[128] T. Cootes, G. J. Edwards, and C. J. Taylor, Active appearance models, Pattern Analysis and Machine Intelligence, IEEE Transactions on, vol. 23, pp. 681-685, 2001.

[129] J. C. Gower, "Generalized procrustes analysis," Psychometrika, vol. 40, pp. 33-51, 1975.

[130] Cerqueira MD, et al.; American Heart Association Writing Group on Myocardial Segmentation and Registration for Cardiac Imaging. Standardized myocardial segmentation and nomenclature for tomographic imaging of the heart. A statement for healthcare professionals from the Cardiac Imaging Committee of the Council on Clinical Cardiology of the American Heart Association. Circulation. 2002 Jan 29;105(4):539-42.

[131] E. Marchandise, J. Remacle, et al. Optimal parametrizations for surface remeshing. Engineering with Computers (2014) 30:383–402

[132] T. Storaaa P. Cain Tissue, et al. Motion imaging of the left ventricledquantification of myocardial strain, velocity, acceleration and displacement in a single image. Eur J Echocardiography (2004) 5, 375e385.

[133] T. Liu, M. Chen, et al. Quality improvement of surface triangular mesh using a modified Laplacian smoothing approach avoiding intersection. PLoS ONE ,2017.

[134] A. Sheffer, E. Praun and K. Rose. Mesh Parameterization Methods and Their Applications. Foundations and Trends in Computer Graphics and Vision, Vol. 2, No 2 (2006) 105–171 2006.

[135] Li J. Denney Ts. Left ventricular motion reconstruction with a prolate spheroidal B-spline model. Phys. Med. Biol. 2006.51.

[136] Osman NF. McVeigh ER. Imaging heart motion using harmonic phase MRI. IEEE Trans Med Imaging 2000;19:186-202.

[137] Denney TS. McVeigh ER. Model-free reconstruction of three-dimensional myocardial strain from planar tagged MR images. I Magn Reson Imaging, 1997;7:799-810.

[138] C.G. Schiros, M.I. Ahmed, et al. Importance of Three-Dimensional Geometric Analysis in the Assessment of the Athlete's Heart. Am J Cardiol 2013; 111:1067e1072.

[139] M.I. Ahmed, J.D. Gladden, et al. Increased Oxidative Stress and Cardiomyocyte Myofibrillar Degeneration in Patients with Chronic Isolated Mitral Regurgitation and Ejection Fraction >60%. Journal of the American College of Cardiology, Vol. 55, No. 7, 2010

[140] M.I. Ahmed, J.D. Gladden, et al. A Randomized Controlled Phase IIb Trial of Beta1-Receptor Blockade for Chronic Degenerative Mitral Regurgitation. Journal of the American College of Cardiology. Vol. 60, No. 9, 2012.

[141] B. Pat, C. Killingsworth, et al. Mast Cell Stabilization Decreases Cardiomyocyte and LV Function in Dogs with Isolated Mitral Regurgitation, Journal of Cardiac Failure Vol. 16 No. 9 2010.

[142] K. Gaddam, C. Corros, Rapid Reversal of Left Ventricular Hypertrophy and Intracardiac Volume Overload in Patients with Resistant Hypertension and Hyperaldosteronism A Prospective Clinical Study. Hypertension. 2010 May;55(5):1137-42. doi: 10.1161/HYPERTENSIONAHA.109.141531. Epub 2010 Mar 29.

[143] C.G. Schiros, M.I. Ahmed, et al. Mitral annular kinetics, left atrial, and left ventricular diastolic function post mitral valve repair in degenerative mitral regurgitation. Frontiers in cardiovascular medicine, 2015, Volume 2, Article 31.

[144] J. Zheng, D. Yancey, et al. Increased Sarcolipin Expression and Adrenergic Drive in Humans with Preserved Left Ventricular Ejection Fraction and Chronic Isolated Mitral Regurgitation. Circ Heart Fail. 2014 January 1; 7(1): 194–202. doi:10.1161/CIRCHEARTFAILURE.113.000519.

[145] Cheng S, Fernandes VR, Bluemke DA, McClelland RL, Kronmal RA, Lima JA. Age-related left ventricular remodeling and associated risk for cardiovascular outcomes: the Multi-Ethnic Study of Atherosclerosis. Circ Cardiovasc Imaging, 2009. 2(3): p. 191–8. pmid:19808592.

[146] F. J. Villarreal, W. Lew, et al. Transmural myocardial deformation in the ischemic canine left ventricle. Circulation Research 1991;68:368-381.

[147] http://mae.uta.edu/~lawrence/me5310/course_materials/me5310_notes/7_Triangular_Elements/7-2_Constant_Strain_Triangle_CST/7-2_Constant_Strain_Triangle_CST.htm

[148] S. Cheng, V. Fernandes, et al. Age-Related Left Ventricular Remodeling and Associated Risk for Cardiovascular Outcomes The Multi-Ethnic Study of Atherosclerosis. Circ Cardiovasc Imaging. 2009;2:191-198.

[149] B. Venkatesh, S. Hong, et al. Age and Gender Related Left Atrial Remodeling With Magnetic Resonance Imaging: Multi Ethnic Study of Atherosclerosis. Circulation. 2017;136:A21264.

[150] Gardin JM, Siscovick D, Anton-Culver H, Lynch JC, Smith VE,Klopfenstein HS, Bommer WJ, Fried L, O’Leary D, Manolio TA. Sex, age, and disease affect echocardiographic left ventricular mass and systolic function in the free-living elderly: the Cardiovascular Health Study.Circulation. 1995;91:1739 –1748.

[151] Levy D. Left ventricular hypertrophy: epidemiological insights from the Framingham Heart Study. Drugs. 1988;35(Suppl 5):1–5.

[152] K. Kaku, M. Takeuchi, et al. Age-Related Normal Range of Left Ventricular Strain and Torsion Using Three-Dimensional Speckle-Tracking Echocardiography. Journal of the American Society of Echocardiography, 2014,Volume 27, Issue 1, Pages 55–64.

[153] D. Patel, C. Lavie, et al. Clinical Implications of Left Atrial Enlargement: A review. The Ochsner Journal, 2006, 9:291-196.

[154] B. Ren, L. Laat, et al. Left Atrial Function in Patients with Mitral Valve Regurgitation. Am J Physiol Heart Circ Physiol. 2014 Nov 15;307(10):H1430-7. doi: 10.1152/ajpheart.00389.2014. Epub 2014 Sep 12.